University of Southampton

Robust Design of Film-cooled High-pressure Turbine Blades in the Face of Real Geometric Variations

by

Jan Kamenik

A thesis submitted in partial fulfillment of the requirements
for the degree of Doctor of Philosophy

in the

Rolls-Royce University Technology Center for Computational Engineering
Computational Engineering and Design Group
Faculty of Engineering and Physical Sciences

September 2018

UNIVERSITY OF SOUTHAMPTON

ABSTRACT

Rolls-Royce University Technology Centre for Computational Engineering
Computational Engineering and Design Group
Faculty of Engineering and Physical Sciences

Doctor of Philosophy

ROBUST DESIGN OF FILM-COOLED HIGH-PRESSURE TURBINE BLADES IN THE FACE OF REAL GEOMETRIC VARIATIONS

by Jan Kamenik

The aerothermal performance of turbine blades is negatively affected by unavoidable variations, for example, those due to the manufacturing process. No blade ever exactly conforms to its nominal design intent geometry and variations, even slight ones, can have detrimental effects on aerodynamic performance, blade temperatures and blade lifespan. As opposed to conventional deterministic design, robust design is one option to tackle the problem posed by deviations by incorporating them directly into the design process. In robust design, both performance mean and scatter can be optimized concurrently to make blades less sensitive. Such a workflow, for the first time based on real variations extracted from 58 digitized 3D turbine blade scans from two turbofan engines, is presented and applied to aerodynamically optimize an industrial turbine rotor. The approach uses high-fidelity geometric models, a non-intrusive uncertainty quantification method and efficient robust optimization to effectively locate Pareto-optimal robust designs. One selected design is validated and shown to be desensitized to the underlying observed manufacturing variability, which is proven to be crucial to obtain realistic results. In addition, the first probabilistic assessment of film cooling hole variations on blade performance is also presented. An accurate reverse engineering workflow for blade shape and film cooling hole variations is used. Particular focus is placed on the trailing edge and the trailing edge film cooling holes due to their impact on performance, for example on capacity. It is shown that positional deviations of film cooling holes from nominal are largely due to blade shape variations as opposed to other sources. Therefore, a new model for film cooling variability termed “virtual film cooling hole manufacture”, which replicates the real manufacturing process of the holes, is introduced. The methodology essentially exploits the finding that blade shape variations are a major cause of film cooling hole variations. Through a comparison with an uncooled setup at the same operating point, it is also shown that trailing edge film cooling hole variability itself is important, especially

for capacity settings. The analysis model choice, either continuous film cooling strips with uniform flow, discrete holes or a combination of both, impacts uncertainty quantification options. The presented workflow enables comprehensive uncertainty quantification and robust design optimization of film-cooled turbine blades with fully-featured geometric models and includes realistic variations of the entire blade shape, of the shroud and of all film cooling holes. Artificially constructed blade models are shown to exhibit the same performance variation as the original measured sample of blade scans and can be used to compute output blade performance statistics for uncertainty quantification.

Contents

List of Figures

List of Tables

Declaration Of Authorship

I, Jan Kamenik, declare that this thesis and the work presented in it are both my own and have been generated by me as the result of my own original research. I confirm that:

1. This work was done wholly or mainly while in candidature for a research degree at this University;

2. Where any part of this thesis has previously been submitted for a degree or any other qualification at this University or any other institution, this has been clearly stated;

3. Where I have consulted the published work of others, this is always clearly attributed;

4. Where I have quoted from the work of others, the source is always given. With the exception of such quotations, this thesis is entirely my own work;

5. I have acknowledged all main sources of help;

6. Where the thesis is based on work done by myself jointly with others, I have made clear exactly what was done by others and what I have contributed myself;

7. Parts of this work, including verbatim sections, have been published at conferences or in peer-reviewed journals:
   Kamenik, Toal, et al. (2018)
   Kamenik, Voutchkov, et al. (2018)

This work has received financial support from the EPSRC Centre for Doctoral Training in Next Generation Computational Modelling grant EP/L015382/1 and Rolls-Royce plc.

Signed: .....

Date: .....

Acknowledgements

First and foremost, I would like to express my sincere gratitude to my supervisors, Prof. Andy J. Keane and Dr. David J. J. Toal, for their continuous support and guidance throughout my research. I would also like to thank Dr. Ivan Voutchkov for his work on OPTIMAT v2 and for making available to me the necessary computational power. Also, this work would not have been the same without the close collaboration with staff from TU Dresden's Chair of Turbomachinery and Flight Propulsion as well as Rolls-Royce Germany. In particular, I would like to thank Lars Högner for his help and expertise with the in-house tools developed at TU Dresden and Dr. Marcus Meyer from Rolls-Royce Germany for the provision of the blade scans. Moreover, I also thank Dr. Shahrokh Shahpar from Rolls-Royce Derby for his training, improvement suggestions and for the original project idea. In addition, I am grateful to Frederic Goenaga from Rolls-Royce Bristol for showing me the manufacturing process and for his expert feedback on my work. I would also like to thank David Radford from Rolls-Royce Derby for his assistance with HYDRA. Furthermore, I really appreciate all advice regarding the NX API from Dr. Leran Wang and Dr. Xu Zhang. Thanks are also due to Dr. Ron Bates and Dr. Akin Keskin for their help with obtaining permission for publication. Finally, I am grateful for the financial support received from the EPSRC and Rolls-Royce through grant EP/L015382/1.

Nomenclature

Abbreviations

B2P, P2B	Blade2Parameter, Parameter2Blade
BCL	BladeCLeaner
BC	Boundary condition
BR	Blowing ratio
CDF	Cumulative distribution function
CFD	Computational fluid dynamics
CI	Confidence interval
COI	Coefficient of importance
DNS	Direct numerical simulation
DOE	Design of experiments
FC	Film cooling
FVM	Finite volume method
GOM	GOM GmbH, manufacturer of optical metrology systems
GP	Gaussian process
HPC, HPT	High-pressure compressor, high-pressure turbine
IR	Momentum flux ratio
LE, TE	Leading edge, trailing edge
MAE	Maximum absolute error
MC	Monte Carlo
MLE	Maximum likelihood estimation
MVM	Mean value model
NISC	Non-intrusive stochastic collocation
NISP	Non-intrusive stochastic projection
NSGA-II	Non-dominated Sorting Genetic Algorithm II
NURBS	Non-uniform rational basis spline
PC	Polynomial chaos
PCE	Percentage error
PDF	Probability density function

PS, SS	Pressure side, suction side
PSO	Particle swarm optimization
QMC	Quasi-Monte Carlo
RANS	Reynolds-averaged Navier-Stokes
RD	Robust design
RDO	Robust design optimization
RE	Reverse engineering
RMSE	Root-mean-square error
RQMC	Randomized quasi-Monte Carlo
RR, RRD	Rolls-Royce, Rolls-Royce Deutschland
SA	Spalart-Allmaras
STL	STereoLithography file format
TMF	Thermo-mechanical fatigue
UQ	Uncertainty quantification

Physical Quantities

Symbol	**Units**	**Description**
α, β	$^\circ$	Film cooling model injection angles
c_p, c_v	$\mathrm{J\,K^{-1}}$	Specific heat capacity at constant pressure, volume
δ	m	Boundary layer displacement thickness
η	%	Isentropic efficiency
$\overline{\eta}_{FC}$	%	Laterally averaged film cooling effectiveness
h	$\mathrm{J\,kg^{-1}}$	Specific enthalpy
κ	–	Heat capacity ratio
$\dot{m}$	$\mathrm{kg\,s^{-1}}$	Mass flow rate
L	m	Hole length
P	m	Hole pitch
p	Pa	Pressure
ϕ	$\mathrm{ms\sqrt{K}}$	Inlet capacity
ρ	$\mathrm{kg\,m^{-3}}$	Density
r	m	Radius
s	–	Non-dimensional span
$\boldsymbol{\tau}$	N m	Torque
T	K	Static temperature
$\vec{u}$	$\mathrm{m\,s^{-1}}$	Circumferential velocity
ν	$\mathrm{m^2\,s^{-1}}$	Kinematic viscosity
$\tilde{\nu}$	–	Spalart variable

$\vec{v}$	$\mathrm{m\,s^{-1}}$	Absolute velocity
w	$\mathrm{J\,kg^{-1}}$	Specific work
$\vec{w}$	$\mathrm{m\,s^{-1}}$	Relative velocity
Ω	$\mathrm{rad\,s^{-1}}$	Rotational speed

Mathematical Symbols

COI	Coefficient of importance
C_v	Coefficient of variation
$\mathbf{\Delta\overline{p}}$	Vector of averaged delta parameters
$\mathbf{d}$	Vector of design variables
E	Expected value
h	Optimal kernel bandwidth
θ, q, λ	Kriging hyperparameters
N	Number of samples
$\mathbf{p}$	Vector of design variables
PCE	Percentage error
R^2	Coefficient of determination
R_s	Specific gas constant
r_s	Spearman's rank correlation coefficient
$\hat{s}$	(Unbiased) sample standard deviation
$\hat{s}^2$	(Unbiased) sample variance
σ	Standard deviation
Var	Variance
$\overline{x}$	Sample mean
$\mathbf{\Psi}$	Kriging correlation matrix

Chapter 1

Introduction

Individual engine components such as the fan, compressor and turbine blades in modern aircraft engines are always slightly different from their nominal CAD design intent. The final designs are typically the result of complex multi-objective, multi-constraint and multidisciplinary optimization procedures. Such designs can be very sensitive to inevitable geometric variations or to varying operating conditions. In reality, blades do not exactly conform to the nominal design intent geometry and almost never operate at the nominal conditions they were initially designed for. For example, deviations can stem from manufacturing variations, corrosion, foreign object damage, creep, fatigue and operating condition abnormalities such as hot streaks. As described in detail in Chapter 2, it is well-known that even very small perturbations in certain areas, whatever the cause, can have substantial detrimental effects on blade performance or even cause initially satisfied constraints to be violated (Duffner, 2008; Högner, Voigt, Nasuf, et al., 2016; Montomoli, Carnevale, et al., 2015; Scharfenstein, Heinze, et al., 2013). Often, engines, stages or blades are tested and found not to possess the intended performance, e.g., to perform less efficiently or to wear more quickly than intended. Typically, the consequence is engine performance degradation and potentially even catastrophic failure.

For fan and compressor blades aerodynamic performance measures such as efficiency, pressure ratio and stability margin are the main focus, whereas for film-cooled high-pressure turbine (HPT) blades both aerodynamic and thermal (aerothermal) performance can be negatively impacted. This includes aerodynamic quantities of interest such as pressure losses, capacity and work produced on one hand, and thermal quantities of interest such as the blades' metal temperature and as a consequence thereof blade life, on the other. To increase engine fuel efficiency and specific work, the turbine inlet temperature has gradually increased in the past. Today's HPT blades must withstand extreme temperatures and heat loads. Film cooling is used to shield the blades from this hot gas along with other cooling techniques, but blades can fail and be damaged

from high temperature oxidation, creep, corrosion or thermo-mechanical fatigue (Sidwell, 2004). Engines are monitored, inspected and repaired in case of damage, with associated downtime and maintenance costs. On top of this, large performance gains become increasingly harder and costlier to achieve, whilst adverse effects due to variations become more and more relevant. This motivates the need to include uncertainties into the design process, the science of which is termed uncertainty quantification (UQ).

Even though the adoption of UQ in industry as of today is still limited, the commercial success of an entire engine could depend on its integration in the near future. As shown in Fig. 1.1, the basic idea is to incorporate variations through a UQ workflow into an optimization loop. This is called robust design optimization (RDO). The main goal of RDO, in this instance, is to design turbine blades, which operate well despite unavoidable variations, *by design*. In the past, the problem of manufacturing variations to some degree was adressed by safety factors and strict control of tolerances, which, however, can quickly lead to overengineering and increased costs (Keane and Nair, 2005). In contrast, the fundamental idea of RDO here is a non-deterministic methodology to create robust turbine blades *by design*, which is vital in moving away from suboptimal safety factors and the expensive practice of tightening quality control tolerance limits. The origin of the term robust design goes back to Japanese automotive engineer Genichi Taguchi and his design philosophy to improve part quality by minimizing effects of variations (Taguchi and Rafanelli, 1993).

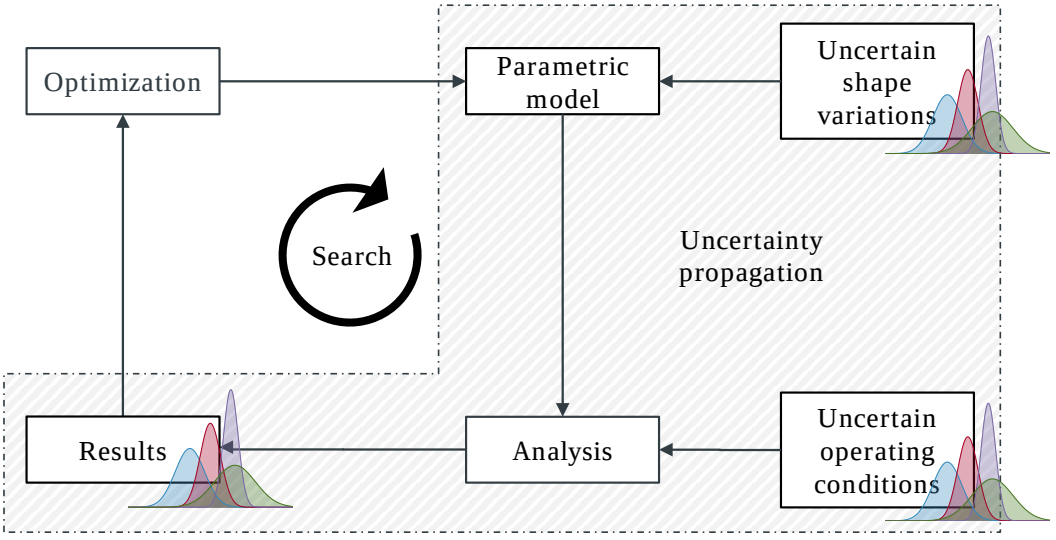

Figure 1.1: A basic robust design optimization workflow

Robust design optimization or simply robust design could be described as the search for designs on plateaus or in flat regions of the design space. It is inherently multi-objective and simultaneously seeks to minimize typically both the *mean* as well as the *variance* of an objective function. In order to illustrate the concept of this methodology,

Fig. 1.2 depicts a simple 1D objective function $f(x)$ of a single input variable x. Visually, it is clear where the regular deterministic optimum lies. However, as an example Gaussian noise for the input can be assumed, although in reality this should ideally be based on real measurements. The result are two very different responses: although point μ_1 is at the deterministic optimum, it exhibits a very high variance in comparison to the other *robust* solution lying on a plateau. This is slightly worse in terms of performance, but has much less variance. Finding a design such as the one at μ_2 is the aim of robust design.

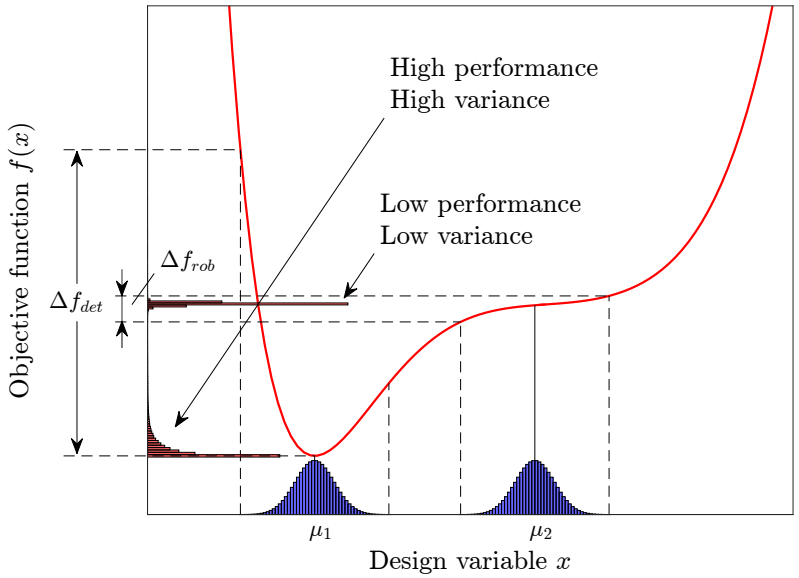

Figure 1.2: Robust design concept

1.1 Scope & Contributions

The main contribution of this work is a coherent robust design methodology for HPT blades based on real geometric variability. This not only includes variations of the blade shape, but also variations of the FC holes, which are introduced through a novel model for FC variability called “virtual manufacture”. The methodology rests on a set of measured turbine scans, which represent real variations from the manufacturing process. The scope of this thesis is limited to aerodynamic performance measures such as isentropic efficiency, capacity and specific work. The workflow presented here does not feature other simulations, e.g., conjugate heat transfer, and does not consider related quantities such as film cooling performance parameters, e.g., film cooling effectiveness, or quantities of interest such as metal temperatures and blade life. Nevertheless, the methodology is universally applicable to any turbine blade and works with realistic, fully-featured geometric models. In line with current industry standards, steady-state Reynolds-

averaged Navier-Stokes (RANS) computational fluid dynamics (CFD) simulations are used to evaluate aerodynamic blade performance.

The main contributions of this thesis to the field are:

- A coherent workflow for robust design optimization (RDO) of HPT blades with real variations of the entire blade shape
- A probabilistic assessment of the impact of real turbine blade shape and FC hole variations on blade performance with accurately reverse-engineered geometries and high-fidelity CFD simulations
- A model for real film cooling hole variations termed “virtual manufacture”, which replicates the real manufacturing process of FC holes
- An uncertainty quantification (UQ) methodology for film-cooled HPT blades with realistic blade shapes and FC holes

1.2 Outline

This thesis is broadly structured as follows:

Chapter 1 serves as an introduction to the problem at hand and briefly outlines the basic concepts of UQ and RDO. Chapter 2 presents an overview of the relevant literature and describes results of previous research about UQ and RDO of HPT blades. Chapter 3 introduces the turbine blade sample to be considered in this work and details the computational approach to reverse engineering of scanned blade geometries used here. A parametric model to construct any number of realistic HPT blades for UQ studies is also presented. Chapter 4 explains the general CFD approach and illustrates models, meshes and quantities of interest. Chapter 5 describes a novel RDO workflow with real variations of the entire blade shape and its application to an industrial HPT blade. Subsequently, Chapter 6 also considers film cooling and variations of FC holes. Among others, a probabilistic assessment of the impact of FC holes is carried out, the “virtual manufacture” method is introduced and the comprehensive UQ method for film-cooled HPT blades is presented. Chapter 7 concludes the thesis, summarizes all findings and presents recommendations for future work. Some specific details from previous chapters are placed in Appendices B - L. Due to proprietary content, some figures are only available in a non-public, restricted section, for which access can be sought.

Chapter 2

Literature Review

The design of turbine blades is complex and highly multi-disciplinary. Engineering disciplines such as fluid dynamics, thermodynamics, solid mechanics, materials science and manufacturing engineering are all essential and interact with each other. Elaborate aerodynamic blade shapes are designed to efficiently extract energy from the flow to produce work with minimal losses. Blades also have to withstand high mechanical and thermal loads with temperatures in excess of 1700 K. Such high combustor exit temperatures well above the material's melting point require surface coatings and cooling schemes, both internal and external, to protect the blades of the first-stage. As a consequence, turbine blade life is a limiting factor and a major design constraint. Manufacturing restrictions, e.g., due to the cooling passages and holes, must be considered too. Additionally, conflicting requirements, e.g., maximal blade life vs. higher temperatures vs. minimization of coolant mass flow rate, must be taken into account. Each discipline interacts with one another and a balanced design compromise has to be found. Ideally, the final turbine blade design is the result of a multi-objective, multi-constraint and multidisciplinary optimization process, where all of this has been considered concurrently. Another important aspect in particular for HPT blades is lifing, i.e., the determination and prediction of the lifespan of a blade. Component lifing of turbine blades typically includes analyses of the main failure mechanisms: creep due to high temperatures, governed by an Arrhenius-type law, fatigue due to repeated load cycling, typically described with the Coffin-Manson curve method, oxidation or high-temperature corrosion, and spalling of the thermal barrier coating, if there is one. However, even if a blade is predicted to meet all demands, the problem is that deterministically designed turbine blades are prone to geometric and operational variations, which can negatively affect aerothermal performance and blade life. As an example of an operational uncertainty, Fig. 2.1 depicts a film-cooled HPT rotor damaged in operation by sand. It is evident that sand deposits have partially blocked FC holes, which can lead to insufficient cooling, lower film effectiveness and reduced blade life (Telisinghe, 2013). Similarly, Fig. 2.2

illustrates the damage done to a HPT blade through a before-and-after comparison after 15 000 h (2700 cycles) in operation.

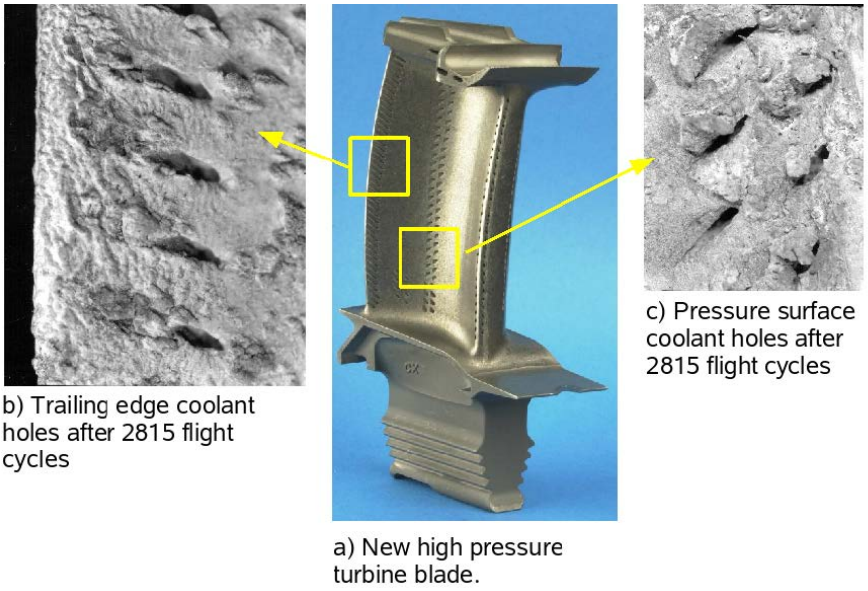

Figure 2.1: Film-cooled HPT rotor affected by sand in operation. Reproduced from the thesis by Telisinghe (2013)

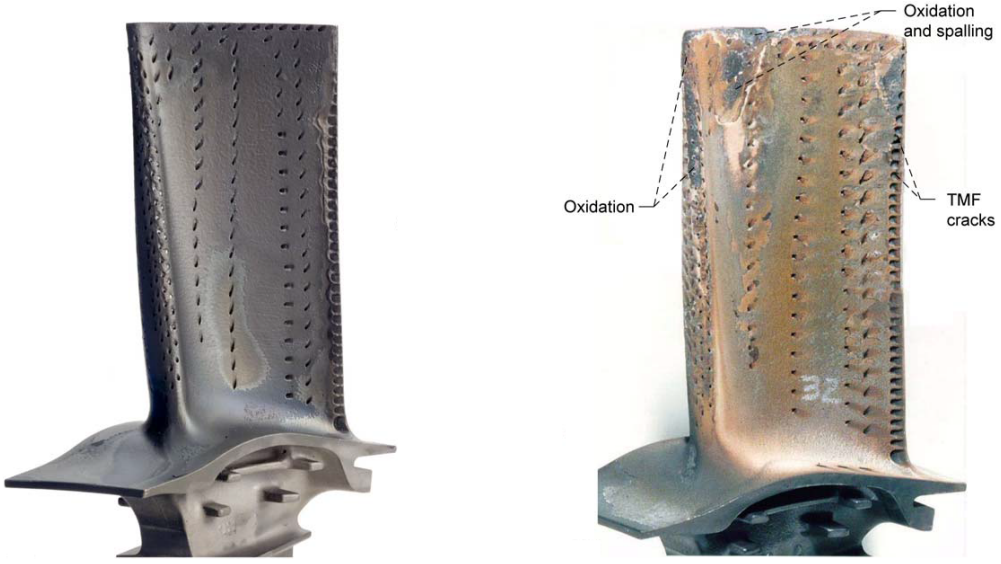

(a) Before (b) After

Figure 2.2: Before-and-after comparison after 15 000 h (2700 cycles) in operation. Reproduced from Zaretsky, Litt, et al. (2012)

2.1 Effects of High-pressure Turbine Blade Variations

One of the main sources on the effects of variations on turbomachinery performance is the book by Montomoli, Carnevale, et al. (2015), which describes past studies involving both compressor and turbine blades, their effects and relevant stochastic methods for UQ. The main HPT uncertainties are the turbine entry temperature magnitude and distribution, real geometric effects and the coolant system. Unsurprisingly, especially the temperature magnitude and distribution is crucial for blade life. Ever-increasing turbine entry temperatures are a particular problem for HP turbine blades and their blade life. The effect of four different inlet temperature distortions and hot streaks has been studied by Salvadori, Montomoli, et al. (2011) using the MT1 HPT stage and unsteady phase-lagged CFD. The results show large variations of static pressure and Nusselt number distributions due to the non-uniformities. As an example for actual geometrical blade features, Montomoli, Massini, et al. (2011) found small uncertainties of the tip gap and fillet radius to have a substantial impact on the component life and efficiency due to altered heat loading and a leakage mass-flow.

Other relevant studies by Montomoli, Carnevale, et al. (2015) include the prediction of metal temperatures in a cooled HP vane with turbulence intensity, thermal barrier coating (TBC) thickness and hot core location as uncertain variables, the influence of PDF tails on UQ predictions, the effects of metal temperature variations during a transient, the impact of tip gap and fillet variations and the impact of filleted edge variations on heat transfer. Montomoli, Carnevale, et al. (2015) also highlight the uncertainty involved in the boundary conditions of simulations due to the difficult measuring environment. Commonly used thermocouples suffer from a number of measurement uncertainties at high temperatures, which at 1500 K can be as high as 1 % or ±15 K. Turbulence levels are equally difficult to measure. Ames and Moffat (1990) numerically modelled the effects of high intensity large-scale turbulence on boundary layer heat transfer of a flat plate with turbulence intensities of up to 19 % and integral lengths scales of 4 cm to 6 cm. The maximally observed increase in heat transfer was 28 %. The experimental study by Krishnamoorthy and Sukhatme (1989) shows similar results with an overall increase of heat transfer coefficients, but also different magnitudes for PS and SS. Voigt, Mücke, et al. (2004) assessed turbine blade lifetimes using FEA and various stochastic parameters, including load, gas and material parameters related to a 3D HPT blade model. This research focussed on damage prediction from thermo-mechanical fatigue (TMF). CFD simulations were not part of this study but the heat transfer coefficients themselves were also stochastic variables. Results included probabilities of failure and sensitivities to the material (highest sensitivity to TMF) and loading parameters.

Other past studies involving the effects of manufacturing variability are also of particular interest for this work. For example, the effects of manufacturing variability on the aerodynamic performance of turbine vanes have been investigated using 2D MISES CFD and principal component analysis (PCA) by Duffner (2008). It was found that the regions most sensitive to perturbations were the throat and trailing edge (TE). Upstream of the throat, performance was found to be nearly completely insensitive to perturbations. Changes in the minimum throat area and shock waves were identified as the main underlying mechanisms. Another study of a Rolls-Royce HP nozzle guide vane (NGV) explored the influence of geometric variations on capacity settings using parametric NGV TE slots (Högner, Voigt, Nasuf, et al., 2016). A one-factor-at-a-time analysis and MC simulations were used and TE position and the suction side (SS) profile offset were found to impact capacity significantly. In another UQ study, manufacturing data was distilled into tolerances for four parameters: ±0.3 mm for the chord length, ±20′ (arcminutes) for the stagger angle, −0.1 mm for the TE radius and ±0.15 mm for the blade height (Kolmakova, Baturin, et al., 2014). This study found stagger angle variations and TE radius variations to have the largest impact on HPT performance. In another paper using real manufacturing variations and a 3D RANS CFD model of an HP turbine stage, Scharfenstein, Heinze, et al. (2013) identified the semi-major axis of the TE ellipse as the most important parameter for efficiency. The stagger angle was singled out as the most important parameter for stage capacity and reaction. The manufacturing variations were based on 500 digitized scans of new and used high-pressure (HP) turbine blades with an accurate high-resolution, structured-light 3D scanner (Heinze, Meyer, et al., 2014).

HPT blades either have continuous TE FC slots, discrete holes or a combination of both and many different configurations exist. Slots, which are mechanically weaker than discrete holes, can provide a more uniform protective film and the Coandă effect can help ensure the film sticks to the surface without lifting off (Yang and Hu, 2012). The geometry to be considered in this work has discrete PS holes located upstream of the TE. Besides this PS ejection configuration, other often used options are TE ejection and PS cutback ejection.

In general, TE geometry and TE FC holes are sensitive to manufacturing deviations due to their influence on mass flow rate, minimum throat area and capacity (Montomoli, Carnevale, et al., 2015). Film cooling also leads to aerodynamic losses from various sources, as summarised in Fig. 2.3, and a compromise solution with minimal losses and sufficient thermal protection has to be found. In another notable paper by Rehder (2009), the effects of coolant ejection on losses and their sources were experimentally investigated. An HPT cascade with three different TE cooling configurations, viz., central TE ejection, a TE with PS cut-back and slot and a PS FC row of holes, was studied and

the contribution of each type of loss was investigated in detail. FC through central TE coolant ejection was observed to exhibit the lowest mixing losses (and the lowest overall losses) in comparison with the other two configurations with PS blowing.

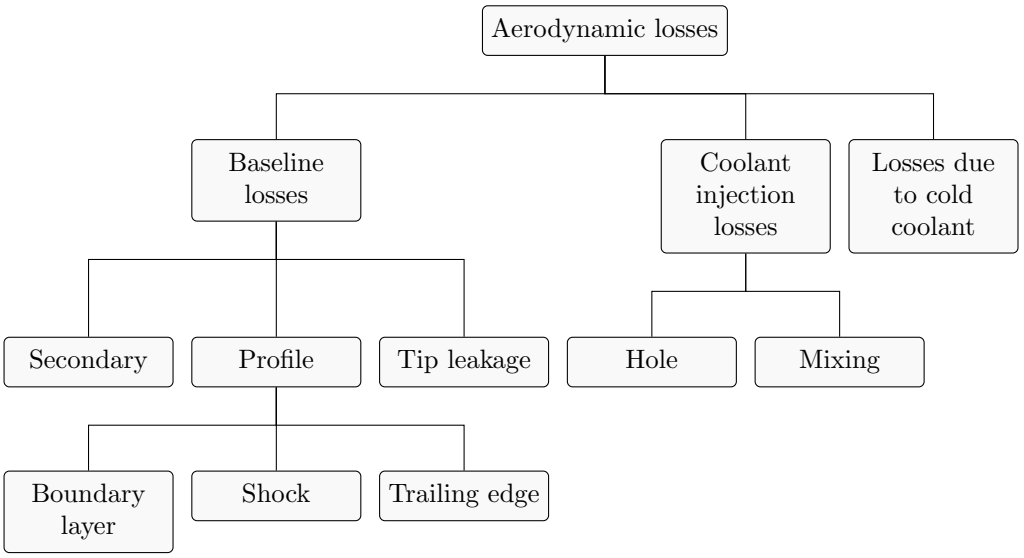

Figure 2.3: Sources of aerodynamic losses reproduced from the thesis by Day (1997)

Moreover, capacity variations are particularly undesirable, since the turbine flow capacity is matched with the compressor. Indeed, HPT and high-pressure compressor (HPC) stages are typically coupled and tuned to operate together. This process is called turbine-compressor matching and its aim is to find suitable corresponding operating points for each component, e.g., in terms of mass flow rate and work. Variations of one component can therefore also negatively impact other components or the entire engine. For example, incorrect capacity settings lead to incorrect performance calculations, which in turn can lead to mismatch of stages and as a consequence to an inaccurate performance evaluation of the whole engine (Povey, Sharpe, et al., 2011). Other effects on blade life, the work generated by downstream turbine sections and upstream compressor sections are possible too. One obvious influence on capacity is the geometric variability of the blades, which can lead to variations of the total throat area. Povey, Sharpe, et al. (2011) list the following effects influencing capacity: losses, 3D pressure distribution, throat area, turbulence, FC air, 3D flow structures, BL separation, TE geometry, TE injection angle and TE FC blowing ratio. Aerodynamic phenomena such as expansion waves, shock waves and wake shedding all occur near the TE. Given all these influences, it is clear that an accurate prediction of capacity is difficult, even for a deterministic case. Moreover, the ejection of the TE coolant leads to a blockage effect and variations of the TE FC hole geometry, e.g., due to the manufacturing process, may have a significant influence on the capacity. Although different configurations exist, the blades analyzed later in Chapter 6

have discrete PS holes located upstream of the TE. These TE holes are particularly prone to manufacturing variations due to rear blade shapes with small ejection angles and can impact blade performance, esp. capacity settings. Choked flow entails the additional challenge that flow angles can deviate and negatively impact downstream stage performance (Hendricks, 2016).

Using a flat plate model, Bunker (2009) identified the FC hole diameter, length-to-diameter ratio, impingement hole axial and lateral spacing-to-diameter ratio and the TE exit slot aspect ratio as important parameters. Notably, FC hole diameter variations of 10 % were estimated to reduce blade life by 33 %. A study by Moeckel, Darmofal, et al. (2007) based on 2D HPT blade sections and probabilistic thermal FEA with an empirical 1D flow network submodel found that the TE FC hole diameter is most sensitive to creep. This study's outcome was to suggest new blade tolerances, as opposed to inbuilt robustness from robust design, however. Similarly, Montomoli, Carnevale, et al. (2015) estimated large effects caused by hole diameter and length-to-diameter variations. A 40% increase in mean metal temperature was estimated to cause a residual life decrease of 83% using the Larson-Miller relation. Another complication is that combustor temperature exit profiles also impact blade life and are very difficult to measure. Both mean temperature and local hot spots are important. In another paper, Bohn and Krewinkel (2006) examined different FC hole variations deterministically. Specifically, the effects of missing thermal barrier coating (TBC) on the edges of FC holes and the effects of FC hole obstructions, e.g., the complete closure of an FC hole as the worst-case scenario, were investigated. Their computational setup examined a TBC-coated film-cooled flat plate (hole diameter 0.2 mm) with conjugate heat-transfer simulations and with BC conditions derived from an actual engine. The results show sizable differences for all configurations, but especially for the worst-case with closed holes. Sidwell (2004) investigated the impact of variability on blade cooling and oxidation life. When modeling effects from heat transfer, the findings show that every blade must be modelled separately in order to find blades with low coolant flow and, as a consequence, higher metal temperatures and reduced blade life. Other outcomes of this research are a flow network model and a selective assembly method to desensitise blades from manufacturing variability.

2.2 Robust Design of High-pressure Turbine Blades

This section serves only to describe past applications of robust design to HPT blades, rather than details about the underlying methods themselves, which are described later. For more details about UQ and RDO methods, refer to Sec. 5.1 and Sec. 5.2.1.

In general, RDO is not yet widely adopted in industry and subject to a lot of current research (Bestle, Flassig, et al., 2011; Javed, Pecnik, et al., 2016; Keane, 2009, 2012;

Vinogradov, Kretinin, et al., 2016). Past RDO studies often lack real manufacturing data, and probability distributions for uncertain parameters are often made-up. For example, uniform probability distributions were assumed for a centrifugal impeller optimization (Javed, Pecnik, et al., 2016). Similarly, a β-distribution was assumed for compressor tip clearance variations (Seshadri, Shahpar, et al., 2014).

The problem is that in reality probability distributions could be entirely different, e.g., in terms of range, shape and correlation, but the variability model is crucial for the final design and its performance. There also have been studies with underlying variability models based on measurements. In one such study of compressor blades, probability distributions and correlations were approximated with a truncated multivariate normal PDF and each blade was analyzed with three 2D MISES solver runs (Bestle, Flassig, et al., 2011). The study hence relied on the assumption that each parameter's marginal distribution is also normally distributed. The restriction to 2D CFD was chosen due to the long CFD runtimes, but three-dimensional effects in the flow were hence neglected. The method to be presented in this thesis improves upon both of these aspects (among others). In another study, a 3D RANS-based robust optimization of a fully-featured turbine blade with PDFs based on over 100 measurements was carried out (Vinogradov, Kretinin, et al., 2016). But besides three operational uncertainties, this study only considered the LE FC row and the tip gap as the sole two geometric noise parameters as the main focus was the inclusion of conjugate heat transfer to compute the actual metal temperatures.

As an example of a deterministic aerothermal optimization in the literature, El Ayoubi (2014) optimized a film-cooled HPT blade with regard to aerodynamic efficiency and FC parameters using RANS-based CFD. Coolant flow parameters and cooling hole geometric design variables were investigated separately using the film-cooled von Karman Institute (VKI) HPT blade. For the coolant flow parameters, two design variables, viz., coolant to mainstream temperature ratios and pressure ratios, for two SS rows were optimized using an artificial neural network. The average FC efficiency was maximized and aerodynamic losses were minimized. Three geometric design variables, viz., compound angle, conical expansion angle and L/D, were used as geometric hole parameters. The thermally optimal hole was found to be a large expanded hole with a high compound angle. Improvements of the cooling efficiency in excess of 100 % were found. In another thesis, Modgil (2013) optimized a Rolls-Royce turbine stage using non-intrusive stochastic collocation. In aeroelasticity, two of the most important phenomena, which may lead to dangerous mechanical failures, are forced response and flutter. In the thesis, a forced response aeromechanics analysis involving CFD and FEA was undertaken to assess the risk of turbine blade failure due to vibration-induced high-cycle fatigue (HCF). In the approach, the VKI blade was first optimized deterministically with regard to aerodynamic aspects.

Then, combined unsteady CFD and FEA in an UQ study with three uncertainties (modal damping, Young's modulus and engine speed) was used to investigate the likelihood of material failure from HCF. The final result of the approach was a probabilistic Goodman diagram, which plots mean stress vs. alternating stress.

2.3 Summary

The previous sections have made clear that variations in the context of HPT blades are a known problem. As has been shown, extensive research has been carried out on a multitude of geometries ranging from flat plates to HPT blades and for a plethora of problems, including the mechanical, thermal and aerodynamic performance. Important conclusions for this thesis are that currently a universally accepted and coherent RDO methodology featuring real variations of the entire blade shape does not exist. A real RDO workflow, not just UQ, is required by research and development departments to actually make use of robust design in practice. Also, the effects of FC hole variations on HPT blades have not been analyzed in previous studies in the literature and have not been part of UQ or RDO studies. It is the aim of this thesis to try to address some of these shortcomings and to suggest solutions for both aspects. The result will be a coherent RDO methodology with real variations for the entire blade shape and FC cooling holes.

Chapter 3

Turbine Blade Scans & Reverse Engineering

This chapter introduces the sample of turbine blade scans and the accurate reverse engineering workflow used to construct blade models for subsequent computational analysis. Both are essential for the approaches described in Chapter 5 and Chapter 6.

3.1 Turbine Blade GOM Scan Sample

Fifty-eight HP turbine blade scans in the form of STL files (stereolithography file format) were provided by Rolls-Royce Germany. Although the blades have been in service briefly with two different airlines and were taken from *used*, *low-cycle* engines, they essentially represent manufacturing variations. All blades were digitized at TU Dresden as part of the HolisTurb project (Heinze, 2013) using the scanning system GOM ATOS SO 4M, a high-resolution, structured-light 3D scanner (Heinze, Meyer, et al., 2014). Due to their significance for this work, some facts from these references are repeated here: the measurement accuracy of the scan system according to the manufacturer is 5 µm, but previous internal investigations with a test specimen revealed that the real observed measurement accuracy is around 8 µm for planar surfaces and about 27 µm near strongly curved areas. The blades were aligned to the nominal part using the upper fir tree surfaces due to their contact with rotating disk surfaces during operation. This ensures the blades are realistically aligned in accordance with their actual operating state. Any measured deviation is thus a superposition of a blade's positional variation, shape variation and variation of the selected fir tree surfaces. Also, gaps from scanned cooling holes are removed from each scan using purpose-built in-house software from TU Dresden (Högner, Voigt, Vogeler, et al., 2015). Doing this ensures that complete airfoil sections are available, which are required for the parametrization to work. With

smoothed patches approximating the local blade curvature, the application of this tool introduces negligible effects for the results.

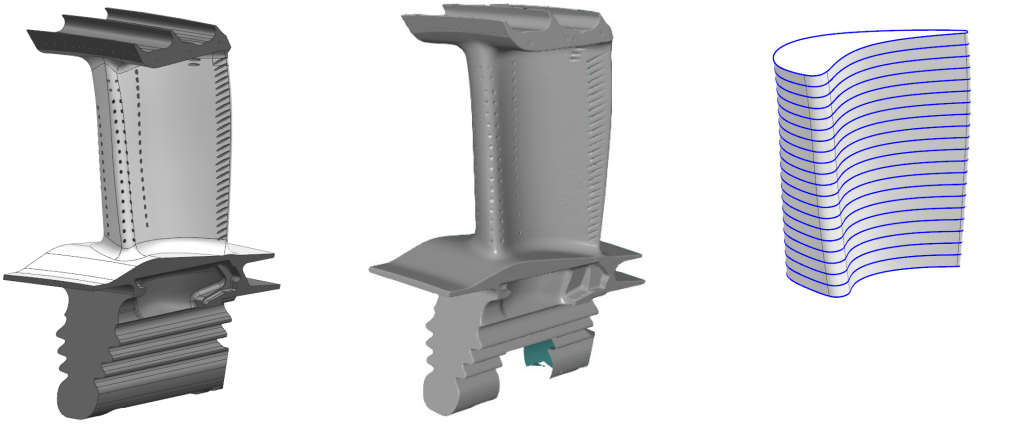

(a) Nominal CAD model (b) Blade scan #1 (c) Reverse engineered NX model

Figure 3.1: High-pressure turbine blade CAD model, scan and reconstruction

As an illustration of one of the scanned HP turbine blades, Fig. 3.1b depicts the STL file of scan #1 with about 2 million triangles. This scan can be compared with the nominal CAD model, the design intent geometry, depicted in Fig. 3.1a. Figure 3.1c shows a reverse engineered NX model of the blade geometry for CFD analysis.

To illustrate some observed deviations from the nominal CAD model, Fig. 3.2 depicts the geometric variations of all 58 scans leading and trailing edges at 50 % span. In Fig. 3.2b near the TE, axially shifted and twisted airfoil shapes are striking. One outlier with a particularly short TE stands out. The manufactured mean is clearly different from the nominal CAD design intent. In general, all variations are superpositions of positional variations of the blades, shape variations of the blades and shape variations of the selected fir tree surfaces.

It is important to recognize that these blade scans already have been analyzed as part of the HolisTurb project (Heinze, 2013). Hence, an in-depth analysis of variations and individual scans is not repeated here. It should be noted that previously, a slightly larger blade sample was examined and that there was no clear distinction between new and used blades. The HolisTurb report is advantageous for this study since it allows validation of the blade alignment. This is particularly useful here since most blades are severely twisted. The comparison with results from HolisTurb reveals that the blade alignment matches previous comparisons and that the entire sample of scans from relatively new blades exhibits similar deviations, which are different to scans from other blades (see Sec. H and Ref. Heinze (2013)).

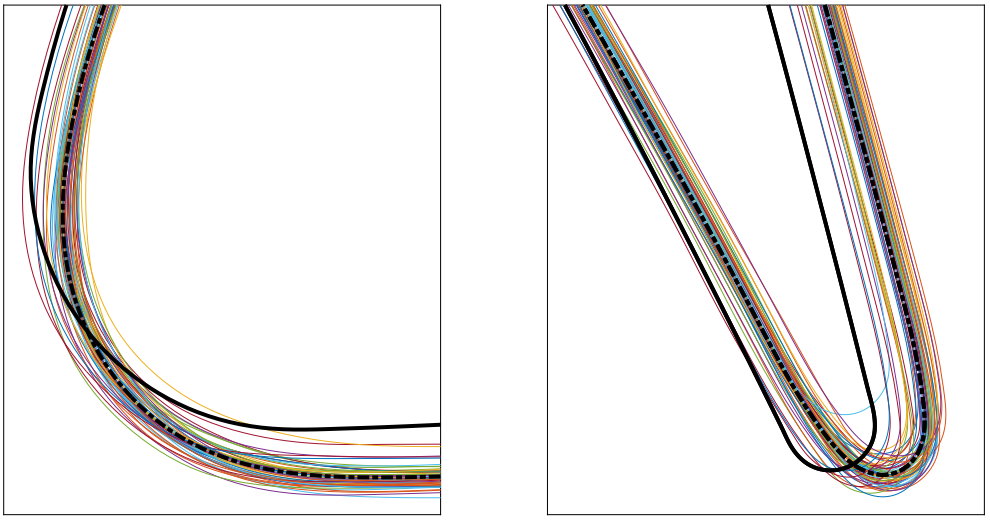

(a) Leading edge.

(b) Trailing edge.

Figure 3.2: Variations of all 58 blade scans (mean – –) vs. the nominal CAD design intent (—) at half-span.

3.2 Construction of Turbine Blade Models from Measurement Data

Numerous models have been developed to transform large numbers of measurement points into a viable set of parameters. As always in optimization, due to the exponential savings potential the principle is: the less parameters, the better. Models can range from free-form deformation, non-uniform rational B-spline (NURBS) curve fitting (Brujic, Ainsworth, et al., 2011), principal component analysis (PCA) (Garzon and Darmofal, 2003) to classical airfoil parameters (Lange, Vogeler, et al., 2009). RRD compressor blade data has already been post-processed in terms of both PCA (Lange, Voigt, Vogeler, and Johann, 2012) and a 14 parameter-based classical airfoil parametrization (Lange, Vogeler, et al., 2009). Lange, Voigt, Vogeler, Schrapp, et al. (2010) investigated the manufacturing variations of 150 compressor blades using a classical airfoil parameterization. Holtzhausen, Schreiber, et al. (2009) presented an automated 3D measuring and analysis procedure for compressor blades. Heinze, Meyer, et al. (2014) developed a parametric model to construct turbine blade models using classical airfoil parameters. The parametric blade design system by Anders, Haarmeyer, et al. (1999) is very similar. This method also uses radially stacked-up quasi-2D sections to build 3D blade models with 20 profile parameters per section. In addition, Gräsel, Keskin, et al. (2004)'s method is comparable too, but requires about one hundred parameters per blade. Brown, Slater, et al. (2003), Garzon and Darmofal (2003), and Sinha, Hall, et al. (2008) all used PCA. In order to use PCA, the normal Euclidean distances of each point of the scanned geometry

with regard to the baseline shape have to be calculated first. This vector can then be transformed into principal components (Jolliffe, 2002). New, perturbed blade shapes can be found by decomposing the variability into a certain number of modes and then adding these modes to a baseline shape. Garzon and Darmofal (2003) showed that 6 modes are sufficient to represent 99 % of variability. Contradictory to this study, Lange, Voigt, Vogeler, and Johann (2012) found that 20 modes were necessary to model 99 % of geometric variations. However, only 93 % of performance variations were modelled. 60 modes, i.e. 60 parameters, had to be used to account for 99 % of performance scatter. Lamb and Darmofal (2004) used PCA to construct perturbed blade models but also determined classical airfoil parameters for a better understanding, since the modes are difficult to interpret. Another approach by Ristic, Brujic, et al. (2004) is to update the original, nominal CAD model geometry by aligning the distorted measurement data with the CAD model. This method is based on Euclidean distance calculations and NURBS control point movements. Yet another technique proposed by Dow and Wang (2015) is to use a Gaussian random field to describe the error between the manufactured and nominal surfaces.

Here, a reverse engineering process based on a set of 14 classical airfoil parameters, implemented in a tool called Blade2Parameter (B2P) developed at TU Dresden, is used (Heinze, Meyer, et al., 2014). As opposed to parameterizing the entire airfoil, based on the assumption that differences are small, deviations are modeled in relation to a baseline blade shape such as the CAD model. This parameterization has two distinct advantages: Firstly, unlike modes from PCA, variations of standard airfoil parameters are straightforward to interpret, whereas PCA modes are more abstract than familiar airfoil parameters. Secondly, only 14 noise parameters (or even fewer, as shown in the sensitivity analysis in Sec. IV. 5.3.2) are required to accurately model geometric deviations. In contrast, the number of PCA modes can be far greater than 14 and also vary significantly depending on the problem, as has been shown in previous UQ studies, e.g., by Garzon and Darmofal (2003) and Lange, Voigt, Vogeler, and Johann (2012).

3.3 Reverse Engineering Workflow in Detail

Here, reverse engineering is carried out with several in-house tools in the following order: BladeCLeaner (BCL), Blade2Parameter (B2P), Parablading, Parapy and NX2BDF. BladeCLeaner is a tool used to remove cooling holes from STL meshes. Blade2Parameter, in its reverse engineering mode, extracts airfoil parameters and airfoil profile sections at specific span positions. Parablading fits NURBS to each section's points and builds 3D NX model from all 2D $m - r\theta$ sections. NX2BDF slices 3D blade models at various

span positions to create `Blade_Definition` files, which specify the blade geometry for the CFD meshing tool PADRAM. Each tool is described in the following subsections.

3.3.1 Blade CLeaner (BCL)

The need for BCL comes from the reverse-engineering workflow employed by B2P, which extracts blade parameters and profile slices. Each slice is required to be a valid turbine airfoil profile. Since gaps from FC holes would interfere with B2P's reverse engineering process, they must be removed. As an example, Fig. 3.3 illustrates two resulting closed holes. BCL's cooling hole closure algorithm is based on the estimation of the mean

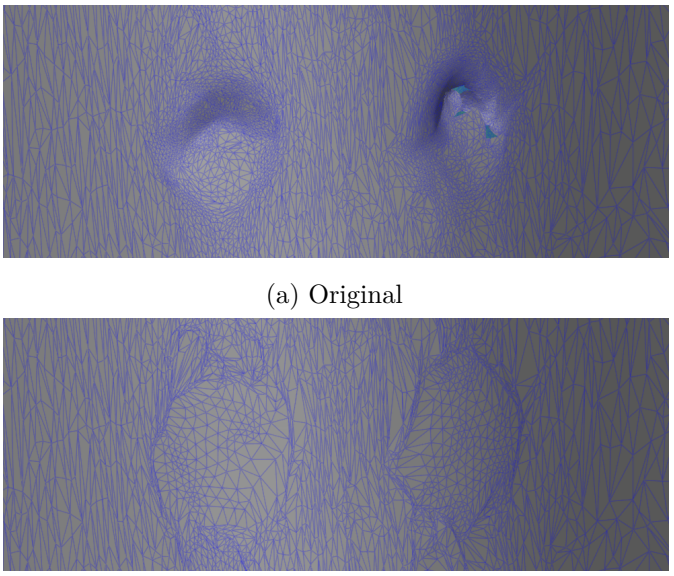

(a) Original

(b) Removed

Figure 3.3: Close-up view of two LE cooling holes closed with BladeCLeaner

curvature of a triangle's vertices according to Dyn, Hormann, et al. (2001). Using a filtering algorithm, a binary curvature property is introduced to classify previously identified areas of high curvature, viz. the cooling holes. Each vertex can either have an area of high curvature, corresponding to one, or not, zero. Since this procedure also captures high-curvature areas of the blade such as edges, which are not in fact FC holes, a verification step involving a cluster area coefficient ensures that all identified areas are indeed FC holes. Another step, local cluster detection and extension tries to identify areas of cooling holes not captured by previous steps, for example fan-shaped cooling holes with smaller curvatures. All identified FC holes are removed using a special closing algorithm (see Högner (2016) for all details). First, cooling hole borderlines are identified and closed using the Method of Advanced Front Meshing from Zhao, Gao, et al. (2007). The resulting mesh is smoothed using a combination of Laplace relaxation and Gauss regression. As an example, Fig. 3.4 depicts the original STL file (Fig. 3.4a), the processed

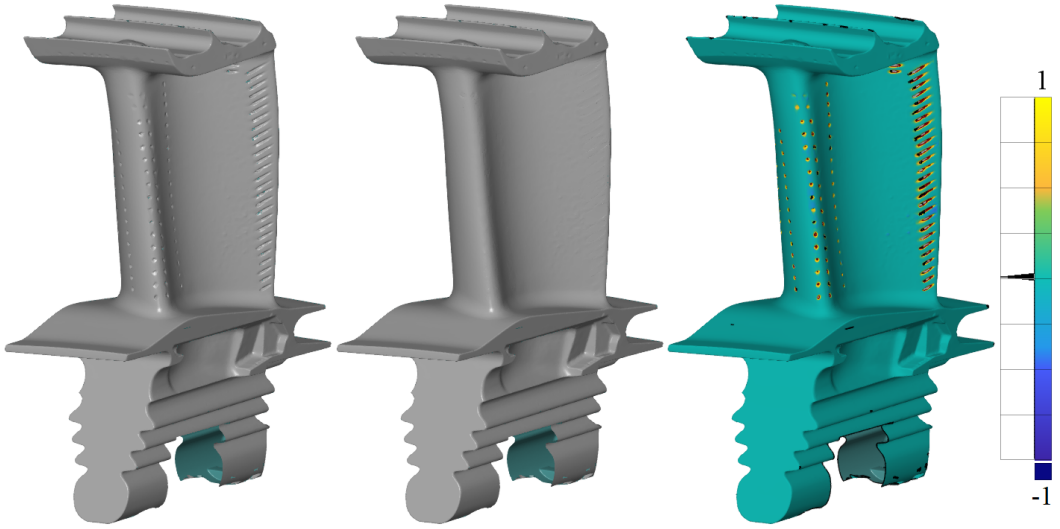

(a) Original blade (b) Cleaned blade (c) Differences

Figure 3.4: BladeCLeaner workflow illustration

STL file (Fig. 3.4b) and the differences between the two (Fig. 3.4c). It was found that the software in its current state generally works well except for holes near the TE, where often holes intersect the TE. Occasionally, these holes are not detected as holes and remain in the original file. Usage (and knowledge) of special expert parameters the program provides or manual closing is necessary to remove such leftover holes.

3.3.2 Blade2Parameter (B2P)

B2P is a reverse engineering and parametrization tool used create stacked turbine blade profile points. In essence, B2P has two main modes of operation: Firstly, it can extract airfoil parameters from a scan's STL file. This mode is called *Blade2Parameter* or *B2P*. Secondly, it can generate new blade geometries given some input parameters. This mode is called *Parameter2Blade* or *P2B*. B2P uses a classical 2D airfoil parametrization with familiar airfoil parameters, chord, thickness and camber distributions. All 14 parameters B2P uses are listed in Table 3.1 and illustrated in Fig. 3.5. Internally, B2P uses the length-preserving $(r\theta, m)$ streamline coordinate system defined in Eq. (3.1),

$$\theta_i = \arctan\left(\frac{y_i}{x_i}\right), \tag{3.1a}$$

$$r_i = \sqrt{x_i^2 + y_i^2}, \tag{3.1b}$$

$$r\theta_i = \theta_i r_i, \tag{3.1c}$$

$$m_i = m_{i-1} + \sqrt{(r_i - r_{i-1})^2 + (z_i - z_{i-1})^2}), \tag{3.1d}$$

where m_i is the projected arc length on the $r_i\theta_i$ plane. As an example, the $(r\theta, m)$ coordinates can be seen on the axes in Fig. 3.5a.

Table 3.1: B2P parameters reproduced from Högner, Voigt, and Nasuf (2016)

Symbol	Unit	Parameter description
ax_{pos}	m	Axial position of LE
tan_{pos}	m	Tangential position of LE
l_c	m	Chord length
γ	°	Stagger angle
β_{LE}	°	Angle of camber line at LE
β_{TE}	°	Angle of camber line at TE
t_{max}	m	Maximum thickness
$pos_{t,max}$	–	Position of maximum thickness
c_{max}	m	Maximum camber
$pos_{c,max}$	–	Position of maximum camber
$c_{t,max}$	m	Camber at maximum thickness position
pos_{TE}	–	Non-dimensional TE position on chord
t_{TE}	m	TE thickness
r_{LE}	m	LE radius

In its B2P mode, B2P can extract airfoil profile slices at predefined span heights from STL mesh files. Only intersection points of a rotation surface with a given radius and the STL triangle edges are extracted. The Cartesian coordinates of these points can be exported and used to reconstruct blade surfaces. Internally, B2P fits fourteen parameters to each extracted 2D profile. All points are converted from Cartesian to streamline coordinates first. At the heart of the parametrization is the reverse approximation of the camber line, for which Voronoi diagrams and Delaunay triangulation are used. Points outside the airfoil profile are filtered to obtain the median line, whose points are used for the parametrization. Outside LE and TE, the camber line is curve fit to a quadratic function using the Levenberg-Marquardt algorithm. Since the camber line obtained with this method does not reach the profile TE and LE, the camber line is somewhat extrapolated. Finally, having obtained the camber line and its intersection points with the airfoil profile, all other parameters can be derived using simple relations. For a more detailed description of all procedures, see Heinze, Meyer, et al. (2014) and Högner, Voigt, and Nasuf (2016).

Technically, there are 14 parameters *per section*. For example, when a blade is modeled with 21 2D airfoil sections, there would be $21 \cdot 14 = 294$ delta parameters in total. As this would be far too many parameters for many purposes, all delta parameters can be radially averaged, which reduces the total number of parameters to just 14. This radial averaging, termed the one mean area approach, can be justified due to the relatively high radial correlations between sections, which are, for the most part, close to one. As an example, the correlations for Δt_{max} are shown in Fig. 3.6, but other delta parameters exhibit similar high correlations. The correlations decrease for sections, which lie further apart from each other, e.g., in Fig. 3.6, the correlation for Δt_{max} between section 1 and section 21 is only $r_s = 0.44$. The reason the radial averaging approach works is that

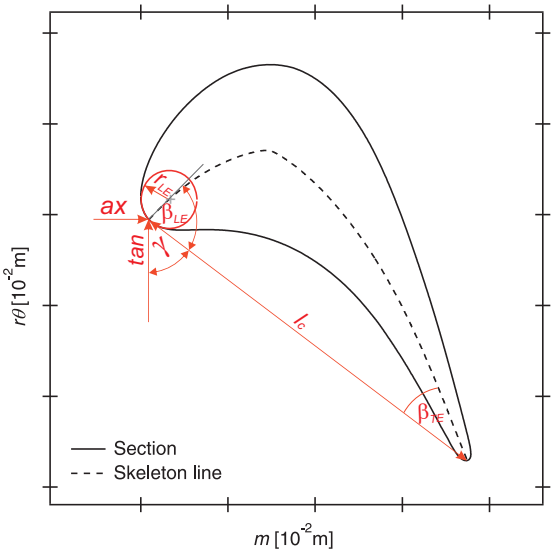

(a) Profile parameters

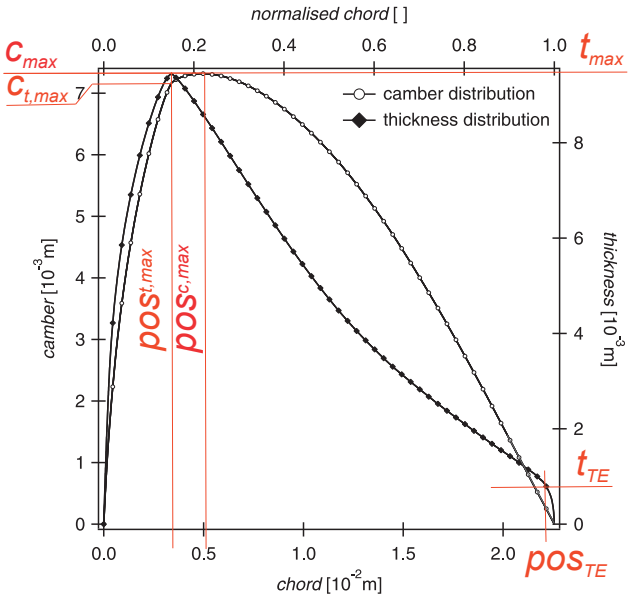

(b) Camber and thickness distribution parameters

Figure 3.5: B2P parameters reproduced from Högner, Voigt, and Nasuf (2016)

in B2P's P2B mode, given a sample of delta parameters, the parameters are added to the baseline blade to add variability. The baseline model's camber, chord and thickness distributions always remain the same. As will be shown later in Sec. 5.3.1.1, disregarding the correlations between samples leads to unrealistic blade geometries and unrealistic performance outputs.

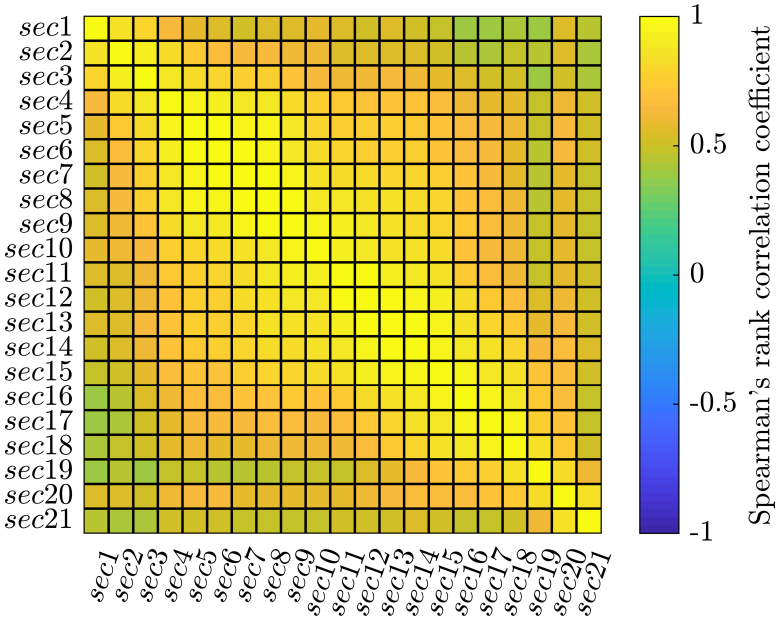

Figure 3.6: Spanwise correlations for Δt_{max} noise parameter

3.3.2.1 Parametric Construction of Realistic Turbine Blade Models

This paragraph describes B2P's P2B mode, which is used to construct artificial turbine blade models in UQ given a set of parameters. The main idea is to use B2P on the nominal geometry *and* on a scanned blade to compute the difference between the parameters. This is emphasized by Eq. (3.2), where $\Delta\mathbf{p}$ constitutes the delta parameter vector, which contains the difference between a scan's parameters $\mathbf{p}^{\text{scan}}$ and the baseline (nominal) model's parameters $\mathbf{p}^{\text{baseline}}$:

$$\Delta\mathbf{p} = \mathbf{p}^{\text{scan}} - \mathbf{p}^{\text{baseline}}. \tag{3.2}$$

At the heart of P2B's functionality, i.e., to create blades with geometric variations, is Eq. (3.3),

$$\mathbf{p}^{i} = \mathbf{p}^{\text{baseline}} + \Delta\mathbf{p}, \tag{3.3}$$

with which B2P creates new blades $\mathbf{p}^{i}$ by adding delta parameters $\mathbf{\Delta p}$ to a baseline blade $\mathbf{p}^{\text{baseline}}$ with camber, chord and thickness distributions for each section. Samples for $\mathbf{\Delta p}$ are obtained by subtracting the baseline model's parameters from those of the scans. Radially averaged delta parameters from the one mean area approach are denoted with $\mathbf{\Delta}\overline{\mathbf{p}}$.

In order to use B2P's (Blade2Parameter's) P2B (Parameter2Blade) UQ functionality, its normal B2P mode is used first to reverse engineer parameters for all scanned blades. Delta parameter samples can then be created by subtracting parameters of real scans from those of the baseline model using Eq. (3.2). These delta parameters from actual blade scans serve as the statistical basis and can then be used in Eq. (3.3) to add variations

onto a baseline blade. For example, when the delta parameter vector $\mathbf{\Delta p}$ of an actual blade scan is used, P2B recreates this turbine blade. However, and this is the main purpose of P2B, it can also be used with a delta parameter vector consisting of a sample of random numbers to create an artificial turbine blade.

For each 2D section in length-preserving $r\theta$-m space, ax_{pos} and tan_{pos} are used to position a new blade. Given this point, stagger angle γ and chord length l_c are added. Next, camber and thickness distributions are both morphed towards their target distribution using several morphing vectors. Then, the morphed camber line is added to the chord line and the morphed thickness distribution is applied to the camber line. This process yields a complete airfoil profile and is repeated for all specified span positions. For details, see Högner, Voigt, and Nasuf (2016).

3.3.2.2 Comparison of Geometric Reconstruction Accuracy

The excellent reconstruction accuracy of the described approach is depicted in Fig. 3.7. In Fig. 3.7a on the left, the magnitude of one of the scanned blade's deviations are shown. Figure. 3.7b in the middle depicts the deviations of a one-to-one, nonparametric reconstruction as described in Sec. 5.2.4 with 19 sections extracted directly from the scan's triangles. On the right in Fig. 3.7c is the fully parameterized blade. The colors and histograms demonstrate that reconstruction errors from the parameterized blade are very small compared to the actually measured deviations. Note that the baseline model used is a so-called mean value model (MVM), which is essentially an average of all blade scans' parameters, thickness, camber and chord distributions. Using the MVM in lieu of the nominal CAD model can lead to better reconstruction accuracy. Figure 3.8 compares reconstructed blades with the nominal CAD model and MVM as baseline models. The histograms, which are depicted again in Fig. 3.9, show that with the MVM baseline model the reconstruction is slightly more accurate than with the nominal CAD model, but differences are very small and negligible in comparison to the overall extent of deviations of the scanned blade.

It is also worth noting that the reverse engineering workflow also supports constructing and varying other geometric features such as the shroud geometry or film cooling hole positions and dimensions. Hub and shroud fillets could be added too. Here, every blade's shroud is shifted axially. This shift is computed by comparing the axial chord midpoints of the topmost airfoil sections of the artificial blade to that of the nominal CAD geometry and the nominal shroud geometry is moved accordingly. As an example, the axially shifted shroud geometry for this rotor is depicted in Fig. 3.10.

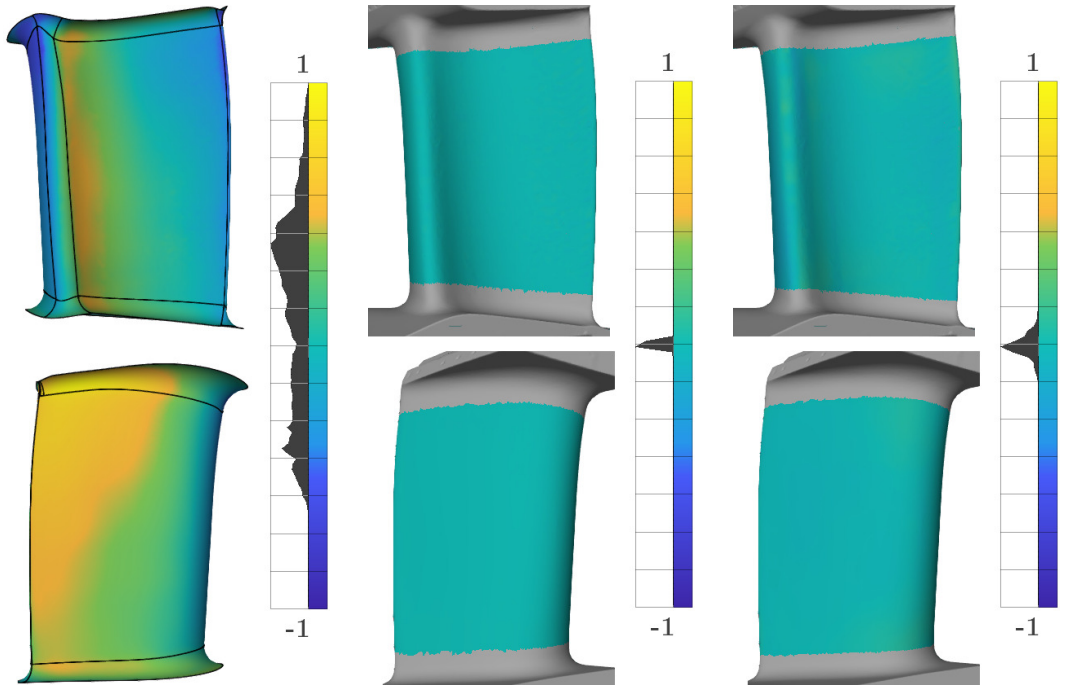

(a) Nominal CAD model vs. scan #1

(b) Nonparametric reconstruction vs. scan #1

(c) Parametric reconstruction vs. scan#1

Figure 3.7: Surface comparisons to illustrate measured blade deviations and reconstruction accuracy (units are normalized).

3.3.2.3 Sample Generation

Pseudorandom samples have to be generated to construct new blade geometries with realistic geometric variations. Later on, the term "artificial blade" is used to refer to these realistic artificially generated blades. Equation (3.3) is key to their construction: delta parameter samples are generated by first applying the blade parameterization to each blade scan. Subtracting each scan's parameters from the baseline model's parameters yields a 58×14 delta parameter sample matrix $\boldsymbol{P}$, which constitutes the statistical basis for the entire workflow. For example, the samples in the first row of $\boldsymbol{P}$ create the parameterized reconstruction of scan #1 as shown in Fig. 3.7. New delta parameter samples $\boldsymbol{\Delta\overline{\mathbf{p}}}$ have to be generated based on the samples in $\boldsymbol{P}$. Since visual inspection and statistical tests showed that parametric PDFs do not fit the data well, each PDF was estimated using KDE. KDE is nonparametric and more flexible, since random variables with any distribution can be handled. Here, a `kde` function using Gaussian kernels and an automatic optimal bandwidth selection process is used, see Botev, Grotowski, et al. (2010) for details. Any KDE estimate is a sum of many "bumps", i.e., kernels, given the observed samples. Here, $n = 58$ realizations for each parameter are extracted from the scans. Each PDF is fitted separately. The kernel density estimator is defined in Eq. (3.4)

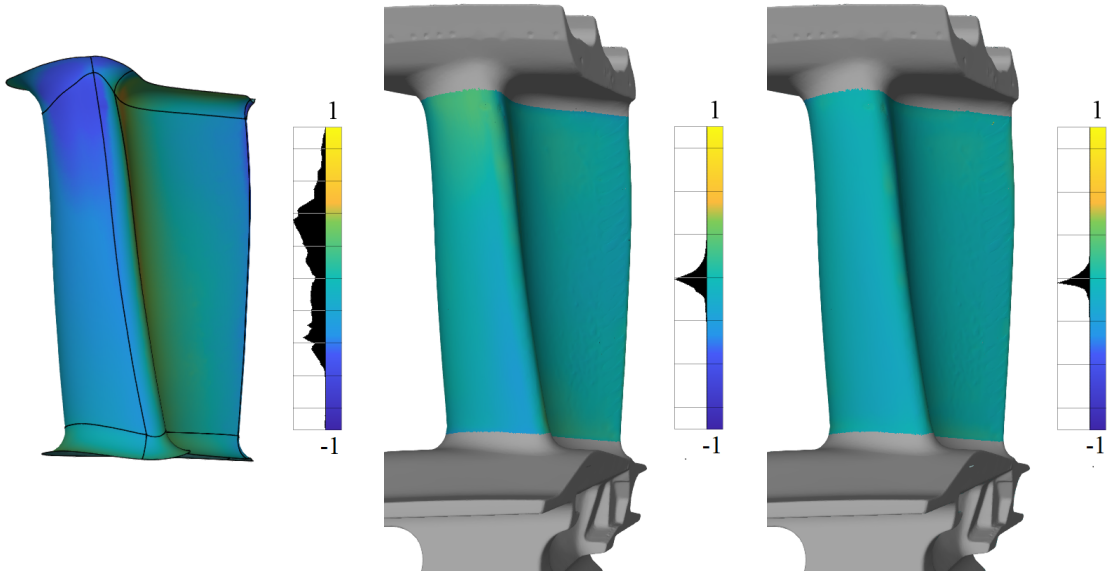

(a) Nominal blade vs. scan #1

(b) CAD baseline reconstruction vs. scan #1

(c) MVM baseline reconstruction vs. scan #1

Figure 3.8: Illustration of reconstruction accuracy with CAD and MVM baseline models (both with one mean area)

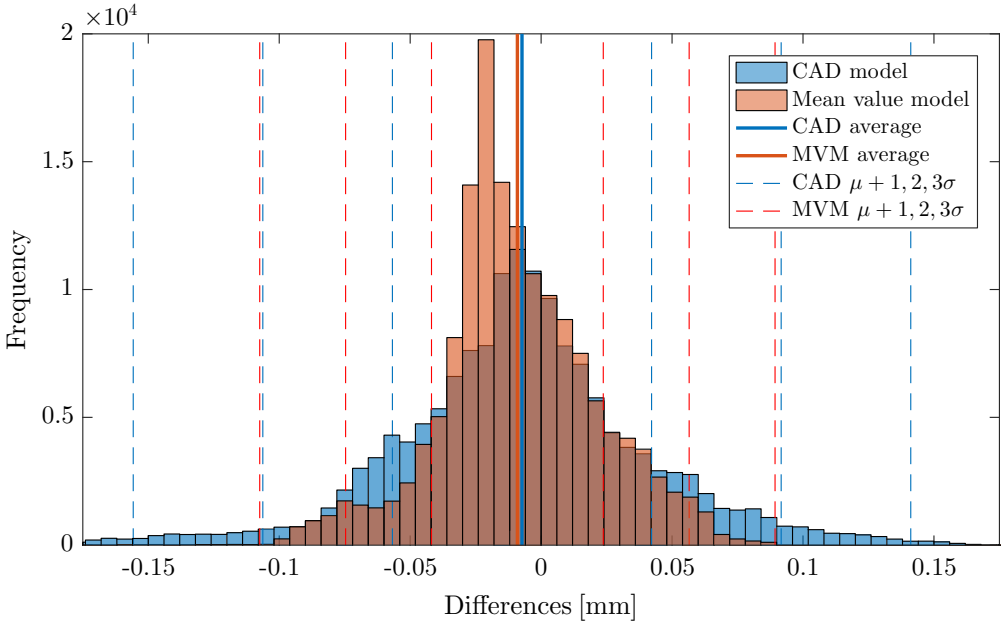

Figure 3.9: Histogram comparing the differences of Scan #1's P2B CAD- and MVM-based reconstructions

as

$$\hat{f}_h(x) = \frac{1}{nh}\sum_{i=1}^{n} K\left(\frac{x - x_i}{h}\right), \quad \text{where } K(x) = \frac{1}{\sqrt{2\pi}} e^{-\frac{1}{2}x^2} \tag{3.4}$$

is the Gaussian kernel (Botev, Grotowski, et al., 2010). h is the bandwidth, which specifies the kernel width. As an example for the maximum thickness Δt_{max} delta parameter, the

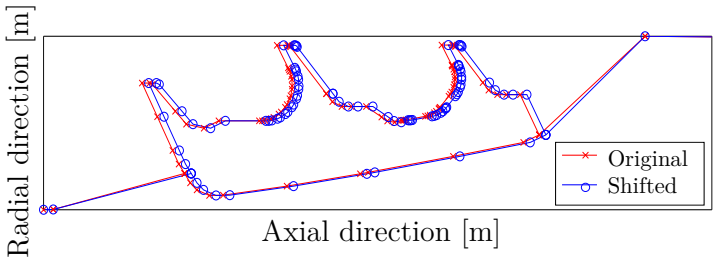

Figure 3.10: Axially shifted turbine blade shroud

empirical cumulative distribution function (ECDF) in Fig. 3.11 illustrates that KDE is able to approximate the given sample data adequately. Similar fits were generated for all other delta parameters. For each delta parameter, minimum and maximum parameter bounds are extracted from the original data in $\boldsymbol{P}$ to effectively truncate the PDFs below and above these values. Random samples with values larger or smaller than these bounds are discarded as in reality blades with extreme variations in violation of the allowed tolerance limits are sorted out.

In order to generate a new, artificial blade model, a 1×14 vector with one sample drawn from each individual KDE is required. A new sample from each KDE is generated by adding values drawn uniformly at random with replacement from each sample X_i to values drawn from the Gaussian $\mathcal{N}(X_i, h)$, i.e., centered at X_i with variance h.

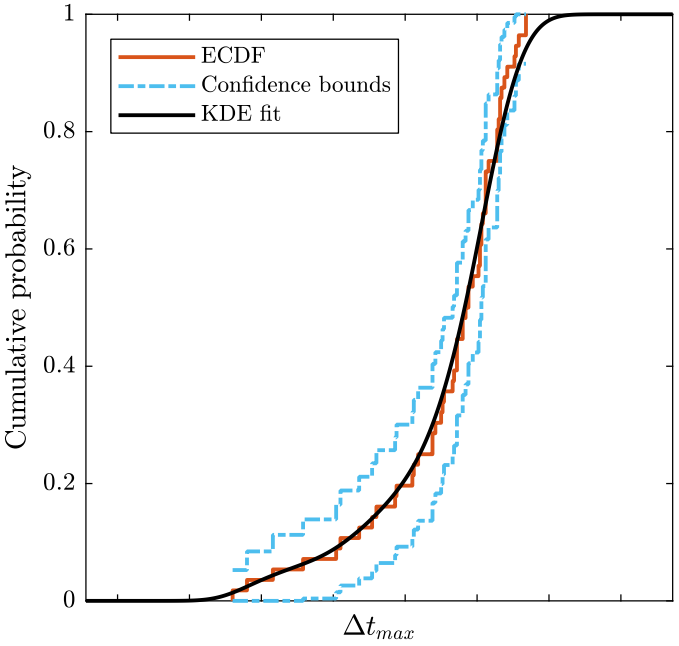

Figure 3.11: Kernel density-estimated cumulative distribution function (CDF) fit of Δt_{max} parameter

To create an artificial turbine blade geometry, the delta parameters are sampled independently from each KDE-fitted PDF. A matrix with N rows of samples for $\mathbf{\Delta\overline{p}}$ could be created and used to construct blades. However, these new blades would be unrealistic without also considering the strong correlations of the original scans' parameters. This is illustrated in Fig. 3.12 using Spearman's rank correlation coefficient r_s to reveal monotonically dependent delta parameters. r_s is defined in Eq. 3.5 with the operator $\mathrm{rg}(X_i)$ for the ranked scores and $\overline{\mathrm{rg}}_X$ for their average (Iman and Conover, 1982):

$$r_s = \frac{\sum_i (\mathrm{rg}(X_i) - \overline{\mathrm{rg}}_X)(\mathrm{rg}(Y_i) - \overline{\mathrm{rg}}_Y)}{\sqrt{\sum_i (\mathrm{rg}(X_i) - \overline{\mathrm{rg}}_X)^2}\sqrt{\sum_i (\mathrm{rg}(Y_i) - \overline{\mathrm{rg}}_Y)^2}} \tag{3.5}$$

It is crucial to ensure the original correlation structure is preserved for newly generated

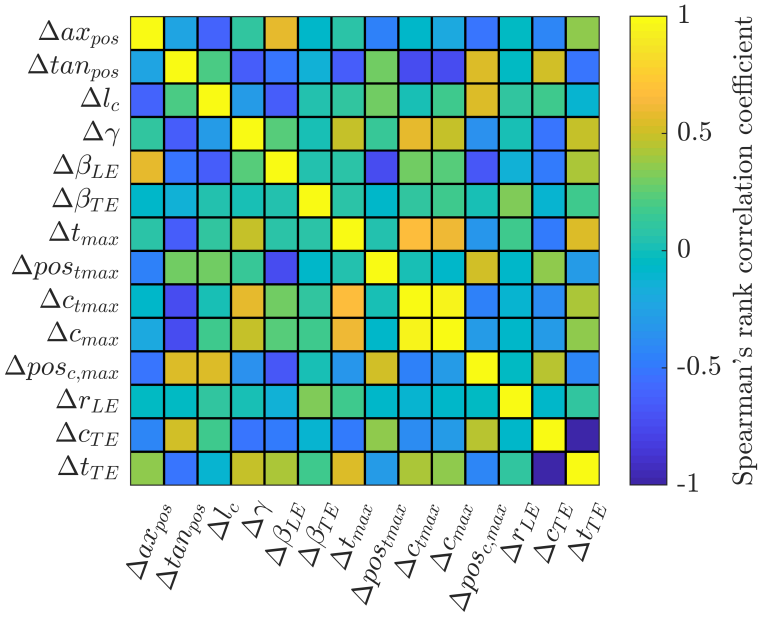

Figure 3.12: Target delta parameter correlation matrix

samples and Iman and Conover's method is used to do this here. Iman and Conover's method is distribution-free and allows the reintroduction of rank correlations *after* independently generating N rows of Monte Carlo samples from $k = 14$ PDFs. This yields a $N \times k$ matrix of samples $\boldsymbol{R}$, which together with a target correlation matrix $\boldsymbol{C}^*$ extracted from the original blade sample's parameters serve as the inputs for Iman and Conover's method. $\boldsymbol{T}$, the sample correlation matrix, is computed first. Next, two lower triangular matrices $\boldsymbol{P}$ and $\boldsymbol{Q}$ are computed via Cholesky decomposition, i.e., $\boldsymbol{C}^* = \boldsymbol{C} = \boldsymbol{P}\boldsymbol{P}^T$ and $\boldsymbol{T} = \boldsymbol{Q}\boldsymbol{Q}^T$. Then, given $\boldsymbol{W}$, a matrix of columnwise randomly permuted van der Waerden scores $\Phi^{-1}(\frac{i}{N+1})$, $i = 1, 2, \ldots, N$, where Φ is the inverse of the standard normal CDF, $\boldsymbol{W}^* = \boldsymbol{W}\boldsymbol{Q}^{-T}\boldsymbol{P}^T$ approximates the desired correlation matrix $\boldsymbol{C}^*$. By rearranging the columns of the input matrix $\boldsymbol{R}$ in terms of the rank indices of $\boldsymbol{W}^*$ the final output matrix $\boldsymbol{R}^*$ can be computed, whose rank correlation matrix is approximately equal to that of $\boldsymbol{C}^*$ (Oberguggenberger, 2014).

3.3.3 Parapy

Parapy is an in-house Python tool from TU Dresden to extrapolate B2P-generated turbine blade sections. This is necessary since the regions below 10 % span and above 90 % span cannot be constructed like the rest of the blade, because the parameterization does not work in this filleted area, where the sections are not airfoil profiles due to fillets. The purpose of `parapy` is to extrapolate sections to bridge this gap. `parapy` computes local displacement vectors between two corresponding points on either the innermost or outermost profiles, which are smoothed using a Savitzky-Golay filter. When all required sections from 0 %-100 % span are available, the final 3D blade geometry can be constructed.

3.3.4 Parablading

Parablading is another Rolls-Royce in-house tool and it is used here to construct NX models from stacked B2P airfoil section points. Parablading uses four cubic B-spline curves to construct airfoil sections. This is done separately for each curve, one each for LE, TE, SS and PS. The final 3D 4-patch blade surface is constructed from all fitted splines. Each surface segment is C^2 continuous to ensure smooth transitions and the fitting essentially acts as a data point smoothing. This smoothing is particularly evident on the PS in Fig. 3.13. On the SS this is much less pronounced due to the lack of cooling holes there. Parablading also names each blade surface, which is a requirement for further processing with NX2BDF.

3.3.5 NX2BDF

NX2BDF is an NX Open tool used to automate the creation of `Blade_Definition` files. Given an input file and a tagged 4-patch NX `.prt` file, blade sections and streamlines are computed in between a predefined radial range. All points are exported as cylindrical coordinates to a `Blade_Definition` file, which can be read by PADRAM.

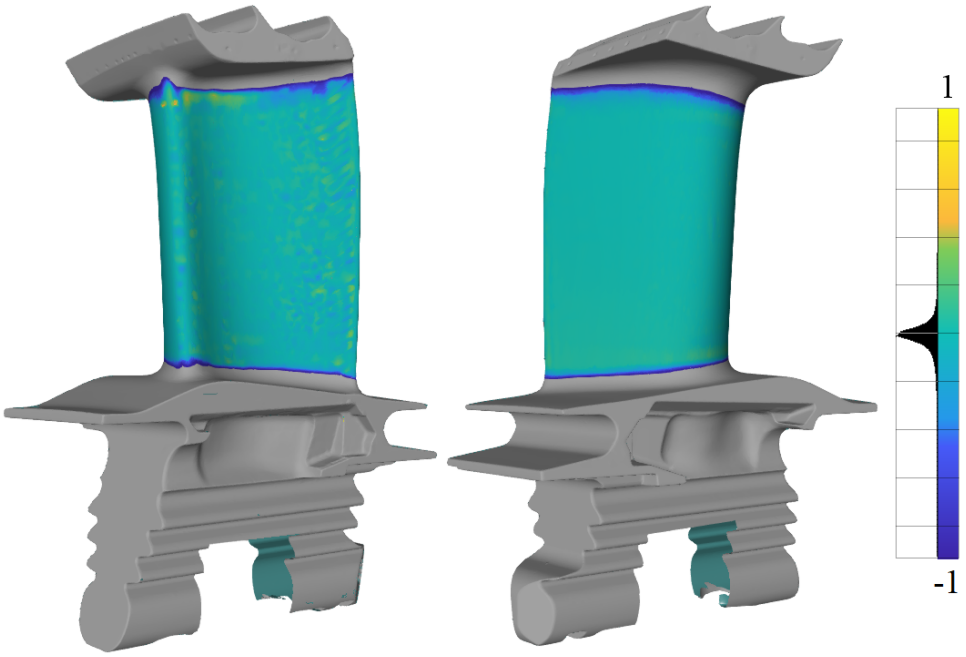

Figure 3.13: Parablading-B2P reconstruction of scan #1 vs. scan #1's BCL-processed STL file. The scale is 10 times smaller than the one in Fig. 3.7

3.4 Summary

Given a sample of 58 turbine blade scans, most of this chapter was dedicated to the construction of geometric turbine blade models, which accurately reflect the actual manufacturing variations of the scans. The brief literature overview in Sec. 3.2 reveals that the selected parameterization method has two distinct advantages over alternative approaches: Only 14 parameters are required to parametrize an entire turbine blade and each of the classical airfoil parameters is straightforward to interpret. Based on this parameterization, a reverse engineering workflow was then described in detail in Sec. 3.3. The main tool, as described in Sec. 3.3.2, is Blade2Parameter (B2P), which can be used in its reverse engineering mode (B2P) to reconstruct the scanned blades, but also in its P2B (Parameter2Blade) mode in order to create artificial, but realistic blade geometries. In Sec. 3.3.2.2 the excellent reconstruction accuracy of the approach is shown in detail.

Chapter 4

Computational Fluid Dynamics Model & Workflow

Having introduced the turbine blade scans and the reverse engineering workflow in Chapter 3, the main purpose of this chapter is to describe the computational analysis workflow and model used to assess the aerodynamic performance impact of blade variations. Steady-state Reynolds-averaged Navier-Stokes (RANS) computational fluid dynamics (CFD) simulations are used to evaluate the performance of each blade. These simulations are also essential for the approaches described in Chapter 5 and Chapter 6.

4.1 Governing Equations

The general CFD approach pursued here is to solve the steady-state 3D compressible RANS equations defined in Eqs. (4.1a)-(4.1b) using Reynolds ($\Phi = \overline{\Phi} + \Phi'$) and Favre averaging ($\Phi = \tilde{\Phi} + \Phi''$) (Gatski and Bonnet, 2013):

$$\frac{\partial \bar{\rho}}{\partial t} + \frac{\partial}{\partial x_j}(\bar{\rho}\tilde{u}_j) = 0, \tag{4.1a}$$

$$\frac{\partial}{\partial t}(\bar{\rho}\tilde{u}_i) + \frac{\partial}{\partial x_j}(\tilde{u}_i\bar{\rho}\tilde{u}_j) = -\frac{\partial \bar{p}}{\partial x_i} + \frac{\partial \overline{\sigma}_{ij}}{\partial x_j} - \frac{\partial R_{ij}}{\partial x_j}, \tag{4.1b}$$

$$\frac{\partial}{\partial t}(\bar{\rho}\widetilde{E}) + \frac{\partial}{\partial x_j}\left(\widetilde{u}_j\bar{\rho}\widetilde{H}\right) = \frac{\partial}{\partial x_j}(\overline{u_i\sigma_{ij}}) - \frac{\partial \bar{q}_j}{\partial x_j} - \frac{\partial \overline{Q}_j}{\partial x_j}. \tag{4.1c}$$

In Eqs. (4.1a)-(4.1c), $\bar{\sigma}_{ij} \approx 2\widetilde{\mu}_t\left(\tilde{S}_{ij} - 1/3\widetilde{S}_{kk}\delta_{ij}\right)$ is the is the viscous stress tensor, $R_{ij} = \bar{\rho}\tau_{ij} = \widetilde{\rho u_i'' u_j''} = \bar{\rho}\widetilde{u_i'' u_j''}$ is the turbulent stress tensor (Reynolds stress), $S_{ij} = 1/2\left(\partial u_i/\partial x_j + \partial u_j/\partial x_i\right)$ is the strain rate tensor, $\bar{\rho}\widetilde{E} = \bar{\rho}c_v\widetilde{T} + 1/2\widetilde{\rho u_i}\widetilde{u}_i + 1/2\overline{R}_{ii}$ is the averaged total energy field, $\bar{\rho}\widetilde{H} = \bar{\rho}c_p\widetilde{T} + 1/2\widetilde{\rho u_i}\widetilde{u}_i + 1/2\overline{R}_{ii} = \bar{\rho}c_p\widetilde{T}_0$ is the averaged total enthalpy, $\bar{q}_j = -\overline{k_T\,\partial T/\partial x_j} \approx -c_p\widetilde{\mu}/Pr\;\partial\widetilde{T}/\partial x_j$ is the mean heat flux vector (Fourier's law) and $\overline{Q}_j = \bar{\rho}c_p\widetilde{u_j''T''} + 1/2\bar{\rho}\widetilde{u_i'' u_i'' u_j''} + \bar{\rho}\widetilde{u}_i\tau_{ij}$ is the turbulent scalar flux. The turbulence closure problem stems from the turbulent stress $\bar{\rho}\tau_{ij}$ and all terms in

$\overline{Q}_j = \bar{\rho} c_p \widetilde{u_j'' T''} + \bar{\rho} \widetilde{u_i'' u_i'' u_j''}/2 + \bar{\rho} \widetilde{u}_i \tau_{ij}$. Here, the one-equation Spalart-Allmaras turbulence model defined in Eq. (4.2) is solved for the Spalart variable $\tilde{\nu}$:

$$\begin{aligned} \frac{\partial \tilde{\nu}}{\partial t} + u_j \frac{\partial \tilde{\nu}}{\partial x_j} = c_{b1}(1 - f_{t2})\tilde{S}\tilde{\nu} - \left[c_{w1} f_w - \frac{c_{b1}}{\kappa^2} f_{t2} \right] \left(\frac{\tilde{\nu}}{d} \right)^2 \\ + \frac{1}{\sigma} \left[\frac{\partial}{\partial x_j} \left((\nu + \tilde{\nu}) \frac{\partial \tilde{\nu}}{\partial x_j} \right) + c_{b2} \frac{\partial \tilde{\nu}}{\partial x_i} \frac{\partial \tilde{\nu}}{\partial x_i} \right]. \end{aligned} \tag{4.2}$$

In compressible flows, the turbulent dynamic eddy viscosity μ_t is computed with the relation $\mu_t = \rho \tilde{\nu} f_{v1}$. For the sake of brevity, exact model constants used in HYDRA are not provided here and all additional model equations, e.g., $f_{v1} = \ldots$, can be found in the original publication by Spalart and Allmaras (1992). The working fluid air is modeled as a calorically perfect gas (specific heat capacity = constant) with heat capacity ratio $\kappa = 1.3$. Thus, it obeys the ideal gas law equations defined in Eq. (4.3),

$$p = \bar{\rho} R_s \tilde{T}, \quad \kappa = \frac{c_p}{c_v}, \quad c_p - c_v = R \quad \text{and} \quad e = c_v T, \tag{4.3}$$

where κ, R_s, c_p and c_v are all constant. In reality, the fluid is a two-phase air-fuel mixture, but the presence of fuel is neglected here.

4.2 CFD Model & Domain

The CFD model consists of the turbine rotor blade only, to keep the computational cost as low as possible. Rotationally periodic boundary conditions are used, so that only a single blade passage needs to be modeled. Although this is a frequently used simplification, one has to keep in mind that this introduces a perfect correlation between all blades around the annulus and entails overestimating the variability of output blade performance measures, e.g., see Högner, Voigt, Nasuf, et al. (2016). However, this is of no concern for the actual trade-off between performance mean and variability, because only their absolute magnitude is affected. Boundary conditions (BCs) are specified for all inlets and outlets and all rotating and stationary surfaces. All walls are adiabatic. A meridional view of the complete turbine stage with all BCs has been presented by Scharfenstein, Heinze, et al. (2013). The main inlet is a normal subsonic inflow, the outlet a non-reflecting subsonic outflow and the two smaller inlets for rim and rail cooling are mass flow inlets with fixed mass flow rates. Rolls-Royce's standard in-house solver HYDRA is used. Numerically, HYDRA makes use of the finite-volume method (FVM) and requires a discretized CFD domain, i.e., a CFD mesh, to solve the RANS equations. A multigrid method with a 5-grid-level W-cycle is used to accelerate convergence. In order to illustrate the fully-featured case, Fig. 4.1 depicts the CFD domain and a mesh created with PADRAM (see Sec. 4.3.1 for details). The Reynolds number (calculated with the blade chord length at 50 % span and averaged inlet values)

for this case is around 475000. Computational grids are presented separately in Sec. 4.5 in detail. Similarly, Sec. 4.4 presents the CFD validation approach pursued here.

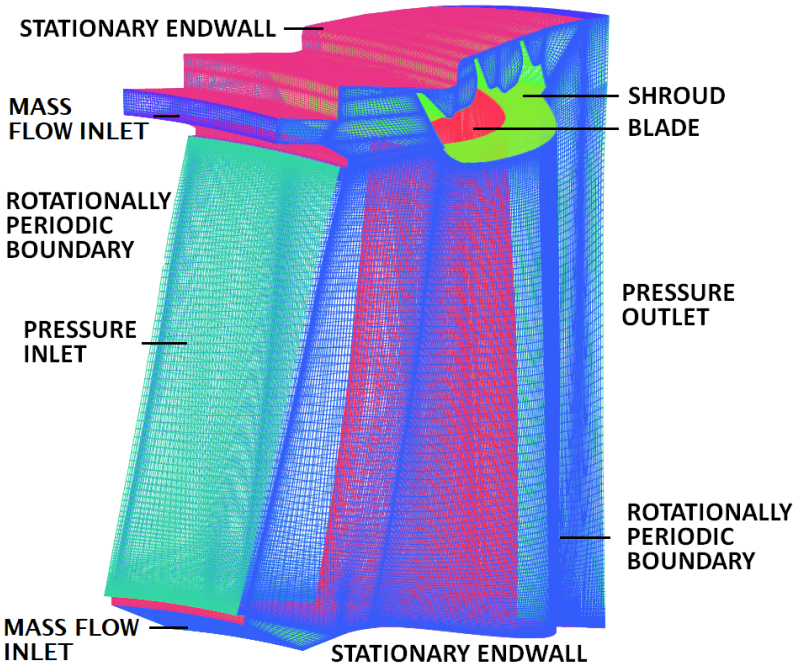

Figure 4.2: PADRAM mesh and domain

Also note that for each blade, the CFD control volume position is fixed in space, so that each blade is installed with whatever deviations it was made with, i.e., as if its fir tree root was attached to the rotating turbine disk. For the CFD model, there are two geometrical simplifications vis-à-vis reality, i.e., the very small shroud and hub gaps are not modeled and instead are continuous in the annulus, as is commonly done. Also, the case here is run "cold" and a cold-to-hot transformation would be necessary for real-engine results. Moreover, since film cooling is not part of the scope of the initial study in Chapter 5, the inlet total pressure was increased to offset the missing coolant mass flow rate from all film cooling holes, i.e., to ensure the same operating point as if cooling was enabled. This is necessary since for this blade, film cooling accounts for roughly 5 % of the total mass flow rate through the annulus, which is significant. Besides the fully-featured case, a defeatured model only consisting of the rotor blade from 10 % to 90 % span, as depicted in Fig. 4.3, is used briefly in Sec. 5.3.1, because it does not involve extrapolated sections. The mesh size for this case is reduced to about 3 million cells.

4.2.1 Quantities of Interest

Typical aerodynamic quantities of interest of a turbine rotor include the isentropic efficiency defined in Eq. (6.5),

Figure 4.3: Defeatured blade model

$$\eta = \frac{\sum\limits_{i=inlets} (\dot{m}h_0)_i - \sum\limits_{i=exits} (\dot{m}h_0)_i}{\sum\limits_{i=inlets} (\dot{m}h_0)_i - \sum\limits_{i=sec\_exits} (\dot{m}h_0)_i - (\dot{m}h_{0,ideal})_{main\_exit}}, \tag{4.4}$$

as the ratio of actual to ideal work for turbines, the inlet capacity in Eq. (6.6),

$$\phi = \frac{\dot{m}_{inlet}\sqrt{T_{0,inlet}}}{p_{0,inlet}}, \tag{4.5}$$

and the specific work produced.

$$w = \frac{\sum_{i=inlets}(\dot{m}H_0)_i - \sum_{i=exits}(\dot{m}H_0)_i}{(\dot{m}T_0)_{main\_inlet}}. \tag{4.6}$$

The work is computed from the rotor torque $\tau = \int \mathbf{r} \times \mathbf{F} \mathrm{d}A$ with all forces from pressure and viscous shear stress terms acting on all rotating walls. Torque and specific work are both directly related to the generated power: $P = \tau\Omega = \dot{m}w$. The degree of reaction, a measure of fluid work on the rotor, is usually also a quantity of interest and typically used as an optimization constraint due to its relation to mechanical bearing loads, which should not be exceeded. However, calculating reaction by definition requires the full stage and it cannot be included without the stator. During post-processing, values from the last 100 CFD iterations are averaged for each quantity of interest due to small oscillations from the steady-state CFD approach. All flow quantities are mass-weighted, i.e., computed with the weighting

$$\frac{\int \phi \, \mathrm{d}m}{\int m \, \mathrm{d}m} = \frac{\sum_{i=1}^{n} \phi_i m_i}{\sum_{i=1}^{n} m_i} \tag{4.7}$$

for any scalar flow field quantitiy ϕ.

4.3 CFD Software

The basic CFD process uses RR's in-house meshing tool PADRAM and solver HYDRA. First, PADRAM is used to generate good quality structured meshes. Every mesh is checked for cells with negative volumes and converted into the `.hyd` format for HYDRA in a separate pre-processing step. Coarser multigrid meshes are constructed, boundary conditions and monitor files are created and the flow is initialised. HYDRA is always run in parallel with the Message Passing Interface (MPI). ParaView and HYDRA monitor files are used for all post-processing.

4.3.1 PADRAM

PADRAM, short for Parametric Design and Rapid Meshing, is the in-house mesh generation and geometry parameterization software. PADRAM can create structured, unstructured and hybrid grids based on C-O-H multi-blocks (Milli and Shahpar, 2012; Shahpar and Lapworth, 2003). It can create both single and multi-stage and multi-passage grids, is able to parametrically modify the geometry and incorporates mesh smoothing options. It constructs blades by stacking section data for previously established airfoils. The input files contain a number of streamline and blade section coordinates. Blade sections are then meshed on unwrapped $\theta - m'$ planes. The rest of the mesh not on these planes is radially interpolated. Cells are clustered towards blade and endwalls using the relevant parameters. Discrete film cooling holes on blade surfaces are not supported.

4.3.2 BOXERMesh

PADRAM does not support discrete cooling holes on the blade surface. For this particular task, the BOXERMesh meshing software, abbreviated as Boxer, is used. First and foremost, Boxer operates on tesselated surfaces, not on the original CAD geometry, so an adequate input resolution is critical. The Delaunay tesselation approach is used here due to its higher accuracy with high curvature geometry than STL tesselation. A quick comparison in GOM Inspect can establish what differences there are in the final mesh in any case. Then, after having defined a bounding box, Boxer creates an octree mesh inside the box up until boundaries defined by the geometry. This initial mesh is then body-fitted to the tesselated geometry. Subsequently, near-wall layers are grown.

4.3.3 HYDRA

HYDRA is a suite of non-linear, linear and adjoint RANS solvers (Lapworth, 2004; Moinier, 1999). For high performance, HYDRA is written in Fortran 77 and supports fast parallel computing through OpenMP and MPI (Reguly, Mudalige, et al., 2015). It is an unstructured solver employing an edge-based finite volume scheme with the flow data

stored at the cell vertices (Moinier, Müller, et al., 2002). Space discretization is based on a finite volume MUSCL-type interpolation scheme (monotonic upstream-centred scheme for conservation laws) (Leer, 1979). An explicit 5-step Runge-Kutta time-stepping method is used to approach the steady-state solution (Martinelli, 1987). A block-diagonal Jacobi preconditioner (Moinier and Giles, 1998) and an element-collapsing multigrid algorithm to generate a sequence of coarser meshes are used to accelerate convergence (Moinier, Müller, et al., 2002).

Boundary conditions in HYDRA can be prescribed either in the stationary or rotating frames of reference. Rotating boundaries are moving around the engine axis with the rotational speed Ω. The absolute velocity $\vec{v}$ (in the stationary frame of reference) of the fluid consists of both the relative velocity $\vec{w}$ and the circumferential velocity $\vec{u}$, where $\vec{u} = \Omega \times \vec{r}$ due to the rotation:

$$\vec{v} = \vec{w} + \vec{u} = \vec{w} + \Omega \times \vec{r} \tag{4.8}$$

4.4 CFD Validation

Since for the scanned turbine rotor no experimental data has been recorded, the CFD approach can only be validated by using the same settings as in Sec. 4 in a different but similar case, for which experimental data is available. One such turbine stage with time-averaged measurements of surface pressure distributions is the MT1 research rig. The experimental data can be found in Beard, Smith, et al. (2014) and geometry and boundary conditions in Maffulli and He (2017). The CFD was set up with a $y^+ \approx 1$ grid, similar to the HPT rotor. The Reynolds number of about 525000 (again calculated with the blade chord length at 50 % span and averaged inlet values) is also close to the main CFD case. Some additional details such as the test bench, the grid and the flow through the stage are depicted in a separate section in Appendix D. Figure 4.4 shows that there is very good agreement with both experimental and numerical results, all using the Spalart-Allmaras turbulence model. Due to the experiments' time-averaging, it comes as no surprise that unsteady phase-lagged BCs perform best. For both steady-state results from HYDRA and Fluent, reproduced from Maffulli and He (2017), there is some disagreement near the SS shock, which is attributable to unsteady effects. For the rest, the agreement is very good. The relatively accurate prediction of flow separation on the SS is only possible with a viscous CFD approach, even though inviscid flow solvers can also provide reasonably accurate pressure distributions around turbine blade profiles. However, inviscid solvers are unsuitable for the prediction of flow separation, pressure losses and secondary flow structures in turbomachinery simulations. While it would have been better to validate the CFD with more experimental data, the graph provided is the only aerodynamic experimental data available for the selected test case. Other data is

only available for thermodynamic quantities of interest such as heat fluxes and Nusselt numbers, which are generally more difficult to predict with CFD than surface pressure distributions and require additional simulations to compute accurate results.

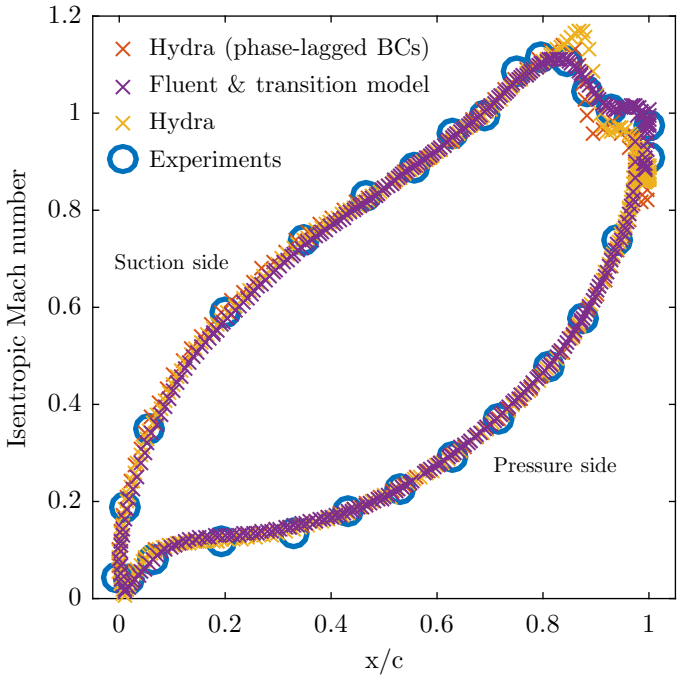

Figure 4.4: Isentropic Mach number distribution of MT1 turbine stator at half-span (○ from Beard, Smith, et al. (2014) and × from Maffulli and He (2017))

4.5 CFD Grids

CFD simulations require good quality grids and grid resolution is crucial for accurate results. This section is intended to showcase the grids from PADRAM and BOXERMesh, as described in Sec. 4.3, in detail. In both cases, the intent is to create structured $y^+ \approx 1$ grids, and, as depicted in Fig. 4.5, this has been achieved.

4.5.1 PADRAM

PADRAM is used to create structured grids for a single passage using a predefined blocking structure with a bent wake. Around the blade, an O-mesh mesh topology surrounded by H-meshes on either side is used. The resulting blocking structure is relatively complex, primarily due to the cavity, shroud and tip gap geometry, for which several subdivisions are required. In terms of mesh quality metrics such as aspect ratio and skewness, unavoidable cells of lower quality are generally located near the TE due to the twisted blade shape. Nevertheless, PADRAM is able to construct adequate meshes for the geometry at hand. In order to investigate the impact of the computational grid

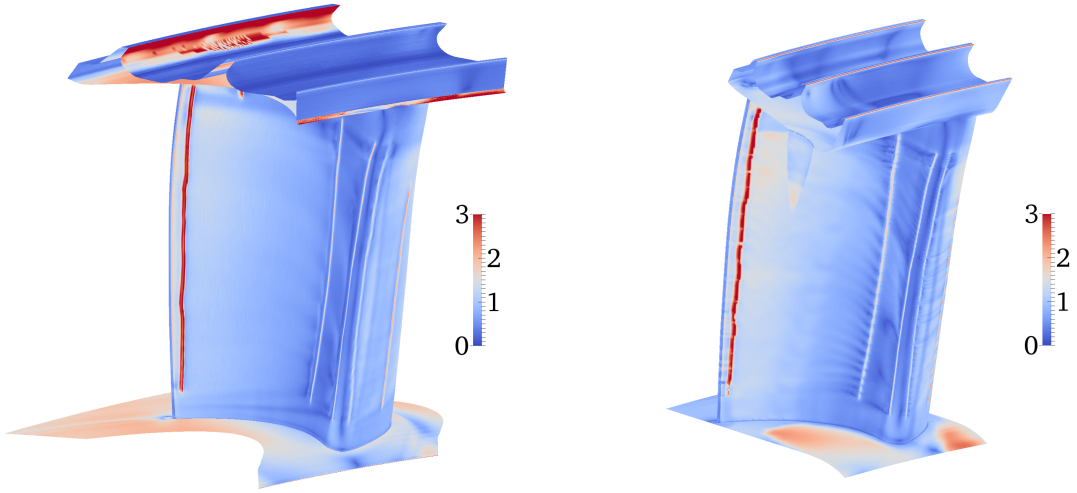

(a) PADRAM (b) BOXERMesh

Figure 4.5: Near wall y^+ values for PADRAM and BOXERMesh grids

on the solution, a mesh independence study (without any film cooling) was carried out to find a final adequate mesh size of around 5.5M cells. Figure 4.6 depicts the results of this study for the isentropic efficiency as the quantity of interest. The finest mesh can serve as the reference solution, which all coarser grids can be compared to. Figure 4.7 depicts a typical convergence history for all monitored quantities of interest for the first 200 iterations. The amplitudes of the oscillations for the converging quantities of interest are about 0.1 %, 0.01 %, 0.17 % and 0.1 % for efficiency, capacity, specific work and mass flow rate respectively. Epistemic meshing variations are investigated later in Sec. 5.2.4.2 in detail and this section only serves to illustrate the mesh itself. Figure 4.8a illustrates the mesh blocking structure and Fig. 4.8b the resulting mesh for the rotor blade. Figures 4.8c-4.8h depict the LE mesh, TE mesh, mid-span airfoil mesh, shroud and tip gap mesh, and boundary layer mesh in detail.

4.5.2 BOXERMesh

Similarly to the previous section, Fig. 4.9 illustrates a 21.3M cell mesh created with BOXERMesh. Epistemic meshing variations are also investigated later in Sec. 6.4.1 in detail. This mesh is used in Chapter 6. All features of the grid are depicted in Fig. 4.9. Radial and meridional views are shown in Figs. 4.9a-4.9b. Figure 4.9c depicts a detailed view of one of the TE cooling hole stubs. The boundary layer mesh around the LE and TE can be seen in Figs. 4.9d-4.9e, and Figs. 4.9f-4.9g depict the boundary layer mesh and the mesh near the TE FC holes. It is evident that a suitable mesh for all geometric features of the blade, including the small FC holes, can be created. The only caveat is that BOXERMesh grids are prone to become quite large in terms of the cell count.

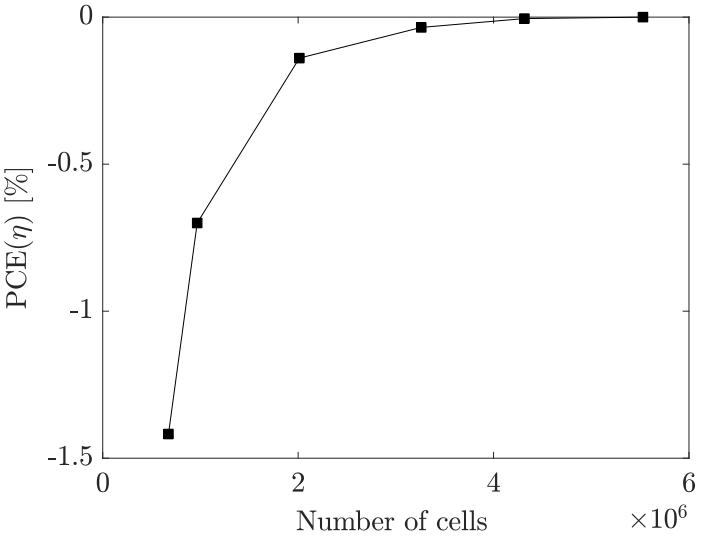

Figure 4.6: Mesh independence study results with PADRAM-built grids

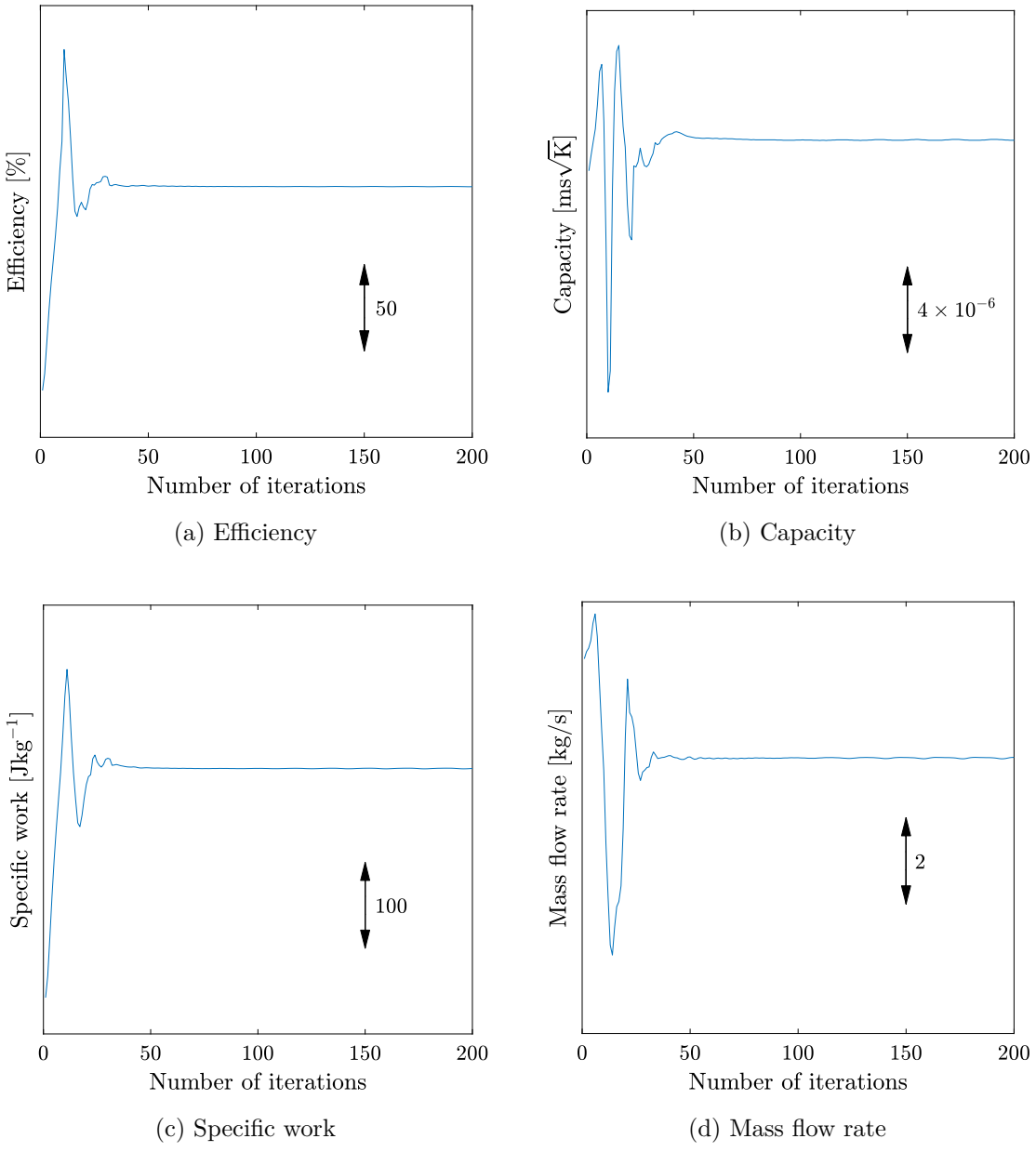

(a) Efficiency

(b) Capacity

(c) Specific work

(d) Mass flow rate

Figure 4.7: Typical convergence history of monitored quantities of interest

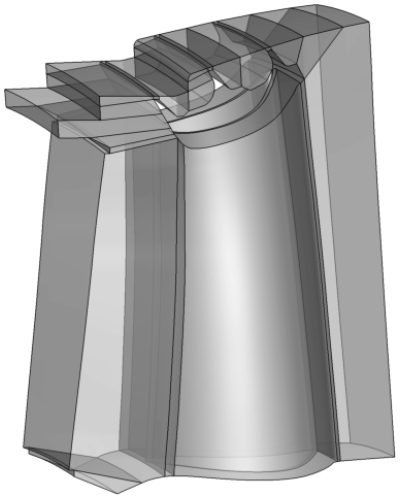

(a) Mesh blocking structure

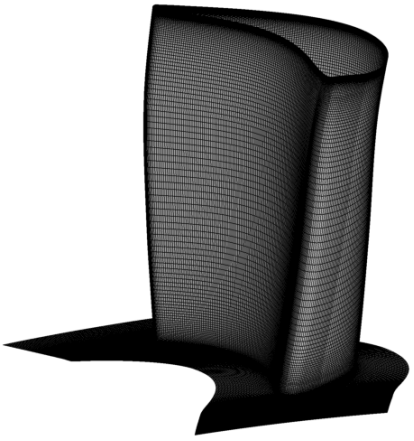

(b) Exposed rotor blade

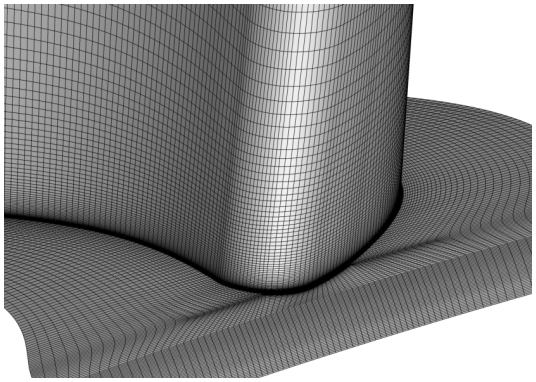

(c) LE

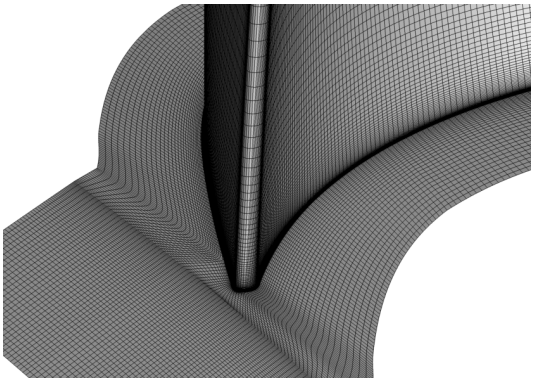

(d) TE

Figure 4.8: PADRAM grid details

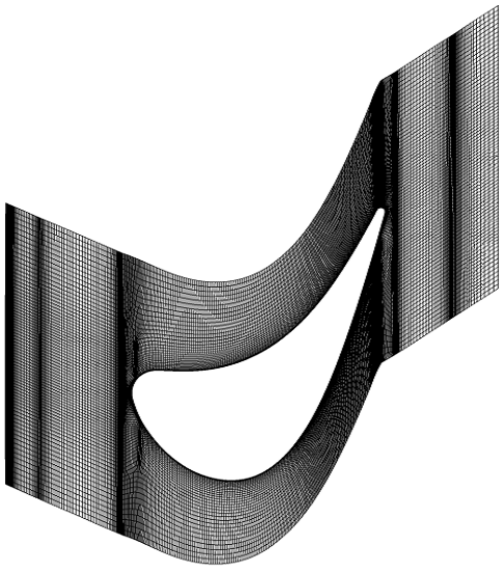

(e) Mid-span airfoil mesh

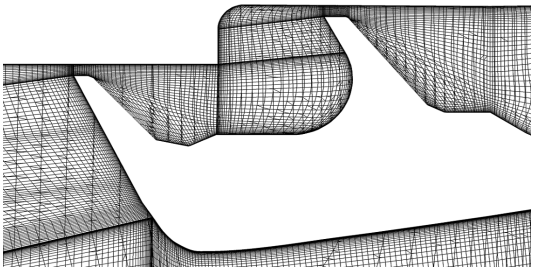

(f) Shroud and tip gap

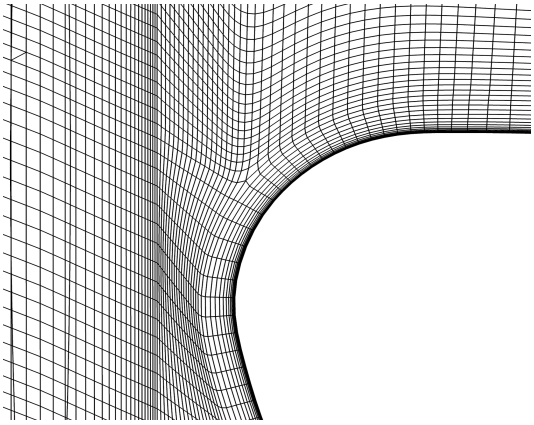

(g) LE boundary layer mesh

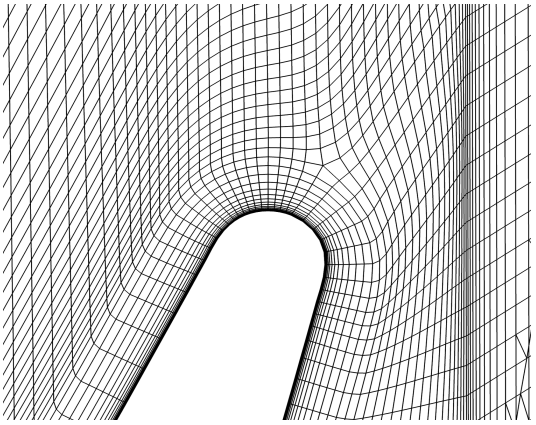

(h) TE boundary layer mesh

Figure 4.8: (cont.) PADRAM grid details

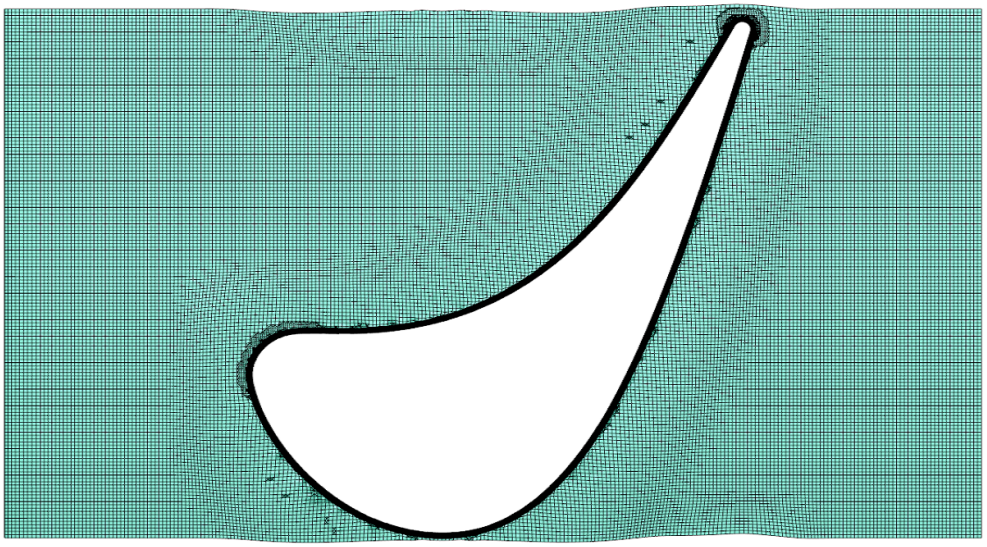

(a) Radial crinkle-cut view of body-fitted mesh

Figure 4.9: 21.3M cell BOXERMesh grid with discrete FC hole stubs

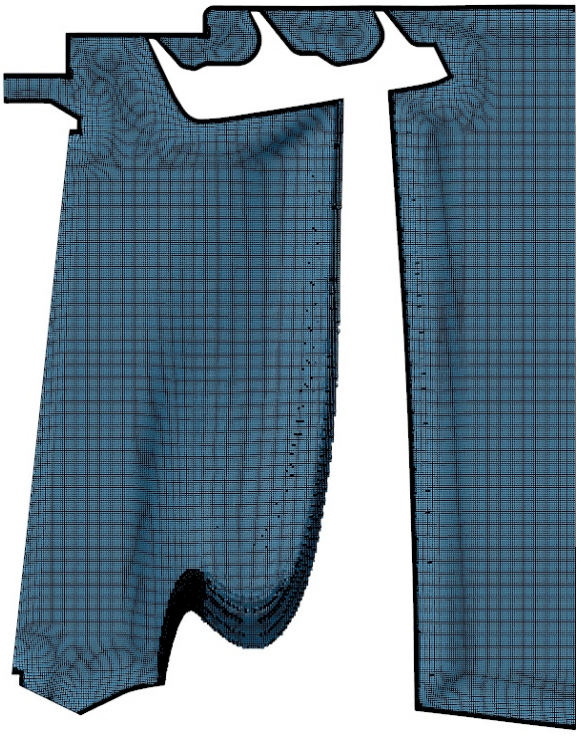

(b) Angular crinkle-cut view of body-fitted mesh

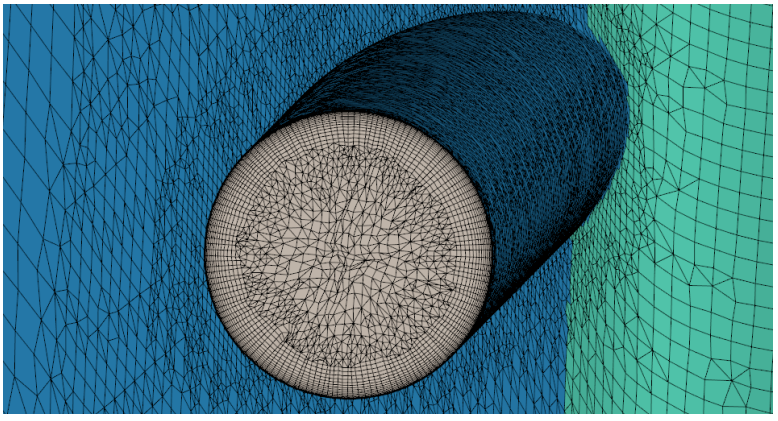

(c) Body-fitted mesh of bottom TE cooling hole stub

Figure 4.9: (cont.) 21.3M cell BOXERMesh grid with discrete FC hole stubs

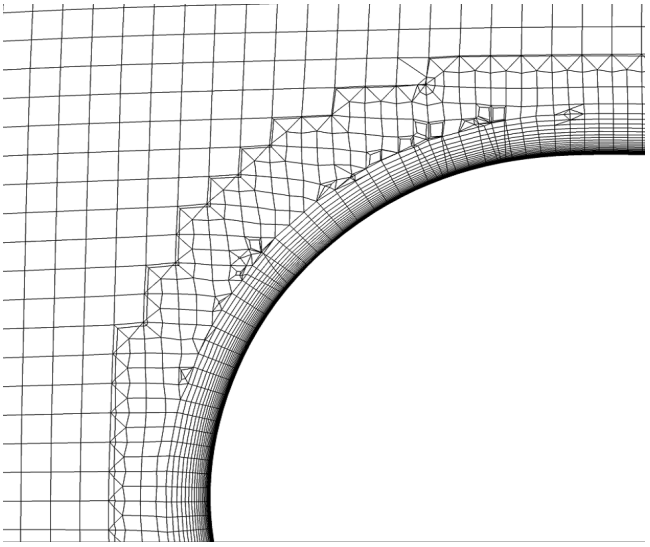

(d) LE boundary layer mesh

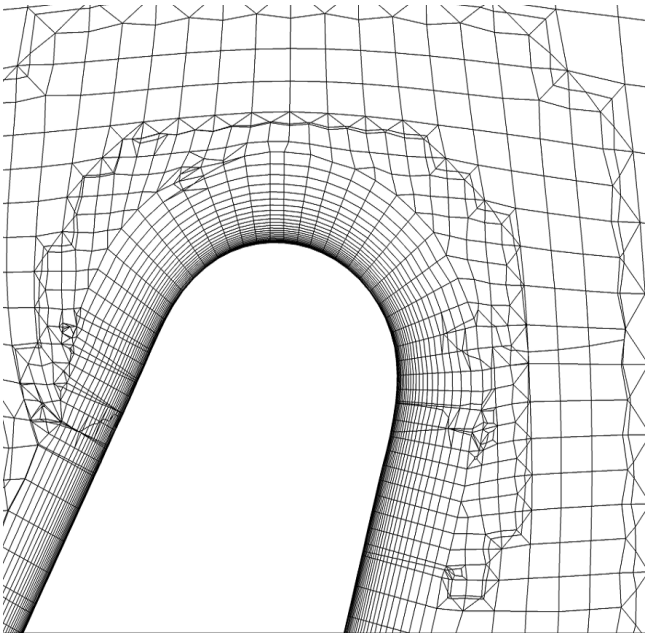

(e) TE boundary layer mesh

Figure 4.9: (cont.) 21.3M cell BOXERMesh grid with discrete FC hole stubs

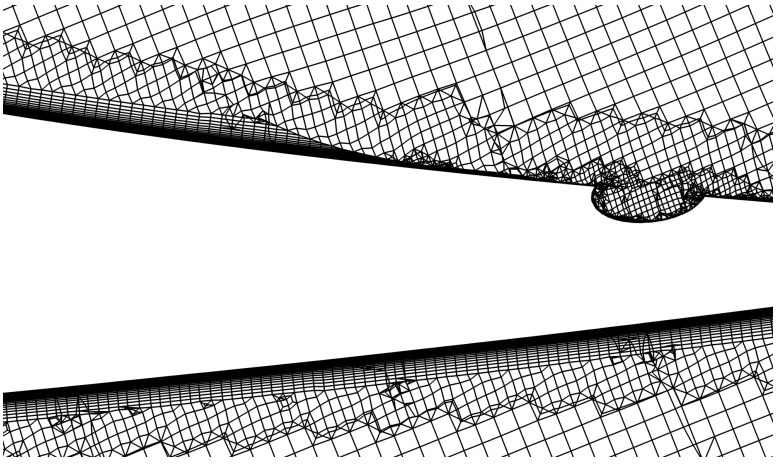

(f) Boundary layer mesh near TE FC hole

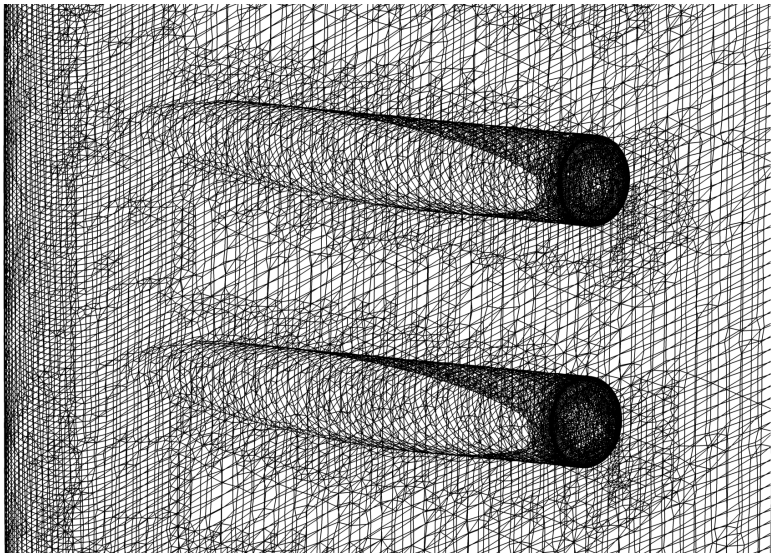

(g) TE FC hole surface mesh

Figure 4.9: (cont.) 21.3M cell BOXERMesh grid with discrete FC hole stubs

4.6 Summary

In this chapter, the governing equations of the pursued CFD approach, the 3D compressible RANS equations, were described at the beginning. Next, the CFD model of a rotating turbine blade, its CFD domain and CFD setup were introduced. Typical aerodynamic quantities of interest for a turbine rotor were defined. Then, the computational approach pursued here with Rolls-Royce's main CFD solver HYDRA at its core was presented. Two different approaches to grid generation, PADRAM and BOXERMesh, were presented, since only BOXERMesh is capable of meshing small discrete film cooling holes on the blade surface. Several figures of each mesh type were used to illustrate the differences between the grids. Finally, an indirect approach using experimental data from the MT1 turbine research rig to validate the CFD results was presented.

The sample of turbine blade scans and the accurate reverse engineering workflow from Chapter 3 can now be combined with the CFD workflow and model described in this chapter into coherent UQ and RDO workflows, which is the subject of Chapter 5.

Chapter 5

Robust Turbine Blade Optimization in the Face of Real Geometric Variations

This short introductory section serves to make clear what is novel in this chapter, what existed before and where the work of others was used. The contribution in this chapter relative to prior work is the incorporation of a previously developed parameterization method, published by Heinze, Meyer, et al. (2014), and of an uncertainty quantification (UQ) workflow, published by Scharfenstein, Heinze, et al. (2013), into a coherent robust design optimization (RDO) workflow for high-pressure turbine (HPT) blades, which is a new heuristic to incorporate real variations of the entire blade shape. It is shown that artificially generated blades for UQ can recreate the stochastic performance of real scans and that the optimization effectively produces robust turbine blade designs. The optimization strategy also improves existing techniques, can handle constraints and has been integrated into Rolls-Royce's optimization tool OPTIMAT v2. OPTIMAT v2 is a surrogate-based optimization tool developed at the University of Southampton's Rolls-Royce University Technology Centre (Voutchkov and Keane, 2010). Its existing optimization methods are used here and these are not part of this work. In OPTIMAT v2, the difference to similar surrogate-based robust optimization methods is that UQ is carried out on a single surrogate and the statistics are passed straight to the optimizer. The construction of another layer of surrogates for mean and standard deviation is not required. Moreover, this is an improvement to related work on compressor blades, where deviations were approximated with a truncated multivariate normal distribution (Bestle, Flassig, et al., 2011). Probability density functions of random parameters are estimated nonparametrically through KDE. This is more flexible and allows the incorporation of random variables with any distribution.

5.1 Uncertainty Quantification & Robust Optimization

Broad categories for UQ methods are sampling-, expansion-, spectral- and quadrature-based approaches. Techniques from each category are also often combined to improve specific deficiencies of individual methods. The distinction between intrusive and non-intrusive methods is also important since intrusive methods (such as the stochastic Galerkin method) require changing the solver, which is often impractical, possibly costly and requires access to the solver's source code. Sampling-based methods are the simplest UQ option and, for example, include the Monte Carlo (MC) and quasi-Monte Carlo (QMC) methods. The main problem with MC is the large number of samples required for convergence. QMC samples are more evenly distributed than MC samples and work with low-discrepancy sequences such as Halton, Sobol or Faure sequences. This leads to a faster rate of convergence close to $\mathcal{O}(1/N)$, versus $\mathcal{O}(1/\sqrt{N})$ for MC (Asmussen and Glynn, 2007). Extensions such as descriptive sampling, importance sampling or other variance reduction techniques such as control variates also exist to improve convergence (Gentle, 2006; Ng and Willcox, 2015). Another related approach, in part similar to Gaussian quadrature, is the sigma point (SP) method, also known as the unscented transform (UT) method. The key concept in this approach is the sample selection using only $2N + 1$ sigma sample points (Julier and Uhlmann, 1996; Mattia, Sergio, et al., 2007; Padulo, Campobasso, et al., 2007). Padulo, Campobasso, et al. (2011) also proposed the closely related non-intrusive univariate reduced quadrature (URQ) UQ method. Often, the problem with these and sparse grid methods, although highly efficient for smooth functions due to the reduced number of points, is that they cannot cope with potentially noisy, discontinuous or missing data points, e.g., due to diverged CFD or parameterization failures. For example, Gerstner and Griebel (2003) presented the tensor-product adaptive sparse quadrature method, which starts off with small grids and then continuously refines the approximation by successively adding more grid points.

Stochastic spectral methods, e.g., the intrusive stochastic Galerkin, non-intrusive stochastic collocation (NISC) and non-intrusive stochastic projection (NISP) methods, are surrogate modeling-based UQ techniques, which work by exploiting and approximating the smoothness of high-dimensional spaces with orthogonal polynomials (orthogonal to the pdf of random input variables). Fewer function evaluations as compared to MC or QMC methods are required and statistical properties and sensitivities can be cheaply calculated (Smith, 2013). Depending on the orthogonal polynomial basis used, these techniques are also known as polynomial chaos (PC), generalised PC and arbitrary PC. Polynomial chaos-based surrogate models are typically restricted to problems with only a few variables. For example, Xiu and Karniadakis (2003) suggests $N \approx 10$ random parameters as a threshold. Special care or extensions to the normal models are also

required for discontinuities, e.g., multi-element generalised PC. Padé-Legendre approximants have also been suggested as an alternative (Ahlfeld, Montomoli, et al., 2018; Chantrasmi, Doostan, et al., 2009). Additionally, the fact that polynomial basis functions remain fixed means that metamodels would have to be regenerated if the distribution of a random input noise parameter was changed. As pointed out by O'Hagan (2013), GP-based modeling approaches do not have these deficiencies and therefore might be a better choice. GP-based approaches have been suggested by Myers and Montgomery (2002), Lee and Park (2006) and Dellino, Kleijnen, et al. (2015). Since a new GP-based method is suggested in this work, differences are explored in detail in Sec. 5.2.

Wavelet expansions, e.g., Haar wavelets or multiwavelets, are closely related to polynomial spectral expansions. In CFD, shocks and the corresponding discontinuous or steep change of quantities across shocks can be an issue to describe with PC approaches based on smooth polynomial basis functions. The idea of wavelet expansions is to improve upon this owing to the piecewise wavelet decomposition, which can model sharp changes more accurately. This improved accuracy comes at the expense of slower convergence, however (Le Matre and Knio, 2010). In another paper, Seshadri, Constantine, Gonnet, et al. (2013) suggest a PC variant using rational expressions instead of polynomials. The method was demonstrated to have faster convergence compared to NISP and NISC. Another new approach is the combination of PC and Kriging techniques, termed polynomial chaos-based Kriging, where the polynomials are used as the trend of a universal Kriging metamodel (Schobi, Sudret, et al., 2015). Using the Ishigami function, the authors find the combined method to be better and never worse than the individual approaches. Yet another option is Multilevel Monte Carlo (MLCMC), which tries to make use of fine and coarse grids. The main idea of MLMC is that statistics such as the expected value can be evaluated by sampling the coarsest grid with correction terms from sampling finer grids (Pisaroni, 2017).

Generally, robust design involves four steps: uncertainty identification, quantification, propagation and solution of an optimization problem. Various approaches to robust optimization such as noisy phenotype schemes have been compared by Keane (2009, 2012). In particular, it was shown that co-Kriging can be very efficient, but also that there is no universal method of choice. Other research in this area tries to make these approaches more efficient. One example would be multi-level recursive co-Kriging with sparse precision matrices of Gaussian-Markov random fields proposed by Perdikaris, Venturi, et al. (2015). However, co-Kriging or other multi-fidelity approaches are typically only options when high- and low-fidelity model outputs are well correlated and otherwise cannot be used. Surrogate model-assisted optimization is typically a suitable choice, whereas direct NSGA-II (Non-dominated Sorting Genetic Algorithm II by Deb, Pratap, et al. (2002)) searches involving a vast number of function evaluations in conjunction

with long CFD runtimes are often prohibitively expensive in practice. NSGA-II is by no means the only option and similar alternatives such as SPEA-2 (Strength Pareto Evolutionary Approach) as proposed by Zitzler, Laumanns, et al. (2001) or MOPSO (Multi-objective Particle Swarm Optimization) from Pulido and Coello (2004) exist. For optimization under uncertainty, Kriging has been shown to be more accurate than other alternatives such as radial basis functions by Jin, Du, et al. (2003). Improved versions of ordinary Kriging can also be used. For example, in gradient-enhanced Kriging gradients from an adjoint method are used to help improve UQ and the surrogate (Roache, 1997). There are also alternative approaches for robust design itself such as PDF matching, as proposed by Seshadri, Constantine, Iaccarino, et al. (2016). The basic idea of this method is to minimize a metric between the PDF of an existing nominal design and the PDF of a target design. PDF matching involves a single objective optimization problem with the particular issue of what kind of target PDF the designer should select, which is unclear. Robust design does not have this problem and reveals the Pareto front of non-dominated solutions, which designers can use to make more informed choices, independent of arbitrary target PDFs, which would influence the final solution from PDF matching.

It is also worth noting that robust optimization can be construed differently, that there is no universal definition for robustness and that different statistics can be used as objectives. For example, minimizing expectation and dispersion, expectation and nominal value or nominal value and dispersion are three possible formulations (Das, 2000). Other approaches with quantiles have also been suggested by Du, Sudjianto, et al. (2004) and by Rhein (2014). By far the most frequent form is to minimize expected value and standard deviation, which is also used here. Hence, the stochastic objectives are to simultaneously minimize the sample mean in Eq. (5.1) and the unbiased sample standard deviation in Eq. (5.2):

$$\overline{x} = \frac{1}{N}\sum_{i=1}^{N} x_i, \tag{5.1}$$

and the (unbiased) sample standard deviation, Eq. (5.2),

$$\hat{s} = \sqrt{\frac{1}{N-1}\sum_{i=1}^{N}(x_i - \overline{x})^2}. \tag{5.2}$$

It is also interesting to note that there is separate research regarding novel ways to find new update points, e.g., “expected worsening” as a new robustness criterion proposed by Jurecka (2007).

5.2 Computational Methodology

The four basic robust optimization steps can be broken down as follows:

1. Construction and evaluation of a design of experiments (DOE) comprising the design *and* noise parameter space
2. Tuning of an ordinary Kriging surrogate model
3. UQ through sampling the surrogate (MC or quasi-Monte Carlo (QMC) sampling)
4. Multi-objective optimization of mean and variance using NSGA-II (Deb, Pratap, et al., 2002)

One part of this robust optimization methodology is novel and differs from existing approaches, e.g., those due to Lee and Park (2006) or Dellino, Kleijnen, et al. (2015). In this thesis, one single Kriging model for the combined design and noise parameters is constructed and then sampled. In both references, however, an intermediate Kriging model is built first, which is then sampled to construct another layer of Kriging models for mean and variance. In this thesis, mean and standard deviation are passed directly to NSGA-II without these additional surrogates, which is more efficient (since only one surrogate has to be optimized) and more accurate (due to the lack of redundant surrogates). The key advantage of this process is the cheap computation of statistics through sampling the surrogate model. In step 3, either pseudorandom numbers, so MC samples, or low-discrepancy sequences (QMC methods) can be used. QMC samples are more evenly distributed and QMC can be superior to MC due to its faster rate of convergence close to $\mathcal{O}(1/N)$, versus $\mathcal{O}(1/\sqrt{N})$ for MC (Asmussen and Glynn, 2007). One of the advantages of the proposed workflow is that the surrogate is independent of the number of UQ samples. To ensure fast UQ, the surrogate, as opposed to the expensive black box function, can be sampled efficiently thousands of times to calculate the statistics.

As the name implies, NSGA-II is an elitist genetic algorithm, which makes use of fast non-dominated sorting to assign classification ranks to each individual. By making use of the target function, non-dominated Pareto front points are assigned a rank order of one, whereas second rank individuals can be dominated by first rank individuals, and so on. Ranks are assigned by comparing each individual with all other individuals of the same population. In addition, NSGA-II uses the crowded-comparison operator to ensure diverse, spread out solutions, which help prevent the algorithm from getting stuck in a local optimum. The crowding distance is used as the main metric to quantify the proximity of solutions. For each new offspring population, other typical features of genetic algorithms such as crossover, mutation and tournament selection are also used. The total computational complexity of NSGA-II is $\mathcal{O}(MN^2)$, where M is number of objectives and N is the population size (Deb, Pratap, et al., 2002).

5.2.1 Robust Optimization

As already noted, robust design generally involves the four steps of uncertainty identification, quantification, propagation and solution of an optimization problem. The quality of the underlying measurement data as the basis for the entire process is especially important. These variations need to be quantified in terms of probability distributions. Mathematical models such as basic Monte Carlo can then be used for uncertainty propagation. The fourth part involves the search for the optimal statistics. The origin of variations or uncertainties in general can be classified as either (1) purely aleatory (inherent), (2) purely epistemic (model-form; reducible) or (3) mixed (aleatory and epistemic) (Zhang and Hosder, 2013). Purely epistemic uncertainties could theoretically be fully removed if 100% accurate models existed. For example, in the case of gas turbines, aleatory uncertainties are variations of inlet boundary conditions and manufacturing variations. Epistemic uncertainties include the accuracy of RANS turbulence models, unsteady effects as well as surface roughness, transition and heat transfer models. Robust design methods typically require the definition of noise factors $\boldsymbol{\xi} = [\xi_1,\ \xi_2, \ldots,\ \xi_p]^T$ and control factors or design variables $\boldsymbol{x} = [x_1,\ x_2, \ldots,\ x_q]^T$ (Keane and Nair, 2005). As their name implies, control factors can be freely manipulated by the designer whereas noise factors are difficult or expensive to control. Robust optimization is applicable when parameters are bounded and some information about uncertainties is available. The definition of robust design involves a stochastic multi-objective optimization process, where any potential outputs of interest $\boldsymbol{f}(\cdot)$ such as the efficiency is stochastic and cannot be computed directly. As a starting point, the deterministic formulation in Eq. (5.3) below generally describes multi-objective optimization problems. In equation (5.3), $\boldsymbol{f} = [f_1, f_2, \ldots, f_n]^T$ is the objective vector function, $\boldsymbol{x}$ is the design variable vector, $\boldsymbol{x}_L$ and $\boldsymbol{x}_U$ are lower and upper bound vectors and $g_i(\boldsymbol{x})$ are the i-th constraints.

$$\begin{aligned} \underset{\boldsymbol{x}}{\text{minimize}} \quad & \boldsymbol{f}(\boldsymbol{x}) \\ \text{subject to} \quad & g_i(\boldsymbol{x}) \leq 0, \qquad i = 1, 2, \ldots, I \\ \text{and} \quad & \boldsymbol{x}_L \leq \boldsymbol{x} \leq \boldsymbol{x}_U \end{aligned} \tag{5.3a}$$

For a robust design optimization, the deterministic formulation in Eq. (5.3) is transformed into a multi-objective stochastic formulation, as shown in Eq. (5.4) below (Augusto, Bennis, et al., 2012; Padulo, Campobasso, et al., 2011):

$$\begin{aligned} \underset{\boldsymbol{x}}{\text{minimize}} \quad & \boldsymbol{f}(\boldsymbol{x}, \boldsymbol{\xi}) \text{ and } \Delta\boldsymbol{f}(\boldsymbol{x}, \boldsymbol{\xi}) \\ \text{subject to} \quad & g_i(\boldsymbol{x}, \boldsymbol{\xi}) + \Delta g_i(\boldsymbol{x}, \boldsymbol{\xi}) \leq 0, \qquad i = 1, 2, \ldots, I \\ \text{and} \quad & \boldsymbol{x}_L \leq \boldsymbol{x} \leq \mathbf{x}_U \\ \text{and} \quad & \boldsymbol{v} - \Delta\boldsymbol{v}_L \leq \boldsymbol{v} \leq \boldsymbol{v} + \Delta\boldsymbol{v}_U \end{aligned} \tag{5.4a}$$

The stochastic objectives are to minimize the mean *and* the dispersion of the quantities of interest. This dispersion can be expressed through some measure such as the variance, standard deviation or interquartile range. The range of this dispersion is expressed below as $\Delta \boldsymbol{f}(\boldsymbol{x}, \boldsymbol{\xi}) = [\Delta f_1, \Delta f_2, \dots \Delta f_k]^T$. The vector $\boldsymbol{v} = [\boldsymbol{x}^T \boldsymbol{\xi}^T]$ combines the design and noise variables and is used in Eq. (5.4) to constrain the variations of the uncertain inputs to prescribed limits.

Furthermore, the solution of multi-objective optimization problems involves the determination of a Pareto front, which contains the Pareto optimal or non-dominated solutions $\boldsymbol{x}^*$. Such solutions are all equally good and can then be used to make trade-offs, e.g., between the mean and the variance. As shown by Miettinen (2012) and Augusto, Bennis, et al. (2012), a necessary condition for Pareto optimality is to satisfy the Karush-Kuhn-Tucker condition in Eq. (5.5), where ω_i is a positive weighting factor for the gradient of the i-th objective function at point $(\boldsymbol{x}^*, \nabla f_i(\boldsymbol{x}^*))$ and λ_j is a weighting factor for the gradient of the j-th inequality constraint function $\nabla g_j(\boldsymbol{x}^*)$.

$$\sum_{i=1}^{k} \omega_i \nabla f_i(\boldsymbol{x}^*) + \sum_{j=1}^{m} \lambda_j \nabla g_j(\boldsymbol{x}^*) = 0 \tag{5.5a}$$

$$\lambda_j g_j(\boldsymbol{x}^*) = 0 \tag{5.5b}$$

$$\lambda_j \geq 0 \tag{5.5c}$$

$$\omega_i \geq 0; \quad \sum_{i=1}^{k} \omega_i = 1 \tag{5.5d}$$

5.2.2 Robust Optimization with an Analytical Function

As an analytical toy problem, a stochastic version of the modified Branin function (Forrester, Sobester, et al., 2008) in Eq. (5.6),

$$f(\boldsymbol{x}) = \overbrace{\left(x_2 - \frac{5.1}{4\pi^2}x_1^2 + \frac{5}{\pi}x_1 - 6\right)^2 + 10\left(1 - \frac{1}{8\pi}\right)\cos x_1 + 10 + \frac{1}{3}(x_1 + 5)}^{\text{Modified Branin function (Forrester, Sobester, et al., 2008)}} + \underbrace{50000 \cdot \left(\frac{\frac{x_3}{8}\left(0.05 + \cos(\frac{x_1}{8} + 1)^4 + \cos(\frac{x_2}{8} + 7)^4\right) + \frac{x_4}{8}\cos(\frac{x_1}{8} + 1)^2 \cos(\frac{x_2}{8} + 7)^2}{(\frac{x_1}{8} + 1)^2 + 2(\frac{x_2}{8} + 7)^2}\right)}_{\text{Extra uncertain / noise term (cf. Keane (2012))}} \tag{5.6}$$

is used, where in addition to the usual design parameters, $x_1 \in [-5, 10]$ and $x_2 \in [0, 15]$, two additional noise parameters, $x_3, x_4 \in [-8, 8]$, are part of the function. Without noise, the modified Branin function is a multimodal function and has a single global minimum in the upper left corner at $f(-\pi, 12.275) \approx 1.0174$.

A bound-constrained multi-objective optimization problem formulation is given by Eq. (5.7):

$$\begin{aligned} \underset{x}{\text{minimize}} \quad & \mathrm{E}[f(\mathbf{x})] \text{ and } \mathrm{Var}[f(\mathbf{x})], \\ \text{subject to} \quad & x_1 \in [-5, 10], \\ \text{and} \quad & x_2 \in [0, 15], \\ \text{and} \quad & x_3, x_4 \in [-8, 8]. \end{aligned} \tag{5.7}$$

To solve this, a 20-point Latin Hypercube DOE for design and noise parameters is generated and evaluated first. The second step is to construct the Kriging surrogate given the parameters and their responses, as described in Sec. 5.2.2.1 in detail. Third, the statistics are computed using 100,000 QMC Sobol samples. Fourth, a multi-objective search is run with NSGA-II. Both population and generation size are set to 100 and a space-filling DOE is used inside NSGA-II at the start. The result of this search is a set of non-dominated, Pareto-optimal update points, which can be added to the initial DOE. The update point selection method first selects points in the middle of the Pareto front, followed by endpoints and points in between. Every new point is compared to existing points to ensure that only truly new points are added. The optimization loop can be repeated until convergence is detected or until a fixed time limit has been reached. Convergence is monitored after every iteration. New Pareto-optimal infill points are compared to all previous points to make sure they are truly new and not too close to existing points. The search is stopped if not a single new Pareto-optimal point can be found for four consecutive iterations. Besides Pareto-optimal update points (exploitation), space-filling update points can also help improve surrogate model accuracy through better space exploration. They are computed with the Euclidean distance by selecting points furthest away from existing points (DOE and update points). In this example, five Pareto-optimal and five space-filling update points are requested in every iteration. Additionally, whenever update points are clustered too closely, again based on a minimum allowed Euclidean distance, a filtering method using a d-dimensional hypersphere replaces such points with space-filling update points.

The results from this methodology applied to Eq. (5.7) are depicted in Fig. 5.1. The resulting estimates of both mean and standard deviation in the design parameter space are shown in Figs. 5.1a-5.1b, respectively. Figure 5.1c shows the final Pareto front in the objective space after 100 iterations through the loop. For validation, the metamodel-based search was compared to a direct NSGA-II search using a 20-point Sobol sequence DOE and 100,000 Halton sequence UQ samples per design point. The agreement of both Pareto fronts in Fig. 5.1c confirms the previous results.

To gauge surrogate model accuracy, metrics such as the coefficient of determination (R^2), the root-mean-square error (RMSE) and the maximum absolute error (MAE) as

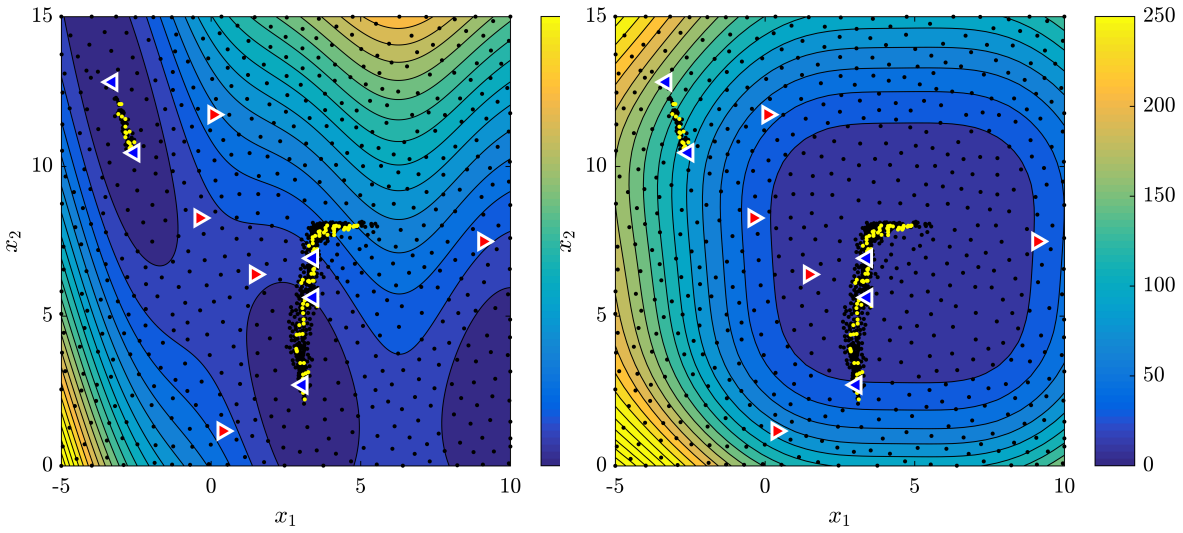

(a) Estimated mean in design space (b) Estimated standard deviation in design space

Figure 5.1: Robust optimization using Eq. (5.6) with 5 Pareto-optimal update points (◀), 5 space-filling update points (▶), all Pareto-optimal points (●) and all evaluated points (●).

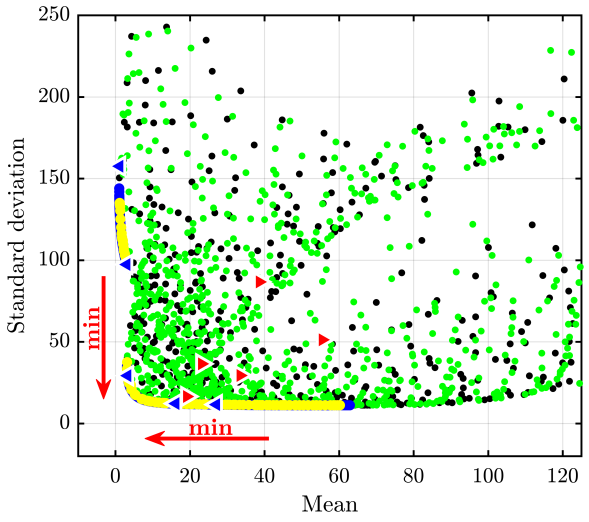

(c) Robust Pareto fronts in objective space

Figure 5.1: (cont.) In addition to markers from Figs. 5.1a-5.1b, direct NSGA-II Pareto front points (●) and corresponding evaluated points (●) are depicted for validation.

defined in Eq. (5.8),

$$R^2 = 1 - \frac{\sum_{i=1}^{n}(f_i - \hat{f}_i)^2}{\sum_{i=1}^{n}(f_i - \bar{f})^2}, \tag{5.8a}$$

$$\mathrm{RMSE} = \sqrt{\frac{1}{n}\sum_{i=1}^{n}\left(f - \hat{f}\right)^2}, \tag{5.8b}$$

$$\mathrm{MAE} = \max\left(|f - \hat{f}|\right), \tag{5.8c}$$

can be computed using k-fold cross-validation, i.e., using k subsets of points. RMSE and MAE are reported in percent with regard to the full range of values, e.g., in Table 5.1. Expectedly, given the huge number of points in only four dimensions, the final surrogate model accuracy is excellent.

Table 5.1: Cross-validated accuracy estimates for surrogate models of $f(\mathbf{x})$.

Error metric	Beginning (20 points)	End (1020 points)
R^2 [%]	91.2214	99.9958
RMSE [%]	6.4896	0.0593
MAE [%]	15.2618	1.0988

5.2.2.1 Kriging Surrogate Models

Ordinary Kriging surrogate models approximate black box function responses $f(\mathbf{x})$ at any point $\mathbf{x}$ with the stochastic process model $y = \mu + \epsilon(\mathbf{x})$, where μ is a constant mean and ϵ a Gaussian error with zero mean and variance σ^2. ϵ is assumed to depend on the distance between observed data points. Based on the choice of basis function, the correlation matrix $\mathbf{\Psi}$ is then constructed. In engineering applications, this is typically the correlation function in Eq. (5.9) (Forrester, Sobester, et al., 2008):

$$\Psi(\boldsymbol{x}^{(i)}, \boldsymbol{x}^{(l)}) = \exp\left(-\sum_{j=1}^{d} \theta_j |x_j^{(i)} - x_j^{(l)}|^{q_j}\right) + \lambda\delta_{ij}. \tag{5.9}$$

Surrogate model hyperparameters θ_j, q_j and λ are tuned using maximum likelihood estimation (MLE), where the concentrated log-likelihood function (CLLF) is optimized with a hybrid optimizer, viz., particle swarm optimization (PSO) followed by a greedy downhill search. λ is a regression constant added to the diagonal of $\mathbf{\Psi}$ to deal with potentially noisy CFD outputs by either interpolating ($\lambda = 0$) or regressing ($\lambda > 0$) observed data points. When $q_j = 2$, Eq. (5.9) is called the Gaussian correlation function. A new ordinary Kriging prediction $\hat{f}$ at update a point $\boldsymbol{x}^N$ is given by Eq. (5.10) with $\boldsymbol{\psi}(\mathbf{x}^N) = \mathbf{\Psi}(\mathbf{x}^N, \mathbf{x}^{(i)})$ as the correlation vector between the point and the DOE:

$$\begin{aligned} \hat{f}(\boldsymbol{x}^N) &= \hat{\mu}_r + \boldsymbol{\psi}^T(\mathbf{\Psi} + \lambda\mathbf{I})^{-1}(\boldsymbol{f} - \mathbf{1}\hat{\mu}_r), \\ \text{where } \hat{\mu}_r &= \frac{\mathbf{1}^T(\mathbf{\Psi} + \lambda\mathbf{I})^{-1}\mathbf{f}}{\mathbf{1}^T(\mathbf{\Psi} + \lambda\mathbf{I})^{-1}\mathbf{1}}. \end{aligned} \tag{5.10}$$

A 1D example of interpolated Kriging with 95 % confidence intervals is depicted in Fig. 5.2.

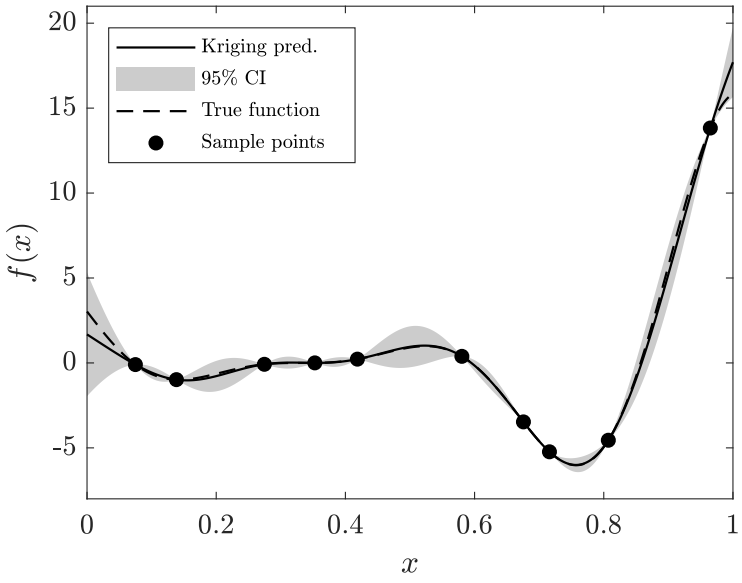

Figure 5.2: 1D interpolated Kriging example with Forrester function and 95% confidence intervals

5.2.3 Robust Optimization Heuristic for Turbine Blades

The robust turbine blade optimization workflow is an extension of the principles described in Sec. 5.2.2 for the analytical example. Figure 5.3 depicts the entire workflow, which can be divided into three main subgroups: In steps 1-3, the initial DOE is generated and evaluated. This involves the geometry construction process as well as the black box CFD objective and constraint functions described later in Sec. 4. The unnumbered steps below steps 1-3 constitute the statistical basis. As described in Sec. 3.3.2.3, based on the 58 optical blade scans, real parameter samples are generated from fitted probability distributions. Also, a target correlation matrix is extracted to generate realistically correlated pseudorandom samples with Iman & Conover's method (see Sec. 3.3.2.3 and Sec. 3.3.2.3). Steps 4-9 constitute the main robust optimization loop. Steps 4-5 correspond roughly to what has been described in the analytical example in Sec. 5.2.2. The full workflow also allows the definition of constraint functions for any quantity of interest. Surrogate models are then built for each objective and each constraint function. Step 5, NSGA-II, yields a set of Pareto-optimal points. Step 6 involves a simple twofold check: On one hand, whether or not to stop because the optimization budget is exhausted, and on the other to leave the loop in case the Pareto front has not changed meaningfully in between four successive iterations. In step 7 the workflow uses incremental increases of the number of UQ samples to speed up UQ search times. Steps 8 and 9 are described in various sections: Sec. 3, Sec. 5.2.4.1 and Sec. 4.

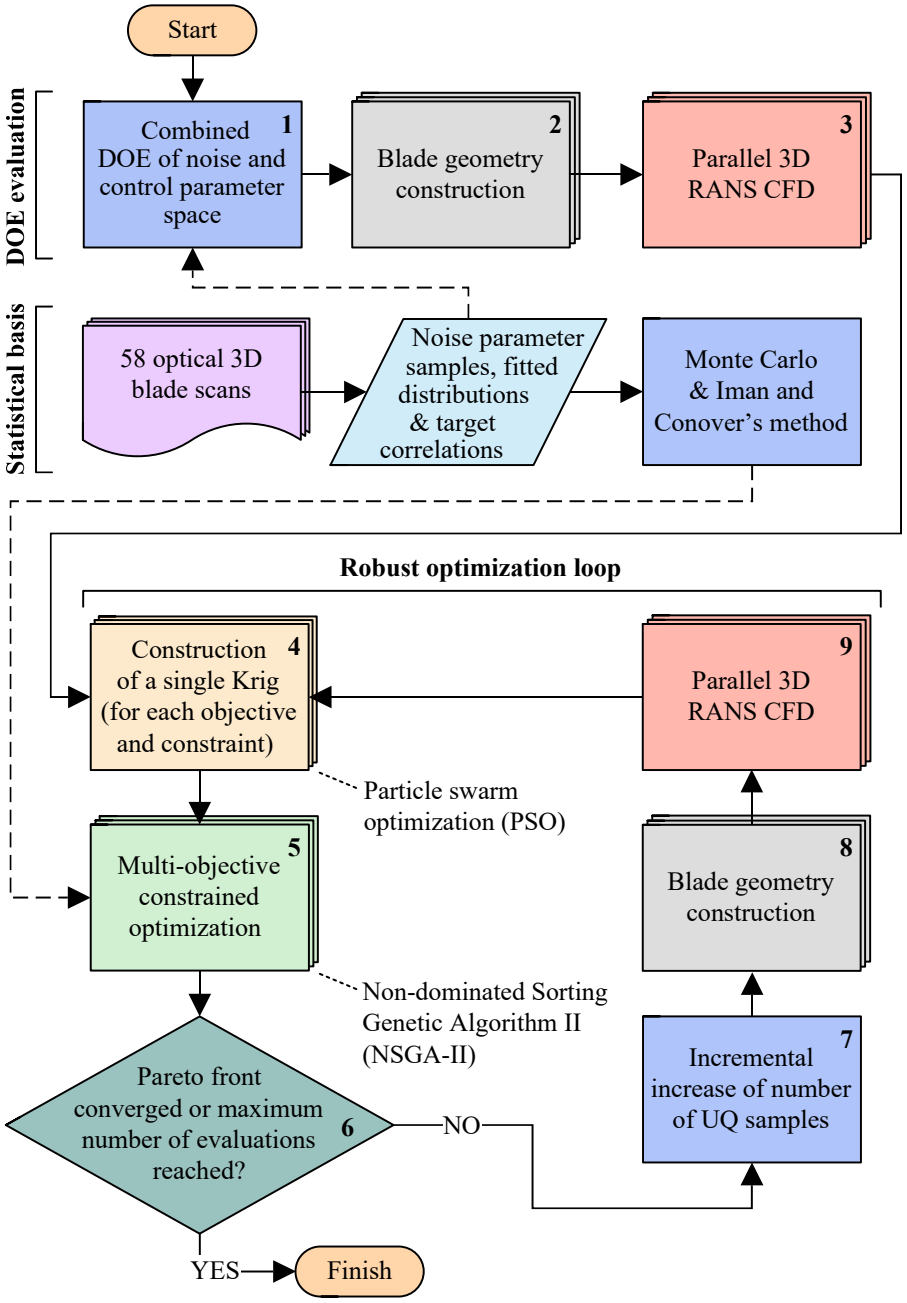

Figure 5.3: Measurement-based robust turbine blade optimization flowchart

The CFD model of the objective function is nearly fully-featured, as described in Sec. 4. Since FC hole variations are not yet modelled here, the inlet total pressure is increased to offset the missing mass flow from the FC holes (see Sec. K for details).

In addition, Fig. 5.4 shows all programs and in-house codes involved in the optimization. Essentially, the top half details the geometry construction workflow from Fig. 5.3 (step eight) and the bottom half the RANS CFD workflow, step nine in Fig. 5.3.

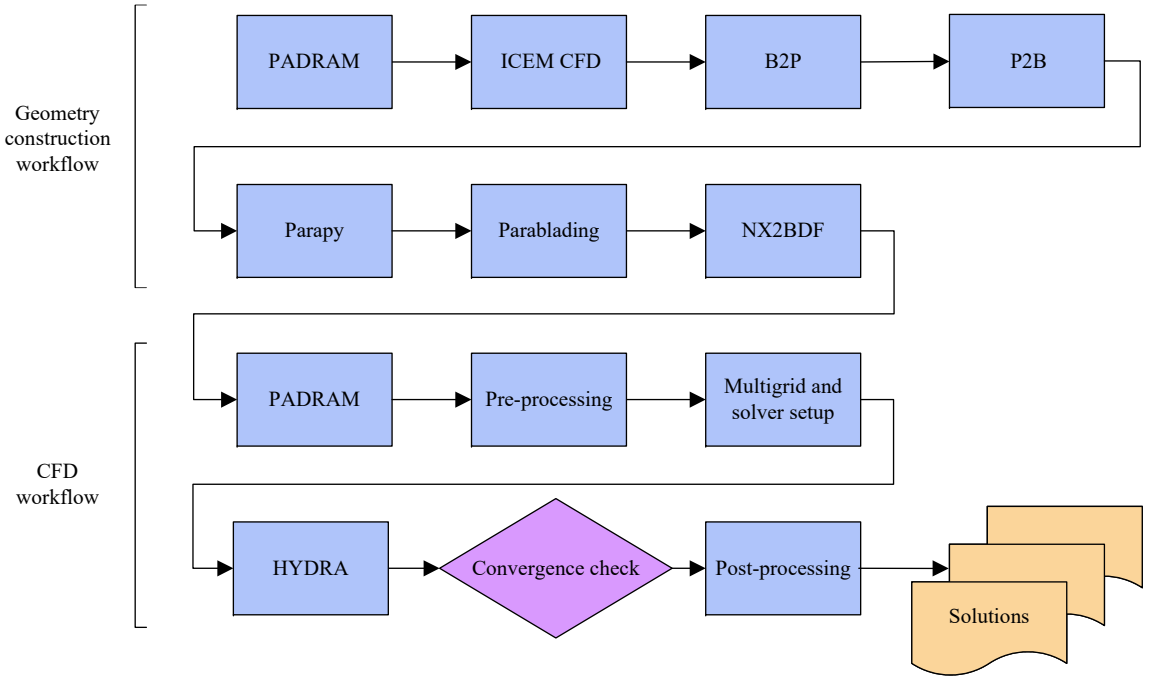

Figure 5.4: Programmatic optimization flowchart

5.2.4 Geometry and Analysis of the Real Scans' Performance

First, to serve as a reference for validation of the parameterized blades for UQ in the next section, the original scans' performance is analyzed by accurately reverse engineering the scanned blade geometries. This is done as follows: First, the FC holes are removed with BCL. Second, B2P is used to extracted blade profiles directly from the STL files by slicing the triangle edges at $n = 41$ radial positions to extract intersection points. These slices are extracted between 10 % and 90 % span to ignore the fillet regions below and above. Third, Parablading is used to create a smooth NX model for each scan. Fourth, NX2BDF is used to create `Blade_Definition` input files for PADRAM with $n = 41$ radial positions. For the defeatured model, the only reconstruction errors are due to the partitioning of scans into discrete airfoil sections and due to the cooling hole removal process. Both are negligibly small. For the fully-featured model, the extrapolated sections below and above 10 % and 90 % are additional sources of epistemic uncertainty. Results are presented in Sec. 5.3.1.

5.2.4.1 Design Parameters

A set of five 3D engineering design parameters are used as controllable design parameters: skew, sweep, lean and LE & TE recambering. As an example, Fig. 5.5a depicts the effects of all five parameters applied at three different radial positions, 0 %, 50 % and 100 % span, so 15 parameters in total. For example, this parameterization has been

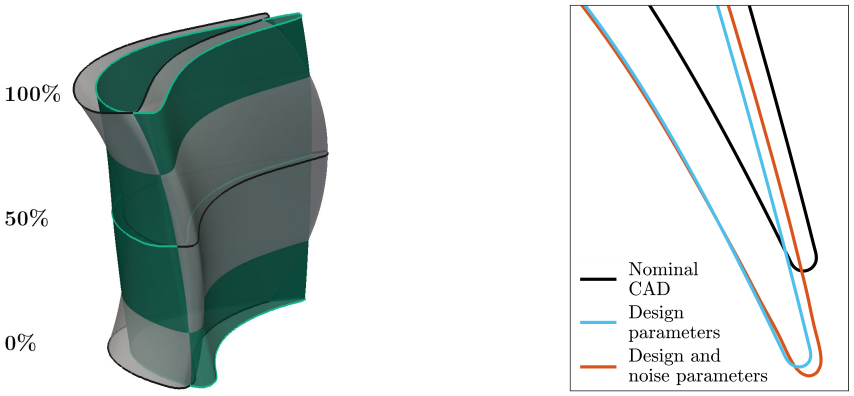

(a) Design parameters at three span positions (b) Design *and* noise parameters at 50 % span

Figure 5.5: Illustration of design and noise parameter effects

used previously in a deterministic aerodynamic turbine optimization to alleviate negative effects from high swirling flows in modern lean-burn combustors (Shahpar and Caloni, 2013). The same reference also details the geometrical changes each parameter brings about. Essentially though, each parameter in some way modifies the 2D airfoil sections: for example, skew rotates them, lean shifts them circumferentially, sweep shifts them axially and both recambering parameters shears them either at the LE or TE. Radially, a B-spline ensures a smooth transition across all airfoil sections. Figure 5.5b illustrates the effects of both the design and the noise parameters. All design parameters are listed in Eq. (5.11),

$$\mathbf{d} = \begin{bmatrix} d_{\text{sweep}}^{(0)} & d_{\text{skew}}^{(0)} & d_{\text{lean}}^{(0)} & d_{\text{lemo}}^{(0)} & d_{\text{temo}}^{(0)} \\ d_{\text{sweep}}^{(0.5)} & d_{\text{skew}}^{(0.5)} & d_{\text{lean}}^{(0.5)} & d_{\text{lemo}}^{(0.5)} & d_{\text{temo}}^{(0.5)} \\ d_{\text{sweep}}^{(1)} & d_{\text{skew}}^{(1)} & d_{\text{lean}}^{(1)} & d_{\text{lemo}}^{(1)} & d_{\text{temo}}^{(1)} \end{bmatrix}, \tag{5.11}$$

where the superscripts refer to the span position, where each parameter is applied.

PADRAM is used to generate new turbine blade shapes given these engineering *design* parameters. Fine, unstructured, triangular surface meshes of each blade are then constructed with ANSYS ICEM CFD. This is done using the "Patch Independent" meshing method with just two parameters to control the mesh size, the "Global Element Seed Size" and "Curvature/Proximity Based Refinement". The first setting controls the global element size and the second one is an adaptive mesh refinement in areas of high curvature, e.g., near the TE. The whole process is automated by running predefined script files in batch mode. The result of this step is simply an exported STL file. Then, baseline parameters and distributions are reverse engineered and the *noise* parameters are applied.

5.2.4.2 Epistemic vs. Aleatoric Uncertainties

In UQ studies, it is important to ensure that epistemic (modeling) uncertainties, i.e., variations stemming from the computational model itself, cause smaller variations than the effects of real aleatoric (inherent) aberrations, i.e., the variations to be quantified. Here, epistemic uncertainties stem from sectioning the blade, meshing, mass averaging over postprocessing planes and averaging of 100 samples for each quantity of interest. Geometric differences as a result of sectioning the blade are negligibly small ($\ll 10\,\mu m$) and hence are of no concern.

As will be shown in Sec. 5.3.1, aleatoric geometric blade variations lead to output variations of roughly 0.2 %, 0.5 % and 0.7 % for efficiency, capacity and specific work, respectively. This stands in contrast to maximal meshing variations of 0.02 % for efficiency, −0.003 % for capacity and −0.015 % for specific work, which were obtained by comparing the outputs from the selected mesh-independent 5.5 million cell mesh with those from finer 8.2 and 15.3 million cell meshes. Hence, meshing uncertainties are at least an order of magnitude smaller than aleatory variations. Since a multitude of simulations have to be carried out, it makes sense to reduce the number of solver iterations down to a minimum. In Sec.4.5, Fig. 4.7 depicts the typical convergence history of the monitored quantities of interest for the first 200 iterations. Visually, it is evident that the outputs converge with far fewer than the initially chosen 1000 iterations. The results in Table 5.2 show that it is sufficient to carry out 300 iterations and that this has a minimal impact on the observed quantities of interest. "Number of iterations" in Table 5.2 refers to full multigrid cycles and does not include the initial multigrid startup with 40 iterations. For the case with 100 iterations, only 50 points are used for the averages.

Table 5.2: Iteration reduction study results

Number of iterations	PCE(η)	PCE(ϕ)	PCE(w)
1000	0	0	0
500	0.0026	1.5457×10^{-4}	0.0022
300	−0.0084	-7.7487×10^{-4}	−0.0185
200	0.0018	1.2000×10^{-3}	0.0036
100	−0.0089	-3.3271×10^{-4}	0.0273

Note: Full multigrid W-cycles after 40 initial cycles with 4 coarse grids

The convergence of the sample mean and the sample standard deviation is shown in Fig. 5.6. It is evident that fluctuations of the mean are very small in comparison to the slower convergence of the standard deviation.

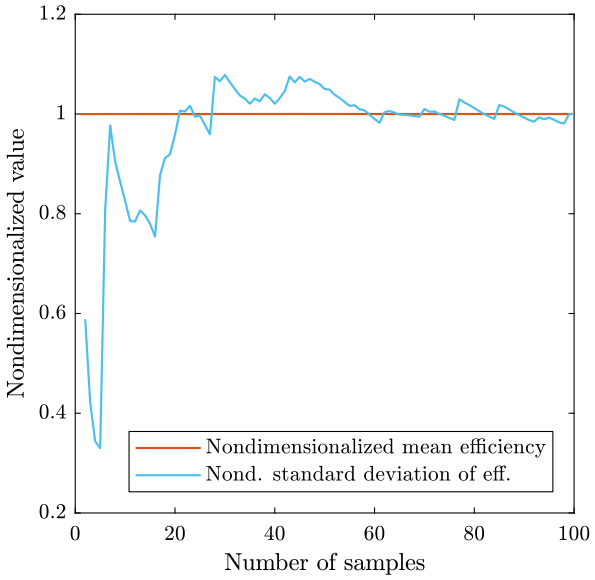

Figure 5.6: Convergence of objectives for 100 artificial blades

5.2.5 Optimization Problem Definition

For a basic aerodynamic optimization of a turbine rotor, the end result ought to be a blade that at some capacity delivers a certain amount of power with a smaller total pressure drop, i.e., higher efficiency. Hence, isentropic efficiency defined in Eq. (6.5) is selected as the objective function. For the purposes of optimization, efficiency is multiplied by negative one to minimize it. Equality constraints for capacity defined in Eq. (6.6) and extracted work defined in Eq. (6.7) are implemented as two inequality constraints each. The capacity constraint for a single HP turbine rotor is chosen to be ±0.1 %, which means the capacity is allowed to vary by ±0.1 % around the nominal design intent's reference value. Often the stator chokes and the rotor is somewhat less critical. The same constraint limits (±0.1 % around the nominal reference value) are chosen for specific work. As will be shown in Fig. 5.7b, the nominal CAD geometry does not satisfy these requirements and hence is not a valid solution. The complete problem formulation is defined mathematically in Eq. (5.12), where the *controllable* PADRAM design parameters are contained in vector $\mathbf{d}$. Since the main intention in this study is to showcase the implementation and design improvements, a 15 design parameter limit is chosen for $\mathbf{d}$. In addition, the vector $\boldsymbol{\Delta}\overline{\mathbf{p}}$ contains the *uncontrollable*, pseudorandom delta noise parameters from Eq. (3.3). The geometry definition hence involves 29 parameters in total. Upper ($\mathbf{d}_U$) and lower ($\mathbf{d}_L$) control parameter bounds in Eq. (5.12) are ±0.2 mm for sweep, ±0.1° for skew, ±0.1° for lean and ±0.05° for LE recambering and ±0.25° for TE recambering. Although these bounds appear to be relatively small in magnitude, the parameters change the blade shape much more than the manufacturing variations. The lower ($\boldsymbol{\Delta}\overline{\mathbf{p}}_L$) and upper ($\boldsymbol{\Delta}\overline{\mathbf{p}}_U$) bounds for the delta noise parameters ensure that no

pseudorandom samples with extreme variations are generated, as described in Sec. 3.3.2.3. The problem tackled is this:

$$\begin{aligned} \underset{x}{\text{minimize}} \quad & \mathrm{E}[-\eta_{is}(\mathbf{d}, \mathbf{\Delta\overline{p}})] \text{ and } \sigma[\eta_{is}(\mathbf{d}, \mathbf{\Delta\overline{p}})], \\ \text{subject to} \quad & 0.999 \cdot w_{\mathrm{CAD}} \leq \mathrm{E}[w(\mathbf{d}, \mathbf{\Delta\overline{p}})] \leq 1.001 \cdot w_{\mathrm{CAD}}, \\ \text{and} \quad & 0.999 \cdot \phi_{\mathrm{CAD}} \leq \mathrm{E}[\phi(\mathbf{d}, \mathbf{\Delta\overline{p}})] \leq 1.001 \cdot \phi_{\mathrm{CAD}}, \\ \text{and} \quad & \mathbf{d}_L \leq \mathbf{d} \leq \mathbf{d}_U, \\ \text{and} \quad & \mathbf{\Delta\overline{p}}_L \leq \mathbf{\Delta\overline{p}} \leq \mathbf{\Delta\overline{p}}_U, \end{aligned} \tag{5.12}$$

where subscript CAD refers to the nominal CAD model's reference performance. There is a key point to be made regarding the definition of constraints in Eq. (5.12), namely that only constraints for *mean values* are enforced here. Given that all stochastic outputs entail some inherent variation, this means certain realizations can violate these mean constraints as optimizers often tend to drive designs close the specified constraint limits.

5.2.6 Computational Implementation & Resources

Due to the large computational demands, the implementation allows for parallel computations for surrogate model training, UQ and searches through MATLAB's parallel pool and CUDA GPU support. The computational setup here consists of an Intel Core i7-4790 and an Nvidia GeForce GTX 750 Ti. CFD simulations run remotely on 14 nodes of a Linux high-performance computing cluster with eight-core Intel Xeon E5-2670 processors. On each cluster node, one instance of the CFD solver can use 16 message passing interface (MPI) processes. The multigrid method and the reduced number of solver iterations also entail a considerable speed-up. Despite all that, the optimization presented in the next section took about two months in total (DOE ≈ 20 days; optimization ≈ 30 days), largely due to the long evaluation time of about eight hours for the CFD. However, using more nodes on a larger cluster and parallelizing more tasks would bring this time down further.

5.3 Results

5.3.1 Validation of Artificial Blade Performance Statistics

The first step is to ensure that randomly built blades exhibit the same statistical performance outputs as the real, original sample of blades. All 58 blade scan models are sliced and built straight from the original STL files, as described in Sec. 5.2.4. 100 artificial blades are constructed for comparison. Due to the good reconstruction accuracy, the expectation is to obtain output performance statistics similar to the real blades. Besides the mean, the coefficient of variation (CV) as defined in Eq. (5.13)

$$C_v = \frac{\hat{s}}{\overline{x}} \tag{5.13}$$

is used to quantify the amount of variability relative to the mean ($\overline{x}$ and $\hat{s}$ are defined in Eq. (5.1) and Eq. (5.2) respectively). CFD results of the defeatured model ($0.1 \leq s \leq 0.9$) are illustrated in Fig. 5.7a. In the figure, the overlapping histograms with outputs from both cases (blue and yellow) show that artificial blades can imitate actual blade performance variations very well. Indeed, the results show that the artificial blades' mean efficiency, capacity and specific work is underpredicted by only 0.01 %, 0.02 % and 0.03 %, respectively. Similarly, CVs were found to be overpredicted by 0.40 %, 1.77 % and 1.44 % only. Good agreement is also observed in Fig. 5.7b for the fully-featured CFD model. The effects the variations have on the fully-featured model are similar to those in Fig. 5.7a for the mean capacity (only −0.02 % difference), but somewhat worse in terms of mean efficiency (−0.07 % difference) and mean specific work (−0.28 % difference).The mean output quantities are all underpredicted by only 0.01 %. Variation is again overpredicted, likely due to the extrapolated sections below 0.1 and above 0.9 span: CVs are 16.19 %, 20.70 % and 2.80 % larger than those of the original scans. In short, results in Fig. 5.7 show that artificially constructed blades are able to faithfully model the performance of real blade scans. The defeatured CFD model can do so a little bit better, probably because it lacks the extrapolated sections used in the fully-featured case.

Figure 5.7 also reveals the impact of the manufacturing variations on blade performance. For the fully-featured blade, mean efficiency drops by about 0.06 %, mean capacity is 0.21 % higher and work produced is 0.08 % lower. Hence, mean capacity is very similar in both models, whereas there are larger differences for efficiency and work. The shift in capacity is attributable to the relatively large deviations from the nominal CAD geometry near the TE, as previously depicted in Fig. 3.2. Due to the manufacturing variations, most blades are skewed with widened throat areas and this has lead to the increase in mean capacity.

5.3.1.1 Impact of Realistic Correlations on Output Statistics

Also briefly worth investigating is the impact of real correlations on performance. In order to quantify this effect, 100 additional, uncorrelated (and hence unrealistic) Sobol sequence samples were evaluated with the defeatured CFD model and compared to the previously analyzed blades built with 100 correlated Monte Carlo samples. In the results for the uncorrelated blades, mean performance errors of −0.11 %, −0.09 % and 0.10 % were observed, so this is considerably worse. Scatter is overpredicted without proper correlations too: uncorrelated CVs were too large with factors of 2.1, 2.6 and 2.4 for efficiency, capacity and work respectively, compared to the results of the real scans. This short analysis leads to the conclusion that real correlations act to reduce the spread of outputs of interest and hence are imperative to obtain realistic results.

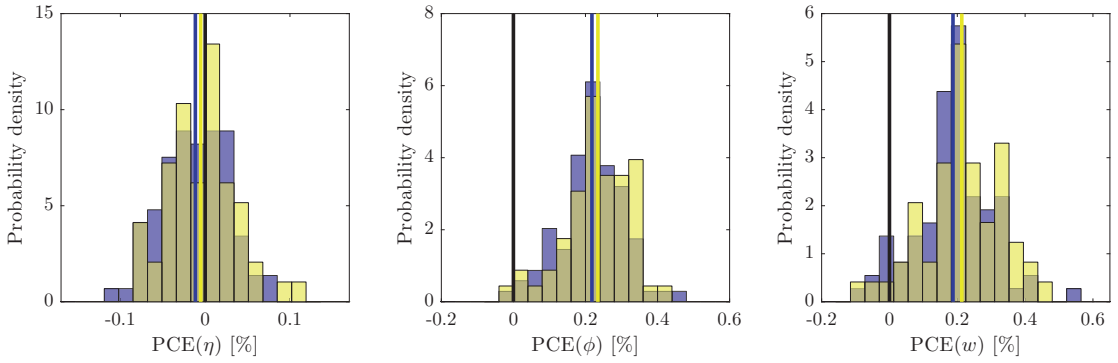

(a) Defeatured CFD model

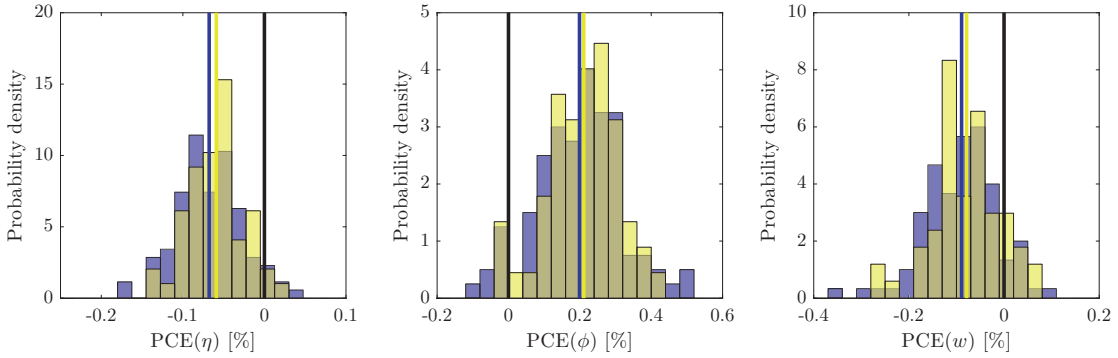

(b) Fully-featured CFD model

Figure 5.7: Comparison of CFD results of 100 artifical blades (samples ■ and mean —) and all 58 original blade scans (samples ■ and mean —) relative to the nominal CAD design intent (—)

5.3.2 Sensitivity Analysis Results

Before optimizing, it is common practice to conduct a sensitivity analysis to reduce the required number of parameters in the model. This can bring about significant computational savings as each omitted variable reduces the size of the sampling space exponentially. Important and potentially irrelevant parameters can be revealed, but the analysis also helps to verify and to understand the model better. Here, for brevity, this is only presented for the noise parameters. Both correlation coefficient-based and surrogate model-based approaches are used, since already evaluated points can be reused and no additional effort is required. Although usage of Spearman's rank correlation coefficient is ill-advised due to the inherent parameter correlations, it is still often used. Other coefficients such as partial correlation coefficients (PCC) or coefficients of importance (COI) overcome this problem somewhat by canceling out effects of other parameters, e.g., see Iooss and Lematre (2015). Here, the COI is used since it is far less sensitive towards correlated input parameters than the rank correlation coefficient. The COI is defined in

Eq. (5.14) as

$$\mathrm{COI} = R^2 - R_o^2, \tag{5.14}$$

where subscript o indicates the model built with one omitted parameter (Scharfenstein, Heinze, et al., 2013). Figure 5.8 presents both the rank correlation coefficient and COI computed with 100 samples and the defeatured CFD model. Many rank correlation coefficients in Fig. 5.8a are not statistically significant, so no conclusions can be drawn from this data. However, TE position and maximum thickness parameters seem to be important. COI-based sensitivities in Fig. 5.8b place much more weight on a few individual parameters and many relations found through rank correlations are not corroborated by the COI. Stagger angle and TE position seem to have the largest effect on efficiency. Similarly, the COI singles out the stagger angle as the most important parameter for capacity and work, but $R_o^2 < 0.8$ is not a reliable result. This corroborates previous results based on a smaller 50-point sample from an earlier UQ-only study based on an older parameterization and a different blade sample (Scharfenstein, Heinze, et al., 2013).

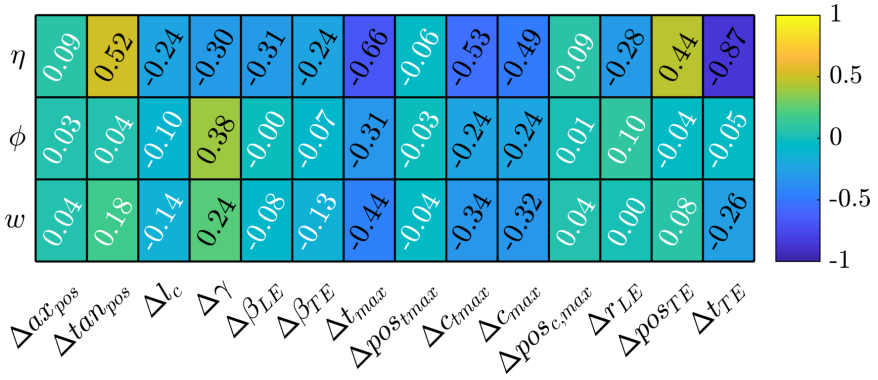

(a) Rank correlation coefficient (SS if $p < 0.05$ black, else white)

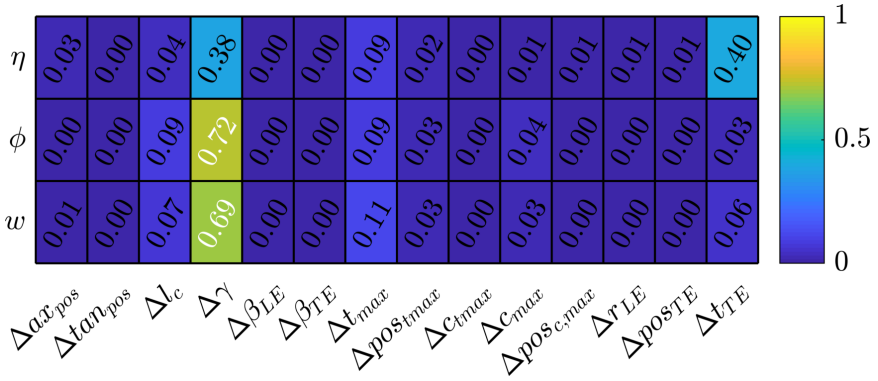

(b) Normalised COI (reliable if $R_o^2 > 0.8$ black, else white)

Figure 5.8: Sampling-based sensitivity analysis results

Surrogate model-based sensitivities were computed to verify the coefficient-based results. Kriging's θ hyperparameters, when suitably non-dimensionalized, serve as

a statistical measure of parameter activity and can be used to produce parameter rankings (Forrester, Sobester, et al., 2008). Here, maximum likelihood estimation as described in Sec. 5.2.2.1 is used to tune Kriging θ hyperparameters within the log-search bounds $\log_{10}(\theta) \in [-10, 3]$. Logarithmic results are presented in Table 5.3 to help identify irrelevant parameters. The previous coefficient-based results are corroborated and the stagger angle is singled out again as the most important parameter for capacity and work, whereas the TE position again is most important for efficiency. Many other parameters are also found to have a meaningful impact. Most importantly though, Kriging identifies the influence of Δtan_{pos}, the tangential position of the blade, as insignificant for all three outputs. Hence, this is the prime candidate for removal from the model. To test whether or not Δtan_{pos} indeed has no significant influence, 100 simulations were repeated without this parameter. Since it still required to build turbine blades though, the value of Δtan_{pos} was fixed to an average taken from the original scan sample matrix $\boldsymbol{P}$. The results, computed using the nominal CAD baseline model and the same random numbers as with all 14 parameters (except for the fixed value for Δtan_{pos}), indeed confirm that Δtan_{pos} can be held fixed. As a matter of fact, the result that Δtan_{pos} is insignificant is a direct consequence of the simulation setup with a single passage. Since only a single blade is modeled at any time and a rotationally periodic mesh is generated around that blade, it does not matter where in the annulus the blade is located, since due to the circumferential periodicity all blades in the annulus are equal. However, Δtan_{pos} would become important if several different blades in the annulus were modeled.

Table 5.3: Kriging surrogate-based sensitivity analysis ($\log_{10}(\theta) \in [-10, 3]$).

	Δax_{pos}	Δtan_{pos}	Δl_c	$\Delta\gamma$	$\Delta\beta_{LE}$	$\Delta\beta_{TE}$	Δt_{max}
$\log_{10}(\theta_\eta)$	−2.38	−10.00	−2.38	−1.88	−4.41	−4.62	−2.20
$\log_{10}(\theta_\phi)$	−2.60	−10.00	−1.47	−0.96	−10.00	−3.86	−1.52
$\log_{10}(\theta_w)$	−3.65	−10.00	−2.78	−2.07	−10.00	−4.36	−2.46

Δpos_{tmax}	Δc_{tmax}	Δc_{max}	$\Delta pos_{c,max}$	Δr_{LE}	Δpos_{TE}	Δt_{TE}
−2.51	−3.39	−2.34	−2.73	−3.92	−2.68	−1.14
−1.81	−3.52	−1.25	−3.05	−5.82	−2.69	−1.50
−3.04	−4.32	−2.40	−4.44	−5.42	−3.94	−2.27

5.3.3 Optimization Results

Following Sec. 5.3.1's findings that artificial blades match the real scans performance and the sensitivity analysis and parameter reduction study in Sec. 5.3.2, the main optimization was carried out. First, a 400-point space-filling Latin hypercube was generated and evaluated. Iman and Conover's method is applied to all noise variables and this does

not interfere with the space-filling structure of the Latin hypercube. 14 update points were requested in every iteration. A threshold of 800 points in total was chosen. For efficiency and accuracy, statistics are computed with 100 UQ samples at the start and up to 1000, with incremental increases by 50 samples in between. Design parameter update points were selected from predicted Pareto front and combined with space-filling noise parameter update points to construct proper blades. For NSGA-II, the number of generations was set to 300 and the population size to 100. Also, it should be noted that the optimization was carried out with all 14 noise variables. The final result of the workflow is the Pareto front depicted in Fig. 5.9. Frequent constraint violations are particularly evident. The axis grid line spacing reveals that mean efficiency is two orders of magnitude larger than the standard deviation. The Krig-predicted performance of the selected Pareto-optimal point is predicted to improve by 0.11 % for the mean and 72.75 % for the standard deviation (compared to the nominal design's performance) and the constraints are predicted to be met. The mean performance improvement is also much larger than the known epistemic uncertainties. A separate validation study is required to verify these surrogate-based predictions, however.

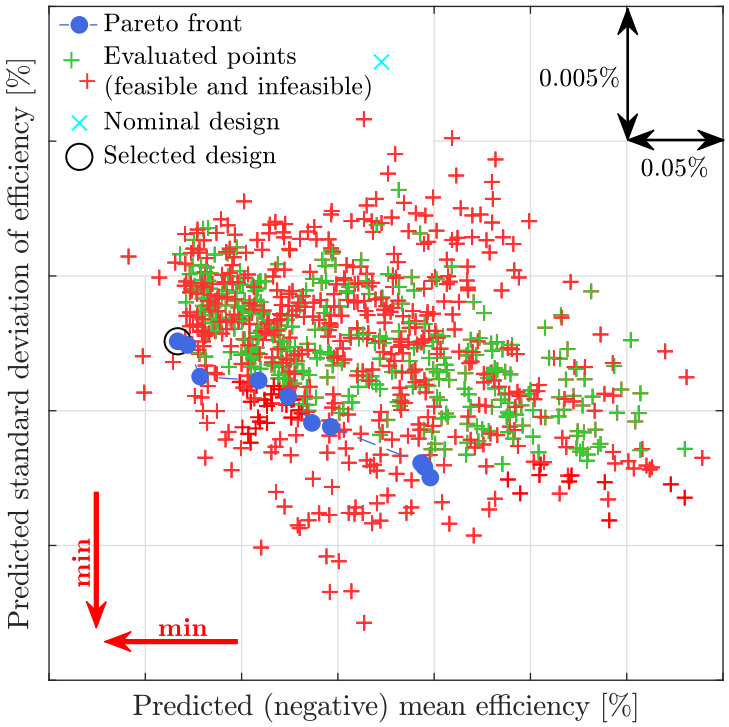

Figure 5.9: Final predicted Pareto front in objective space

As a first step towards validation, it is straightforward to assess all surrogate model accuracies by comparing the predictions to the baseline design's known performance. Based on 1000 samples, the surrogate can be used to predict mean efficiency and standard deviation of the nominal blade. Respective percentage errors are 0.03 % and −25.67 %.

The prediction of the mean efficiency is hence very accurate, whereas the standard deviation is underpredicted. The surrogate model error metric estimates in Table 5.4 also suggest that discrepancies exist. The efficiency surrogate is the least accurate of the three with an MAE of 14.88 %. Update points were added only to the Pareto front and no space-filling update points were added to improve the global accuracy, so it comes as no surprise that the final surrogates are found to be less accurate.

Table 5.4: Cross-validated surrogate accuracy metrics.

	η_{is}	ϕ	w
	Beginning (400 points)		
R^2 [%]	95.7897	99.9620	97.2490
RMSE [%]	3.5985	0.2768	3.0048
MAE [%]	15.2438	1.7487	10.2997
	End (800 points)		
R^2 [%]	97.5879	99.933	97.5152
RMSE [%]	3.1168	0.0311	2.3619
MAE [%]	14.8887	2.3565	10.6251

5.3.4 Validation of Results

Any surrogate model's predictions must be validated, especially given the estimated error in the standard deviation's prediction of 25.67 %. Using the rotor's black box function (geometry construction and CFD performance evaluation) and one of the designs from the Pareto front, it has to be proven *without* the surrogates that the probabilistic performance really is better than that of the baseline design and that is does indeed satisfy the constraints. The encircled design in Fig. 5.9 is selected for this purpose. Figure 5.10b depicts the selected blade's shape. The comparison with the nominal model's shape in Fig. 5.10c highlights the new design, which should be considered in conjunction with the manufacturing variations. The design parameters are listed in Eq. (5.15), where the superscripts refer to the respective span position:

$$\mathbf{d}_{sel} = \begin{bmatrix} 0.170^{(0)}_{\text{sweep}} & 0.014^{(0)}_{\text{skew}} & 0.025^{(0)}_{\text{lean}} & -0.050^{(0)}_{\text{lemo}} & 0.036^{(0)}_{\text{temo}} \\ 0.197^{(0.5)}_{\text{sweep}} & -0.068^{(0.5)}_{\text{skew}} & -0.075^{(0.5)}_{\text{lean}} & 0.027^{(0.5)}_{\text{lemo}} & 0.028^{(0.5)}_{\text{temo}} \\ -0.200^{(1)}_{\text{sweep}} & -0.100^{(1)}_{\text{skew}} & -0.100^{(1)}_{\text{lean}} & -0.050^{(1)}_{\text{lemo}} & -0.245^{(1)}_{\text{temo}} \end{bmatrix}. \tag{5.15}$$

100 correlated samples for this selected design were created and evaluated with full CFD to test the probabilistic response, which is depicted in Fig. 5.11. The comparison to the baseline design's response shows that the mean efficiency has indeed been improved by 0.11 % but the standard deviation in actual fact by only 32.79 %. Again, only the full CFD results (and no surrogates) have been used for this comparison. Then, the surrogate's

predictions can also be taken into account. The improvement of the standard deviation was overpredicted by the surrogates at 127.25 %, which is far too optimistic, whereas the mean performance prediction is excellent in comparison. The mean performance prediction is indeed 0.11 %, which matches the value from the validation study. Considering predicted versus actual performance improvement, the difference is only 2.12 % and −16.88 % for mean and standard deviation, respectively. In addition, it is evident in Fig. 5.11 that all constraints are satified and that the optimizer has driven them very close to the upper and lower constraint limits. One likely cause for the differences is that the improvement of the standard deviation is more affected by UQ sampling noise than the mean (cf. Fig. 5.6). Also, the real noise model is more complex to approximate for the surrogates than the simple shape in Sec. 5.2.2's analytical example. Compared to 1000 points in the analytical example with only four dimensions, i.e., 250 points per dimension, now 800 points are used to approximate a much larger space over 29 variables. Consequently, it is no surprise that the surrogates are somewhat inaccurate. Nevertheless, if so desired, prediction errors could be reduced by adding more points, e.g., space-filling update points. It should also be stressed that the practical purpose of surrogate models is to guide the optimizer to regions with better designs and that the surrogate's accuracy itself is not a priority as long as a superior design can be found, as has been the case here. All in all, the entire approach has been shown to be a viable option for robust design optimization. While standard deviation predictions are unmistakably less accurate than with the simple analytical noise model, a robust design with respectable performance gains for both objectives has been found. The mean constraints were accurately modeled too. Validation results have shown that the probabilistic performance prediction must be verified in any case.

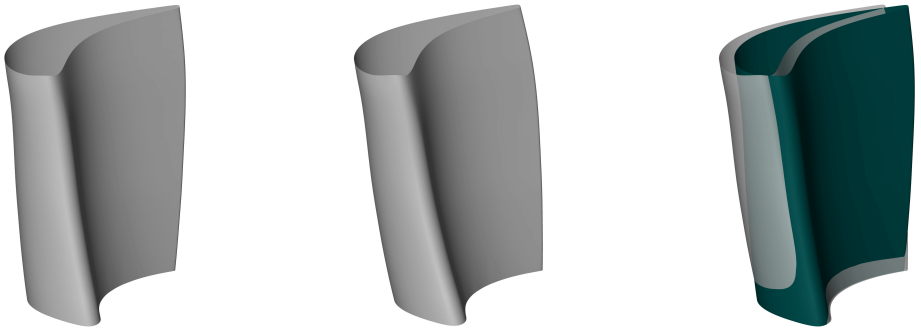

(a) Baseline design (b) Selected optimized design (c) Comparison of both shapes

Figure 5.10: Turbine blade shape comparison

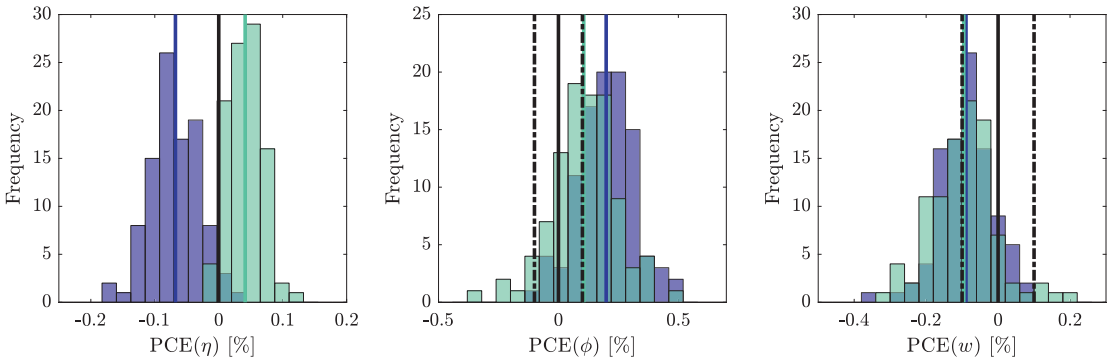

Figure 5.11: Robustness assessment of baseline (nominal CAD) geometry (with noise) (samples ■ and mean —) and selected robust blade (with noise) (samples ■ and mean —) relative to the nominal CAD design intent (—)

5.4 Summary

A complete workflow for robust design optimization of turbine blades given real manufacturing variations has been presented. The performance impact of these deviations has been analyzed and assessed. It has been shown that artificial blades with the same performance statistics as the original scans can be constructed and used for UQ. Through a sensitivity analysis, it has been shown that prior to optimization, the Δtan_{pos} parameter can be removed from the model. However, this is a direct consequence of the simulation setup with a single passage and hence only applicable in this case. Finally, a robust aerodynamic optimization of a turbine rotor has been presented. Validation of one selected Pareto-optimal design showed that both probabilistic objectives were improved and that tight constraints for average capacity and specific work were met. In the following chapter, the workflow is extended to include film cooling holes and their positional variations. Other features such as heat transfer computations and a cold-to-hot transformation could be added in future work.

Chapter 6

Modeling and Impact of High-pressure Turbine Blade Trailing Edge Film Cooling Hole Variations

Due to the importance of manufacturing deviations for this chapter, the manufacturing process of turbines blades and film cooling (FC) holes is briefly explained first. The main contribution of this chapter is a new model for real FC variations termed "virtual manufacture", which replicates the real manufacturing process of film cooling holes. This model is then integrated into a high-fidelity uncertainty quantification (UQ) methodology for film-cooled HPT blades.

6.1 Turbine Blade Manufacture

In general, turbine blades and nozzle guide vanes are manufactured by investment casting. In order of an increasing resistance to high-temperature creep, investment cast blades and vanes can have an equiaxed, directionally solidified crystal or single crystal grain structure. The two latter methods require a preheated chill plate to cool down the blades on one end from which the crystals (or just the single-crystal) start growing (Kalpakjian, 2013). In the investment casting process, firstly wax patterns are produced. Then, runners are removed and multiple blades are attached to a single wax runner, which gets dipped into a ceramic slurry. Then, after drying, the wax is melted out leaving the ceramic moulds. Blades are produced by casting the metal into the mould (Ganesan, 2010). Ceramic cores are used for the internal cooling channels of the wax pattern and have to be dissolved after casting. Thakur (2010) provides a fairly detailed description of this process. The fir tree is also machined after casting and the blades are cleaned

from feeders, etc. Thermal barrier coatings can also be applied on the blade surfaces. Prior to this, the blades are deburred with abrasive brushes and degreased. Different milling tools are used for the shroud, hub and airfoils, which are also semi-finished and finished with different milling cutters. Turbine blades are usually made from nickel-based superalloys such as Inconel (nowadays mostly proprietary alloys) and machining them is generally difficult due to the material, the complex geometry and the required accuracy.

6.1.1 TE FC Hole Manufacture

Typically, FC hole diameters are diminutive, e.g., in the range of 0.3 mm – 0.7 mm with tolerances of 0.1 mm or less. In principle, holes can be produced using electrical discharge machining (EDM), also known as electrical discharge drilling (EDD) or spark eroding, electrochemical machining (ECM) or laser drilling (LD), which is cost-efficient, relatively accurate and hence often used (Steen, Watkins, et al., 2010). ECM using an electrode and a high current is somewhat more accurate, but the method is slower and more expensive. ECM can also be used for other features such as hub grooves, however. Drilling through a thermal barrier coating (TBC) is particularly challenging. Whilst lasers are well suited to drill through TBC layers, EDM and ECM are not easily possible due to the non-conductive TBC layer, which often consists of yttria-stabilised zirconia ceramics (zirconium dioxide ZrO_2 stabilised with yttrium oxide Y_2O_3). When ECM is used to drill the holes, FC holes must be drilled before the TBC is applied. The holes are masked during this process. As an illustrative example, the paper by Voisey and Clyne (2004) describes and illustrates the laser drilling process of an FC hole through a TBC layer in detail. For an in-depth description of all manufacturing techniques, which is out of scope here, see Li, Wei, et al. (2015). In the case studied here, the blades do not have a TBC and the holes were drilled with an Nd-YAG (neodymium-doped yttrium aluminium garnet) laser. Special types of wax or plastic inserts are used to protect the blades whilst drilling the holes. Blade geometries are typically checked with coordinate measuring machines at a number of predefined positions. Cooling holes are flow-checked with needles and airflow-tested by measuring the mass flow rate through the entire blade. Hence, these tests are holistic and do not establish whether or not dimensions, angles or position of each individual hole are indeed acceptable.

6.1.2 Film Cooling

There are five basic cooling concepts: convection, impingement, film (divided into local and full-coverage), transpiration and water/steam cooling. Convection, impingement cooling and thermal barrier coatings are internal cooling methods whereas film and transpiration cooling are external methods. Internal methods work well for temperatures around 1300 K – 1600 K, but only external methods can cope with temperatures in excess

of 1600 K (Bräunling, 2009). The basic principle of FC is to inject air from a range of cooling holes to form a protective layer on the blade surface. Parameters such as the injected coolant's velocity and turbulence levels influence the coolant mixing and in turn the FC efficiency and local heat transfer coefficients.

One problem with FC is the inherent occurrence of aerodynamic losses, which, for example, Lakshminarayana (1995) summarises as follows: "Lost work or power in the coolant flow; increased profile losses due to thicker blade profiles arising from coolant holes; interaction of the coolant film with the blade boundary layer; mixing losses; and the modification of transition, boundary layer and wakes". There is also an unfavourable effect associated with FC termed "heat transfer coefficient augmentation". Due to the formation of a turbulent boundary layer, the mixing increases the heat transfer coefficient and thereby also increases the transferred heat load to the blade surface (Bogard and Thole, 2006). As Cunha and Chyu (2006) point out, the trailing edge would sustain damage before any other airfoil region due to its fast thermal response (due to its small size). However, cooling holes or slots cannot be oversized either because of both aerodynamic and mechanical constraints and a balanced, optimal design has to be found. Designs range from cooling holes to cooling slots and many different sub-configurations for each type exist. As Yang and Hu (2012) point out, slots can provide a more uniform protective film and the Coandă effect ensures the film sticks to the surface without lifting off. Cooling slots typically are mechanically weaker than cooling holes, however. In general, there has been a lot of research in this area, both experimentally and numerically, e.g., by Brundage, Plesniak, et al. (2007), Wong, Ireland, et al. (2015), and Yang and Hu (2012). Many shaped holes have been shown to outperform classical cylindrical holes (El Ayoubi, 2014). TE cooling holes are commonly located on the PS.

Film cooling in general is influenced by many parameters such as the hole shape, the distribution of holes, blowing ratio, etc. Bunker (2009) has shown that FC is crucial in reducing the total heat flux and that two parameters in particular stand out: the hole diameter and L/D, the length-to-diameter ratio. Both factors can lead to metal temperature changes of up to 40 °C, leading to increased creep and to a corresponding lifetime reduction. Regarding the TE aerodynamics, it is known that a variety of parameters such as the velocity ratio, mass flow rate, hole size and ejection angle influence the mixing losses (Schobeiri, 2005). For FC in general, Han (2004) identifies the "coolant-to-mainstream pressure ratio (blowing ratio), temperature ratio (density ratio), film hole geometry (hole size, spacing, shape, angle from the surface, and number of rows), and location (leading edge, trailing edge, pressure and suction sides, end wall, and blade tip) under representative engine flow conditions (Reynolds number, Mach number, combustion-generated high free-stream turbulence, and unsteady wake flow)" as influential parameters. According to Logan Jr (2003), the most relevant parameters are

the hole diameter, the hole spacing to diameter ratio, the axial inclination of the hole axis and the blowing rate. Additional influential parameters are the "number of rows, row spacing, location coordinated with a hot spot, internal cooling geometry, surface curvature, pressure gradient, density ratio and main-stream turbulence level". Notably, using a film-cooled flat plate and a similarity analysis with the Buckingham π theorem, Baldauf and Scheurlen (1996) showed that the (laterally averaged) FC effectiveness $\overline{\eta}_{FC}$ depends on the following parameters:

$$\overline{\eta}_{FC} = f\left(Tu, IR, BR, \frac{x}{D}, \alpha, \frac{P}{D}, \frac{\delta}{D}, \frac{L}{D}\right) \tag{6.1}$$

In order of appearance in Eq. (6.1), the parameters are the turbulence level, the momentum flux ratio, the blowing ratio, the downstream distance (dimensionless through D), the ejection angle, the hole spacing (pitch), the boundary layer displacement thickness and the hole length.

There are also numerous studies related to the influence of different hole geometries and hole arrangements on FC performance (Bunker, 2005; Goldstein, Eckert, et al., 1974; Gritsch, Schulz, et al., 2000; Lee and Kim, 2010; Makki and Jakubowski, 1986). The sheer number of parameters and the complexity of the models involved makes clear that finding an optimal design is a difficult task, but this is also part of research, e.g., by Pappu and Schobeiri (1997).

6.1.3 Film Cooling CFD

As Han, Dutta, et al. (2012) note, few experiments using real engine conditions and rotating blades have ever been conducted due to the inherent difficulties with measurements in hostile, high-pressure, high-temperature environments. Instead, experimental studies often use simple flat plates. However, experiments can be carried out with temperature- or pressure-sensitive paint. For example, Ahn, Schobeiri, et al. (2006) measured the FC effectiveness for a turbine rotor's LE. As another example, Elsayed, Owis, and Abdel Rahman (2013) investigate the effect of different film cooling parameters such as inlet velocity direction, lateral and forward diffusion angles, blowing ratio, and streamwise angles on a flat plate using an in-house 3D RANS code. Their comparison of the numerical film effectiveness with experimental results shows that RNG and normal $k-\epsilon$ turbulence models provide reasonable accuracy in case of the flat plate. A similar study of the film-cooled GE-E3 blade corroborates these results as well (Elsayed, Owis, and Rahman, 2014). Han (2004) also summarises other film cooling studies, which involve real blade models. Moreover, experimentally decreases of FC effectiveness (and blade life) due to unsteady turbulent effects are described.

As pointed out by several authors, e.g., by Bogard and Thole (2006) and Johnson (2012), film cooling RANS CFD has problems in particular with modeling 3D coolant jet

lift-off and separation. In optimization studies, and even more so with UQ, steady-state RANS-based CFD is typically the only affordable methodology. Another issue is often the small size of FC holes, which require fine mesh sizes for the flow to be adequately resolved. This can quickly lead to large mesh sizes and, as a consequence, often studies are restricted to a few holes or rows only. Special tools such as the Immersed Mesh Block approach, in which fine meshes for FC holes are inserted into a coarser host blade mesh, are being developed to allow the aerothermal design of fully-featured turbine blades (Lad and He, 2013a). For example, a deterministic optimization of a pressure side FC array using a GA and RANS-based CFD was carried out by Johnson (2012). The thesis also provides a comprehensive overview of HP turbine CFD studies, including the performance of various turbulence models. Objectives included injection angles, compound angles, cooling row patterns, hole sizes and hole positions. This work was solely focussed on FC and involved 1800 cooling designs and 13 generations. The optimized design and the corresponding performance parameters were experimentally validated. Wilcox's $k-\omega$ turbulence model was used for all simulations (Wilcox, 1988).

In other research, for example, the realizable k-ε, k-ω, k-ω SST and the Baldwin Lomax turbulence models have been used. The study by Montis, Ciorciari, et al. (2014) shows that k-ω SST RANS-based CFD can accurately predict the loading, separation and losses of a film-cooled, TE-slotted HP NGV in combination with the γ-$\mathrm{Re}_{\theta t}$ transition model. Not surprisingly, for example, Acharya, Tyagi, et al. (2001) find DNS and LES superior to k-ε, k-ω and other turbulence model-based RANS CFD results. Voigt, Noll, et al. (2010) compared RANS & URANS approaches. For RANS, the study included the k-ω SST turbulence model, the advanced Speziale-Sarkar-Gatski (SSG) Reynolds stress model and a k-ε explicit algebraic Reynolds stress model. For URANS, k-ω SST and a scale-adaptive simulation (SAS) model. The geometry was a film-cooled flat plate. Whereas it was shown that RANS approaches were poor, URANS and SAS simulations managed to match the experimental data. Specifically for the TE of a NGV, Ravelli, Miranda, et al. (2013) investigated the applicability and performance of steady-state RANS for a cooled NGV with 2 rows of cooling holes and a cutback TE slot. Using the RNG k-ε turbulence model and Fluent's enhanced wall treatment, the authors found reasonable agreement of the FC effectiveness results with experimental data. Problems were found as well however, e.g. worse predictions in specific regions such as near the cutback slot, overpredictions at the slot exit und in the stream-wise direction. Additionally, the amount of separation at the hole exit was underpredicted.

Ginibre, Lefebvre, et al. (2001) used the Spalart-Allmaras turbulence model to validate CFD results of a film-cooled turbine blade (von Karman Institute blade). A relatively good agreement for isentropic Mach numbers and heat fluxes was observed, even with this one-equation model. Nadali Najafabadi (2015)'s experimentally validated study even

showed that Spalart-Allmaras turbulence model-based CFD results of NGV PS holes were more accurate than realizable k-ε and k-ω SST models, which overpredicted the FC efficiency. Examining 2D slot film cooling, Cruz (2008) found the Spalart-Allmaras to perform well in modeling the FC effectiveness. The RANS-based optimization of 2 cooling hole rows by El Ayoubi (2014) also comprises an extensive literature survey with regard to film cooling CFD. The conclusion is that "no general consensus exists" on which model to choose. They, too, used the k-ω SST model for all simulations. Another issue with steady-state RANS CFD is the difficulty of modeling heat transfer correctly. Here, this is out of scope in any case, however, but, to give one example, large differences between numerical and experimental values can be observed in the paper by Johnson, King, et al. (2011), where the Wilcox k-ω turbulence model is used.

All in all, this section has shown that RANS-based CFD can be accurate at a reasonable cost, but also that this is not always the case in every situation and that there is no general agreement on which model to choose when. Even the one-equation Spalart-Allmaras model can sometimes provide accurate FC results and outperform more complex models.

6.2 TE FC Hole Variations

For the HP turbine blade geometry at hand, there are 27 TE FC holes in total. Whilst all holes have the same diameter, not all holes share the same cylinder axis direction. Although almost identical, holes 1-12 and 13-27 respectively share the same hole axis directions. TE FC hole variations are depicted in Fig. 6.1 for a selection of eight blade scans. Visually, positional hole variations are immediately evident and clearly recognizable. Fluctuations are particularly evident for the top half of the blades. Hole lengths appear to become larger towards the top of the blades. Sudden changes in hole length in between holes seem to be rare, but can be observed too. Hole diameter variations are not visually identifiable.

6.2.1 TE FC Hole Variations in Terms of UV Coordinates

All FC hole variations can be measured using dimensionless UV coordinates. This 3D to 2D mapping allows one to move cooling holes on the blade surface according to these coordinates. UV hole coordinates are extracted manually by superimposing each scan's STL file on its reconstructed NX model, which is constructed with Blade2Parameter, the in-house tool developed at TU Dresden. All blades ares radially extended below 10 % span and above 90 % span with the in-house code `parapy`. The blade reconstruction process is as described in Chapter 3. UV coordinates are extracted manually by locating the centre of each cooling hole. In order to obtain the nominal CAD model's reference

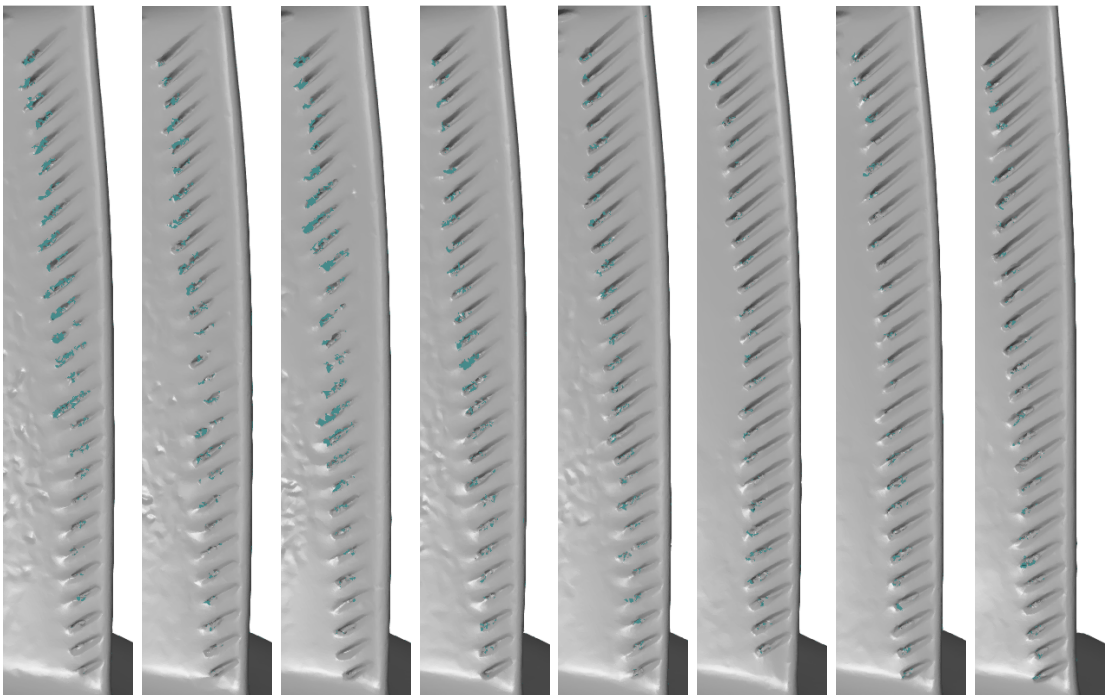

(a) Scan #1016 (b) Scan #1017 (c) Scan #1019 (d) Scan #1028 (e) Scan #1034 (f) Scan #1310 (g) Scan #1315 (h) Scan #1317

Figure 6.1: Illustration of trailing edge film cooling hole variations for selected blades with original scan STL files

hole positions, intersection points of all TE cooling hole axes and the reconstructed pressure side surface were extracted. Note that a reconstruction of the CAD model has to be used to ensure consistency across all surfaces since UV coordinates depend on the surface itself. Using C#, nominal UV coordinates can then be computed using NX Open's `AskFaceParm` method.

The result of this approach is depicted in Fig. 6.2a. Note that individual colors do not have any particular significance. In Fig. 6.2a, V is the horizontal surface coordinate. $V = 0$ refers to the bottom edge of the pressure side surface and $V = 1$ to its top edge. Similarly, U is the horizontal surface coordinate, where $U = 0$ refers to the aft edge of the pressure side surface and $U = 1$ to its front edge. For example, values of $U = 0.1$ and $V = 0.2$ refer to the position on the blade's pressure surface at 10 % for U and at 20 % for V. The comparison of nominal CAD trailing edge UV coordinates to the manufactured average of all blades reveals large deviations, especially for the top half of trailing edge holes. Discrepancies are worst for the topmost cooling holes. Essentially, this confirms results from the previous visual assessment in Sec. 6.2. Figure 6.2b examines the impact on the observed cooling hole length. As an additional illustration, Fig. 6.3 depicts the major axis TE FC hole length, which Fig. 6.2b refers to. The TE hole shape obviously depends on the local TE geometry, but typically closely resembles an ellipse. Hence, since

the nominal TE hole shape is approximately an ellipse, major axes endpoints of all TE holes were extracted to quantify length variations. Lengths correspond to the Euclidean distance of each pair of endpoints. Results show that the more the holes deviate from the nominal design intent, the longer they become. On average, the topmost cooling holes exhibit the largest deviation and are on average 34.1 % longer than intended. The largest top hole is 53.5 % longer and the smallest one is still 11.3 % longer.

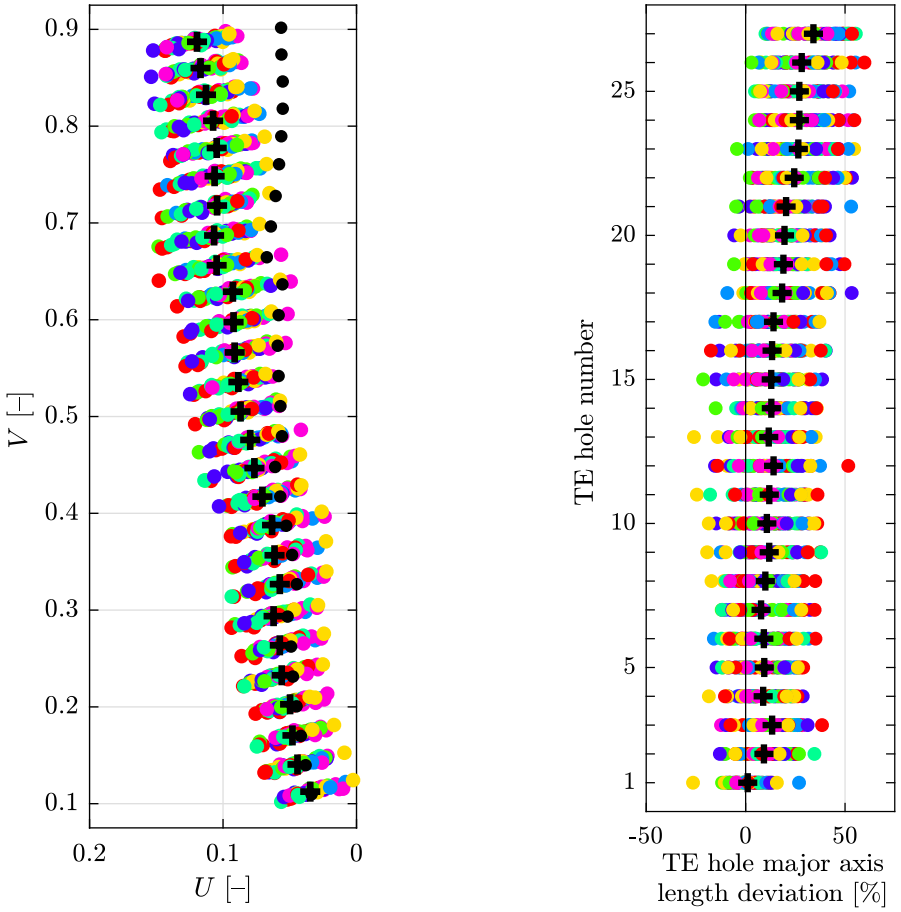

(a) UV TE FC hole center point variation (b) TE FC hole major axis length variation

Figure 6.2: Blade scan trailing edge film cooling hole center point position (a) and major axis length (b) variations with the manufactured average (✚) in relation to the nominal design intent (•)

6.2.2 Cause of TE Hole Variations

The question remains as to what has caused these deviations. In principle, there are three plausible sources as potential causes for TE FC hole variations. First, manufacturing variations due to the machining method, i.e., the orientation and position of the laser. Second, fir tree surface variations can cause misalignment errors during scanning and as a consequence measurement errors. Third, blade shape variations from any other

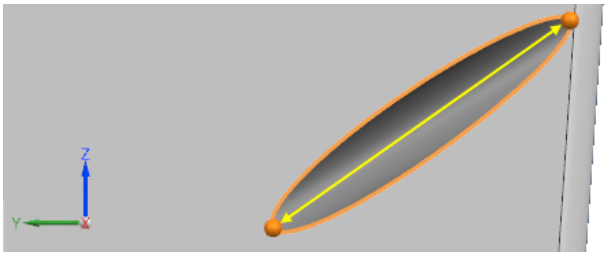

Figure 6.3: Trailing edge film cooling hole major axis length

step used in production. Whilst with option one the laser itself would be to blame, in options two and three the laser would cut holes either into misaligned blades, clamped in wrong positions, or into aberrant blades with varying shapes. Great care was taken to rule out any blade misalignment (Heinze, Meyer, et al., 2014). Figure 3.2 depicts strong evidence suggesting that option three, blade shape variations, is the main cause. Although only 10 % and 90 % span sections are shown, similar variations can be plotted for any spanwise position. Even though large axial shifts for the TE are apparent, the blades are not simply moved axially. Rather, as shown in Fig. G.1 for scan #1001, often an entire portion of a blade, e.g., colored red in Fig. G.1b, is twisted. For this scan, only the top SS seems to have been affected, whereas Fig. G.1a shows that the entire LE conforms to the nominal geometry much better (green color; differences near naught). With such obvious blade shape variations, diverging FC holes, which must be cut into the metal, come as no surprise, since the laser alignment is not changed to suit individual blades, but is instead set up to deal with the nominal geometry.

6.3 Computational Methodology

The steady-state RANS CFD workflow presented in Chapter 4 with a single passage high-fidelity model of an industrial HP turbine rotor is employed here. In addition, the accurate reverse engineering method using B2P from Chapter 3 based on all 58 blades scans is used. The complete CFD workflow with all steps involved is depicted in Fig. 6.4. In this chapter, the focus is laid on FC, how to best model it, its impact on performance and the integration of FC into an UQ workflow. Steady-state CFD is used to keep the computational cost low, even though it is known to be poor at predicting heat transfer-related quantities correctly. As an example, in the thesis by Telisinghe (2013) about aerodynamic experiments of film-cooled HPT trailing edges the conclusion was drawn that steady-state CFD was only able to capture the trends of the experiments, but not the magnitude of quantities such as film effectiveness or heat transfer coefficients. Large discrepancies due to the unsteady flow field lead to the recommendation of unsteady CFD instead. To avoid these issues with steady-state CFD, only aerodynamic quantities

of interest are in the scope of this thesis. The Spalart-Allmaras (SA) turbulence model is used here, which can for example be justified with the work by Ginibre, where CFD results of the von Karman Institute film-cooled turbine blade were validated with good agreement for isentropic Mach numbers and heat fluxes (Ginibre, Lefebvre, et al., 2001). In another paper by Nadali, the experimentally validated study showed that SA turbulence model-based CFD results of NGV PS holes were more accurate than realizable k-ε and k-ω SST models, which overpredicted the FC efficiency. Rolls-Royce's in-house solver HYDRA is used to solve the 3D compressible RANS equations (Lapworth, 2004). PADRAM (Milli and Shahpar, 2012) and BOXERMesh[1] are used to generate structured meshes, see Sec. 4.3, now augmented with FC features.

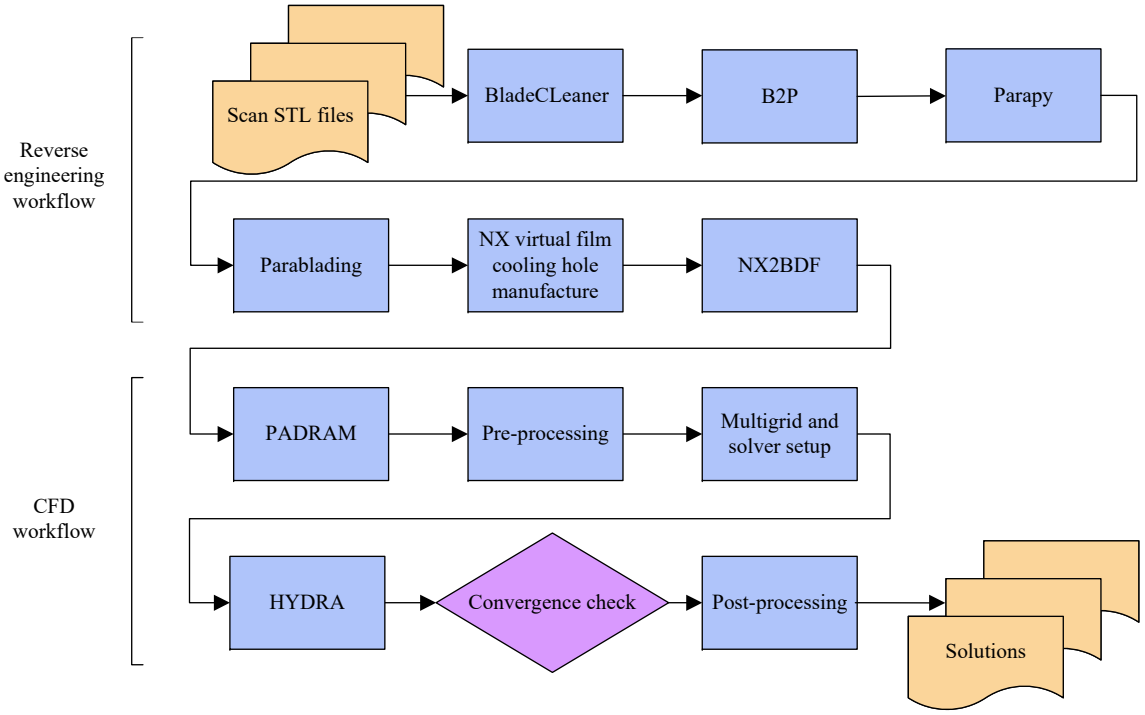

Figure 6.4: Flowchart of CFD workflow with reverse engineered blade scans

6.3.1 Film Cooling

From a converged CFD simulation of the nominal CAD geometry, it can be shown that for the turbine blade considered here only about 1 % of the total mass flow enters through the cavities (rim and rail cooling; for details see Ref. Scharfenstein, Heinze, et al., 2013), but a more significant proportion of about 5 % is due to film cooling. Of this 5 % mass flow, a significant part of 32 % is due to the trailing edge film cooling holes and the remaining 68 % come from other holes. This can be seen in Fig. 6.5, which depicts the mass flow rate of each strip as defined in the original boundary conditions.

[1] BOXERMesh: http://www.cambridgeflowsolutions.com/boxer-mesh/

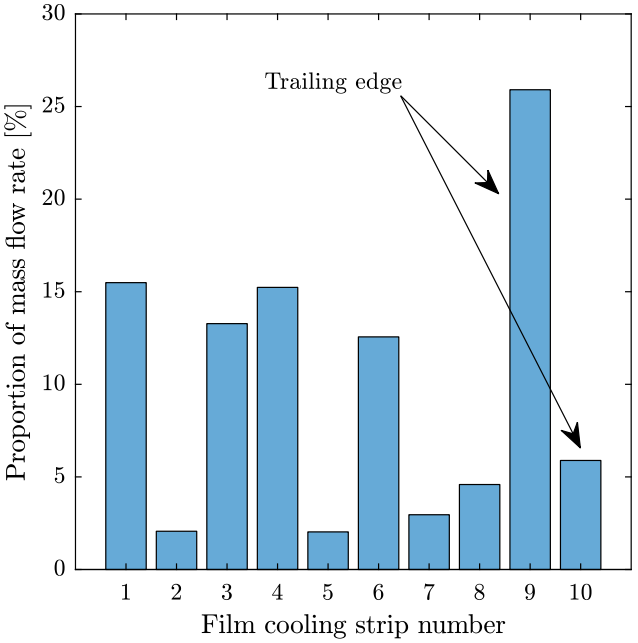

Figure 6.5: FC strip model mass flow rate distribution from boundary conditions

6.3.1.1 Film Cooling Models

Two FC models are used in this work: discrete hole stubs with normal, uniform-flow inlets or a low-fidelity strip model, also known as a Crawford-type strip model (Crawford, Kays, et al., 1980). The strip model's attraction stems from the CFD mesh size. Hundreds of thousands of elements are required to mesh a single FC hole due to the very small size, but with cooling strips this is not necessary as source terms are placed in the flow to model the effects of FC instead. In a recent study, the impact of this strip model on aerodynamic loss, was analyzed by replacing two SS strips with discrete holes (Occhioni, Shahpar, et al., 2017). The authors' conclusion was that the strip model is sufficient for aerodynamic performance analyses. Before exploring this strip model further, a few alternative methods in the literature are discussed. For example, there is a volumetric source term-based FC model, which also removes the need to mesh the holes (Kampe and Volker, 2011). Flat plate correlations are used to predict 3D flow fields. Very similar to the strip model used here is an injection model, which was used to model FC on a nozzle guide vane (Dahlander, Abrahamsson, et al., 1998). Discrepancies between numerical FC effectiveness results and experiments seemed quite large, however. Also, the model's injection distance must be tuned to every case, which is a similar problem with the strip model used here. Another modeling approach has been to inject a 2D flow field into the CFD downstream of the hole (Burdet, Abhari, et al., 2007). In yet another strategy termed the immersed mesh block approach, a coherent mesh with plenum, hole and immersed region is inserted for every hole (Lad and He, 2013b). The problem with this

is the method's intrusive nature, which requires significant adaption of the CFD solver's code. A source term model was also developed and applied by Tartinville and Hirsch (2008). Results showed reasonable agreement with experiments. Similarly, the model by Andrei et al. also relies on source terms (Andrei, Innocenti, et al., 2017). Their idea was to first construct discrete FC holes and to then intersect them with the blade surface. Then, they use the delimited shapes as FC hole inlets.

6.3.1.1.1 Film Cooling Strip Model

HYDRA's strip model adds the effects of cooling flows with mass flow source terms and thereby removes the need to mesh the holes. At specified positions on the blade surface, uniform flow is ejected along continuous, thin rectangular strips. As an example, Fig. 6.7 depicts a single PS FC strip. In the spanwise direction, the ejected flow is also uniform. The direction of injection of the grid is used by the pre-processing tool to identify mesh cells, where the FC model is to be applied. Position, injection depth (synonym: penetration depth) and angles (film cooling strip injection angles α and β) are set up in the pre-processing phase and then remain fixed. The ejection depth of the strips hence cannot interact with the main flow, but the ejected coolant itself can once it has left the FC strip. The Spalart-Allmaras variable $\tilde{\nu}$ is set to zero for all strips. Mass flow rate, density and temperatures can be altered through an input file. Boundary conditions for the strips stem from another Rolls-Royce in-house tool for turbine cooling analyses and the RANS CFD analyses here are constrained by the data in these files. All boundary conditions are specified in the absolute frame of reference. Table 6.1 provides an overview of the required aerodynamic boundary conditions for each film cooling strip.

Table 6.1: Required aerodynamic boundary conditions for each film cooling strip

Quantity	Unit
Mass flow rate	$\mathrm{kg\,s^{-1}}$
Direction of injection	–
Hole pitch	–
Injection angles	°
Injection area	$\mathrm{m^2}$
Abs. tot. temperature	K
Density	$\mathrm{kg\,m^{-3}}$
Penetration distance	m
Turbulence	–
Fuel fraction	–

The FC hole geometry is not modeled with FC strips. As opposed to discrete FC holes, no information whatsoever about the FC hole geometry, e.g., hole diameter or hole shape, is carried over to the CFD model. For example, the FC strip model cannot distinguish between cylindrical or fan-shaped FC holes.

6.3.1.1.2 Discrete Film Cooling Holes

Discrete holes can also be modeled as stubs with normal, uniform-flow mass flow inlets with BCs inferred from the strips for comparison. Modeling the holes as stubs also avoids meshing the inner cavity and keeps mesh sizes smaller, but neglects internal cooling hole flow effects. In the strips, BCs are provided for each row in the absolute frame of reference. Since the mass flow inlets of all FC holes are part of the rotor, BCs are subsequently converted into the rotating reference frame. Given the known values for $\dot{m}$, ρ and the circular inlet surface area of each hole A, the absolute velocity v_h at the inlet of each cooling hole can be computed as:

$$v_h = \frac{\dot{m}}{\rho A}. \tag{6.2}$$

The definition of the relative total temperature is

$$T_{0,rel} = T + \frac{\vec{w}^2}{2c_p}, \tag{6.3}$$

so only the static temperature T, which is invariant to the frame of reference, the relative velocity $\vec{w}$, and $c_p = R \cdot \gamma/(\gamma - 1)$ are required. The static temperature can be computed using Eq.(6.4),

$$T = T_{0,abs} - \frac{\vec{v_h}^2}{2c_p}, \tag{6.4}$$

and $\vec{w} = \vec{v} - \vec{u}$ can be calculated given the tangential speed $\vec{u}_\perp = \Omega r_h$. Here, BC values for the Spalart variable $\tilde{\nu}$ are estimated through an empirical correlation for fully developed pipe flow. This requires the kinematic viscosity of the air in the holes, which can be computed with CoolProp[2] given the known density and temperature to calculate the Reynolds number in the hole. Turbulence intensity can then be computed with $I = 0.16 \cdot Re^{-1/8}$ and the Spalart variable can be estimated with the hole diameter for the turbulent length scale l: $\tilde{\nu} = \sqrt{3/2}(uIl)$. As an example, Fig. 6.6 illustrates the flow with discrete film cooling holes on the whole blade.

6.3.2 Modeling of Film Cooling Hole Variations

Scan #1322 and its TE FC hole variations are depicted in Fig. I.2a. Modeling these FC hole variations with a method suitable for UQ or RDO is the aim of this section. Figure I.2c depicts the projection of the TE holes, mapped with the real measured UV coordinates. This is done via the UV coordinate mapping from Sec. 6.2.1 to model FC hole variations on reconstructed blades at their respective correct positions as a reference for the new method. Finally, Fig. I.2d shows the result of a new approach to approximate the real hole position termed "virtual manufacture". Based on the premise that FC

[2]CoolProp: https://github.com/CoolProp/CoolProp

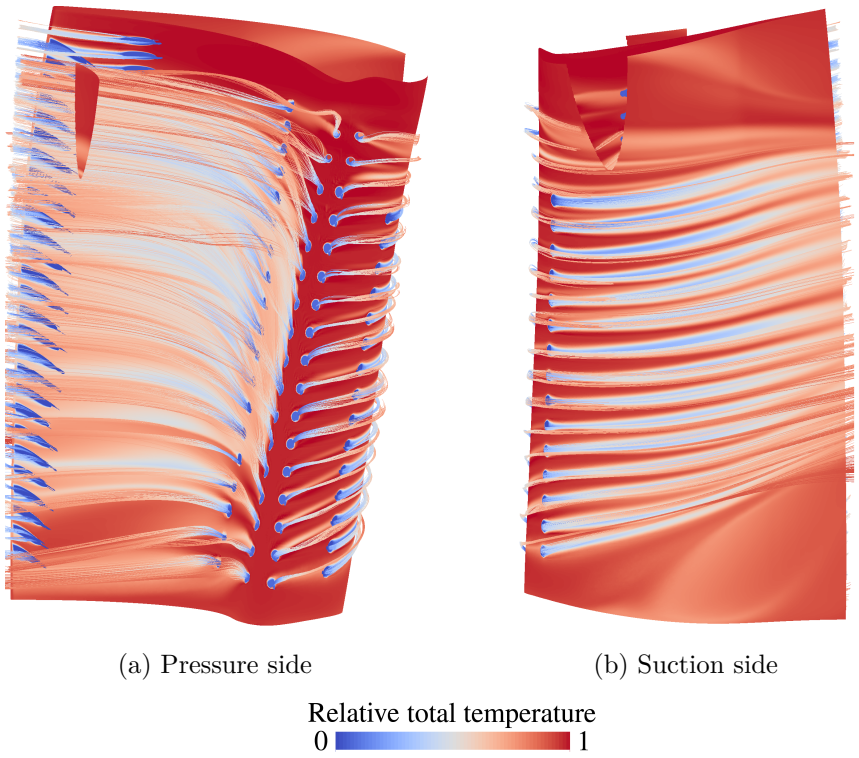

(a) Pressure side (b) Suction side

Figure 6.6: Nominal CAD model with discrete FC holes

hole variations are largely due to varying blade shapes, this workflow uses the nominal cooling hole axes and intersects them all with surfaces on reconstructed blades to create intersection points, which define the position of discrete FC holes or FC strips on the blade. By doing this, it essentially replicates the manufacturing process of the holes, i.e., a fixed laser, cutting holes into clamped blades. Here, since the FC strip model's injection angles α and β are defined through a local plane perpendicular to the radial direction at the hole, the injection angles can also be measured and extracted from each NX model. Figure 6.10 illustrates the basic idea of the "virtual manufacture" approach. α is the injection angle from the surface at the location of the hole in the local plane ($\alpha = 90°$ would be normal to the surface) and β is the radial injection angle of the coolant and the local plane ($\beta = 0°$ would inject the coolant in the local plane). The Siemens NX API was used to implement this in a C# program, which computes the intersection point coordinates, each local injection plane and the injection angles. The code exploits the fact that turbine blades built with Parablading are split into four named surfaces. These surfaces can be retrieved using the NX API by searching for the corresponding surface string, e.g., for the `LEADING_EDGE`. The same principle is also used for the curves, named `STRIP_1_CURVE_1`, `STRIP_1_CURVE_2` and so on. Intersection points are then created for the surfaces and curves using the `CreatePoint` method. The result is a list of intersection points, which, after a conversion from Cartesian to cylindrical coordinates, are written out in the geometry definition file. FC strip input files for HYDRA can be

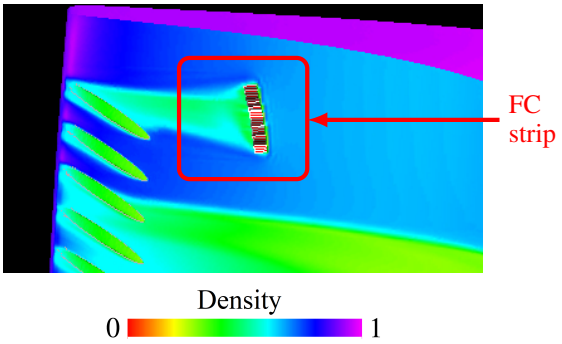

Figure 6.7: Illustration of CFD model with both film cooling model types, i.e., the strip model (middle) for three film cooling holes on the pressure side and individual discrete holes (left) for the trailing edge

written out for any blade geometry. If only discrete holes were required, they can also be constructed through an automatic NX workflow, but this is outside the scope of this thesis.

The advantage of the virtual manufacture approach, as opposed to UV coordinates, is that no measurements are required and that it can be readily integrated into a UQ workflow as only the nominal cooling hole axes and an artificial blade model are required.

6.3.3 Quantities of Interest

The main quantities of interest examined here are efficiency, capacity and work. The isentropic efficiency of a turbine is defined by the actual work divided by the ideal, isentropic work as defined in Eq. (6.5),

$$\eta = \frac{\sum\limits_{i=inlets} (\dot{m}h_0)_i - \sum\limits_{i=exits} (\dot{m}h_0)_i}{\sum\limits_{i=inlets} (\dot{m}h_0)_i - \sum\limits_{i=sec\_exits} (\dot{m}h_0)_i - (\dot{m}h_{0,ideal})_{main\_exit}}, \tag{6.5}$$

where h_0 is the total enthalpy. Inlet capacity is defined in Eq. (6.6),

$$\phi = \frac{\dot{m}_{inlet}\sqrt{T_{0,inlet}}}{p_{0,inlet}}, \tag{6.6}$$

and specific work in Eq. (6.7),

$$w = \frac{\sum_{i=inlets}(\dot{m}H_0)_i - \sum_{i=exits}(\dot{m}H_0)_i}{(\dot{m}T_0)_{main\_inlet}}. \tag{6.7}$$

Another quantity of interest is the mass flow rate at the outlet. The general definition of the mass flow rate through any surface $\mathbf{A}$ is given in Eq. (6.8):

$$\dot{m} = \iint_A \rho \mathbf{u} \cdot \mathrm{d}\mathbf{A}. \tag{6.8}$$

All quantities of interest are mass-averaged and computed directly via integration of flow quantities at inlets and exits with 100-sample averages over the iterations. Since the

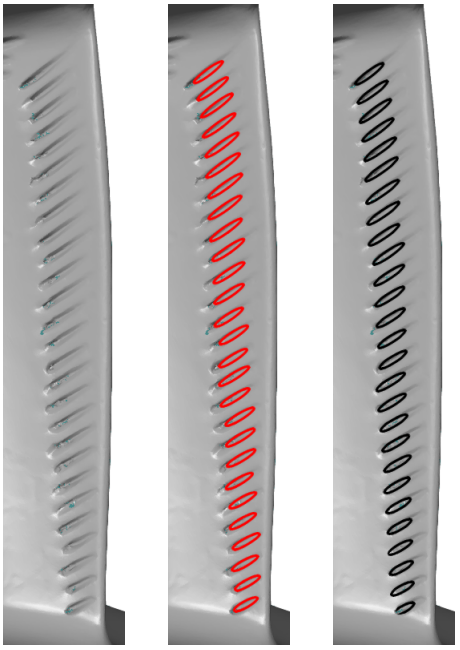

(a) Scan #1322

(b) Projected UV-mapped manufactured TE holes (—)

(c) Projected trailing edge holes from virtual manufacture workflow (—)

Figure 6.8: Comparison of FC hole variation modeling strategies: UV-coordinates and "virtual manufacture"

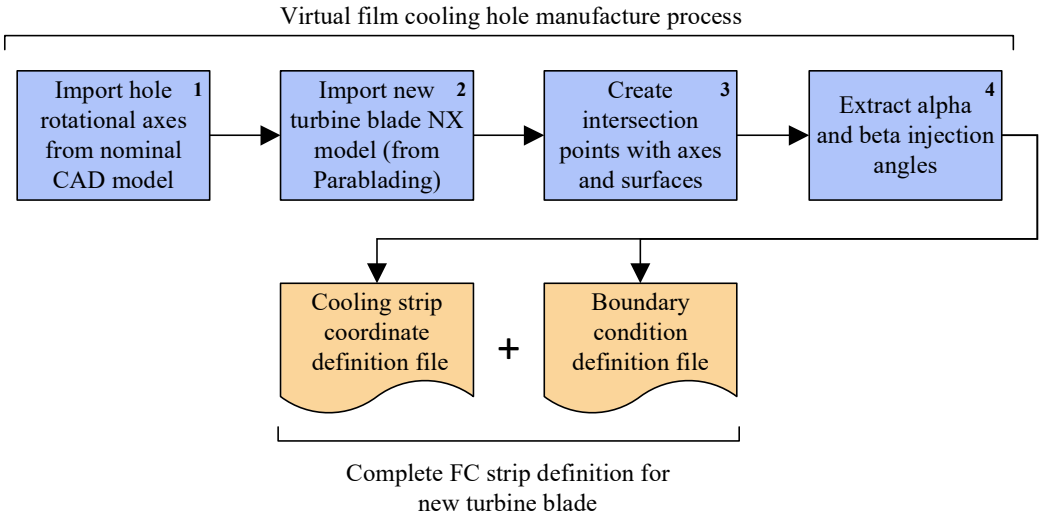

Figure 6.9: Virtual film cooling hole manufacture flowchart

flow quantities are integrated at inlets and exits, it is especially important to ensure a

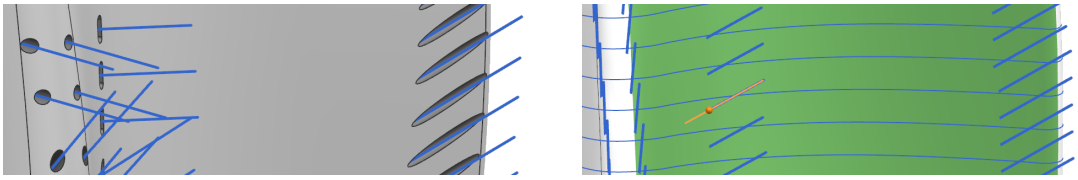

(a) Nominal cooling hole axes (b) Generation of intersection points

Figure 6.10: Positional film cooling hole movement through virtual manufacture workflow

sufficiently dense mesh resolution, which is highlighted in Fig. 6.11. Inadequate cell sizes can lead to stark differences in solutions solely due to the mesh.

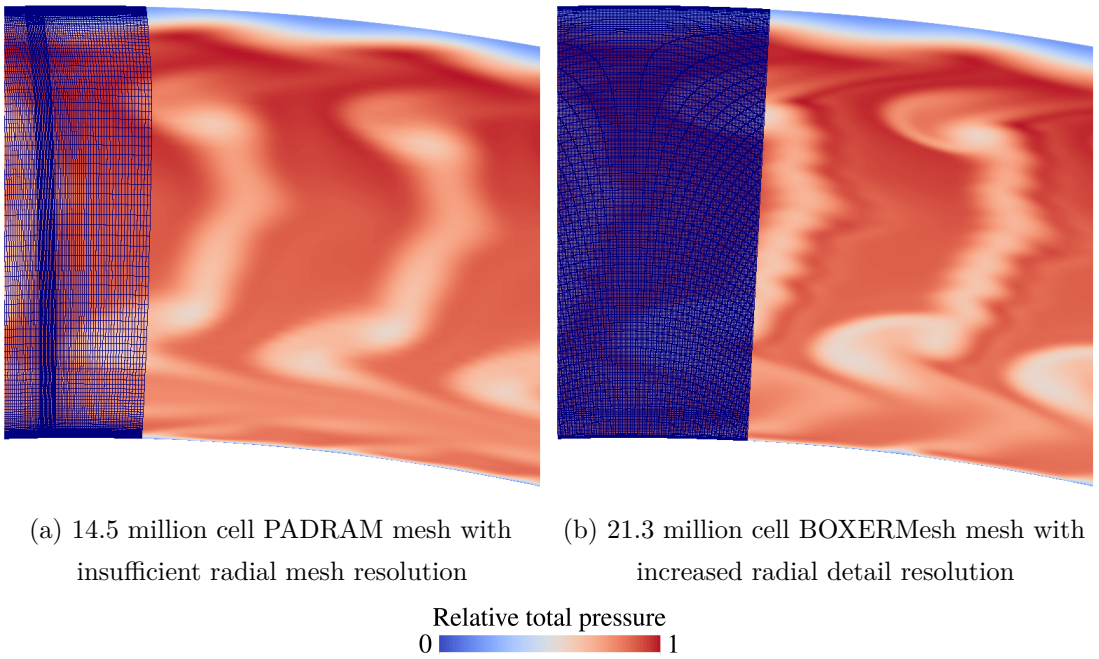

(a) 14.5 million cell PADRAM mesh with insufficient radial mesh resolution

(b) 21.3 million cell BOXERMesh mesh with increased radial detail resolution

Figure 6.11: Relative total pressure results on exit plane for two different meshes

Other relevant heat transfer-related quantities of interest such as film effectiveness or heat flux into the walls are beyond the scope of this thesis, but, in principle, aerothermal CFD with HYDRA is straightforward to implement. For example, relevant parameters affecting film cooling performance such as blowing, density, velocity or momentum flux ratio, as defined in Eq. (6.9) respectively, are available for future analysis and UQ, but are outside the scope of the analysis here.

$$BR = \frac{\rho_c V_c}{\rho_\infty V_\infty}, \quad DR = \frac{\rho_c}{\rho_\infty}, \quad VR = \frac{V_c}{V_\infty}, \quad IR = \frac{\rho_c V_c^2}{\rho_\infty V_\infty^2}. \tag{6.9}$$

Table 6.2: Impact of FC model and mesh on quantities of interest

FC model	Strips	Strips	Strips	Strips	Strips	Strips & discrete TE holes		Discrete holes
Mesher	P	P	B	B	B	B	B	B
Number of cells	5.2 M	14.5 M	14.8 M	21.3 M	36.6 M	38.4 M	46.7 M	46.2 M
$\Delta\eta$ [%]	0.27	0.23	0.26	0.29	0.31	0.58	0.56	0.00
$\Delta\phi$ [%]	−0.17	−0.13	−0.04	−0.03	−0.03	0.03	0.01	0.00
Δw [%]	0.17	0.12	0.29	0.35	0.35	0.54	0.53	0.00
$\Delta\dot{m}_{\text{out}}$ [%]	−0.16	−0.13	−0.05	−0.03	−0.03	0.02	0.01	0.00

[1] Mesher: P = PADRAM, B = BOXERMesh

6.4 Results

6.4.1 Epistemic Uncertainties & Impact of FC Model

Before real, statistical (aleatoric) uncertainties can reveal the impact of variations on performance, modeling (epistemic) uncertainties again need to be quantified. Epistemic uncertainties are investigated for all quantities of interest and both FC models (and hence both PADRAM and BOXERMesh grids). The results are listed in Table 6.2 in relation to the high-fidelity model with discrete FC holes, which is assumed to have a percentage error of naught. The results show that changing the FC model from discrete holes to FC strips everywhere but the TE changes isentropic efficiency and specific work by 0.58 % and 0.54 % respectively. Interestingly, capacity and mass flow rate are virtually unaffected with a maximal change of only 0.03 % for capacity. Further lowering the fidelity by modeling all holes as FC strips also nearly affects no changes for capacity or mass flow rate. Variations of efficiency and work are much larger in comparison. Moving from PADRAM to BOXERMesh and thereby changing the type of grid leads to changes of −0.17 % and −0.16 % for capacity and mass flow rate. This can also be compared to the results without FC from Sec. 5.2.4.2, where the maximal variation in capacity was just −0.003 %. Hence, a significant part of the meshing uncertainty in the case with FC cooling can be attributed to the application of the FC strips to different meshes. Given only PADRAM's grids, it is evident that meshing variations are small, e.g., 0.06 % and 0.04 % differences for efficiency and capacity. As an example, Fig. 6.12 depicts the differences in the FC flow given two typical BOXERMesh and PADRAM grids. All simulations with the FC model were carried out with the strips' injection distance set to a quarter of the original value from the Rolls-Royce case setup. More details about this problem are provided in Sec. 6.4.1.1.

Visually, Fig. 6.13 compares the relative total pressure with all three types of FC models and the finest meshes for each case. While it is apparent that the results with discrete holes in Fig. 6.13c and discrete TE holes and strips in Fig. 6.13b are closer to

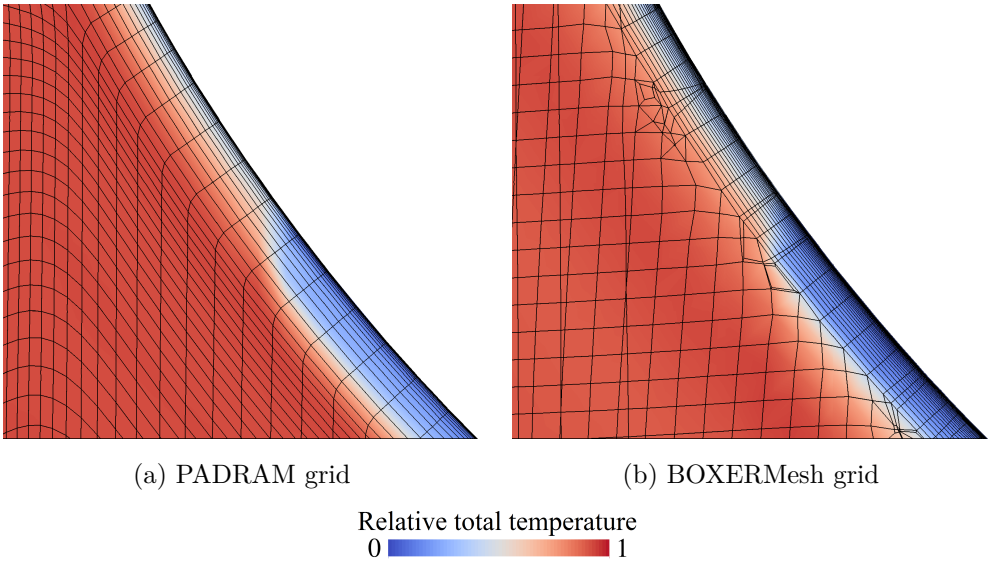

(a) PADRAM grid (b) BOXERMesh grid

Figure 6.12: Film cooling strip flow differences with different grids (on the suction side at 50 % span)

each other, the pure strip model's results in principle are not far-off, although some differences can be identified. Similarly, Fig. 6.14 compares the flows of both FC strips and FC holes through the blade's surface streamlines. On the whole, visual differences are small, but the continuous flow of the FC strips is apparent and distinctly different to the real holes' flow. Figure 6.15 depicts isosurfaces of the relative Mach number for several FC hole models and, similarly, differences in the flow due to the discrete FC holes are readily apparent. Due to the FC strip model's continuity assumption, discrete FC flows from each hole cannot be modeled. The strips only represent an average approximation without any details about the actual FC flows.

6.4.1.1 Impact of FC Strip Penetration Distance

In order to highlight the effect of the FC strip penetration distance parameter, Fig. 6.16 depicts its effect on flow and temperatures. The cool spot at the LE in Fig. 6.16 with the original penetration distance is a numerical anomaly of the FC strip model. With other penetration distances, e.g., half or quarter the original distance, this problem disappears. Due to this issue, choosing Rolls-Royce's original penetration distance, which typically is also used for much larger engine types, is not advisable. Generally, with smaller penetration distances, the coolant temperature decreases. Figure 6.17 shows how the penetration depth influences the temperature: the lower the depth, the cooler the blade surface. It is unknown, what value for the penetration depth is realistic for this case. A separate CFD analysis *with* discrete holes would have to be set up in order to tune the strip model to the correct penetration depths for each strip, but, obviously, modeling discrete holes defeats the point of having a strip model, whose sole purpose is

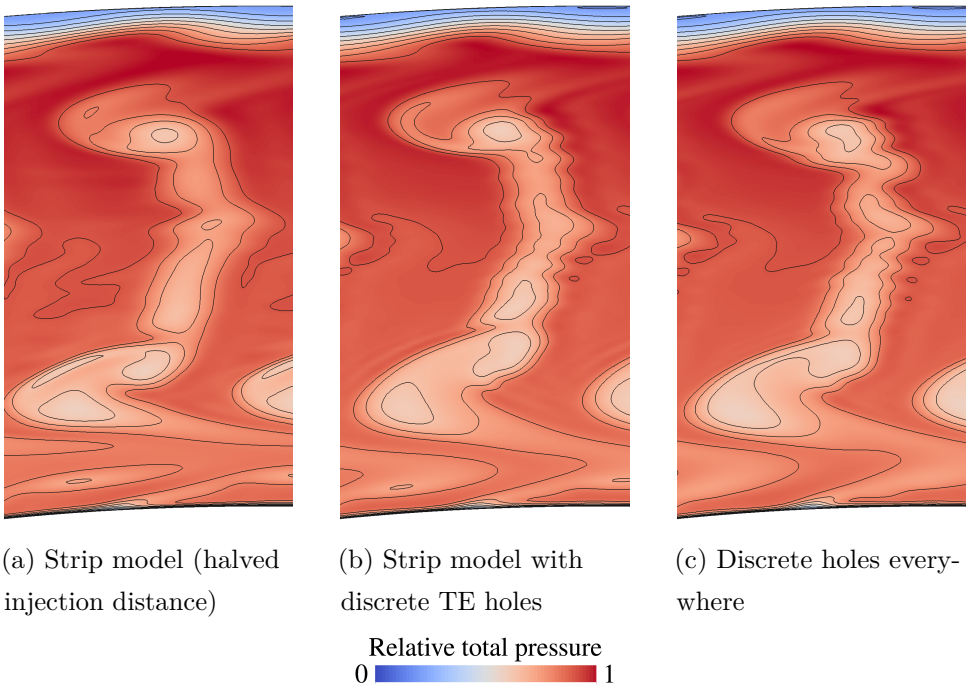

(a) Strip model (halved injection distance)

(b) Strip model with discrete TE holes

(c) Discrete holes everywhere

Figure 6.13: Comparison of relative total pressure at exit plane with different film cooling models

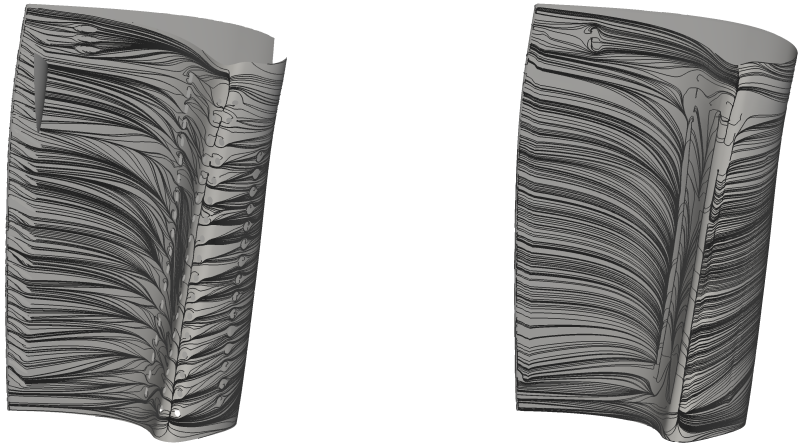

(a) Discrete holes

(b) FC strips

Figure 6.14: Comparison of surface streamlines from both FC models for the nominal CAD model

not to model each hole. Nevertheless, in the context of UQ and RDO, the strip model is still immensely useful since every simulation requires far less computational resources and the cost of a single simulation with discrete holes might be acceptable to tune the strips. Next, Fig. 6.18 quantifies the penetration distance impact on the main quantities of interest and variations are generally very small compared to the outputs variations geometric uncertainties. Capacity and mass flow rate are only affected by changes to

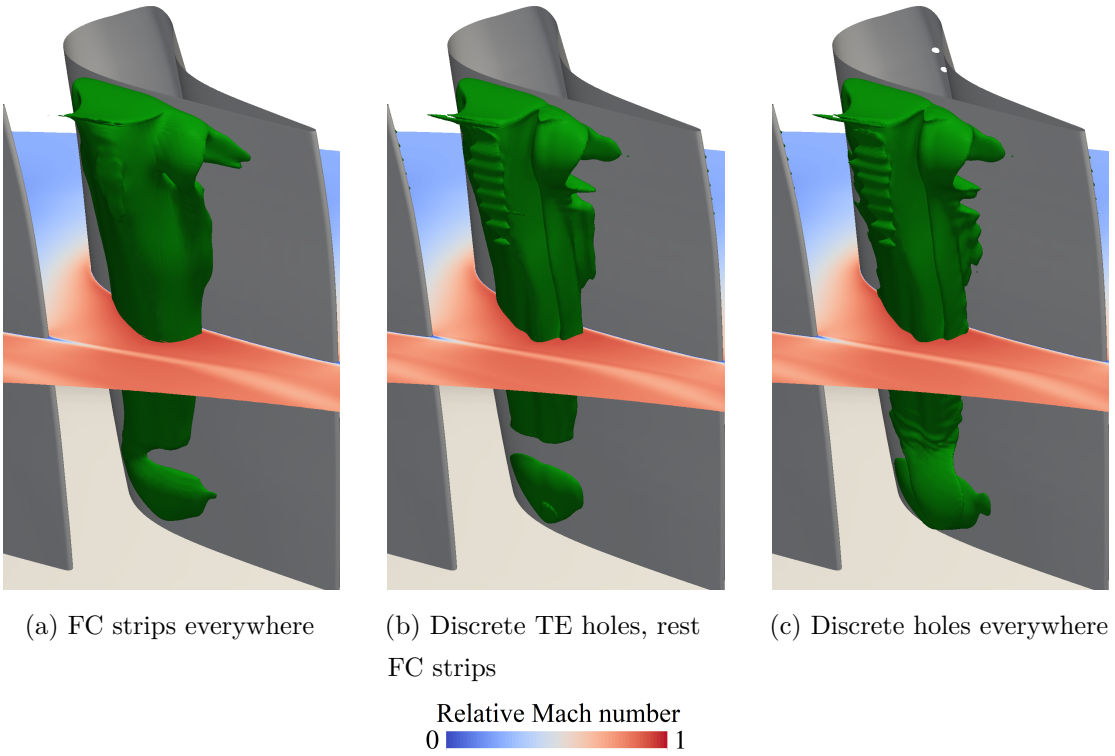

(a) FC strips everywhere (b) Discrete TE holes, rest FC strips (c) Discrete holes everywhere

Figure 6.15: Comparison of relative Mach numbers of the flow with different film cooling models. The contour plot is located at 50 % span and the green isosurface at $M_{rel} = 1.1$.

the TE FC cooling strips and not by any other FC strip. Note that the quantities in Fig. 6.18 are plotted in relation to the CFD solution with the penetration distance for all strips set to one quarter of the default value.

Finally, Fig. 6.19 compares the FC strip flow, its injection distance into the hot gas path and its temperature to the case with real discrete FC holes. It is evident that the chosen FC strip penetration distance (1/4 of the original value used by Rolls-Royce) is too small. The coolant ejected from the real holes extends further into the mainstream everywhere except at the TE due to the shallow injection angle there. Hence, the original penetration distance used by Rolls-Royce is indeed a suitable value. However, questionable numerical artifacts such as the one in Fig. 6.16 can occur with the FC strip model. In addition, the continuity of the FC strips is also evident as, for example in Fig. 6.19b, in actuality at this particular span position there is no SS FC cooling or FC hole, but with strips this is present anyway. The same difference is evident in the other figures as well, e.g. in Fig. 6.19d and Fig. 6.19c, where only a small amount of coolant is ejected from a part of the real FC hole, since only a small fraction of it is present in the cut at 50 % span. With the FC strips, a thicker protective layer of coolant is present. Also, slight differences in coolant temperatures for both cases can be observed too. As has been highlighted in Fig. 6.17, this is due to the temperature's dependence on the FC strips' penetration distance.

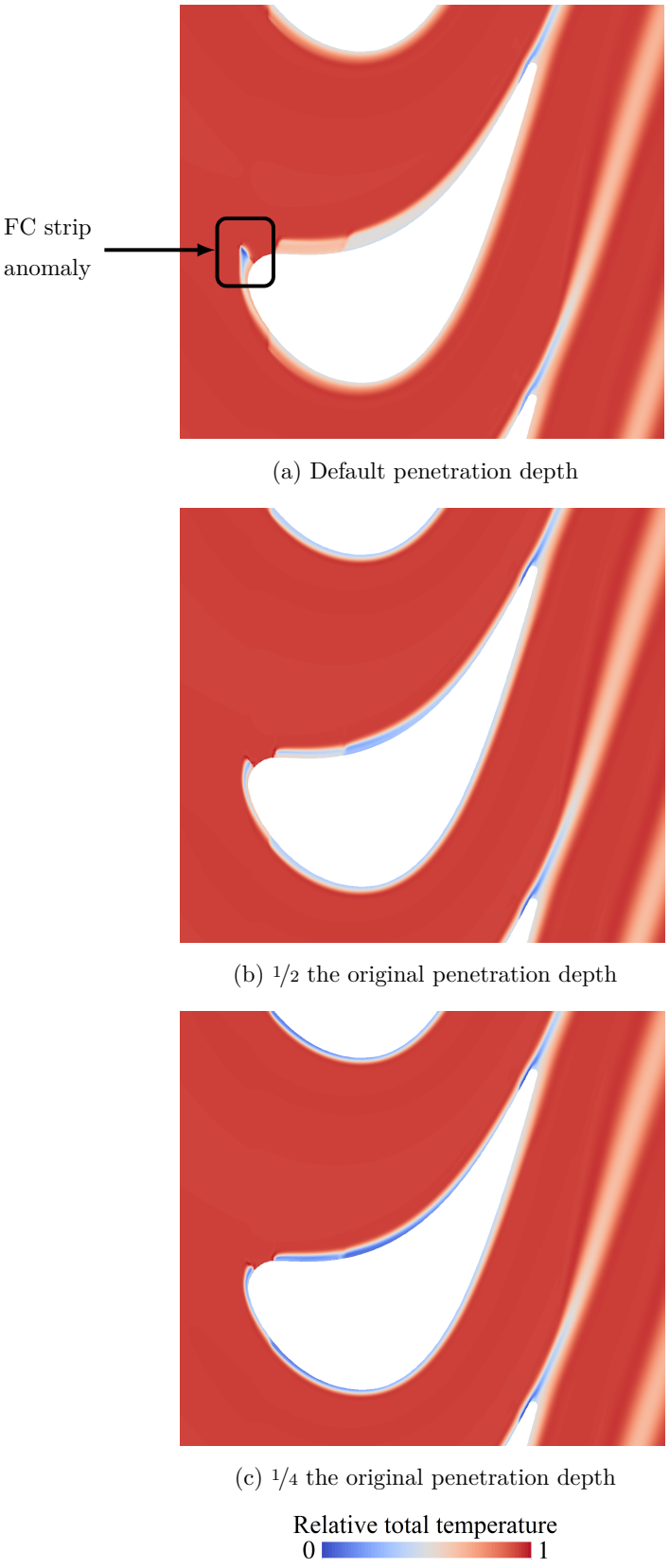

(a) Default penetration depth

(b) 1/2 the original penetration depth

(c) 1/4 the original penetration depth

Figure 6.16: Impact of film cooling model penetration distance on flow and temperature

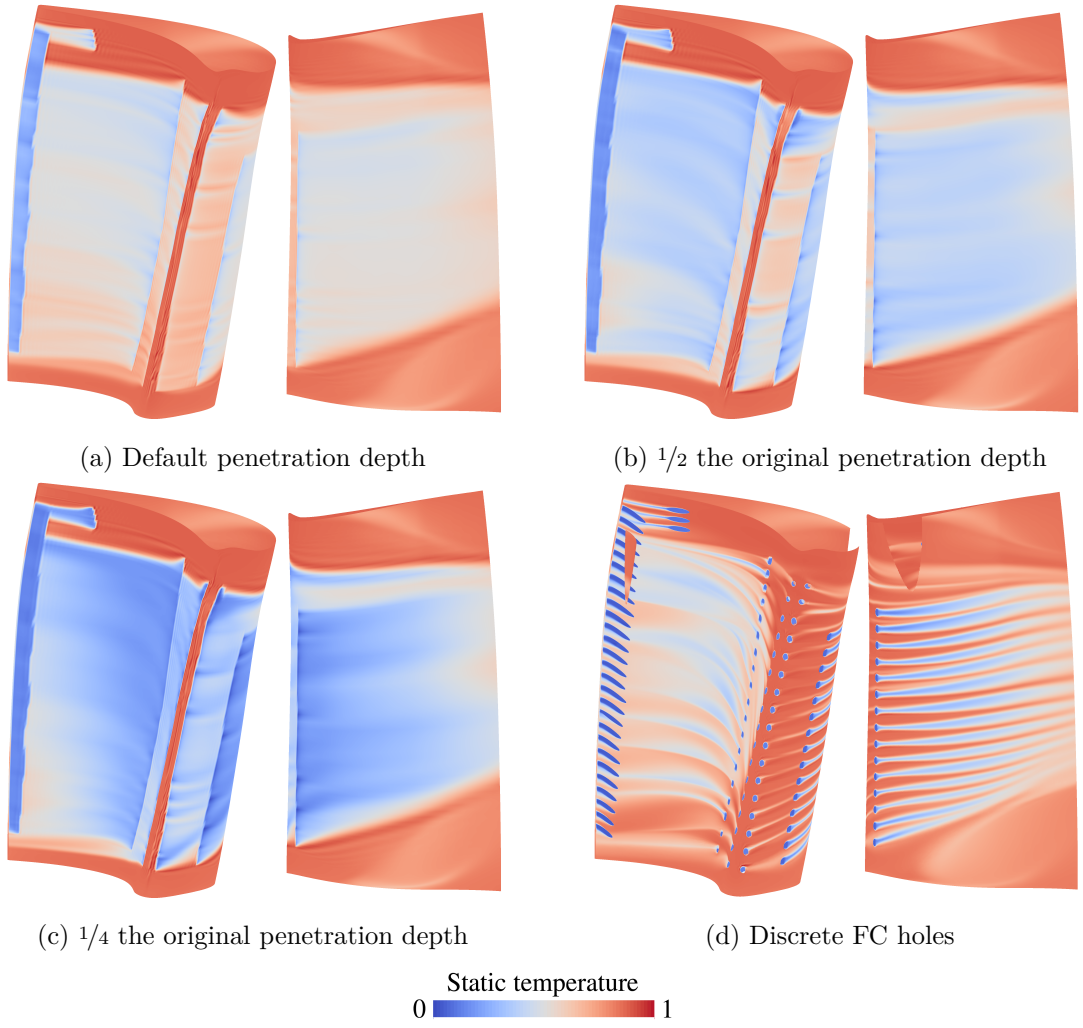

(a) Default penetration depth

(b) 1/2 the original penetration depth

(c) 1/4 the original penetration depth

(d) Discrete FC holes

Figure 6.17: Comparison of static temperature on blade surface with various penetration distances

Generally, the results show that with a decrease of the penetration depth, the temperature of the protective FC layer decreases too. This is a sensible result, since the same amount of coolant from the holes still protects the blade, regardless of the penetration distance. Due to the reduced penetration distance, the hot gas and the coolant cannot mix as much. Hence, the coolant's properties more closely reflect its initial boundary conditions. Similarly, since the density of the hot gas is much lower than that of the coolant, the density of the FC layer increases, when the penetration distance is reduced. Also, again due to the boundary conditions of the coolant, the pressure of the protective layer tends to be slightly higher with a reduced penetration distance, and the velocity is slightly lower. The previous observations make clear that the penetration distance parameter directly influences all relevant quantities in the flow field. Since there is no way knowing which value for the penetration distance is adequate in a given case, it is advisable to validate its setting using a different FC model, e.g., discrete FC hole

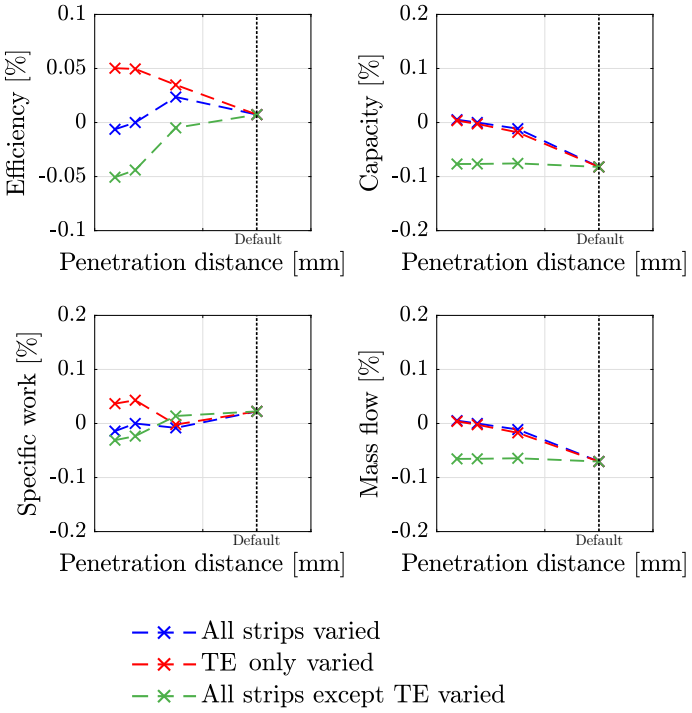

Figure 6.18: Impact of penetration distance parameter on quantities of interest (default, 1/2, 1/4 and 1/8 the original penetration depth). All quantities are plotted in relation to the CFD solution with the penetration distance for all strips set to one quarter of the default value.

stubs. This is particularly relevant for simulations involving heat transfer. Otherwise unvalidated results might easily be called into question.

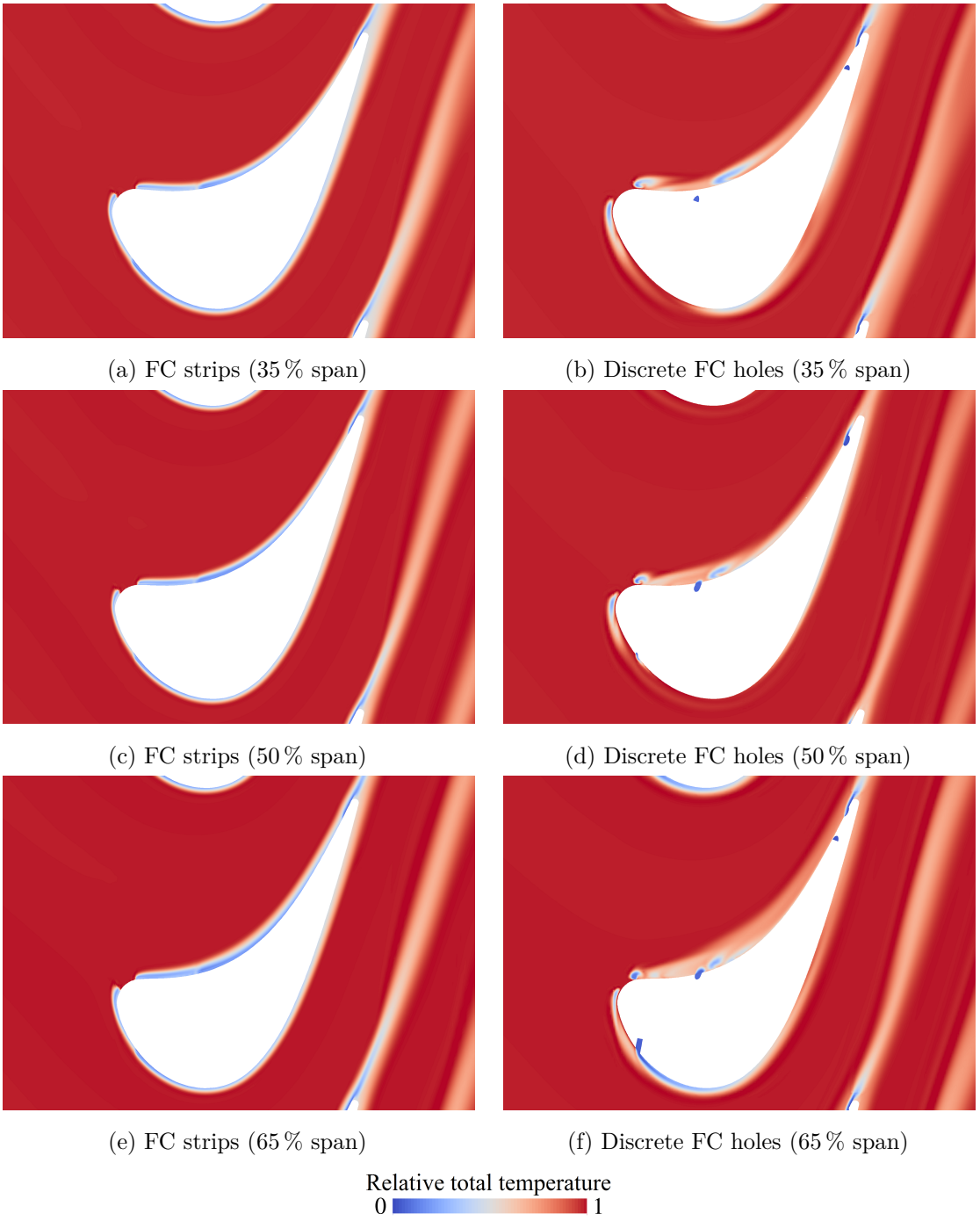

(a) FC strips (35 % span)

(b) Discrete FC holes (35 % span)

(c) FC strips (50 % span)

(d) Discrete FC holes (50 % span)

(e) FC strips (65 % span)

(f) Discrete FC holes (65 % span)

Figure 6.19: Penetration distance comparison between FC strips and discrete FC holes over a range of 500 K at 35 %, 50 % and 65 % span. The penetration distance for the FC strips is set to $^1/_4$ of the case's original penetration depth.

6.4.2 Impact of TE FC Hole Variations

The impact of TE FC hole variations is quantified in this section in two ways: first, by considering the results of both the *UV* and virtual manufacture workflow and comparing

these results to the epistemic uncertainties from Sec. 6.4.1. Second, the impact of FC hole variations on the outputs is assessed by way of comparison with a case without FC.

Figure 6.20 depicts the resulting quantities of interest of both *UV* and virtual manufacture workflow. Visually, it is immediately evident that both approaches nearly produce the same output statistics. The close proximity of their means, as indicated by red and yellow lines, shows that on average both approaches approximately yield the same output values. The same holds true for the spread. Roughly speaking, the min-max range of variations is 0.3 % for efficiency, 0.7 % for capacity, 0.3 % for specific work and 0.7 % for mass flow rate. In relation to the nominal design intent's geometry, the efficiency of manufactured turbine blades modeled with either workflow is actually slightly better, if only by about 0.02 %. Capacity and mass flow rate on average are both shifted by about 0.3 %. The work produced by the blades on average is reduced by 0.05 %.

The results in Table 6.2 reveal that with PADRAM and FC strips aleatoric variations from Fig. 6.20 are larger than epistemic uncertainties for all monitored quantities of interest. However, simulations with the two other FC hole models must also be considered. In Table 6.2, it is evident that a change of the FC hole model produced variations of a similar magnitude as the min-max variations observed in Fig. 6.20 for efficiency and specific work. This is not the case, however, for capacity and mass flow rate, where the observed aleatoric variations are far larger than epistemic uncertainties arising from switching the FC model.

Moreover, it is examined whether or not both FC variation models identify *the same* turbine blade with the largest capacity deviation from nominal. Despite their good agreement on average, this is not the case, however. With the virtual manufacture workflow, the largest capacity deviation is detected for blade scan #1016 and it is 0.70 %. With *UV*-mapped strips, blade scan #1322 is found to have the largest deviation of 0.63 %. For scan #1322, the virtual manufacture workflow found a capacity deviation of 0.67 % (compared to 0.63 % from the *UV* workflow). In contrast, scan #1016's performance prediction with UV-coordinates is 0.56 % (compared to 0.70 % from the virtual manufacture workflow). Hence, the differences are just 0.04 % and 0.14 % respectively. Although each approach has identified different worst-case blades, their performance prediction is similar. The absolute magnitude of these deviations is significant since, for example, often deviations on the order of ±0.1 % or less are deemed acceptable.

Finally, Fig. 6.21 shows the magnitude of variations solely due to FC variations, i.e., in contrast to just blade shape variations. This was done through a comparison at the same operating point: in the case without FC, the missing mass flow rate of about 5 % attributable to FC is offset by increasing the inlet total pressure accordingly. Both cases then have the same total mass flow rate. Basically, the results in Fig. 6.21 show that FC

variations matter for all considered quantities of interest. Especially for capacity and mass flow rate, mean value shifts are considerable and outputs have broader ranges of variation in the case of film-cooled HPT blades.

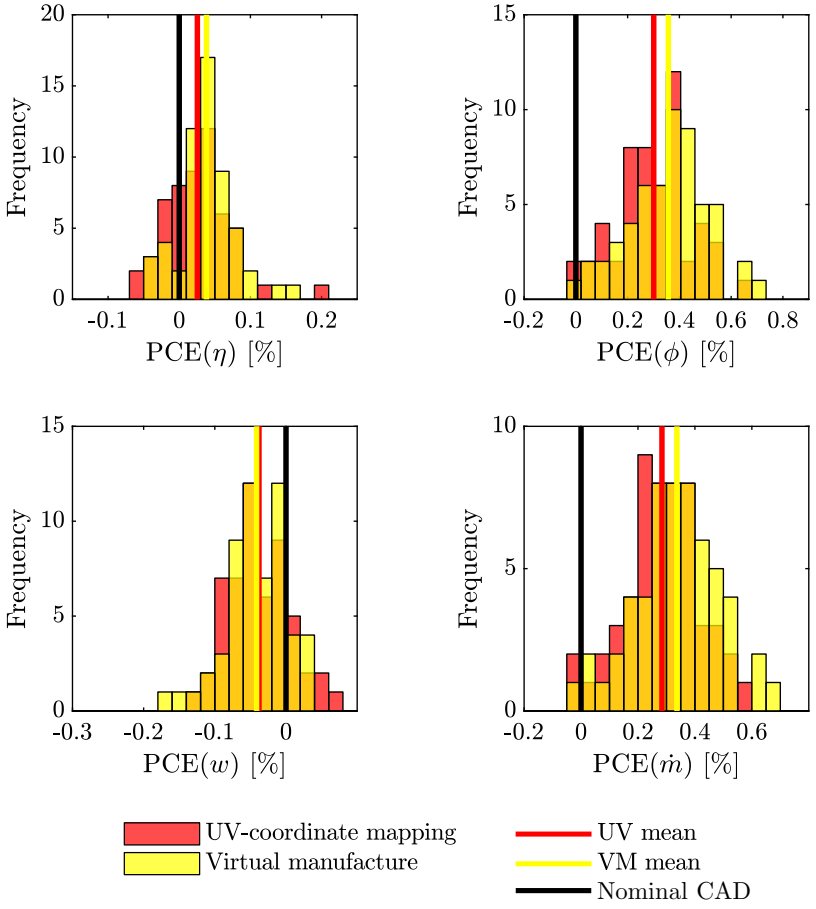

Figure 6.20: Comparison of UV-coordinate and virtual manufacture workflow results, both with film cooling strips

6.4.3 Detailed Analysis for One Blade Scan

The purpose of this section is to expand on the previous analysis by focussing on the TE with discrete TE holes. For brevity, only one single blade scan, viz. scan #1016, is analyzed in detail. The previous FC strip-based CFD found a maximum capacity variation from nominal of 0.70 % for this blade. The comparison of results in Table 6.3 with both FC models, strips vs. strips *and* discrete TE holes, show that percentage point differences between both cases are rather small for capacity and mass flow rate, but large in comparison for efficiency and specific work. The percentage point difference for the latter two quantities is basically as large as the whole min-max range of variations in Fig. 6.20. Even worse, a decrease for specific work with strips and an increase with strips and discrete TE holes is observed. With FC strips, epistemic uncertainties exceed

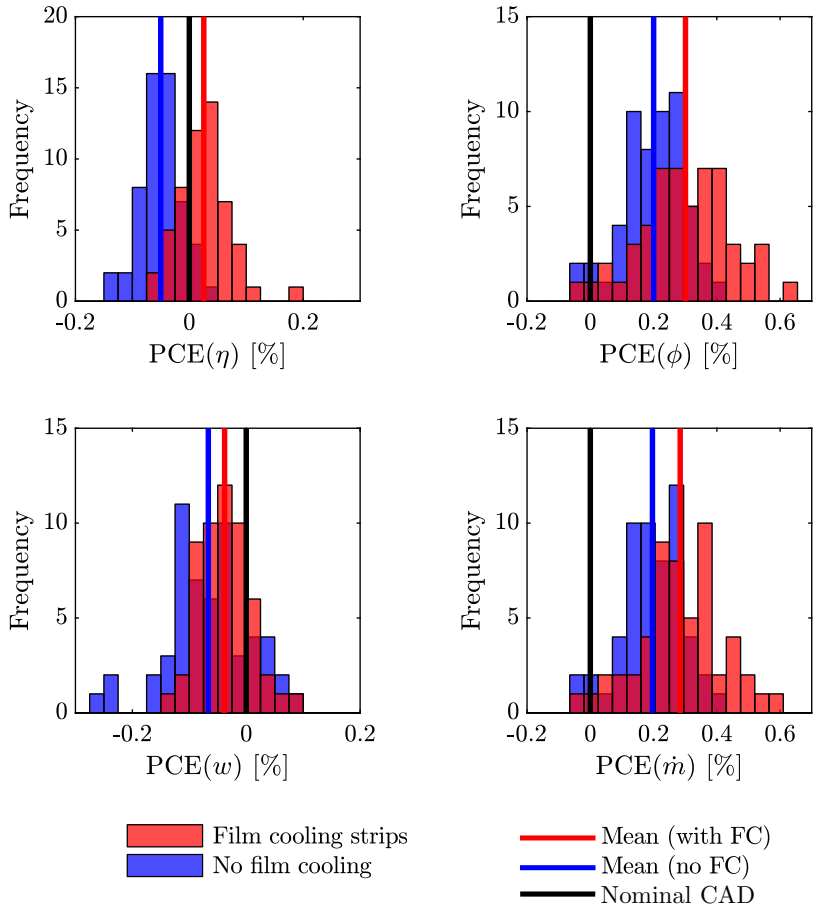

Figure 6.21: Comparison of results with film cooling (UV-mapped FC strips) and no film cooling at all (but at the same operating point)

aleatoric uncertainties for efficiency and work. However, UQ is possible for mass flow rate and capacity, where trend and magnitude of variations agree much better. The results in Table 6.3 emphasize that the discrepancy for efficiency and work between PADRAM and BOXERMesh grids is too large. In relation to the BOXERMesh grid with discrete holes, the percentage point difference for efficiency and work between strips and strips with discrete TE holes is much smaller. Given the monitored quantities of interest here, inter-mesh variations between BOXERMesh and PADRAM grids are too large to permit UQ for any outputs other than capacity. In other words, with the film cooling strip model only variations of the capacity and the mass flow rate can be considered. Figure 6.22 compares CFD solutions to investigate effects due to the various FC models. In Fig. 6.22, it is evident that for the nominal geometry the spike in Mach number with FC strips occurs later than with real holes. This is due to the long semi-major axis of the TE holes' ellipse, as FC strips are simply applied in the middle (at each hole's intersection of semi-minor and semi-major axis). Hence, solutions at the TE do not fully agree. For the scan, isentropic Mach numbers, as defined in Eq. (6.10), are generally higher and clearly

distinct from the nominal CAD design intent:

$$M_{is} = \sqrt{\left(\left(\frac{p_0^{inlet}}{p}\right)^{\frac{\gamma-1}{\gamma}} - 1\right) \cdot \frac{2}{\gamma - 1}}. \tag{6.10}$$

Figure 6.23 similarly reveals differences in terms of temperatures between the FC models. The reference solution with discrete FC holes in Fig. 6.23c clearly depicts areas of the flow with different temperatures magnitudes compared to Fig. 6.23a and Fig. 6.23b with FC strips, although the overall structure of the flow is very similar.

Table 6.3: Comparison of results for blade scan #1016 using two different grid types (and two film cooling modeling strategies). The results are shown in relation to the nominal geometry's results with the finest PADRAM and BOXERMesh grid. For the grids, cf. Table 6.2.

FC model	Strips	Strips & discrete TE holes	Percentage point difference
Mesher	PADRAM	BOXERMesh	
$\Delta\eta$ [%]	0.02	0.25	0.23
$\Delta\phi$ [%]	0.70	0.79	0.09
Δw [%]	−0.03	0.27	0.30
$\Delta\dot{m}$ [%]	0.66	0.73	0.07

(a) Results in relation to the finest PADRAM grid

FC model	Strips	Strips & discrete TE holes	Percentage point difference
Mesher	PADRAM	BOXERMesh	
$\Delta\eta$ [%]	0.02	−0.06	0.08
$\Delta\phi$ [%]	0.70	0.59	0.11
Δw [%]	−0.03	−0.11	0.08
$\Delta\dot{m}$ [%]	0.66	0.55	0.11

(b) Results in relation to the finest BOXERMesh grid

6.4.4 Artificial Blades with Real Artificial Film Cooling Hole Variability for Uncertainty Quantification

Finally, a comprehensive UQ workflow for film-cooled turbine blades is presented. UQ often requires hundreds of samples to compute the probabilistic responses and hence as many blades as necessary have to be constructed in order to compute statistics such as sample mean and variance. The proposed methodology is founded on accurately reconstructed blade shapes and high-fidelity steady-state RANS CFD simulations, as presented in Chapter 3 and Chapter 4 respectively. Both of these chapters describe the process chain employed here and its setup in detail. In the UQ workflow, turbine blades

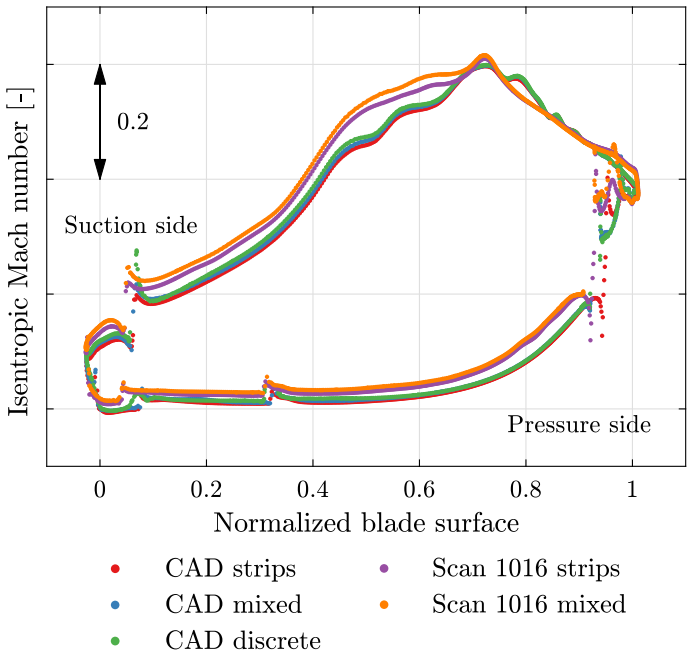

Figure 6.22: Isentropic Mach number comparison at half-span

are constructed according to the underlying measurement data using Blade2Parameter as the main tool to add variability onto a baseline blade shape, given 14 airfoil noise parameters per blade. The novelty of the presented workflow here is that real FC variability is introduced using the virtual manufacture approach, which replicates the real manufacturing process, as presented in Sec. 6.3.2. For comparison see a previous publication, where the FC variability was *not* modeled and the nominal hole positions were emulated for each constructed artificial turbine blade (Scharfenstein, Heinze, et al., 2013). Here, given the previous findings from Sec. 6.2.2 that trailing edge hole deviations are largely due to aberrant blade shapes, film cooling hole variations are added with the virtual manufacture methodology. The other alternative for modeling FC hole variations, UV coordinates, requires more effort as for every analysis all UV measurements would have to be extracted from all scans and it relies on identically constructed blade surfaces. Virtual manufacture has the benefit that no FC hole measurements are required and there are no blade surface restrictions. Previous analyses in this chapter have used all 58 reverse engineered blade scans and their performance can serve as a reference, to which a number of artificially created geometries can be compared. Then, this process must be tested to show whether or not artificial blades, i.e., HPT blades with artificial shapes *and* corresponding artificial FC holes, have the same stochastic response as the actual sample.

To check this, 100 correlated Monte Carlo samples were generated, as described in Sec. 3.3.2.3, and 100 corresponding artificial film-cooled HPT blade models were

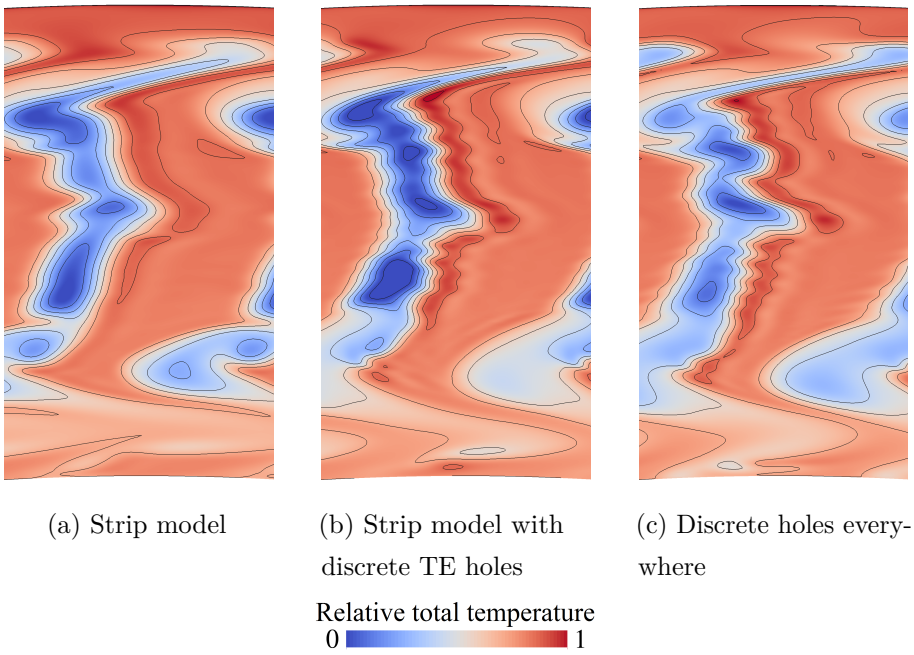

(a) Strip model

(b) Strip model with discrete TE holes

(c) Discrete holes everywhere

Figure 6.23: Comparison of relative total temperature over a range of 200 K for different FC models and the nominal geometry at the exit plane

constructed. With the NX model of each blade, FC hole positions are computed through the artificial manufacture workflow, as described in detail in Sec. 6.3.2. The flowchart with all steps involved is depicted in Fig. 6.24. As previously mentioned, details regarding each step in the workflow can be found in Chapter 3 for the reverse engineering process and Chapter 4 for the CFD simulations. The key difference to the workflow from Chapter 5 is the model for the FC variability and the representation of FC holes through the FC strip model in the CFD. Even though FC holes are represented through FC strips in this workflow, this could easily be changed to discrete FC holes if desired, although at the cost of greater computing effort. Obviously, the FC model choice has a direct impact on what quantities of interest can be analyzed as part of the UQ study, as described in Sec. 6.4.1. Due to the use of the FC strip CFD model in this analysis, epistemic uncertainties for isentropic efficiency and specific work outputs exceed aleatoric uncertainties. Figure 6.25 reveals that the performance of the artificial film-cooled blades matches the performance of the real blade sample. For example, the percentage point difference for the monitored quantities of interest, i.e., isentropic efficiency, capacity, specific work and mass flow rate, between 100 artificial blades and the actual sample is only 0.01 %, −0.03 %, 0.01 % and −0.02 % respectively. Mean values nearly overlap, ranges of fluctuations are close and all histograms are very similar. This shows that the new model for the film cooling variability, the virtual manufacture approach, can indeed model the film cooling variability well.

At present, the presented workflow enables aerodynamic UQ for HPT blades. Although out of scope in this thesis, the approach also allows the detailed investigation of

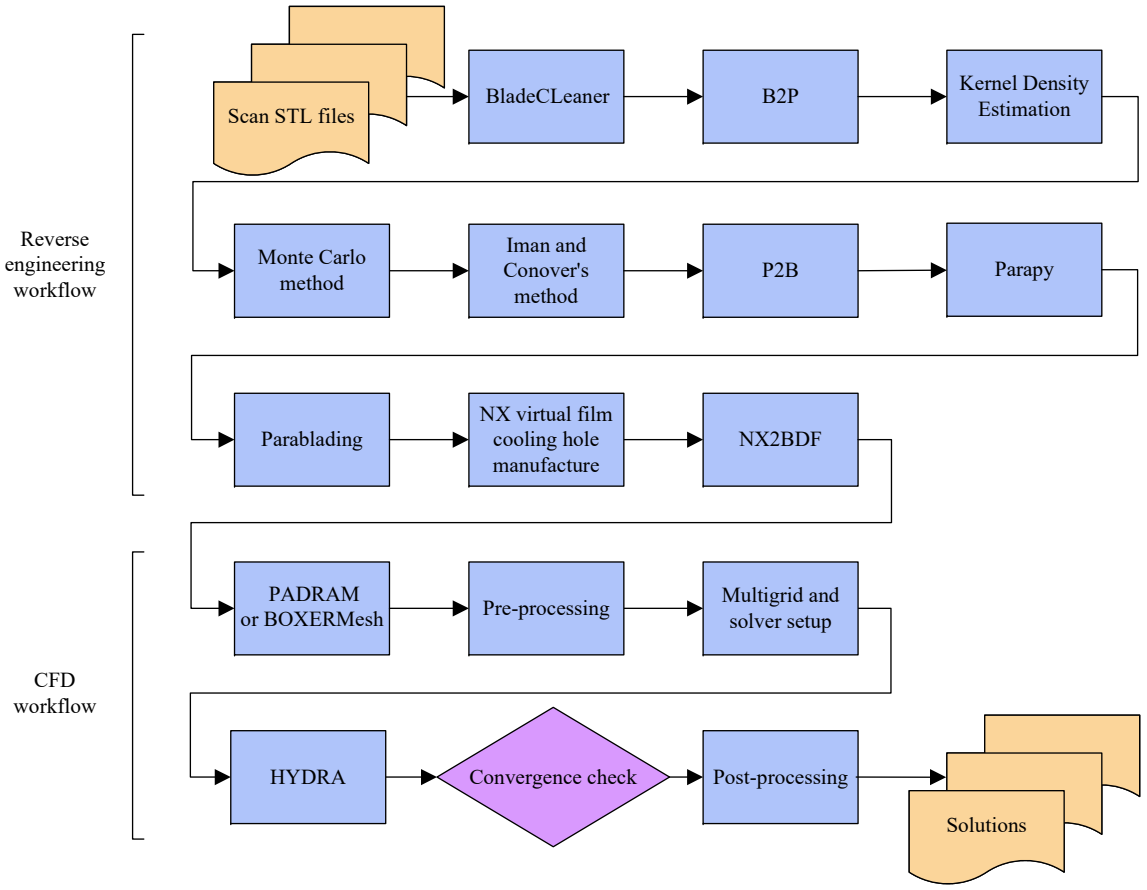

Figure 6.24: Uncertainty quantification flowchart for fully-featured film-cooled turbine blades

other known important factors, e.g., of cooling hole diameter variations or of the film hole length-to-diameter ratio. Variations of heat transfer-related quantities, e.g., of the FC effectiveness, of the metal temperatures and of the blade life, have also been out of scope in this thesis. Nevertheless, these quantities can easily be computed with very few adaptions to the existing workflow, e.g., by adding holes in the NX models and scripting the mesh generation process with BOXERMesh instead of PADRAM. When UQ for aerodynamic quantities of interest other than the mass flow rate or capacity is desired, the results in this chapter have shown that it is advisable to avoid using the current FC strip model in favor of a more detailed representation in the CFD model.

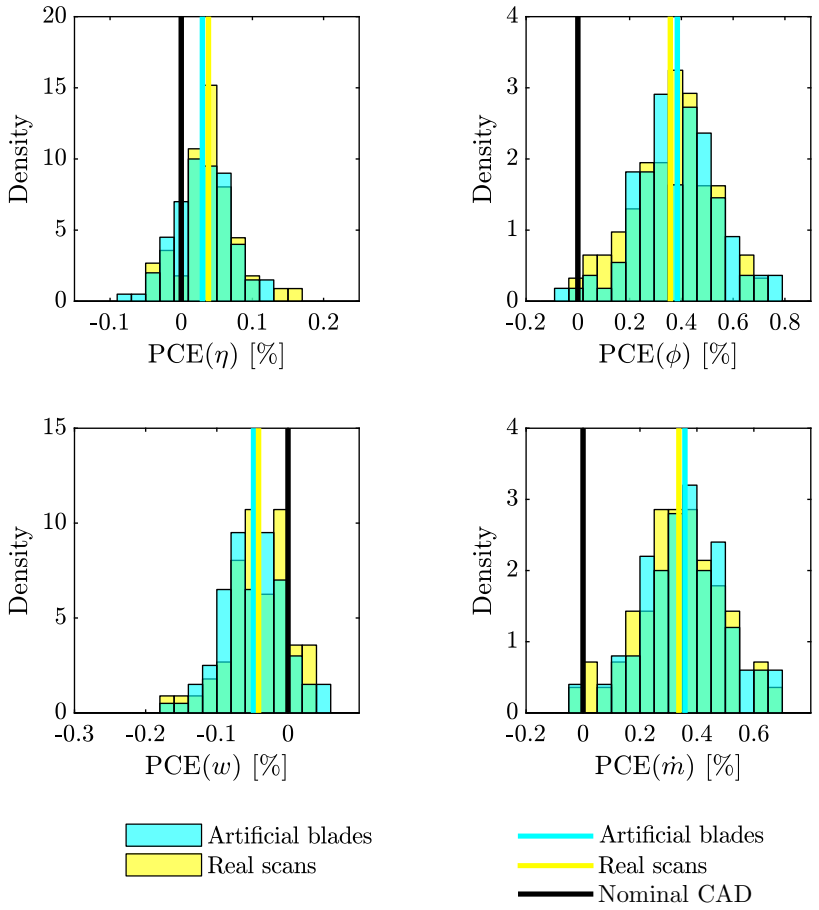

Figure 6.25: Comparison of HYDRA results of artificial blades and real scans with virtual manufacture-mapped film cooling strips

6.5 Summary

The methodology introduced here enables the high-fidelity probabilistic modeling of film cooled turbine blades. Based on real measurements, variability is introduced for turbine blade shapes *and* film cooling holes. A new computational model for the film cooling variability termed the "virtual manufacture" approach is shown to adequately approximate the experimentally observed variations. This exploits the finding that, as has been shown, trailing edge film cooling hole variations are mainly due to blade shape deviations as opposed to other sources. Another advantage of this approach is that it can be readily integrated in an automatic robust design optimization or uncertainty quantification workflow. On top of blade shape variations, it has been shown that film cooling hole variations are important in general, in particular for capacity and mass flow rate. For basic aerodynamic design, the simple film cooling strip model is adequate as long as only capacity and mass flow rate as the quantities of interest are considered. With the film cooling strip model and the observed variations, epistemic and aleatoric

uncertainties here are of similar magnitude for efficiency and specific work and prevent meaningful uncertainty quantification. Hence, for other quantities of interest, more detailed models of the film cooling geometry such as discrete hole stubs must be used for analysis.

Chapter 7

Conclusions & Recommendations

The literature overview in Chapter 2 has made clear that variations in the context of turbomachinery and high-pressure turbine (HPT) blades, in particular, are a known problem. Whilst extensive research in the field has been carried out, a coherent robust design optimization (RDO) methodology for HPT blades, required by industrial research and development departments to make use of the robust design methodology, has not yet been presented. Similarly, there used to be a lack of studies about film cooling (FC) hole variations, about their effects on performance and about their incorporation into RDO workflows. The aim of this thesis is to address these shortcomings and to propose suitable approaches for the robust design of fully-featured film-cooled HPT blades based on real geometric variability.

The reverse engineering and blade geometry construction approach presented in Chapter 3 incorporates the actual variations of a sample of 58 blade scans, which represent real manufacturing variations. The stochastic information extracted from this sample forms the basis of a computational turbine blade geometry generation workflow, which enables the construction of an arbitrary number of realistic, yet artificial blades. This process, developed by Heinze, Meyer, et al. (2014), has an excellent reconstruction accuracy and only requires the use of 14 airfoil parameters per blade. Realistically correlated samples are generated with the successive application of Monte Carlo and Iman and Conover's method.

Each generated blade geometry is evaluated with computational fluid dynamics (CFD) simulations as described in Chapter 4. Steady-state Reynolds-averaged Navier-Stokes (RANS) simulations are carried out using the model of an industrial turbine rotor. Typical aerodynamic quantities of interest are defined and the computational approach based on Rolls-Royce's suite of CFD codes is described in detail. Two different grid generators, PADRAM and BOXERMesh are introduced since PADRAM is incapable of meshing discrete FC holes on the blade surface. CFD results were validated using an indirect

approach with experimental data from the MT1 turbine research rig since for the given industrial case no data for validation is available.

Chapter 5 then combines both previous chapters into a novel, coherent robust design methodology for HPT blades based on real geometric variability, which is an extension of the uncertainty quantification (UQ) workflow by Scharfenstein, Heinze, et al. (2013). It is shown that artificially constructed blades, built using the reverse engineering workflow and evaluated with the CFD workflow, exhibit the same performance statistics as the original scans, which allows their usage for UQ and, by extension, RDO. Also, the impact of deviations on aerodynamic blade performance was analyzed and assessed, but disregarding FC hole variations for simplicity. Through a sensitivity analysis, it is shown that prior to optimization, the Δtan_{pos} parameter can be removed from the model. A complete robust aerodynamic optimization study was then used to showcase the proposed approach, first using an analytical example and second using the actual case. The validation of one selected Pareto-optimal design showed that both probabilistic objectives were improved and that both constraints were met. The presented RDO methodology is universally applicable to any turbine blade and works with realistic, fully-featured geometric models, high-fidelity RANS-based steady-state CFD and non-intrusive UQ.

Finally, Chapter 6 extends the previous analysis workflow and also incorporates realistic FC hole variations. Hence, now the analysis includes realistic variations of the blade shape and of the FC holes. A novel strategy to map FC hole variations termed "virtual manufacture" is introduced, which replicates the real manufacturing process of FC holes. A new probabilistic assessment of the real observed FC hole variations, which were mapped by means of measured UV coordinates, is carried out and the new approach is shown to faithfully model the actual variations in terms of output performance statistics. The results also show that UQ of film-cooled HPT blades using a FC strip model, whereby only the effects of FC, but not the FC holes themselves are modeled, is possible for certain quantities of interest with large fluctuations, e.g., for capacity and mass flow rate. For other quantities of interest, more accurate high-fidelity FC models such as discrete FC hole stubs are required, which come at the expense of greater computational cost since fine meshes are required for each of the many small holes. The combination of the RDO methods of Chapter 5 and the UQ of Chapter 6 represents further works beyond the scope of the present thesis. Operational uncertainties are also out of scope, but could easily be integrated in the workflow if desired.

The scope of this thesis has also been limited to aerodynamic performance measures such as isentropic efficiency, capacity and specific work. Future work should also investigate the impact of real variations on thermodynamic or mechanical quantities of interest. In particular, this concerns FC performance parameters such as FC effectiveness, metal temperatures and blade life. For example, conjugate heat transfer simulations and a

cold-to-hot geometry transformation would be a useful addition to the workflow. The fidelity of the CFD model should also be further investigated, ideally using a case where plenty of experimental data is available. Similarly, sources of epistemic uncertainties could be further investigated and decreased as much possible. For example, the FC hole strip model, which can only be used as a rough approximation of the real coolant's flow, could be further refined too.

Public Appendices

Appendix A

List of Used Software

Table A.1: List of used software

Software	**Version**
Blade2Parameter	6.6.0
BladeCLeaner	1.5
GOM Inspect	2016
HYDRA	7.2.3
MATLAB	2015b
Multigrid pre-processor	7.1.0
NX2BDF	1.3
Open MPI	1.4.3
OPTIMAT	v2
PADRAM	7.9.2
Parablading	4.0.1.1
Post-processor (ParaView)	5.0.6
Pre-processor	7.1.0
Python	2.7.12
Siemens NX	9

Appendix B

Optical Measurement Details

Details about the optical blade scanning procedure are reproduced here from Heinze (2013) and Heinze, Meyer, et al. (2014) due to their significance for this research. With regard to Fig. B.4, the top firtree surfaces used for the alignment were chosen due to their contact with other surfaces during operation, i.e., due to centrifugal forces. This measurement methodology ensures that blades are realistically aligned in accordance with their actual operating conditions.

Figure B.1: Example of a titanium dioxide coated, used turbine blade. This image is reproduced from the report by Heinze (2013).

Each blades was scanned and a cloud of measurement points was gathered. These points were processed using GOM-supplied software. Each blade is the result of measurements from 80 individual views, as shown in Fig. B.3. The end result for each blade is always a tessellated `.stl` (STereoLithography) file, which solely contains the coordinates

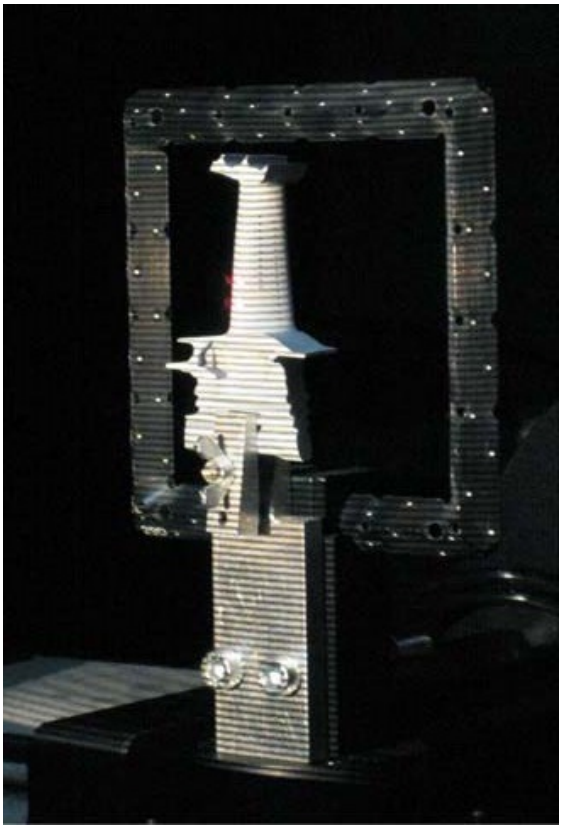

Figure B.2: Fringe patterns used by the optical recording system. This image is reproduced from the report by Heinze (2013).

Figure B.3: 3D blade measurement with 80 individual views based on reference points. Each 3D blade scan is constructed based on 80 individual views. This image is reproduced from the report by Heinze (2013).

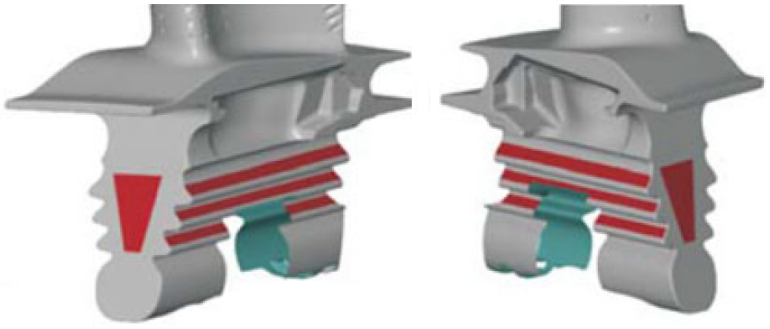

Figure B.4: Blade alignment with firtree surfaces to align the scans to the nominal blade. This image is reproduced from Heinze, Meyer, et al. (2014).

of a vast number of small triangles. Most scans' `.stl` files consist of about 2 million triangles. These `.stl` files were provided by RRD.

An example of the `.stl` resolution of scan #1 at about half-span is depicted in Fig. B.5.

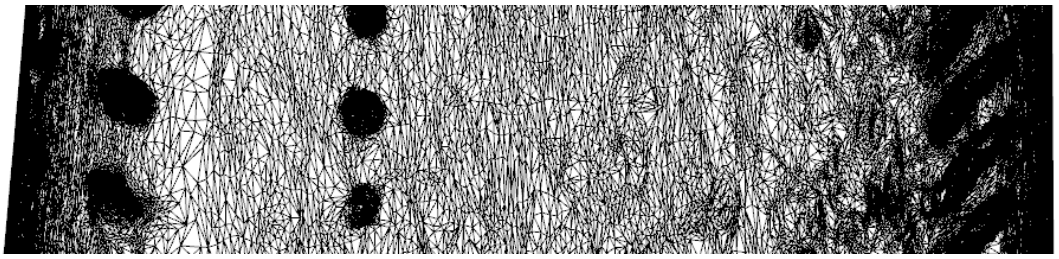

(a) Pressure side

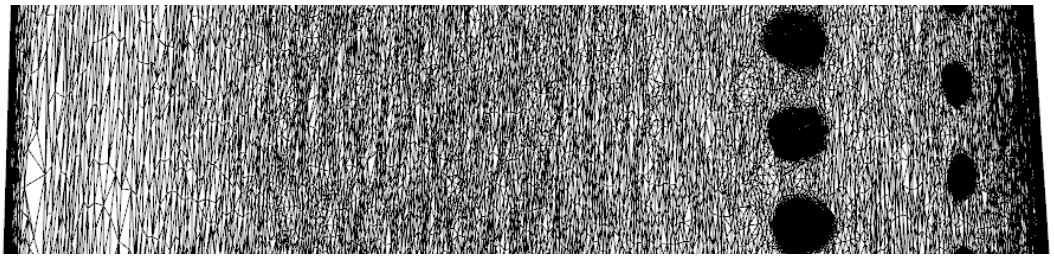

(b) Suction side

Figure B.5: STL file triangle resolution of scan #1 at about half-span

In order to get an idea of the size of the triangles, Fig B.6 reveals the average triangle edge lengths of a single scan and the minimum, average and maximum edge lengths are plotted. It is evident that for this particular scan, most edge lengths on average are smaller than 100 µm with a peak at around 30 µm.

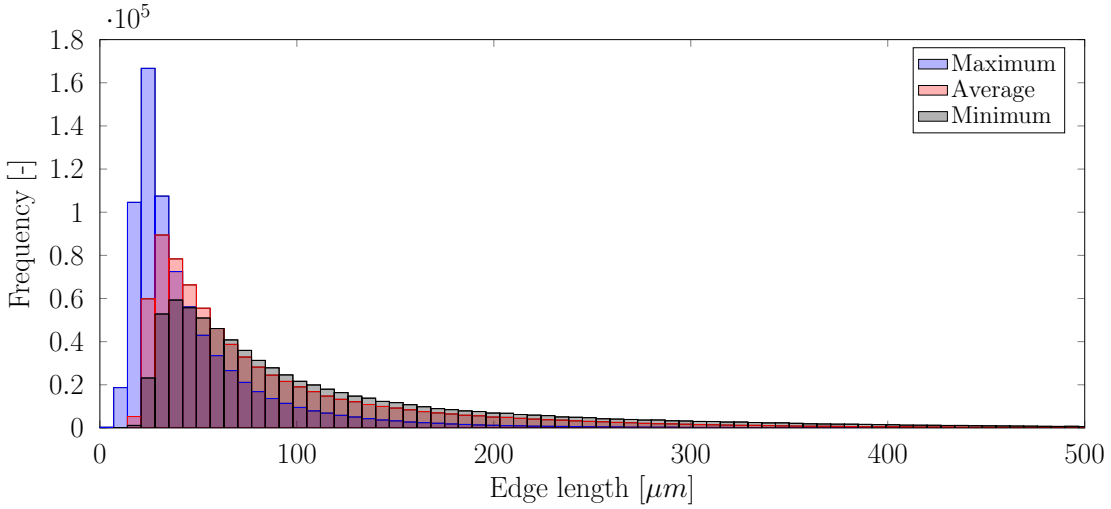

Figure B.6: Histogram of triangle edge lengths of scan #1

Appendix C

GOM Scan Artifacts

Scans with artifacts after processing with BCL were not analyzed and were removed from the sample. Examples of scan artifacts are shown in Fig. C.1.

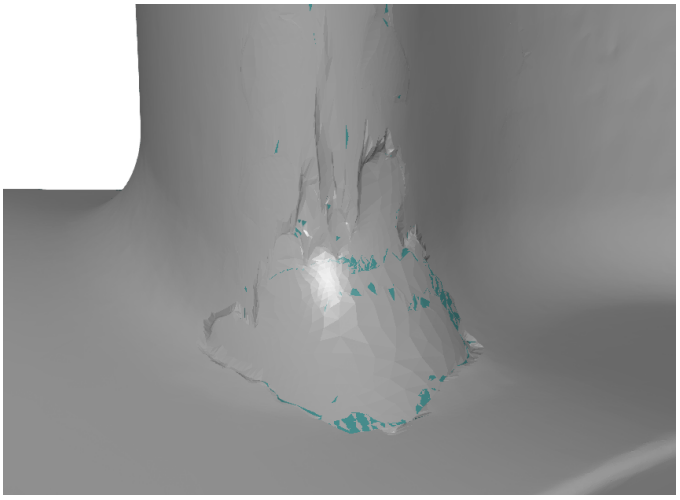

(a) LE bottom

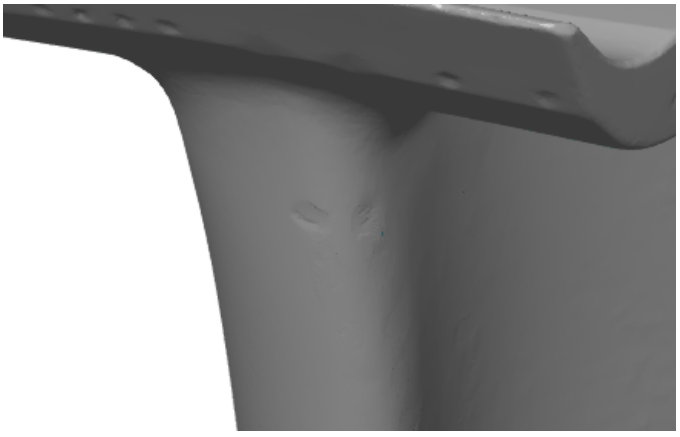

(b) LE top

Figure C.1: Artifacts of scan #1006

Appendix D

Computational Fluid Dynamics Validation with MT1 Turbine

Figure D.1: MT1 turbine stage test bench at QinetiQ (source: see footnote[1])

[1]Source: http://ec.europa.eu/research/transport/projects/items/tatef_2_en.htm

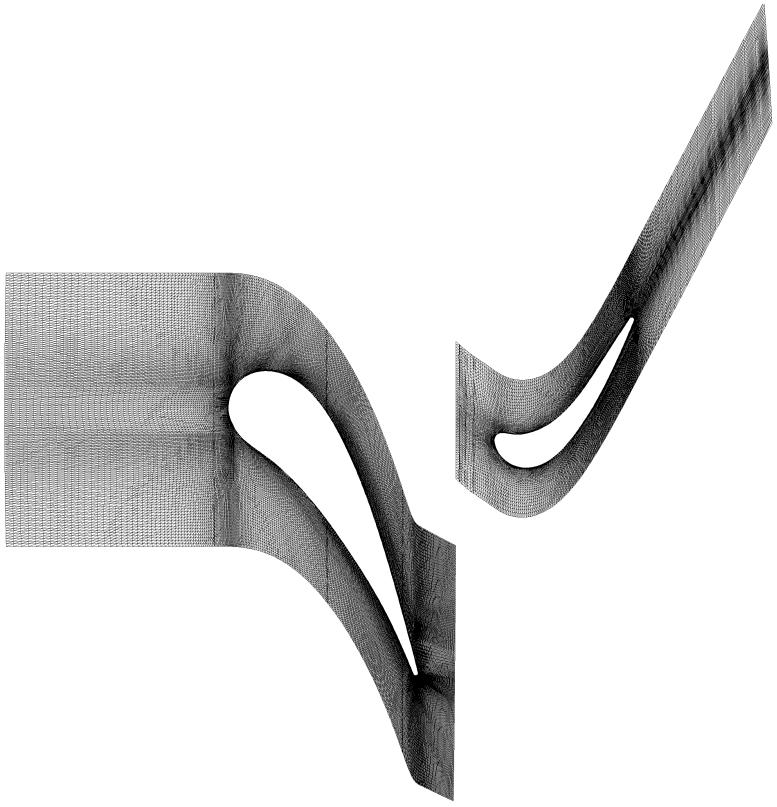

Figure D.2: Mesh of the MT1 turbine stage at 50 % span

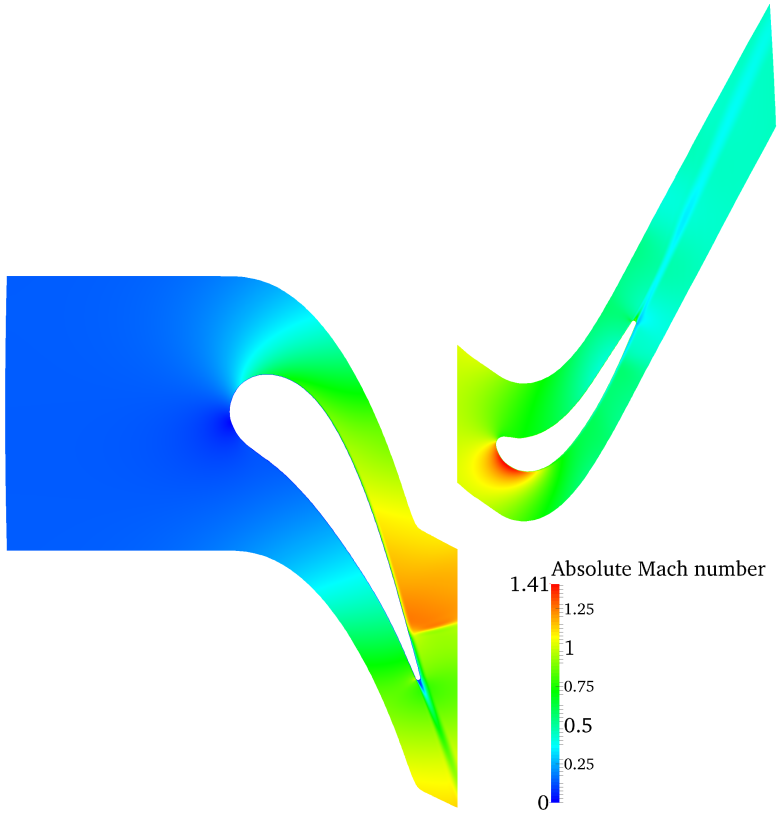

Figure D.3: Absolute Mach number of the MT1 turbine stage at 50 % span

Restricted Appendices

Appendix E

P2B Parametrization Steps

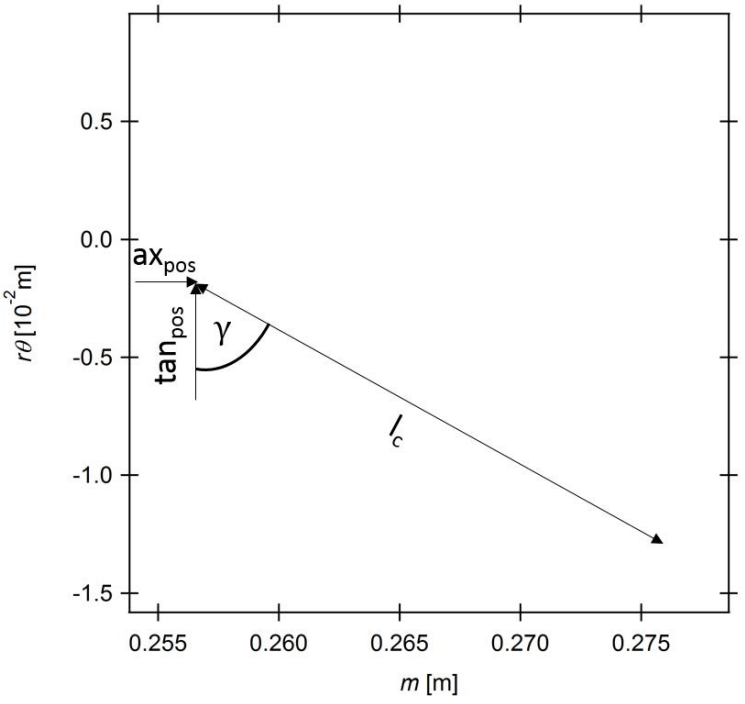

Figure E.1: P2B geometry reconstruction step 1: Profile positioning and orientation (reproduced from Högner, Voigt, and Nasuf (2016))

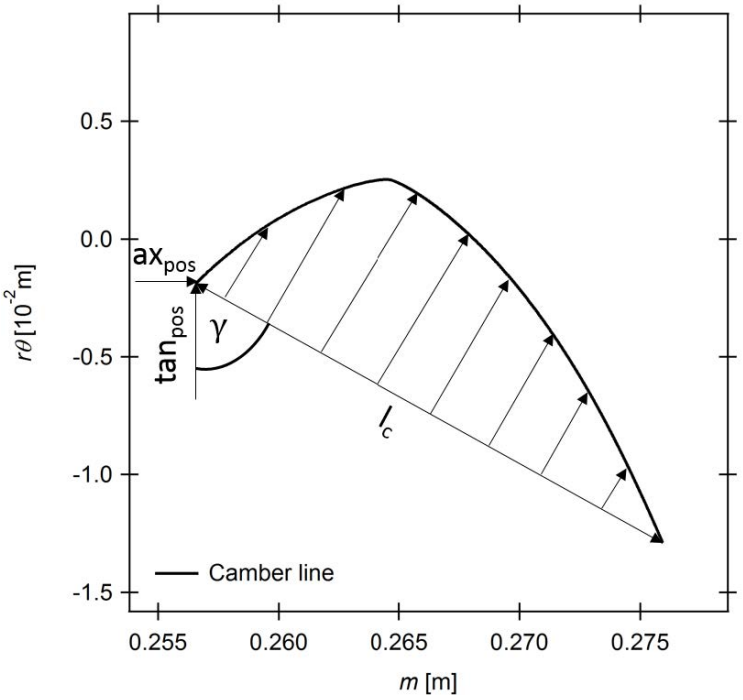

Figure E.2: P2B geometry reconstruction step 2: Application of camber to chord (reproduced from Högner, Voigt, and Nasuf (2016))

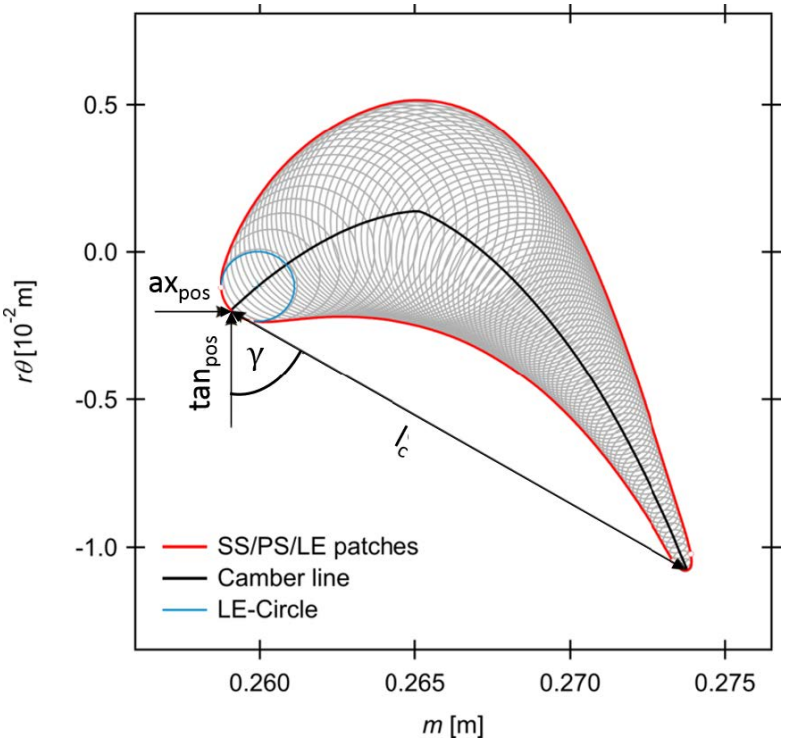

Figure E.3: P2B geometry reconstruction step 3: Application of thickness to camber line (reproduced from Högner, Voigt, and Nasuf (2016))

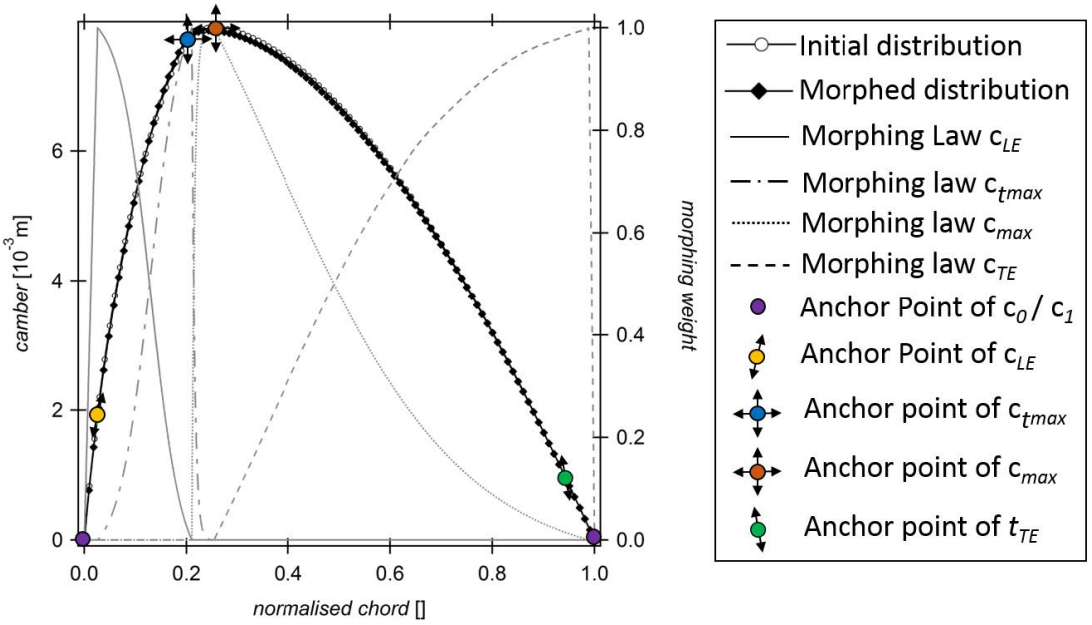

Figure E.4: P2B geometry reconstruction camber line morphing (reproduced from Högner, Voigt, and Nasuf (2016))

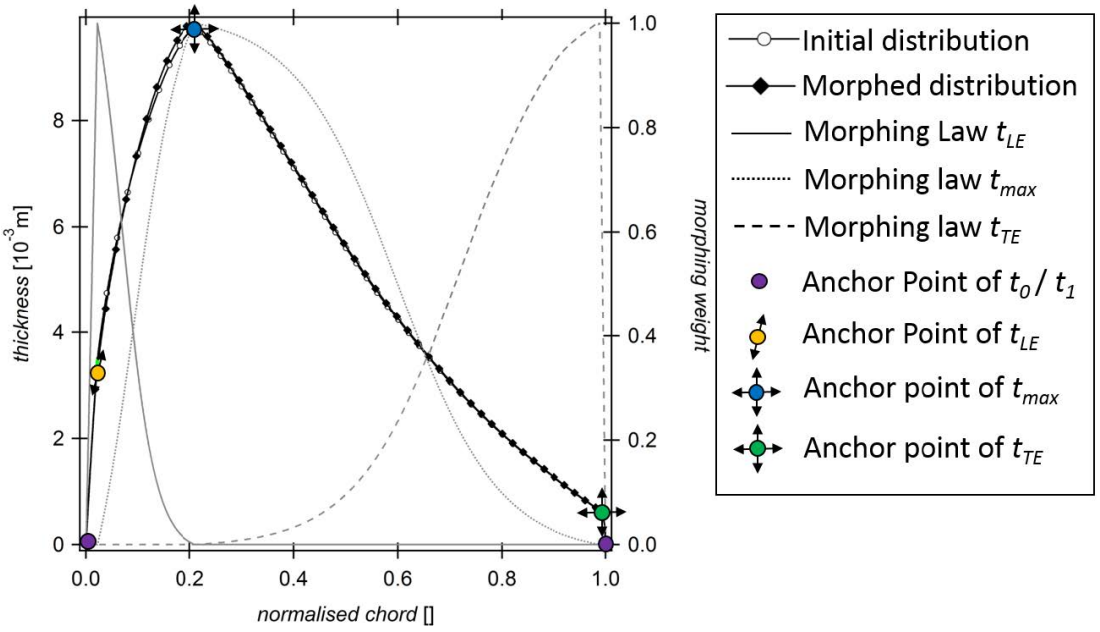

Figure E.5: P2B geometry reconstruction thickness morphing (reproduced from Högner, Voigt, and Nasuf (2016))

Appendix F

Blade2Parameter Details

Non-parametric B2P and parametric P2B slices can also be compared to visually examine the differences the parameterization brings about. Fig. F.1 compares P2B's parametric rebuild of scan #1 with original 1-to-1 B2P profiles. To be as close to the final usage scenario, the profile points are extracted from the Parablading-processed `.prt` CAD files using an NX GRIP script. Every single profile was plotted using 5000 linearly spaced points. It is evident that all profiles are very similar, although slight differences are evident near the LE and TE.

Having established that B2P is able to parameterize and create blade geometries satisfactorily, another issue at hand the span range B2P can be applied in. Due to its parameterization of 2D airfoil sections, B2P does *not* work well near the hub and the shroud. The reason for this behaviour is the fact that due to the blade's fillets in these areas, the cross-sectional planes are shaped differently than other airfoil sections closer to the middle. When the differences become too large, the estimated parameters and sections gradually become worse, up to the point where B2P fails entirely. As an example, Fig. F.2, notably Fig. F.2a, makes clear that it is the increasing blade thickness, which causes B2P problems in the filleted areas.

One way to proceed is to examine B2P's results at various span heights in the affected areas. Moreover, typically acceptable ranges of application are near 5 %-95 % and 10 %-90 % span (Högner, Voigt, and Nasuf, 2016). In this case, it was found that only the latter span range provided reliable and accurate results for all scans. The fillets themselves are not intersected anymore after about 8 % and 91 % span for the bottom and top fillet respectively. Therefore, the range from 10 %-90 % span was selected and used. The bumps at 5 % and 95 % span in Fig. F.2a are not present at these new span heights and can be avoided. The extracted one-to-one B2P points in Fig. F.3 illustrate the remaining extent of the applicable range on the blade.

For sake of completeness, Fig. F.4 shows the hub and shroud curves used for both BCL and B2P. To create the curves, parts of the curves on the blade were extracted

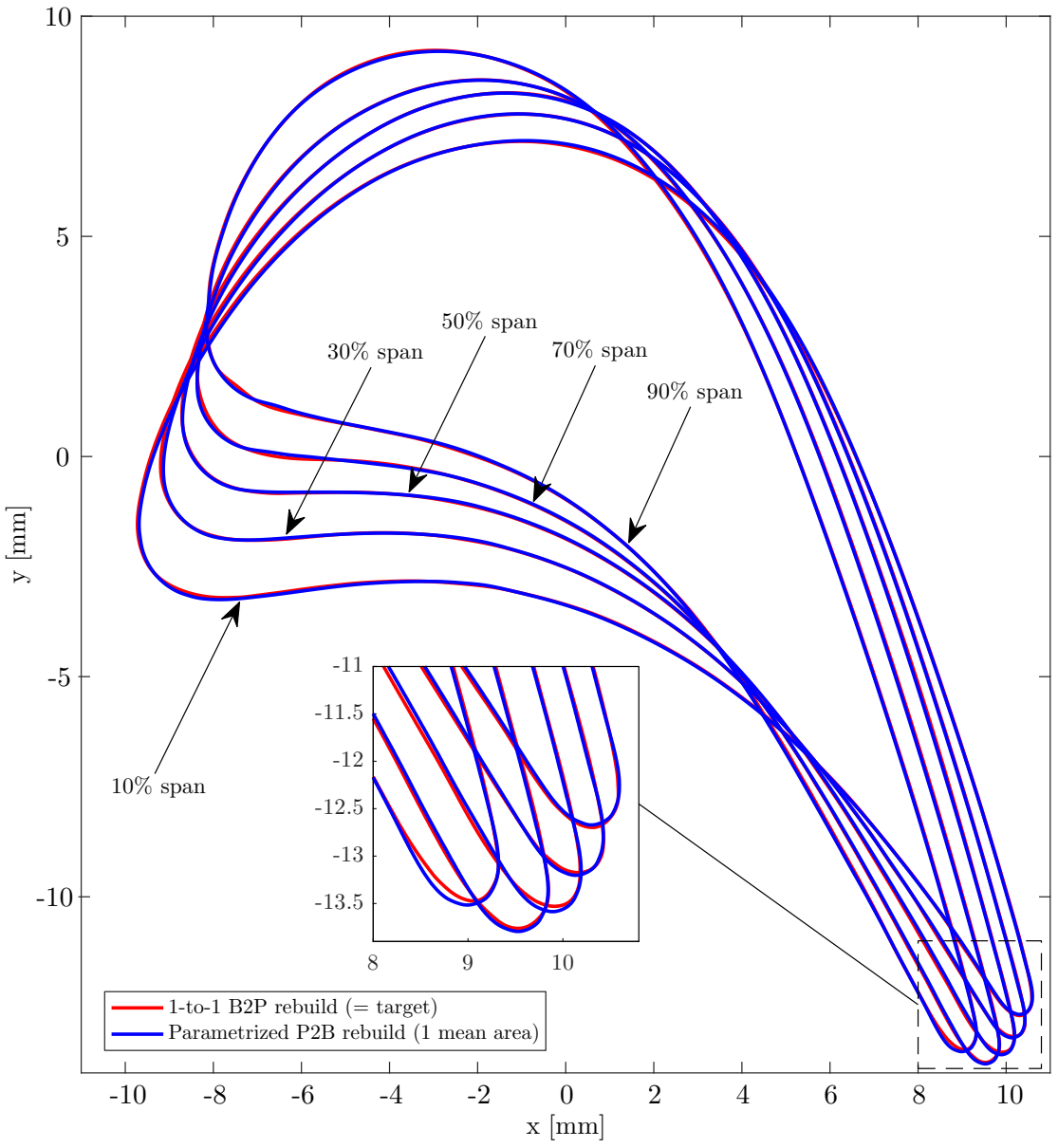

Figure F.1: Illustration of profile deviations due to P2B's parametrization

right from the CAD model. These curves were combined with points from the original `Blade_Definition` file for the areas to the left and right of the shroud. Figure. F.4a depicts the original curves used, but after consultation with RRD the setup in Fig. F.4b was recommended and was used instead. Essentially, the removed kink near the front of the shroud helps to even out the estimated airfoil sections.

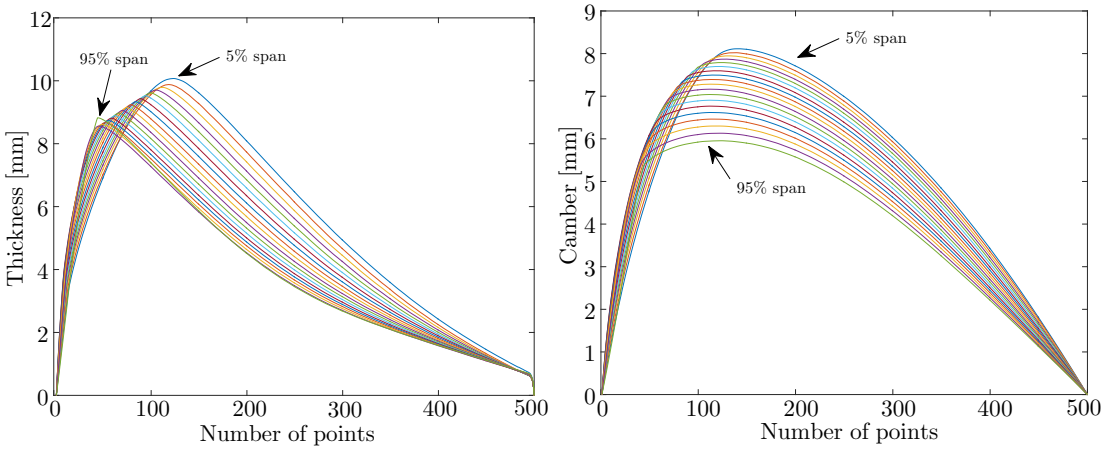

(a) CAD thickness (b) CAD camber

Figure F.2: Thickness and camber distributions of CAD model between 5% and 95% span

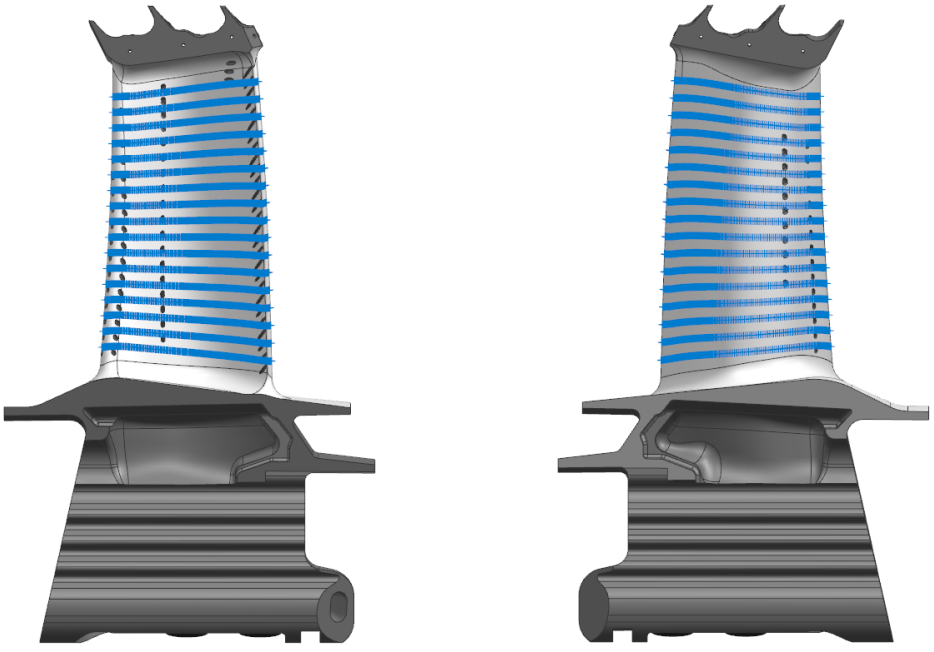

(a) Left side (b) Right side

Figure F.3: Extent of applicable range for B2P from 10 % to 90 % span

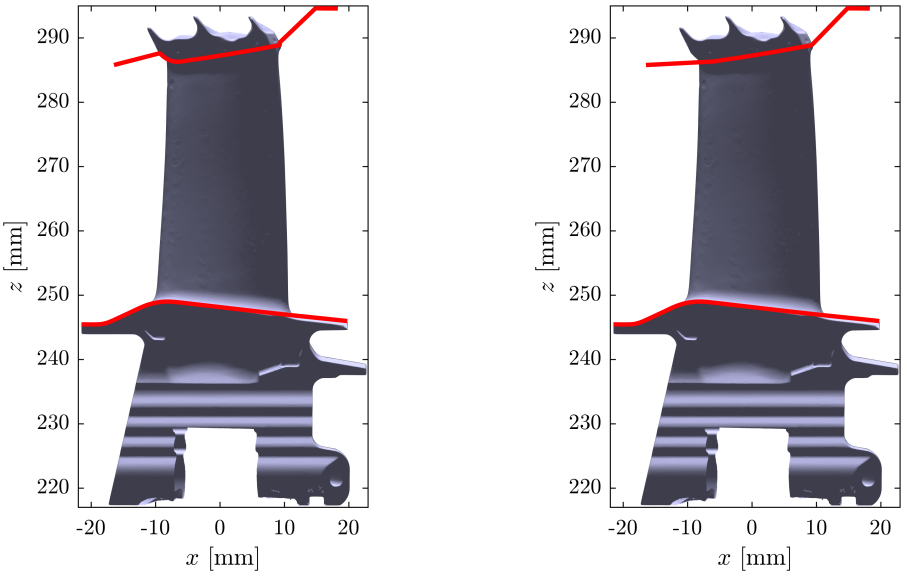

(a) Original hub and shroud curves for BCL and B2P overlayed over a scanned blade

(b) New hub and shroud curves for BCL and B2P overlayed over a scanned blade

Figure F.4: Hub and shroud curves for BCL and B2P

Appendix G

CAD and GOM Scan Comparisons

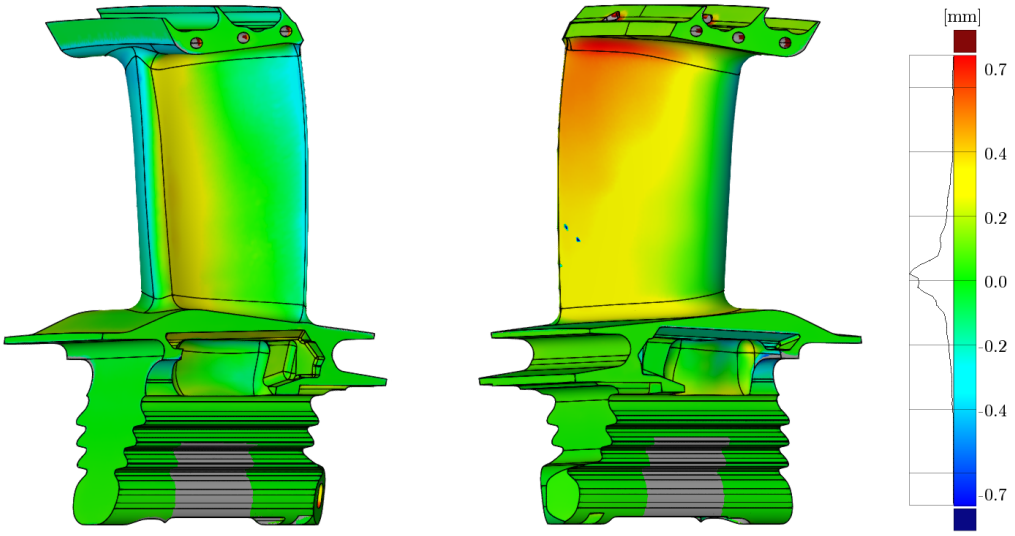

(a) Pressure side (b) Suction side

Figure G.1: Comparison of nominal CAD geometry and GOM scan #1 (cleaned)

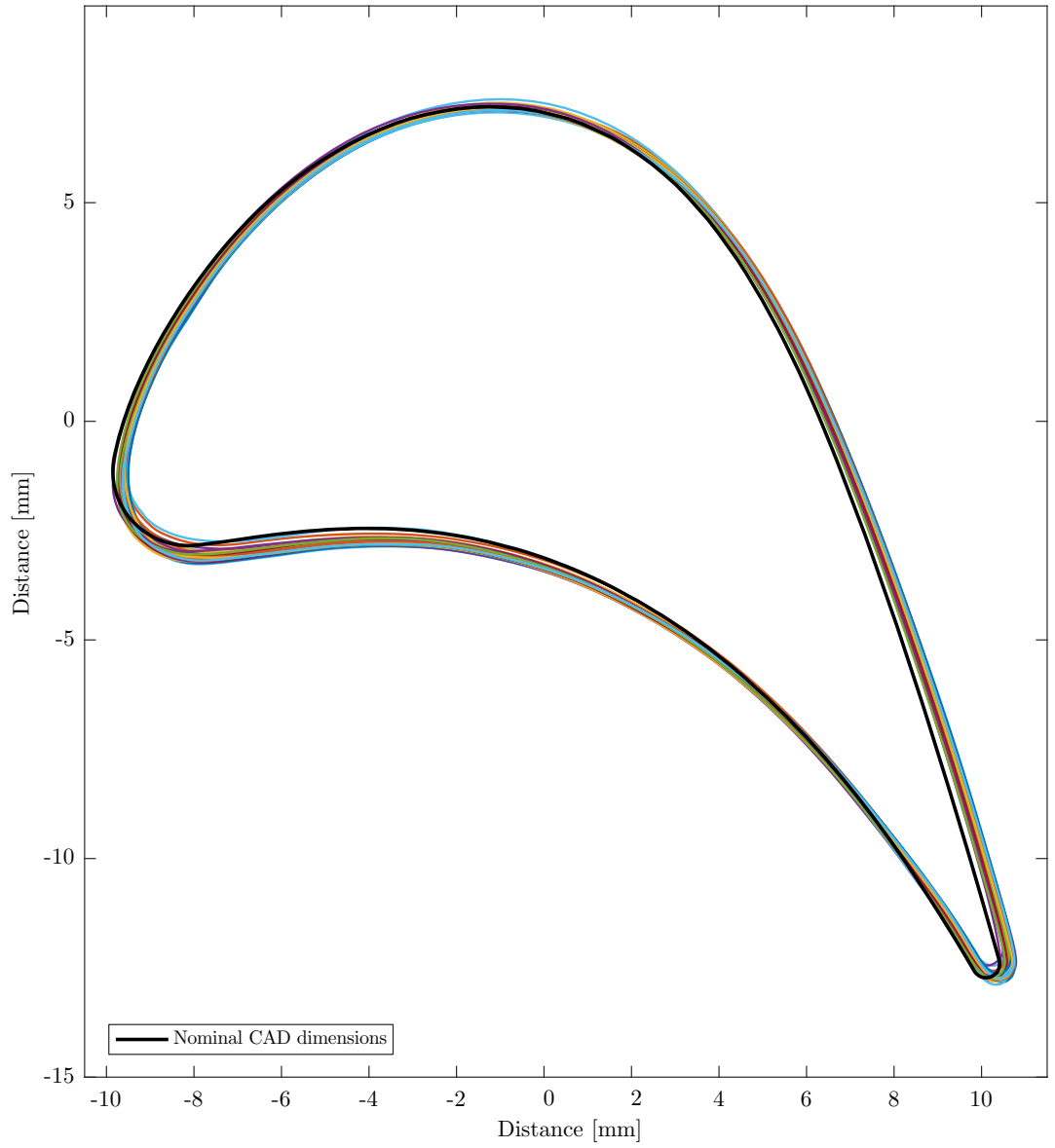

(a) Extracted airfoil profiles

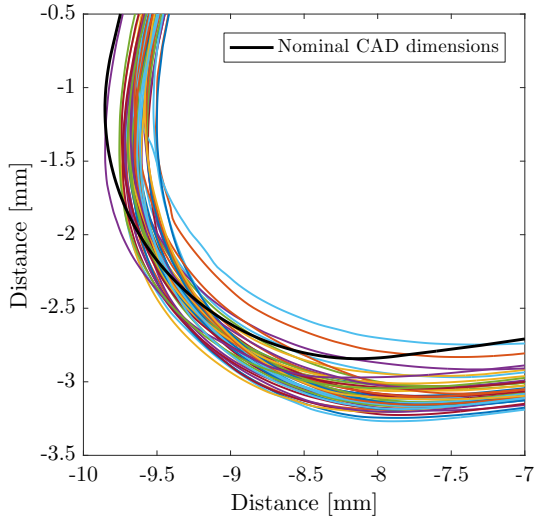

(b) Leading edge in detail

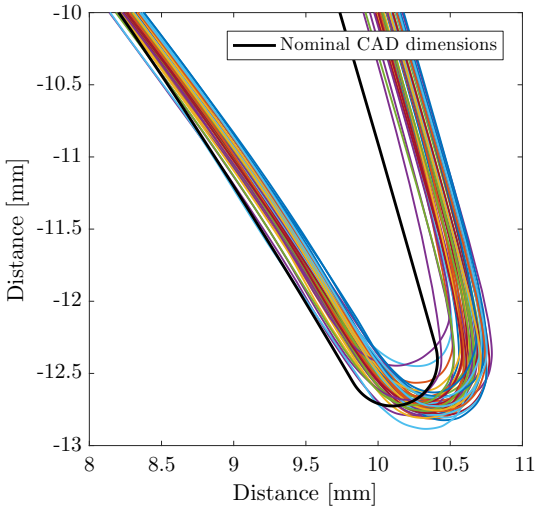

(c) Trailing edge in detail

Figure G.2: Airfoil deviations of all used blades at 10% span

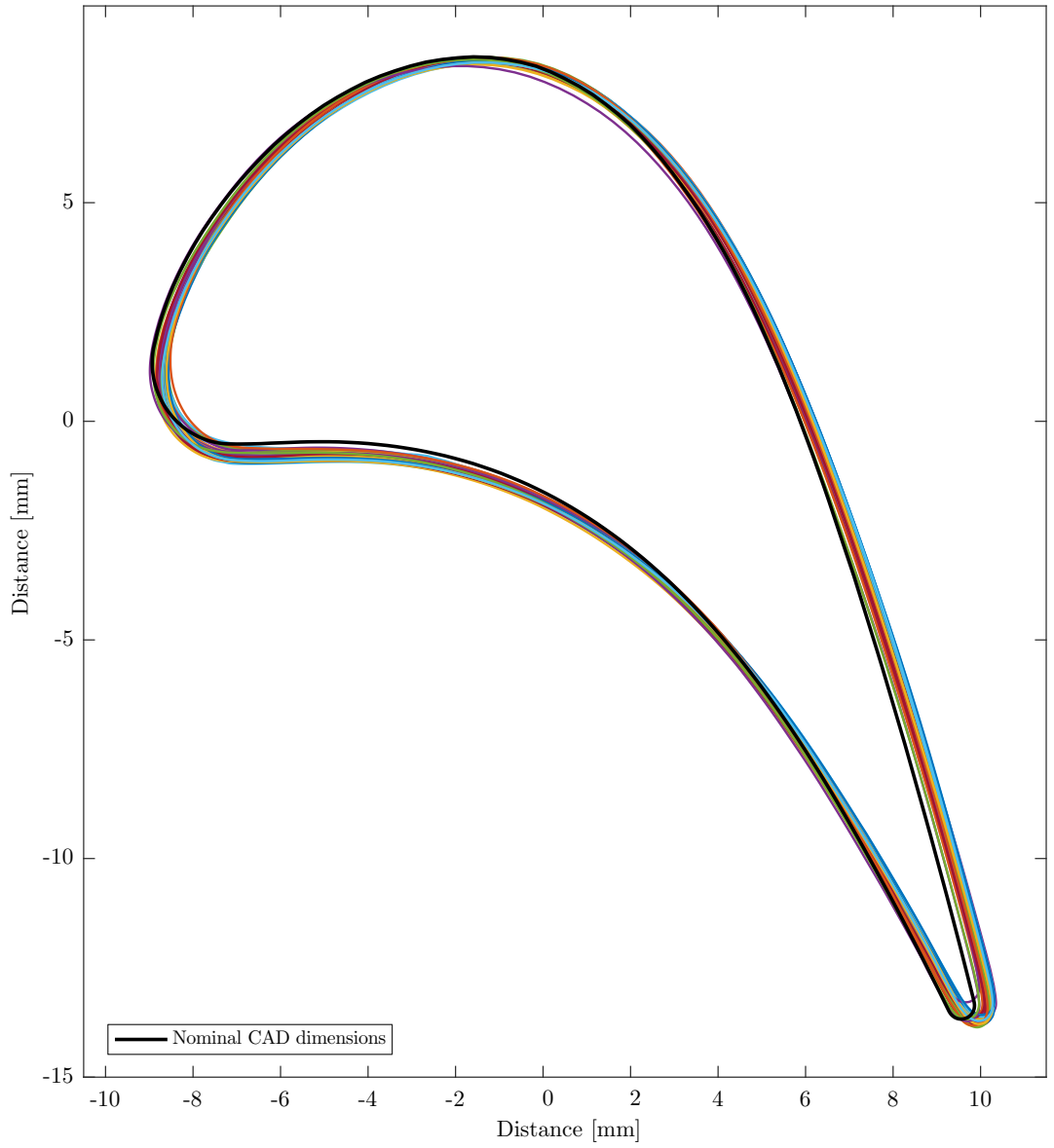

(a) Extracted airfoil profiles

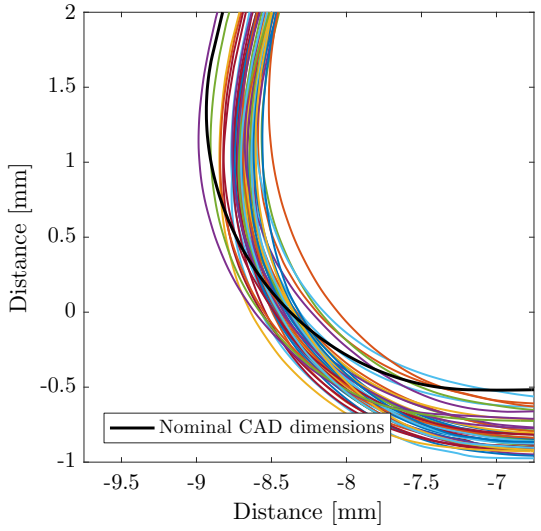

(b) Leading edge in detail

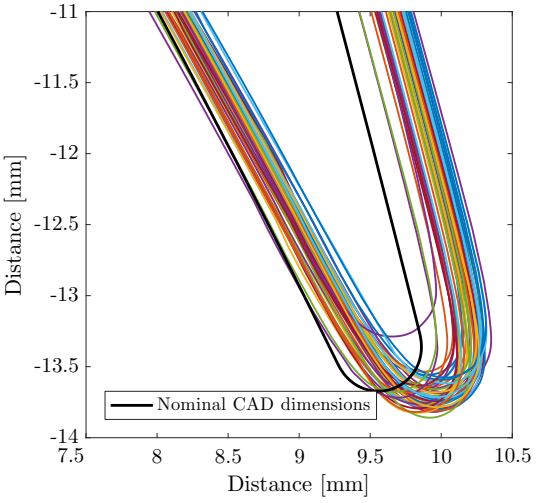

(c) Trailing edge in detail

Figure G.3: Airfoil deviations of all used blades at 50% span

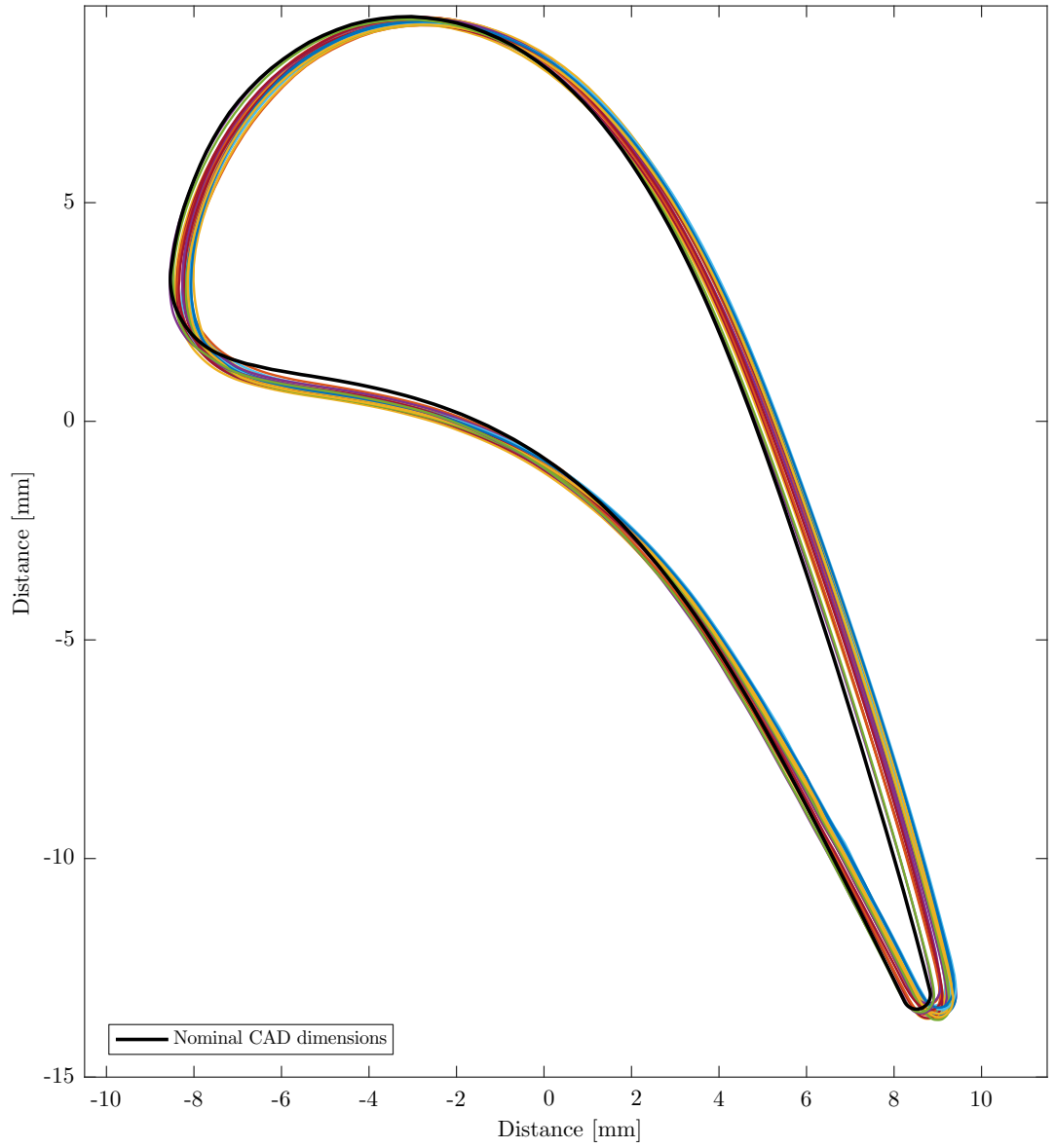

(a) Extracted airfoil profiles

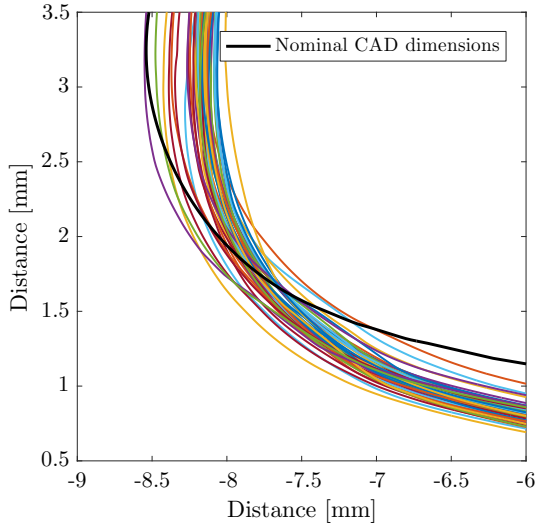

(b) Leading edge in detail

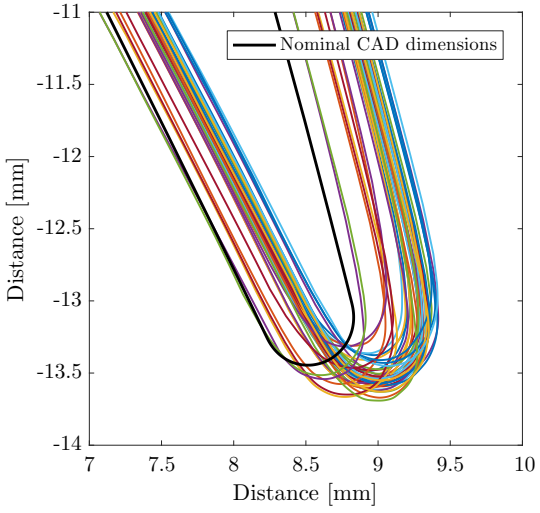

(c) Trailing edge in detail

Figure G.4: Airfoil deviations of all used blades at 90% span

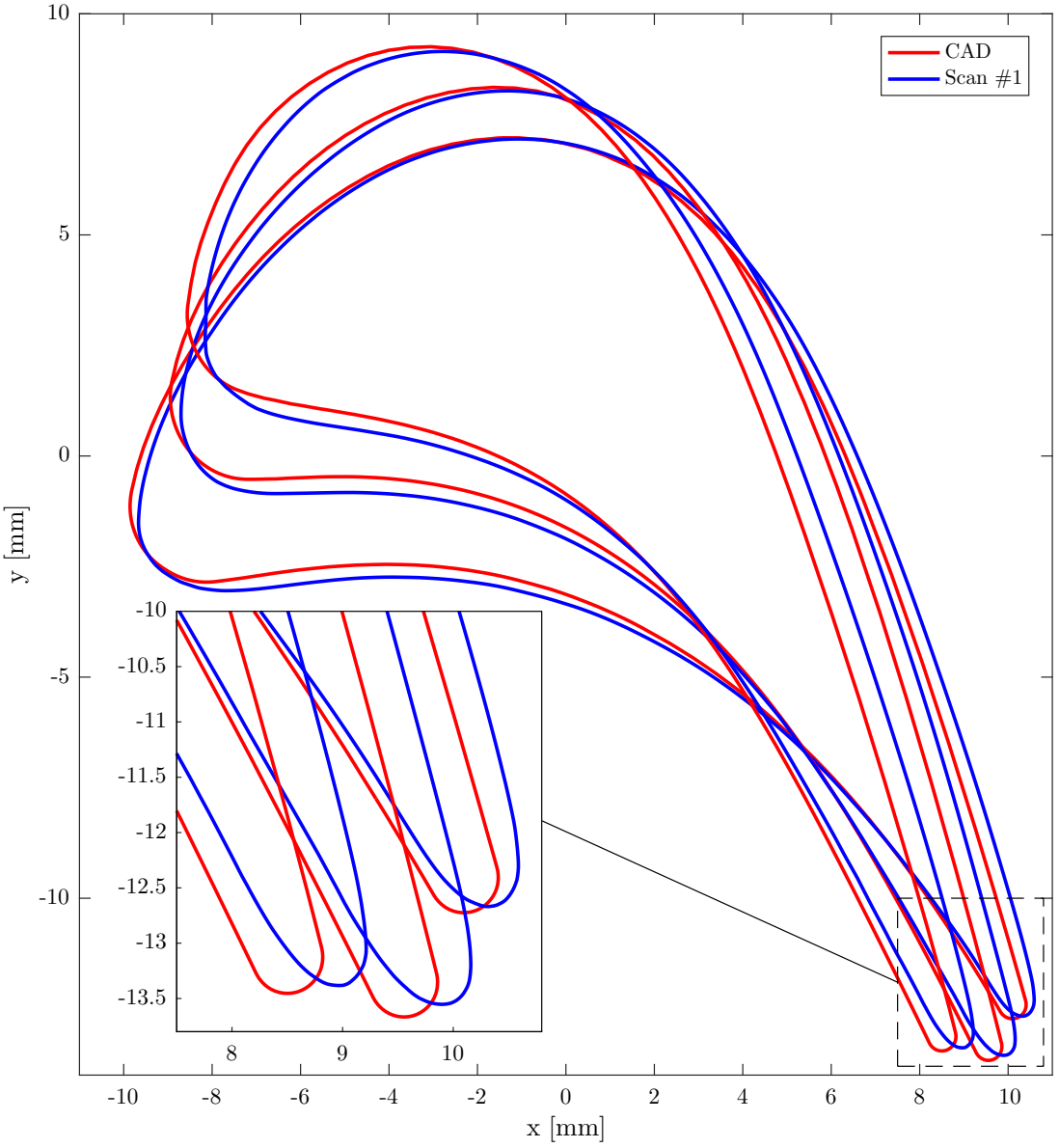

Figure G.5: Comparison of CAD model and blade #1 at 10%, 50% and 90% span

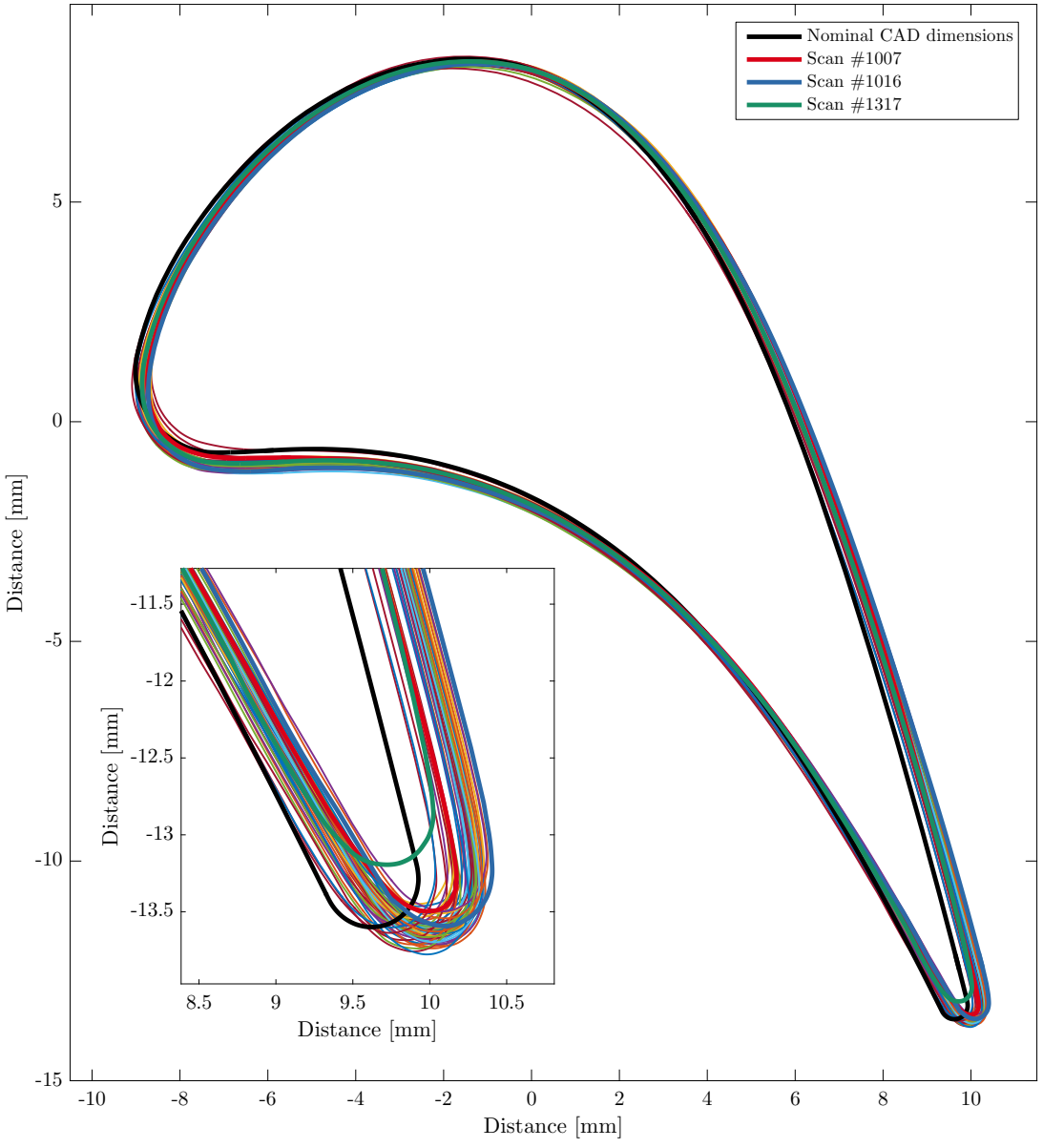

Figure G.6: Selected realizations at 50% span

Appendix H

Comparison with HolisTurb Project

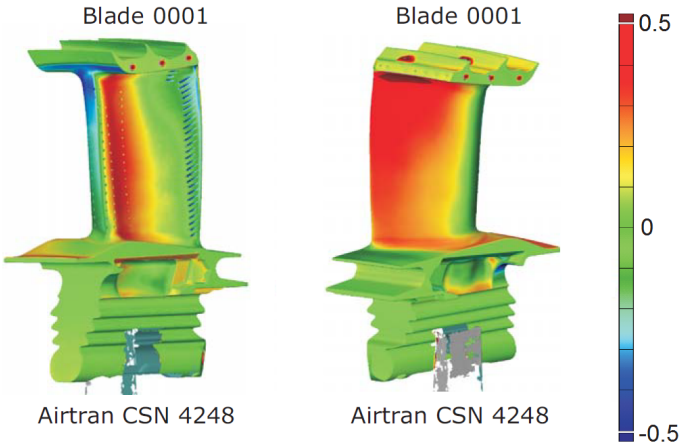

(a) Original differences reproduced from the report by Heinze (2013)

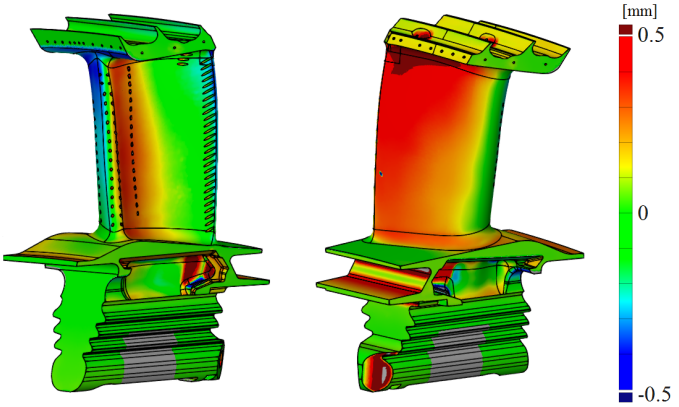

(b) Results in this study. Note that some differences are due to the fact that Heinze (2013) used a non-standard colorbar and the reproduced one does not exactly match the original.

Figure H.1: Results comparison with previous project HolisTurb and alignment sanity check

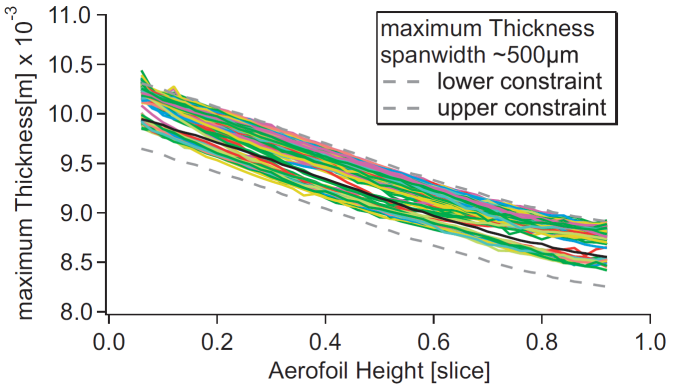

(a) Original plot reproduced from the report by Heinze (2013).

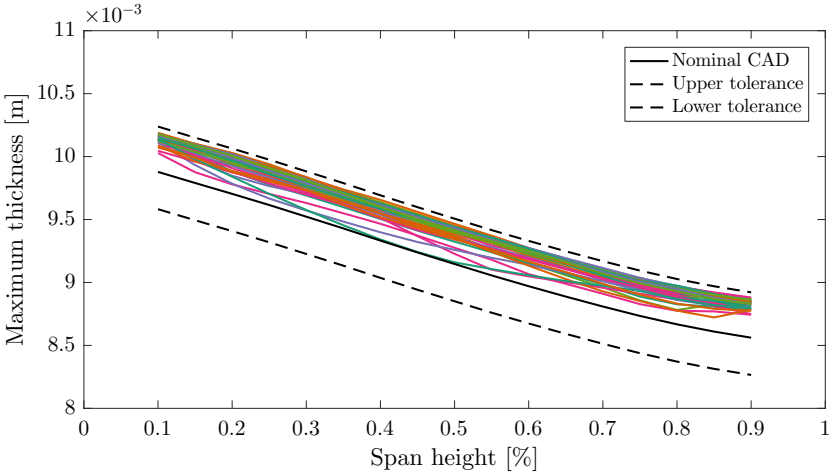

(b) Results in this study with the provided *used* scans. The spanwidth is ~1.86 mm (17 B2P sections).

Figure H.2: Comparison of maximum thickness parameter behaviour with previous results from project HolisTurb. B2P's maximum thickness parameter is plotted along the blade height for each scan and the CAD model. The manufacturing tolerance limits are also depicted. In the previous project, *used* blades were found to lie in the upper and *new* blades in the lower tolerance range (Heinze, 2013). As expected, the results in Fig. H.2b confirm that the scan sample of "used", low-cycle blades used in this project also lies in the upper range. The tolerance limits are not violated in either figure.

Appendix I

Detailed Trailing Edge Film Cooling Hole Variations

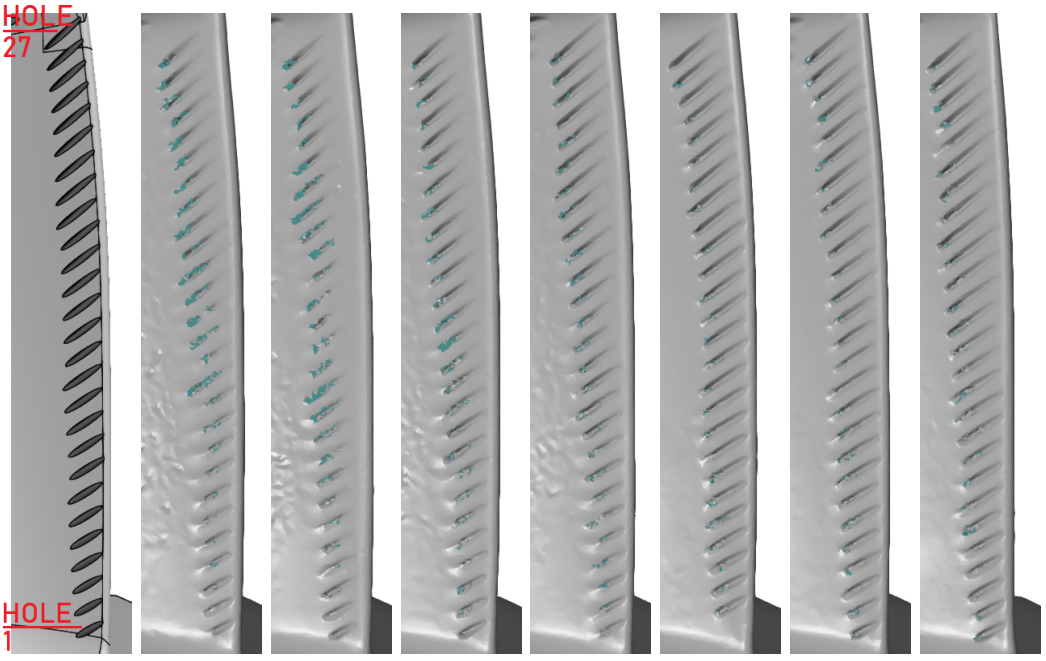

(a) Nominal CAD | (b) Scan #1016 | (c) Scan #1019 | (d) Scan #1028 | (e) Scan #1034 | (f) Scan #1310 | (g) Scan #1315 | (h) Scan #1317

Figure I.1: Illustration of TE FC hole variations for selected blades with original scan STL files

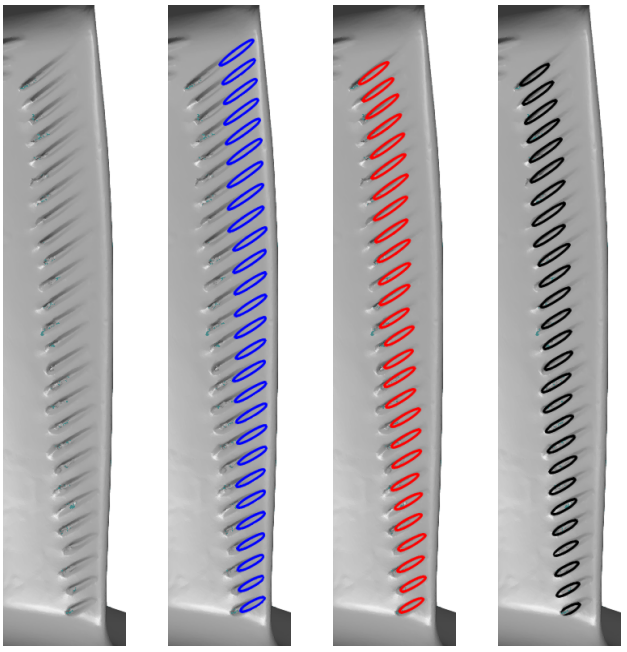

(a) Scan #1322

(b) Projected UV-mapped *nominal* TE holes (—)

(c) Projected UV-mapped manufactured TE holes (—)

(d) Projected TE holes from virtual manufacture workflow (—)

Figure I.2: Comparison of FC hole variation modeling strategies: UV-coordinates vs. virtual manufacture

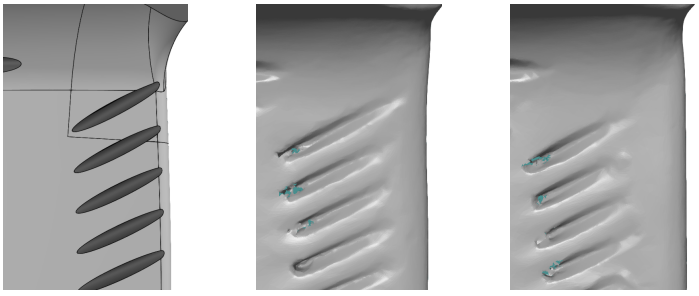

(a) Nominal CAD

(b) Scan #1001

(c) Scan #1024

Figure I.3: Comparison of selected top TE cooling hole position and length variations in detail

Appendix J

List of Blade Scans

Table J.1: List of 69 *used*, *low-cycle* GOM turbine blade scans provided by Rolls-Royce Deutschland. All blades were scanned as part of the Holistic Turbine project "HolisTurb" (Heinze, 2013) at Dresden University of Technology's Chair for Turbomachinery and Flight Propulsion.

Original number	`.stl` file name	ESN	Operator	CSN	S/N
1	1001	13150	AirTran	4248	058121806H
2	1002	13150	AirTran	4248	057832106H
3	1003	13150	AirTran	4248	057840412H
4	1004	13150	AirTran	4248	057831503H
5	1005	13150	AirTran	4248	057703909H
6	1006	13150	AirTran	4248	058053005H
7	1007	13150	AirTran	4248	058052803H
8	1008	13150	AirTran	4248	057840411H
9	1009	13150	AirTran	4248	057831708H
10	1010	13150	AirTran	4248	058052807H
11	1011	13150	AirTran	4248	057833103H
12	1012	13150	AirTran	4248	058052908H
13	1013	13150	AirTran	4248	057775303H
14	1014	13150	AirTran	4248	058052207H
15	1015	13150	AirTran	4248	057832110H
16	1016	13150	AirTran	4248	057832905H
17	1017	13150	AirTran	4248	057705012H
18	1018	13150	AirTran	4248	058052402H
19	1019	13150	AirTran	4248	058052909H
20	1020	13150	AirTran	4248	058121401H
21	1021	13150	AirTran	4248	057831604H
22	1022	13150	AirTran	4248	058121801H
23	1023	13150	AirTran	4248	057706003H
24	1024	13150	AirTran	4248	058052401H
25	1025	13150	AirTran	4248	058052210H
26	1026	13150	AirTran	4248	057831910H
27	1027	13150	AirTran	4248	058052205H
28	1028	13150	AirTran	4248	057997105H
29	1029	13150	AirTran	4248	057997205H
30	1030	13150	AirTran	4248	058121704H

Continued on next page

Table J.1 – continued from previous page

Original number	`.stl` file name	ESN	Operator	CSN	S/N
31	1031	13150	AirTran	4248	057775012H
32	1032	13150	AirTran	4248	057763105H
33	1033	13150	AirTran	4248	057704706H
34	1034	13150	AirTran	4248	057705503H
35	1035	13150	AirTran	4248	057832705H
36	1036	13150	AirTran	4248	057840511H
37	1037	13150	AirTran	4248	058052206H
297	1297	13279	Hawaiian	3432	71026910
298	1298	13279	Hawaiian	3432	103729806
299	1299	13279	Hawaiian	3432	103572607
300	1300	13279	Hawaiian	3432	59489208
301	1301	13279	Hawaiian	3432	59910109
302	1302	13279	Hawaiian	3432	101806803
303	1303	13279	Hawaiian	3432	59388512
304	1304	13279	Hawaiian	3432	59721210
305	1305	13279	Hawaiian	3432	71026507
306	1306	13279	Hawaiian	3432	103836804
307	1307	13279	Hawaiian	3432	71026608
308	1308	13279	Hawaiian	3432	59386912
309	1309	13279	Hawaiian	3432	71026906
310	1310	13279	Hawaiian	3432	71027211
311	1311	13279	Hawaiian	3432	59908803
312	1312	13279	Hawaiian	3432	59908708
313	1313	13279	Hawaiian	3432	103572712
314	1314	13279	Hawaiian	3432	58759707
315	1315	13279	Hawaiian	3432	104535001
316	1316	13279	Hawaiian	3432	59108412
317	1317	13279	Hawaiian	3432	59570408
318	1318	13279	Hawaiian	3432	103655705
319	1319	13279	Hawaiian	3432	103852805
320	1320	13279	Hawaiian	3432	71027104
321	1321	13279	Hawaiian	3432	59210704
322	1322	13279	Hawaiian	3432	71027106
323	1323	13279	Hawaiian	3432	71026504
324	1324	13279	Hawaiian	3432	103819008
325	1325	13279	Hawaiian	3432	59386910
326	1326	13279	Hawaiian	3432	101265501
327	1327	13279	Hawaiian	3432	103655512
328	1328	13279	Hawaiian	3432	71026601

Appendix K

Inlet Total Pressure Increase

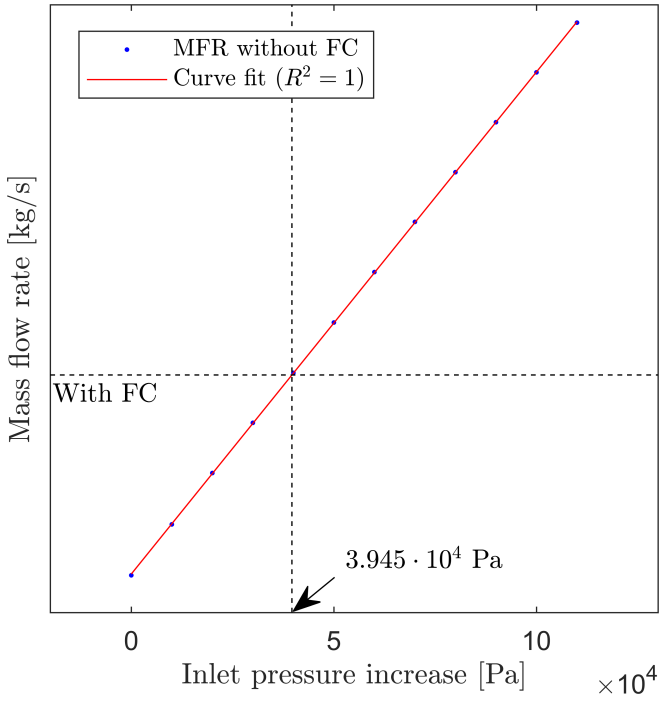

Figure K.1: Inlet total pressure increase

Appendix L

HYDRA Monitor File Setup

A HYDRA monitor file for a single turbine rotor has to be specified manually.

Listing L.1: Turbine blade efficiency monitor code snippet in `input.hyd`

```
1  file("mon_H01R_EXIT_turb_stage_eff_mass.dat") = {grplbl="H01R/EXIT";
       type=turb_stage_eff; save=1; average=mass; matlbl="H01R/INLET";
       sec_inlets=user; sec_exits=user; fc_zones=user; torq_walls=user;
       mix_planes=user;
2  in_grp=("H01R/USCAVSHR01", "H01R/USCAVH01");
3  ex_grp=();
4  fc_grp=("H01R");
5  wl_grp=("H01R/MERGEOGV", "H01R/MERGEHUB", "H01R/MERGECAS",
       "H01R/MERGECS2");
6  mp_grp=("H01R/INLET"); }
```

Bibliography

Acharya, S., M. Tyagi, and A. Hoda (2001). "Flow and heat transfer predictions for film cooling". In: *Annals of the New York Academy of Sciences* 934.1, pp. 110–125. DOI: 10.1111/j.1749-6632.2001.tb05846.x.

Ahlfeld, R., F. Montomoli, M. Carnevale, and S. Salvadori (2018). "Autonomous uncertainty quantification for discontinuous models using multivariate Padé approximations". In: *Journal of Turbomachinery* 140.4, p. 041004. DOI: 10.1115/1.4038826.

Ahn, J., M. Schobeiri, J.-C. Han, and H.-K. Moon (2006). "Film cooling effectiveness on the leading edge region of a rotating turbine blade with two rows of film cooling holes using pressure sensitive paint". In: *Journal of Heat Transfer* 128.9, pp. 879–888. DOI: 10.1115/1.2241945.

Ames, F. E. and R. J. Moffat (1990). "Effects of simulated combustor turbulence on boundary layer heat transfer". In: *Heat Transfer in Turbulent Flow (A93-54620 24-34)*, pp. 11–17. URL: http://adsabs.harvard.edu/abs/1990httf.rept...11A.

Anders, J. M., J. Haarmeyer, and H. Heukenkamp (1999). *A parametric blade design system (Part I + II)*. BMW Rolls-Royce GmbH. URL: http://www.atech.de/wp-content/uploads/2014/02/vki.pdf.

Andrei, L., L. Innocenti, A. Andreini, B. Facchini, and L. Winchler (2017). "Film cooling modeling for gas turbine nozzles and blades: Validation and application". In: 139.1, p. 011004. DOI: 10.1115/1.4034233.

Asmussen, S. and P. W. Glynn (2007). *Stochastic simulation: algorithms and analysis*. Vol. 57. Springer Science & Business Media, p. 265. DOI: 10.1007/978-0-387-69033-9.

Augusto, O. B., F. Bennis, and S. Caro (2012). "Multiobjective engineering design optimization problems: A sensitivity analysis approach". In: *Pesquisa Operacional* 32.3, pp. 575–596. DOI: 10.1590/S0101-74382012005000028.

Baldauf, S. and M. Scheurlen (1996). "CFD based sensitivity study of flow parameters for engine like film cooling conditions". In: *ASME 1996 International Gas Turbine*

and Aeroengine Congress and Exhibition. American Society of Mechanical Engineers, V004T09A037–V004T09A037. DOI: 10.1115/96-GT-310.

Beard, P. F., A. D. Smith, and T. Povey (2014). "Effect of combustor swirl on transonic high pressure turbine efficiency". In: *Journal of Turbomachinery* 136.1, p. 011002. DOI: 10.1115/1.4024841.

Bestle, D., P. M. Flassig, and A. K. Dutta (2011). "Robust design of compressor blades in the presence of manufacturing noise". In: *Proceedings of the 9th European conference on turbomachinery, fluid dynamics and thermodynamics*. Ed. by M. Sen, G. Bois, M. Manna, and T. Arts. Vol. 1. Florence, Italy: European Turbomachinery Society - Euroturbo, pp. 1303–1314. URL: https://opus4.kobv.de/opus4-UBICO/frontdoor/index/index/docId/7198.

Bogard, D. G. and K. A. Thole (2006). "Gas turbine film cooling". In: *Journal of Propulsion and Power* 22.2, pp. 249–270. DOI: 10.2514/1.18034.

Bohn, D. and R. Krewinkel (2006). "The effects of unintentional deviations due to manufacturing of cooling holes and operation on transpiration cooling efficiency". In: *ASME Turbo Expo 2006: Power for Land, Sea, and Air*. American Society of Mechanical Engineers, pp. 689–699. DOI: 10.1115/GT2006-90856.

Botev, Z. I., J. F. Grotowski, and D. P. Kroese (2010). "Kernel density estimation via diffusion". In: *The Annals of Statistics* 38.5, pp. 2916–2957. DOI: 10.1214/10-AOS799.

Bräunling, W. J. G. (2009). *Flugzeugtriebwerke: Grundlagen, Aero-Thermodynamik, ideale und reale Kreisprozesse, Thermische Turbomaschinen, Komponenten, Emissionen und Systeme*. Springer-Verlag Berlin Heidelberg. DOI: 10.1007/978-3-540-76370-3.

Brown, J. M., J. Slater, and R. V. Grandhi (2003). "Probabilistic analysis of geometric uncertainty effects on blade modal response". In: *ASME Turbo Expo 2003, collocated with the 2003 International Joint Power Generation Conference*. American Society of Mechanical Engineers, pp. 247–255. DOI: 10.1115/GT2003-38557.

Brujic, D., I. Ainsworth, and M. Ristic (2011). "Fast and accurate NURBS fitting for reverse engineering". In: *The International Journal of Advanced Manufacturing Technology* 54.5-8, pp. 691–700. DOI: 10.1007/s00170-010-2947-1.

Brundage, A. L., M. W. Plesniak, P. B. Lawless, and S. Ramadhyani (2007). "Experimental investigation of airfoil trailing edge heat transfer and aerodynamic losses". In: *Experimental Thermal and Fluid Science* 31.3, pp. 249–260. DOI: 10.1016/j.expthermflusci.2006.04.004.

Bunker, R. S. (2005). "A review of shaped hole turbine film-cooling technology". In: *Journal of Heat Transfer* 127.4, pp. 441–453. DOI: 10.1115/1.1860562.

Bunker, R. S. (2009). "The effects of manufacturing tolerances on gas turbine cooling". In: *Journal of Turbomachinery* 131.4, p. 041018. DOI: 10.1115/1.3072494.

Burdet, A., R. S. Abhari, and M. G. Rose (2007). "Modeling of film cooling - Part II: Model for use in three-dimensional computational fluid dynamics". In: *Journal of Turbomachinery* 129.2, pp. 221–231. DOI: 10.1115/1.2437219.

Chantrasmi, T., A. Doostan, and G. Iaccarino (2009). "Padé-Legendre approximants for uncertainty analysis with discontinuous response surfaces". In: *Journal of Computational Physics* 228.19, pp. 7159–7180. DOI: 10.1016/j.jcp.2009.06.024.

Crawford, M. E., W. M. Kays, and R. J. Moffat (1980). "Full-coverage film cooling on flat, isothermal surfaces: Data and predictions". In: *NASA STI/Recon Technical Report N* 80. URL: https://ntrs.nasa.gov/archive/nasa/casi.ntrs.nasa.gov/19800007104.pdf.

Cruz, C. A. (2008). "Experimental and numerical characterization of turbulent slot film cooling". PhD thesis. University of Maryland. DOI: 1903/8145.

Cunha, F. J. and M. K. Chyu (2006). "Trailing-edge cooling for gas turbines". In: *Journal of Propulsion and Power* 22.2, pp. 286–300. DOI: 10.2514/1.20898.

Dahlander, P., H. Abrahamsson, H. Mårtensson, and U. Håll (1998). "Numerical simulation of a film cooled nozzle guide vane using an injection model". In: *ASME 1998 International Gas Turbine and Aeroengine Congress and Exhibition*. American Society of Mechanical Engineers, V004T09A078–V004T09A078. DOI: 10.1115/98-GT-439.

Das, I. (2000). "Robustness optimization for constrained nonlinear programming problems". In: *Engineering Optimization+ A35* 32.5, pp. 585–618. DOI: 10.1080/03052150008941314.

Day, C. (1997). "Aerodynamics of an annular film-cooled turbine cascade". PhD thesis. University of Oxford.

Deb, K., A. Pratap, S. Agarwal, and Meyarivan (2002). "A fast and elitist multiobjective genetic algorithm: NSGA-II". In: *IEEE Transactions on Evolutionary Computation* 6.2, pp. 182–197. DOI: 10.11094235.996017.

Dellino, G., J. P. C. Kleijnen, C. Meloni, and C. Meloni (2015). "Uncertainty management in simulation-optimization of complex systems: Algorithms and applications". In: New York: Springer US. Chap. Metamodel-Based Robust Simulation-Optimization: An Overview, pp. 27–54. DOI: 10.1007/978-1-4899-7547-8_2.

Dow, E. A. and Q. Wang (2015). "The implications of tolerance optimization on compressor blade design". In: *Journal of Turbomachinery* 137.10, p. 101008. DOI: 10.1115/1.4030791.

Du, X., A. Sudjianto, and W. Chen (2004). "An integrated framework for optimization under uncertainty using inverse reliability strategy". In: *Journal of Mechanical Design* 126.4, pp. 562–570. DOI: 10.1115/1.1759358.

Duffner, J. D. (2008). "The effects of manufacturing variability on turbine vane performance". PhD thesis. Massachusetts Institute of Technology. DOI: 1721.1/57599.

Dyn, N., K. Hormann, S.-J. Kim, and D. Levin (2001). "Optimizing 3D triangulations using discrete curvature analysis". In: *Mathematical Methods for Curves and Surfaces* 38.8, pp. 135–146. URL: http://dl.acm.org/citation.cfm?id=570828.570841.

El Ayoubi, C. (2014). "Three-dimensional aero-thermal optimization of film cooling in a high pressure turbine". PhD thesis. Concordia University. URL: https://spectrum.library.concordia.ca/978687/.

Elsayed, A. M., F. M. Owis, and M. M. Abdel Rahman (2013). "Film cooling optimization using numerical computation of the compressible viscous flow equations and simplex algorithm". In: *International Journal of Aerospace Engineering* 2013. DOI: 10.1155/2013/859465.

Elsayed, A. M., F. M. Owis, and M. M. A. Rahman (2014). "Numerical computation and optimization of turbine blade film cooling". In: *Advances in Mechanical Engineering* 6, p. 528031. DOI: 10.1155/2014/528031.

Forrester, A., A. Sobester, and A. J. Keane (2008). *Engineering design via surrogate modelling: A practical guide*. John Wiley & Sons, pp. 51–56, 196. DOI: 10.1002/9780470770801.

Ganesan, V. (2010). *Gas Turbines*. 3rd ed. New Delhi, India: Tata McGraw-Hill Education.

Garzon, V. E. and D. L. Darmofal (2003). "Impact of geometric variability on axial compressor performance". In: *ASME Turbo Expo 2003, collocated with the 2003 International Joint Power Generation Conference*. American Society of Mechanical Engineers, pp. 1199–1213. DOI: 10.1115/1.1622715.

Gatski, T. B. and J.-P. Bonnet (2013). *Compressibility, turbulence and high speed flow*. Oxford, UK: Academic Press, pp. 21–59. DOI: 10.1016/B978-0-12-397027-5.00009-5.

Gentle, J. E. (2006). *Random number generation and Monte Carlo methods*. 2nd ed. Springer Science & Business Media. DOI: 10.1007/b97336.

Gerstner, T. and M. Griebel (2003). "Dimension-adaptive tensor-product quadrature". In: *Computing* 71.1, pp. 65–87. DOI: 10.1007/s00607-003-0015-5.

Ginibre, P., M. Lefebvre, and N. Liamis (2001). "Numerical investigation of heat transfer on film-cooled turbine blades". In: *Annals of the New York Academy of Sciences* 934.1, pp. 377–384. DOI: 10.1111/j.1749-6632.2001.tb05873.x.

Goldstein, R., E. Eckert, and F. Burggraf (1974). "Effects of hole geometry and density on three-dimensional film cooling". In: *International Journal of Heat and Mass Transfer* 17.5, pp. 595–607. DOI: 10.1016/0017-9310(74)90007-6.

Gräsel, J., A. Keskin, M. Swoboda, H. Przewozny, and A. Saxer (2004). "A full parametric model for turbomachinery blade design and optimisation". In: *ASME 2004 International Design Engineering Technical Conferences and Computers and Information in Engineering Conference*. American Society of Mechanical Engineers, pp. 907–914. DOI: 10.1115/DETC2004-57467.

Gritsch, M., A. Schulz, and S. Wittig (2000). "Film-cooling holes with expanded exits: Near-hole heat transfer coefficients". In: *International Journal of Heat and Fluid Flow* 21.2, pp. 146–155. DOI: 10.1016/S0142-727X(99)00076-4.

Han, J.-C. (2004). "Recent studies in turbine blade cooling". In: *International Journal of Rotating Machinery* 10.6, pp. 443–457. DOI: 10.1155/S1023621X04000442.

Han, J.-C., S. Dutta, and S. Ekkad (2012). *Gas turbine heat transfer and cooling technology*. 2nd ed. Boca Raton, USA: CRC Press. DOI: 10.1201/b13616.

Heinze, K. (2013). *ISM Bericht 2013 - HolisTurb - 2009-2012 - Abschlussbericht Teilprojekt 2 - Realgeometrieeffekte von Hochdruckturbinenschaufeln*. Tech. rep. Institut für Strömungsmechanik, Technische Universität Dresden (Germany).

Heinze, K., M. Meyer, J. Scharfenstein, M. Voigt, and K. Vogeler (2014). "A parametric model for probabilistic analysis of turbine blades considering real geometric effects". In: *CEAS Aeronautical Journal* 5.1, pp. 41–51. DOI: 10.1007/s13272-013-0088-6.

Hendricks, E. S. (2016). "Meanline analysis of turbines with choked flow in the object-oriented turbomachinery analysis code". In: *54th AIAA Aerospace Sciences Meeting*, p. 0119. DOI: 10.2514/6.2016-0119.

Högner, L. (2016). *BladeCLeaner 1.3.0: User guide*. Technische Universität Dresden.

Högner, L., M. Voigt, K. Vogeler, M. Meyer, and C. Berridge (2015). "A curvature based algorithm for treatment of cooling holes in polygon meshes of turbine blades". In: *ASME Turbo Expo 2015: Turbine Technical Conference and Exposition*. American Society of Mechanical Engineers, V02BT39A025. DOI: 10.1115/GT2015-42841.

Högner, L., P. Voigt, and A. Nasuf (2016). *Blade2Parameter: Geometry reconstruction user guide*. Version 6.2.1. Technische Universität Dresden.

Högner, L., P. Voigt, A. Nasuf, M. Voigt, M. Meyer, F. Goenaga, C. Berridge, and K. Vogeler (2016). "Analysis of high pressure turbine nozzle guide vanes considering geometric variations". In: *ASME Turbo Expo 2016: Turbine Technical Conference and Exposition*. American Society of Mechanical Engineers, V02CT45A025. DOI: 10.1115/GT2016-57502.

Holtzhausen, S., S. Schreiber, C. Schone, R. Stelzer, K. Heinze, and A. Lange (2009). "Highly accurate automated 3D measuring and data conditioning for turbine and compressor blades". In: *ASME Turbo Expo 2009: Power for Land, Sea, and Air*. American Society of Mechanical Engineers, pp. 37–41. DOI: 10.1115/GT2009-59902.

Iman, R. L. and W.-J. Conover (1982). "A distribution-free approach to inducing rank correlation among input variables". In: *Communications in Statistics-Simulation and Computation* 11.3, pp. 311–334. DOI: 10.1080/03610918208812265.

Iooss, B. and P. Lematre (2015). "A review on global sensitivity analysis methods". In: *Uncertainty Management in Simulation-Optimization of Complex Systems*. Springer, pp. 101–122. DOI: 10.1007/978-1-4899-7547-8.

Javed, A., R. Pecnik, and J. P. van Buijtenen (2016). "Optimization of a centrifugal compressor impeller for robustness to manufacturing uncertainties". In: *Journal of Engineering for Gas Turbines and Power* 138.11, p. 112101. DOI: 10.1115/1.4033185.

Jin, R., X. Du, and W. Chen (2003). "The use of metamodeling techniques for optimization under uncertainty". In: *Structural and Multidisciplinary Optimization* 25.2, pp. 99–116. DOI: 10.1007/s00158-002-0277-0.

Johnson, J. J. (2012). "Genetic algorithm optimization of a film cooling array on a modern turbine inlet vane". PhD thesis. Air Force Institute of Technology. URL: http://www.dtic.mil/dtic/tr/fulltext/u2/a568602.pdf.

Johnson, J., P. King, J. Clark, R. Anthony, P. Koch, M. Ooten, E. Kasik, and R.-H. Ni (2011). "Three-dimensional film-cooled vane CFD simulations and preliminary comparison to experiments". In: *49th AIAA Aerospace Sciences Meeting including the New Horizons Forum and Aerospace Exposition*, p. 499. DOI: 10.2514/6.2011-499.

Jolliffe, I. (2002). *Principal component analysis*. Wiley Online Library. DOI: 10.1007/B98835.

Julier, S. J. and J. K. Uhlmann (1996). *A general method for approximating nonlinear transformations of probability distributions*. Tech. rep. Technical report, Robotics

Research Group, Department of Engineering Science, University of Oxford. URL: http://citeseerx.ist.psu.edu/viewdoc/summary?doi=10.1.1.46.6718.

Jurecka, F. (2007). *Robust design optimization based on metamodeling techniques*. Aachen, Germany: Shaker Verlag. URL: https://mediatum.ub.tum.de/doc/607314/446546.pdf.

Kalpakjian, S. (2013). *Manufacturing engineering and technology*. 7th ed. Singapore: Pearson Education.

Kamenik, J., D. J. J. Toal, A. J. Keane, L. Högner, M. Meyer, and S. Shahpar (2018). "Modeling and impact of high-pressure turbine blade trailing edge film cooling hole variations". In: *Journal of Turbomachinery*. Submitted.

Kamenik, J., I. Voutchkov, D. J. J. Toal, A. J. Keane, L. Högner, M. Meyer, and R. Bates (2018). "Robust turbine blade optimization in the face of real geometric variations". In: *Journal of Propulsion and Power*. In press. DOI: 10.2514/1.B37091.

Kampe, T. auf dem and S. Volker (2011). "Application of a CFD-based film cooling model to a gas turbine vane cascade with cylindrical and shaped hole endwall film cooling". In: *ASME 2011 Turbo Expo: Turbine Technical Conference and Exposition*. American Society of Mechanical Engineers, pp. 35–44. DOI: 10.1115/GT2011-45117.

Keane, A. J. (2009). "Comparison of several optimization strategies for robust turbine blade design". In: *Journal of Propulsion and Power* 25.5, pp. 1092–1099. DOI: 10.2514/1.38673.

Keane, A. J. (2012). "Co-kriging for robust design optimization". In: *AIAA Journal* 50.12, pp. 2351–2364. DOI: 10.2514/1.J051391.

Keane, A. J. and P. Nair (2005). *Computational approaches for aerospace design: The pursuit of excellence*. John Wiley & Sons, pp. 327–329. DOI: 10.1002/0470855487.

Kolmakova, D., O. Baturin, and G. Popov (2014). "Effect of manufacturing tolerances on the turbine blades". In: *ASME 2014 Gas Turbine India Conference*. American Society of Mechanical Engineers, V001T02A004–V001T02A004. DOI: doi.org/10.1115/GTINDIA2014-8253.

Krishnamoorthy, V. and S. P. Sukhatme (1989). "The effect of free-stream turbulence on gas turbine blade heat transfer". In: *Journal of Turbomachinery* 111.4, pp. 497–501. DOI: 10.1115/1.3262299.

Lad, B. and L. He (2013a). "An immersed mesh block (IMB) approach for conjugate heat transfer predictions". In: *ASME Turbo Expo 2013: Turbine Technical Conference and*

Exposition. American Society of Mechanical Engineers, V03BT11A007–V03BT11A007. DOI: 10.1115/GT2013-94383.

Lad, B. and L. He (2013b). "Use of an immersed mesh for high resolution modeling of film cooling flows". In: *Journal of Turbomachinery* 135.1, p. 011022. DOI: 10.1115/1.4006398.

Lakshminarayana, B. (1995). *Fluid dynamics and heat transfer of turbomachinery*. 1st ed. Wiley-Interscience. DOI: 10.1002/9780470172629.

Lamb, C. T. and D. L. Darmofal (2004). "Performance-based geometric tolerancing of compressor blades". In: *ASME Turbo Expo 2004: Power for Land, Sea, and Air*. American Society of Mechanical Engineers, pp. 203–210. DOI: 10.1115/GT2004-53592.

Lange, A., K. Vogeler, V. Gümmer, H. Schrapp, and C. Clemen (2009). "Introduction of a parameter based compressor blade model for considering measured geometry uncertainties in numerical simulation". In: *ASME Turbo Expo 2009: Power for Land, Sea, and Air*. American Society of Mechanical Engineers, pp. 1113–1123. DOI: 10.1115/GT2009-59937.

Lange, A., M. Voigt, K. Vogeler, and E. Johann (2012). "Principal component analysis on 3D scanned compressor blades for probabilistic CFD simulation". In: *53rd AIAA/ASME/ASCE/AHS/ASC Structures, Structural Dynamics and Materials Conference*. American Institute of Aeronautics and Astronautics, pp. 1–16. DOI: 10.2514/6.2012-1762.

Lange, A., M. Voigt, K. Vogeler, H. Schrapp, E. Johann, and V. Gümmer (2010). "Probabilistic CFD simulation of a high-pressure compressor stage taking manufacturing variability into account". In: *ASME Turbo Expo 2010: Power for Land, Sea, and Air*. American Society of Mechanical Engineers, pp. 617–628. DOI: 10.1115/GT2010-22484.

Lapworth, L. (2004). "Hydra-CFD: A framework for collaborative CFD development". In: *International Conference on Scientific and Engineering Computation (IC-SEC), Singapore, June*. Vol. 30. URL: https://www.researchgate.net/profile/Leigh_Lapworth/publication/316171819_HYDRA-CFD_A_Framework_for_Collaborative_CFD_Development/links/58f51082458515ff23b56169/HYDRA-CFD-A-Framework-for-Collaborative-CFD-Development.pdf.

Le Matre, O. P. and O. M. Knio (2010). *Spectral methods for uncertainty quantification*. 1st ed. Springer Netherlands. DOI: 10.1007/978-90-481-3520-2.

Lee, K.-D. and K.-Y. Kim (2010). "Shape optimization of a fan-shaped hole to enhance film-cooling effectiveness". In: *International Journal of Heat and Mass Transfer* 53.15, pp. 2996–3005. DOI: 10.1016/j.ijheatmasstransfer.2010.03.032.

Lee, K.-H. and G.-J. Park (2006). "A global robust optimization using kriging based approximation model". In: *JSME International Journal Series C Mechanical Systems, Machine Elements and Manufacturing* 49.3, pp. 779–788. DOI: 10.1299/jsmec.49.779.

Leer, B. van (1979). "Towards the ultimate conservative difference scheme. V. A second-order sequel to Godunov's method". In: *Journal of Computational Physics* 32.1, pp. 101–136. DOI: 10.1016/0021-9991(79)90145-1.

Li, Z. Y., X. T. Wei, Y. B. Guo, and M. P. Sealy (2015). "State-of-art, challenges, and outlook on manufacturing of cooling holes for turbine blades". In: *Machining Science and Technology* 19.3, pp. 361–399. DOI: 10.1080/10910344.2015.1051543.

Logan Jr, E. (2003). *Handbook of turbomachinery*. Boca Raton, USA: CRC Press. DOI: 10.1201/9780203911990.

Maffulli, R. and L. He (2017). "Impact of wall temperature on heat transfer coefficient and aerodynamics for three-dimensional turbine blade passage". In: *Journal of Thermal Science and Engineering Applications* 9.4, p. 041002. DOI: 10.1115/1.4036012.

Makki, Y. and G. Jakubowski (1986). "An experimental study of film cooling from diffused trapezoidal shaped holes". In: *4th Thermophysics and Heat Transfer Conference, Fluid Dynamics and Co-located Conferences*, p. 1326. DOI: 10.2514/6.1986-1326.

Martinelli, L. (1987). "Calculations of viscous flows with a multigrid method". PhD thesis. Princeton University. URL: https://www.osti.gov/biblio/7029684-calculations-viscous-flows-multigrid-method.

Mattia, P., C. M. Sergio, and G. M. Dimitrov (2007). "Comparative analysis of uncertainty propagation methods for robust engineering design". In: *Guidelines for a Decision Support Method Adapted to NPD Processes*, pp. 59–60. URL: https://www.designsociety.org/publication/25352/Comparative+Analysis+of+Uncertainty+Propagation+Methods+for+Robust+Engineering+Design.

Miettinen, K. (2012). *Nonlinear multiobjective optimization*. Vol. 12. Springer Science & Business Media. DOI: 10.1007/978-1-4615-5563-6.

Milli, A. and S. Shahpar (2012). "PADRAM: Parametric design and rapid meshing system for complex turbomachinery configurations". In: *ASME Turbo Expo 2012: Turbine*

Technical Conference and Exposition. American Society of Mechanical Engineers, pp. 2135–2148. DOI: 10.1115/GT2012-69030.

Modgil, G. A. (2013). "Design optimization and uncertainty quantification for aeromechanics forced response of a turbomachinery blade". PhD thesis. Purdue University. URL: https://docs.lib.purdue.edu/dissertations/AAI3592047/.

Moeckel, C. W., D. L. Darmofal, T. R. Kingston, and R. J. G. Norton (2007). "Toleranced designs of cooled turbine blades through probabilistic thermal analysis of manufacturing variability". In: *ASME Turbo Expo 2007: Power for Land, Sea, and Air*. American Society of Mechanical Engineers, pp. 1179–1191. DOI: 10.1115/GT2007-28009.

Moinier, P. and M. B. Giles (1998). "Preconditioned Euler and Navier-Stokes calculations on unstructured meshes". In: *Numerical Methods for Fluid Dynamics VI*. Ed. by M. J. Baines, pp. 417–424. URL: https://www.researchgate.net/profile/Pierre_Moinier/publication/2507830_Preconditioned_Euler_and_Navier-Stokes_Calculations_on_Unstructured_Meshes/links/54b794c30cf2bd04be33a798.pdf.

Moinier, P. (1999). "Algorithm developments for an unstructured viscous flow solver". PhD thesis. Oxford University. URL: http://people.maths.ox.ac.uk/gilesm/files/pierre_thesis.pdf.

Moinier, P., J.-D. Müller, and M. B. Giles (2002). "Edge-based multigrid and preconditioning for hybrid grids". In: *AIAA Journal* 40.10, pp. 1954–1960. DOI: 10.2514/2.1556.

Montis, M., R. Ciorciari, S. Salvadori, M. Carnevale, and R. Niehuis (2014). "Numerical prediction of cooling losses in a high-pressure gas turbine airfoil". In: *Proceedings of the Institution of Mechanical Engineers, Part A: Journal of Power and Energy*, p. 0957650914542630. DOI: 10.1177/0957650914542630.

Montomoli, F., M. Massini, and S. Salvadori (2011). "Geometrical uncertainty in turbomachinery: Tip gap and fillet radius". In: *Computers & Fluids* 46.1, pp. 362–368. DOI: j.compfluid.2010.11.031.

Montomoli, F., M. Carnevale, A. D'Ammaro, M. Massini, and S. Salvadori (2015). *Uncertainty quantification in computational fluid dynamics and aircraft engines*. Springer. DOI: 10.1007/978-3-319-14681-2.

Myers, R. H. and D. C. Montgomery (2002). *Response surface methodology: Process and product optimization using design experiments*. Hoboken, USA: John Wiley & Sons.

Nadali Najafabadi, H. (2015). "On film cooling of turbine guide vanes: From experiments and CFD-simulations to correlation development". PhD thesis. Linköping University Electronic Press. DOI: 10.3384/diss.diva-117029.

Ng, L. W. T. and K. E. Willcox (2015). "Monte Carlo information-reuse approach to aircraft conceptual design optimization under uncertainty". In: *Journal of Aircraft* 53.2, pp. 427–438. DOI: 10.2514/1.C033352.

Oberguggenberger, M. (2014). "Sensitivity and reliability analysis of engineering structures: Sampling based methods". In: *Computational Engineering*. Ed. by G. Hofstetter. Cham: Springer International Publishing, pp. 85–112. DOI: 10.1007/978-3-319-05933-4_4.

Occhioni, G., S. Shahpar, and H. Li (2017). "Multi-fidelity modelling of a fully-featured HP turbine stage". In: *ASME Turbo Expo 2017: Turbomachinery Technical Conference and Exposition*. American Society of Mechanical Engineers, V02AT40A027–V02AT40A027. DOI: 10.1115/GT2017-64478.

O'Hagan, A. (2013). "Polynomial chaos: A tutorial and critique from a statistician's perspective". URL: http://tonyohagan.co.uk/academic/pdf/Polynomial-chaos.pdf.

Padulo, M., M. S. Campobasso, and M. D. Guenov (2011). "Novel uncertainty propagation method for robust aerodynamic design". In: *AIAA Journal* 49.3, pp. 530–543. DOI: 10.2514/1.J050448.

Padulo, M., M. S. Campobasso, and M. D. Guenov (2007). "Comparative analysis of uncertainty propagation methods for robust engineering design". In: *International Conference on Engineering Design*. URL: https://www.designsociety.org/publication/25352/Comparative+Analysis+of+Uncertainty+Propagation+Methods+for+Robust+Engineering+Design.

Pappu, K. R. and M. T. Schobeiri (1997). "Optimization of trailing edge ejection mixing losses: A theoretical and experimental study". In: *ASME 1997 International Gas Turbine and Aeroengine Congress and Exhibition*. American Society of Mechanical Engineers, V001T03A106–V001T03A106. DOI: 10.1115/1.2821991.

Perdikaris, P., D. Venturi, J. O. Royset, and G. E. Karniadakis (2015). "Multi-fidelity modelling via recursive Co-kriging and Gaussian-Markov random fields". In: *Proceedings of the Royal Society A* 471.2179, p. 20150018. DOI: 10.1098/rspa.2015.0018.

Pisaroni, M. (2017). "Multi level Monte Carlo methods for uncertainty quantification and robust design optimization in aerodynamics". PhD thesis. École Polytechnique Fédérale de Lausanne. DOI: 10.5075/epfl-thesis-8082.

Povey, T., M. Sharpe, and A. Rawlinson (2011). "Experimental measurements of gas turbine flow capacity using a novel transient technique". In: *Journal of Turbomachinery* 133.1, p. 011005. DOI: 10.1115/1.4000481.

Pulido, G. T. and C. A. C. Coello (2004). "Using clustering techniques to improve the performance of a multi-objective particle swarm optimizer". In: *Genetic and Evolutionary Computation Conference*. Springer, pp. 225–237. DOI: 10.1007/978-3-540-24854-5_20.

Ravelli, S., M. Miranda, and G. Barigozzi (2013). "Steady CFD simulations of trailing edge film cooling in a linear nozzle vane cascade". In: *10th European Turbomachinery Conference*, pp. 15–19. URL: http://www.euroturbo.eu/paper/ETC2013-073.pdf.

Reguly, I. Z., G. R. Mudalige, C. Bertolli, M. B. Giles, A. Betts, P. H. J. Kelly, and D. Radford (2015). "Acceleration of a full-scale industrial CFD application with OP2". In: *IEEE Transactions on Parallel and Distributed Systems* 27.5, pp. 1265–1278. DOI: 10.1109/TPDS.2015.2453972.

Rehder, H.-J. (2009). "Investigation of trailing edge cooling concepts in a high pressure turbine cascade: Aerodynamic experiments and loss analysis". In: *ASME Turbo Expo 2009: Power for Land, Sea, and Air*. American Society of Mechanical Engineers, pp. 171–183. DOI: 10.1115/1.4004748.

Rhein, B. (2014). "Robuste Optimierung mit QuantilmaSSen auf globalen Metamodellen". PhD thesis. University of Cologne. URL: http://kups.ub.uni-koeln.de/5604/.

Ristic, M., D. Brujic, and I. Ainsworth (2004). "Measurement-based updating of turbine blade CAD models: A case study". In: *International Journal of Computer Integrated Manufacturing* 17.4, pp. 352–363. DOI: 10.1080/0951192032000159148.

Roache, P. J. (1997). "Quantification of uncertainty in computational fluid dynamics". In: *Annual Review of Fluid Mechanics* 29.1, pp. 123–160. DOI: 10.1146/annurev.fluid.29.1.123.

Salvadori, S., F. Montomoli, F. Martelli, P. Adami, K. S. Chana, and L. Castillon (2011). "Aerothermal study of the unsteady flow field in a transonic gas turbine with inlet temperature distortions". In: *Journal of Turbomachinery* 133.3, p. 031030. DOI: 10.1115/1.4002421.

Scharfenstein, J., K. Heinze, M. Voigt, K. Vogeler, and M. Meyer (2013). "Probabilistic CFD analysis of high pressure turbine blades considering real geometric effects". In: *ASME Turbo Expo 2013: Turbine Technical Conference and Exposition*. American Society of Mechanical Engineers, V06BT43A005–V06BT43A005. DOI: 10.1115/GT2013-94161.

Schobeiri, M. (2005). *Turbomachinery flow physics and dynamic performance*. Springer. DOI: 10.1007/978-3-642-24675-3.

Schobi, R., B. Sudret, and J. Wiart (2015). "Polynomial-chaos-based Kriging". In: *International Journal for Uncertainty Quantification* 5.2. URL: 10.1615/Int.J.UncertaintyQuantification.2015012467.

Seshadri, P., P. Constantine, P. Gonnet, G. Parks, and S. Shahpar (2013). "Stable multivariate rational interpolation for parameter-dependent aerospace models". In: *Collection of Technical Papers-AIAA/ASME/ASCE/AHS/ASC Structures, Structural Dynamics and Materials Conference*. URL: https://www.semanticscholar.org/paper/Stable-Multivariate-Rational-Interpolation-for-Seshadri-Constantine/5567b77f0c139da213f4f5b3565e550077d5f140.

Seshadri, P., P. Constantine, G. Iaccarino, and G. Parks (2016). "A density-matching approach for optimization under uncertainty". In: *Computer Methods in Applied Mechanics and Engineering* 305, pp. 562–578. DOI: 10.1016/j.cma.2016.03.006.

Seshadri, P., S. Shahpar, and G. T. Parks (2014). "Robust compressor blades for desensitizing operational tip clearance variations". In: *ASME Turbo Expo 2014: Turbine Technical Conference and Exposition*. American Society of Mechanical Engineers, V02AT37A043–V02AT37A043. DOI: 10.1115/GT2014-26624.

Shahpar, S. and S. Caloni (2013). "Aerodynamic optimization of high-pressure turbines for lean-burn combustion system". In: *Journal of Engineering for Gas Turbines and Power* 135.5, pp. 055001–11. DOI: 10.1115/1.4007977.

Shahpar, S. and L. Lapworth (2003). "PADRAM: Parametric design and rapid meshing system for turbomachinery optimisation". In: *ASME Turbo Expo 2003, collocated with the 2003 International Joint Power Generation Conference*. American Society of Mechanical Engineers, pp. 579–590.

Sidwell, C. V. (2004). "On the impact of variability and assembly on turbine blade cooling flow and oxidation life". PhD thesis. Massachusetts Institute of Technology. DOI: 1721.1/17814.

Sinha, A., B. Hall, B. Cassenti, and G. Hilbert (2008). "Vibratory parameters of blades from coordinate measurement machine data". In: *Journal of Turbomachinery* 130.1, p. 011013. DOI: 10.1115/1.2749293.

Smith, R. C. (2013). *Uncertainty quantification: Theory, implementation, and applications*. Vol. 12. Raleigh, USA: SIAM.

Spalart, P. R. and S. R. Allmaras (1992). "A one equation turbulence model for aerodynamic flows". In: *30th aerospace sciences meeting and exhibit*. DOI: 10.2514/6.1992-439.

Steen, W., K. G. Watkins, and J. Mazumder (2010). *Laser material processing*. 4th ed. London, UK: Springer Science & Business Media. DOI: 10.1007/978-1-84996-062-5.

Taguchi, G. and A. J. Rafanelli (1993). *Taguchi on robust technology development: Bringing quality engineering upstream*. DOI: 10.1115/1.800288.

Tartinville, B. and C. Hirsch (2008). "Modelling of film cooling for turbine blade design". In: *ASME Turbo Expo 2008: Power for Land, Sea, and Air*. American Society of Mechanical Engineers, pp. 2219–2228. DOI: 10.1115/GT2008-50316.

Telisinghe, J. C. (2013). "Film cooling of turbine blade trailing edges". PhD thesis. University of Oxford. URL: https://ora.ox.ac.uk/objects/uuid:86c06246-16e9-4378-9a61-e09317d31a92.

Thakur, N. (2010). "Probabilistic manufacturing variability quantification from measurement data for robust design of turbine blades". PhD thesis. University of Southampton. URL: http://eprints.soton.ac.uk/342797/.

Vinogradov, K., G. Kretinin, K. Otryahina, R. Didenko, D. Karelin, and Y. Shmotin (2016). "Robust optimization of the HPT blade cooling and aerodynamic efficiency". In: *ASME Turbo Expo 2016: Turbine Technical Conference and Exposition*. American Society of Mechanical Engineers, V02CT45A003. DOI: 10.1115/GT2016-56195.

Voigt, M., R. Mücke, K. Vogeler, and M. Oevermann (2004). "Probabilistic lifetime analysis for turbine blades based on a combined direct Monte Carlo and response surface approach". In: *ASME Turbo Expo 2004: Power for Land, Sea, and Air*. American Society of Mechanical Engineers, pp. 327–335. DOI: 10.1115/GT2004-53439.

Voigt, S., B. Noll, and M. Aigner (2010). "Aerodynamic comparison and validation of RANS, URANS and SAS simulations of flat plate film cooling". In: *ASME Turbo Expo 2010: Power for Land, Sea, and Air*. American Society of Mechanical Engineers, pp. 1471–1480. DOI: 10.1115/GT2010-22475.

Voisey, K. T. and T. W. Clyne (2004). "Laser drilling of cooling holes through plasma sprayed thermal barrier coatings". In: *Surface and Coatings Technology* 176.3, pp. 296–306. DOI: 10.1016/S0257-8972(03)00748-5.

Voutchkov, I. and A. J. Keane (2010). "Multi-objective optimization using surrogates". In: *Computational Intelligence in Optimization: Applications and Implementations*.

Ed. by Y. Tenne and C.-K. Goh. Berlin Heidelberg: Springer, pp. 155–175. DOI: 10.1007/978-3-642-12775-5_7.

Wilcox, D. C. (1988). "Reassessment of the scale-determining equation for advanced turbulence models". In: *AIAA Journal* 26.11, pp. 1299–1310. DOI: 10.2514/3.10041.

Wong, T. H., P. T. Ireland, and K. P. Self (2015). "Film cooling effectiveness measurements on engine representative trailing edge slots including cutback surface protuberances". In: *Proceedings of 11th European Conference on Turbomachinery Fluid dynamics & Thermodynamics (ETC11)*. URL: http://www.euroturbo.eu/paper/ETC2015-254.pdf.

Xiu, D. and G. E. Karniadakis (2003). "Modeling uncertainty in flow simulations via generalized polynomial chaos". In: *Journal of Computational Physics* 187.1, pp. 137–167. DOI: 10.1016/S0021-9991(03)00092-5.

Yang, Z. and H. Hu (2012). "An experimental investigation on the trailing edge cooling of turbine blades". In: *Propulsion and Power Research* 1.1, pp. 36–47. DOI: 10.1016/j.jppr.2012.10.007.

Zaretsky, E. V., J. S. Litt, R. C. Hendricks, and S. M. Soditus (2012). "Determination of turbine blade life from engine field data". In: *Journal of Propulsion and Power* 28.6, pp. 1156–1167. DOI: 10.2514/1.B34375.

Zhang, Y. and S. Hosder (2013). "Efficient robust design with stochastic expansions". English. In: *Surrogate-Based Modeling and Optimization*. Ed. by S. Koziel and L. Leifsson. Springer New York, pp. 247–284. DOI: 10.1007/978-1-4614-7551-4_11.

Zhao, W., S. Gao, and H. Lin (2007). "A robust hole-filling algorithm for triangular mesh". In: *The Visual Computer* 23.12, pp. 987–997. DOI: 10.1007/s00371-007-0167-y.

Zitzler, E., M. Laumanns, and L. Thiele (2001). "SPEA2: Improving the strength Pareto evolutionary algorithm". In: *TIK-report* 103. DOI: 10.3929/ethz-a-004284029.